

*Fatigue of welded high strength steels for automotive
chassis and suspension applications*

Kadhun Mehdy Shrama

B.Sc., M.Sc.

Thesis submitted for the degree of Doctor of Philosophy



School of Engineering

Cardiff University

UK

Supervisors:

Prof. Sam Evans, Dr. Rhys Pullin and Dr. Alastair Clarke

Declaration and Statements

Declaration

This work has not previously been accepted in substance for any degree and is not concurrently submitted in candidature for any degree.

Signed..... (Kadhun Shrama) Date.....

STATEMENT 1

This thesis is being submitted in partial fulfilment of the requirements for the degree of PhD.

Signed..... (Kadhun Shrama) Date.....

STATEMENT 2

This thesis is the result of my own independent work/investigation, except where otherwise stated. Other sources are acknowledged by explicit references. The views expressed are my own.

Signed..... (Kadhun Shrama) Date.....

STATEMENT 3

I hereby give consent for my thesis, if accepted, to be available for photocopying and for inter-library loan, and for the title and summary to be made available to outside organisations.

Signed..... (Kadhun Shrama) Date.....

Abstract

The automotive industry is under expanding legislative pressure to decrease vehicle weight in order to enhance fuel efficiency; and to improve crash performance as well. For this purpose, hot rolled FB590 is a high strength steel (HSS) which can be used in automotive chassis and suspension applications. A major problem affecting mainly car underbodies is the effect of corrosion, often nucleating at sites where stone chipping has damaged protective coatings. Therefore, car components are frequently exposed to aggressive environments as a consequence of aqueous salts from the street coming into contact with affected and unprotected steel. This circumstance significantly decreases both the life and the appearance of the influenced parts, and may result in compromised structural strength leading to catastrophic failure.

The main aim of this research is to further the understanding of the effects of simulated operational environments. Fatigue tests were initially carried out on mild steel under tensile loading and two severity-levels of corrosion as preliminary tests. Then a comprehensive programme of fatigue tests was performed on FB590 and its welds under bending and tensile loading and covering the range of environmental conditions experienced in automotive applications. There is no available data for FB590 in terms of fatigue performance in various environments and under bending and tensile loading as well. Additional techniques such as surface profilometry, scanning electron microscopy and so on were added to support the findings. The other aim was to monitor fatigue tests using a combination of Acoustic Emission (AE) and Digital Image Correlation (DIC) to identify the damage mechanisms that occur during failure although there had been limited research in this area. The combination of AE and DIC can provide much useful information to help to distinguish the different AE signals originating from various possible failure mechanisms such as plastic deformation, delamination of corrosion products or DIC paint and crack initiation and propagation. This might be utilized for an effective and powerful approach to monitoring multiple failure mechanisms; this has significant applications in automotive chassis testing.

This information can provide a very valuable tool for the purpose of assessing material for automotive designers, which can then be used to decide on appropriate safety factors to avoid over-designing products and in order to ensure reliability and robustness of new products. In addition, the steel industry can also benefit from this research, as these findings can assist in enhancing the products and diminishing the effects of these environments on structural integrity.

Acknowledgements

I would like to express my deepest gratitude and thanks to my supervisors, Professor Sam Evans, Dr. Rhys Pullin and Dr. Alastair Clarke for their effort, many hours of advising and guidance, encouragement and proof-reading throughout the duration of this work.

I would also like to thank Dr. Gary Bright, Dr. Matthew Pearson and Dr. Johen McCory for their advice and help. I am also grateful to TATA steel UK for their support and help in my research. I must not forget to thank the technical staff at Cardiff School of Engineering especially Ian King, Steffan Jones, Richard Thomas and Harry Lane for their help, support and technical advice throughout my experimental investigations. I would also like to thank my friends and colleagues whom I have not mentioned here.

Further gratitude and appreciation is expressed to my country, Iraq (Ministry of Higher Education and Scientific Research/Ministry of Electricity) for funding my study and giving me this opportunity.

Last but not least, I cannot find words to express my feeling and gratitude to the memory of my mother, and I am indebted to my father for his continuous support for the whole of my life. I am also thankful to all my family in Iraq especially my brother Dr. Raisan Aljabery for his great support. I also owe sincere thankfulness to my wife Mrs Nawal Aljabery for her continuous support and patience throughout these years.

Contents

Declaration and Statements	ii
Abstract	ii
Acknowledgements	iii
Contents	iv
1. Introduction	1
1.1 Introduction	1
1.2 Novelty Claimed	3
1.3 Published outputs	4
1.4 Outline of the Thesis	5
1.5 Project aims and objectives	6
2. Literature Review	9
2.1 Introduction	9
2.2 Steels for automotive chassis and suspension applications	9
2.3 Fatigue strength of welded structures	11
2.4 Mechanical testing for automotive chassis	13
2.5 Introduction to fatigue	14
2.5.1 Fatigue limit (Endurance Limit)	16
2.5.2 Staircase method	17
2.5.3 Fatigue crack initiation and propagation	18
2.5.4 Influence of notches on the fatigue life	19
2.6 Fatigue of four point bending	20
2.7 Corrosion	22
2.7.1 Types of corrosion	23
2.7.2 Corrosion-Failure Mechanisms	23
2.7.3 Test standards for cyclic corrosion tester	25
2.8 Automotive E-Coating	27
2.9 Stone Chipping	29
2.10 Surface topography	31
2.11 Acoustic Emission	34
2.12 Digital Image Correlation	39
2.13 Combination of AE and DIC techniques	41
2.14 Conclusion	42

3. Experimental equipment, procedures and techniques	56
3.1 Introduction	56
3.2 Materials and specimens preparation	56
<i>3.2.1 Welded Test specimens preparation</i>	56
<i>3.2.2 Welding Trials at Warwick Manufacturing Group</i>	57
3.3 Tensile strength measurements	58
3.4 Specimens design	59
<i>3.4.1 Mild steel fatigue specimen design</i>	59
<i>3.4.2 FB590 fatigue specimen design</i>	60
<i>3.4.3 FB590 four-point bending fatigue specimen design and preparation</i>	61
3.5 Fatigue loading and test set up	62
<i>3.5.1 Loading Calculation</i>	62
<i>3.5.2 Loading machines</i>	63
<i>3.5.3 Bending loading frame set-up and dimensions</i>	64
<i>3.5.4 Fatigue test monitoring</i>	64
3.6 Fractographic sample preparation	64
3.7 Acoustic emission instrumentation and techniques	65
<i>3.7.1 Data acquisition and storage</i>	65
<i>3.7.2 AE sensors</i>	65
<i>3.7.3 Sensor mounting and Couplant</i>	66
<i>3.7.4 Hsu-Nielsen source</i>	66
3.8 Preparing digital image correlation	67
3.9 MTS measurement and DIC comparison	68
3.10 Dye penetrant inspection	69
3.11 Stone Chipping Test Method	69
3.12 Corrosion test Characterization	72
3.13 Surface profile measurements	73
<i>3.13.1 Corrosion depth measurement</i>	74
3.14 E-coating Setup and procedure	75
3.15 Metallurgy test of mild and high strength steel	76
4. Preliminary Experimental Studies with Mild Steel Samples	101
4.1 Introduction	101
4.2 Tensile performance of mild steel	101
4.3 Corrosion surface measurement and assessment	102

4.4 Fatigue Performance of mild steel	104
4.5 Acoustic Emission analysis for mild steel fatigue tests	107
<i>4.5.1. Results and acoustic emission analysis</i>	107
<i>4.5.2 Fractography characterization</i>	108
<i>4.5.3 Plastic deformation</i>	109
4.6 Conclusions	113
5. The Preparation of Experimental Studies for FB590	131
5.1 Introduction	131
5.2 Material properties	131
5.3 Tensile performance of FB590	132
5.4 Hand calculation for four-point bending tests	133
5.5 Fatigue performance of FB590	134
5.6 Metallurgy test of MIG Welds of FB590	134
5.7 Micro hardness measurements	135
5.8 Acoustic Emission for FB590 fatigue tests	136
<i>5.8.1 Results and Acoustic Emission analysis</i>	137
5.9 Conclusions	140
6. Fatigue properties of FB590	156
6.1 Introduction	156
6.2 Evaluation of surface quality	156
<i>Surface assessment of as received and Ecoated samples</i>	156
<i>Surface assessment of stone chipping specimens Group 2</i>	157
<i>Surface assessment of Group 3 and 4</i>	157
<i>Surface assessment of Group 5</i>	157
<i>Measuring surface roughness parameters</i>	158
6.3 Surface assessment description	158
6.4 Performance of FB590 Products	160
<i>6.4.1 Base line E coated only (Group 1) S-N Curves</i>	161
<i>6.4.2 Tension and Bending S-N Curves for Group 2</i>	161
<i>6.4.3 Tension and Bending S-N Curves for Group 3</i>	162
<i>6.4.4 Tension and Bending S-N Curves for Group 4</i>	162
<i>6.4.5 Tension and Bending S-N Curves for Group 5</i>	162
6.5 S-N curves	163
6.6 Stress concentration due to weld geometry and stone chipping	164

6.7 Fractography of fatigue bending specimens	165
6.8 Fractography of fatigue tension specimens	166
6.9 Conclusions.....	167
7. Discussion.....	190
7.1 Introduction.....	190
7.2 Materials Selection.....	190
<i>7.2.1 Steel Grades</i>	<i>190</i>
<i>7.2.2 Comparison of FB590 with other materials</i>	<i>193</i>
7.3 Effect of corrosion, stone chipping and welding on fatigue life	194
<i>7.3.1 Effect of stress magnitude on fatigue life</i>	<i>194</i>
<i>7.3.2 Effect of stone chipping on fatigue life</i>	<i>195</i>
<i>7.3.3 Effect of weld on fatigue life</i>	<i>197</i>
<i>7.3.4 Effect of pre-corrosion on fatigue life</i>	<i>199</i>
7.4 Combination of monitoring using AE and DIC techniques	202
7.5 The Possible Applications of this study	203
7.6 Research limitations and implications	205
7.7 Conclusion	207
8. Conclusions and further work	224
8.1 Conclusion	224
8.2 Future work.....	224
References.....	230
Appendix A: Summary of fatigue test.....	243
Appendix B- Published Papers	246

1. Introduction

1.1 Introduction

Automotive vehicles play an important role in our daily life. This makes it important to continually attempt to reduce their production costs in accordance with the advancement of innovation, this need for effective designs is more noteworthy than at any time before. Nowadays, with progressively tighter legislation on vehicle emissions, the automotive industry is under increased pressure to produce vehicles that are more fuel efficient and with better crash performance as well as to meet customer requests for comfort, safety, performance and numerous different qualities. Consumers often desire vehicles that have reasonable fuel consumption and fall within low tax brackets, which are governed by CO₂ emissions, so the pressure for efficiency does not solely originate from government legislation. Thus it is safe to say that gauge reduction of steel sheets for cars has represented a reaction to the market demands. In this way, decreasing vehicle mass is a key concern for all car makers in today's market atmosphere.

Various steels families have been utilized for vehicle chassis and suspension systems throughout the years, where car makers are continuously looking for higher strength steels in order to down-gauge. The uses of high strength steel (HSS) sheets are growing as one of the methods for meeting the requirements of the modern automotive industry. Most work to date has concentrated on body applications, since this is the heaviest part of the vehicle, however this presents significant challenges in maintaining sufficient ductility for forming operations and crashworthiness. There has been limited work on the use of high strength steels in chassis and suspension applications, but these components may comprise as much as 25% of vehicle weight and there are particular dynamic performance benefits in reducing unsprung mass (Kawano, 2003, Fournalis et al., 2007).

Heat treatment is one way to obtain higher strength without increasing weight. However, the corrosion-fatigue resistance of this steel decreases when it is quenched and tempered to increase its strength. In this manner, there is an undeniable trade off between high strength and the material's failure to perform

well in corrosive environments. Thus, automotive engineers are interested in optimizing the strength of alloy steels whilst maintaining good corrosion resistance (AHSS, 2014).

Previous studies (Bright, 2012, Ellwood, 2003) carried out to date by Tata steel aimed to identify fatigue lives for materials used in chassis and suspensions applications under tensile loads only. However, these studies concentrated on the as-received material and did not take the effect of the operational environment such as the stone chipping and corrosion on fatigue lives of steel products and their welds. With this in mind, the focus of this study is on evaluating the fatigue performance of FB590 Tata steel grade and its welds under tensile and bending loading taking into account the range of environmental conditions to which the steel could be exposed in service. Fatigue data in axial loading are insufficient for assessing high cycle fatigue limit stress which often occurs in components that are subjected to flexural loading like chassis. Therefore, it is essential to investigate the bending fatigue master curves behaviour so as to obtain sufficient fatigue data for a meaningful fatigue strength assessment of actual components. Particular emphasis was placed on identifying and understanding the effect of the stone chipping and corrosion on fatigue lives, with a view to minimising or eliminating their influences, this eventually contributes to promote the confident and efficient use of Tata Steel materials.

Acoustic Emission (AE) is proposed as a structural health monitoring (SHM) tool to continuously monitor many structural systems throughout the qualification testing and eventually replace the periodic Non Destructive Testing (NDT). AE is able to provide early warning of fatigue within the structure without interruption of the test schedule. The cost of removal and installation to the rig could be eliminated. Further benefits include identification of the particular load case and critical load at which damage occurs. This could greatly improve the understanding of the occurrence of failure (Baxter, 2007). Digital Image Correlation (DIC) is a full-field strain measurement technique, and was used to support the understanding of the detected AE signals and validate the findings. DIC provides a clear depiction of the surface strain field evolution. The complementary use of DIC and AE helps to minimise the assumptions in the

interpretation of the AE data. This combination of AE and DIC can also provide much useful information in attempting to distinguish the different AE signals originating from various possible failure mechanisms such as plastic deformation, delamination of corrosion product or DIC paint, and crack initiation and propagation. The research presented in this study also includes a wider project which ultimately aims to develop a fatigue test monitoring system to identify crack initiation from background noise for both mild steel and high strength steel (FB590) and its welded structure which is produced by Tata steel, after overcoming the problems such as background noise, time misalignment with cycles and so on. Figure 1.1 shows the first work plan which was implemented on mild steel and Figure 1.2 shows the developed work plan which was applied to FB590.

The FB590 work plan is explained in detail since it is more comprehensive than the mild steel work plan, and includes refinements to experimental technique developed during the mild steel phase of work. Five sets of tensile and bending fatigue specimens were prepared from welded and un-welded material and then tested following exposure to different environmental conditions shown in Figure 1.2, in order to cover all the possibilities of the operational environment, each group consisting of 8 samples. These sets of fatigue specimens were prepared to simulate the actual working conditions encountered by the chassis in use, and to examine the effect of damage due to environmental exposure on the initiation of fatigue cracks. The first set was the control group of intact specimens. The second set had the aim of assessing the susceptibility of FB590 to stone chipping, whereas the third and fourth aim was to assess the susceptibility of FB590 to exposure to low and high levels of corrosion following stone chipping, respectively. Finally, the fifth set was exposed to a high level of corrosion only, without stone chipping.

1.2 Novelty Claimed

The work focuses on performing a comprehensive experimental fatigue investigation for FB590 steel grade. These kinds of information constitutes as experimental model can help the steel maker and automotive industry to assess the

material in high cycle fatigue and in the service environment. The novelty of the work is highlighted below:

- The main aim of this work is to provide novel S-N curves data for FB590 and its weldment under tension and bending fatigue loading. Moreover performing these tests under range of environmental conditions experienced in automotive applications.
- Fatigue testing for mild steel under tensile loading and two severity-levels of pre-corrosion are unknown previously.
- Actual simulate for the operational or service conditions such as stone chipping and corrosion chamber.
- The effects of the stone chipping on corrosion and on fatigue properties were performed for the first time in this study, where most studies focussed on the determination and evaluation of coating resistance to chipping damage by stones or other flying objects.
- The fatigue tests under bending loading were rarely conducted in general. In this study these test were carried out for the first time for unnotch specimen of FB590 and its weldment under different environmental conditions.
- This work aimed to establish a full understanding of the use of a combination of AE and DIC under fatigue loading in order to provide valuable experimental data interpretation and this contributes to enriching the limited literature in this field, where these techniques helpful in distinguishing different mechanisms which take place in the way of final failure.

1.3 Published outputs

As a result of the work of this project, numerous studies have been presented as posters and some published with respect to the fatigue crack monitoring using acoustic emission and digital image correlation. There are other studies not published yet with respect to the fatigue properties of FB590 and environment effect.

Journal papers:-

- Shrama, K., Pullin, R., Clarke, A. and Evans, S.L., 2015. “Fatigue crack monitoring in mild steel specimens using acoustic emission and digital image correlation”. *Insight-Non-Destructive Testing and Condition Monitoring*, 57(6), pp.346-354

Conference papers:-

- Kadhum Shrama, Rhys Pullin, Alastair Clarke, S.L. Evans. “Detection of Cracking in Mild Steel Fatigue Specimens Using Acoustic Emission and Digital Image Correlation”, 31st Conference of the European Working Group on Acoustic Emission (EWGAE) – We4B2, (2014).

Manuscript papers:-

- Shrama, K., Pullin, R., Clarke, A. and Evans, S.L., “Fatigue damage characterization in welded plates using Acoustic Emission and Digital Image Correlation”, in preparation for submission.
- Shrama, K., Pullin, R., Clarke, A. and Evans, S.L., “The influence of operational environment on the fatigue life of FB590 TATA steel grade under tension and bending loading”, in preparation for submission.

1.4 Outline of the Thesis

The objectives of this research have been identified, together with background information on the subject of the research, in this chapter. The following chapters contain the details of this research. Chapter two provides the previous studies and an overview of literature pertinent to the subjects covered in this thesis. Chapter three, describes the test specimens and the experimental equipment, procedures and techniques used in this study. Preliminary experimental studies using mild steel samples are presented in Chapter four. Chapter five summarizes the preparations of experimental studies for FB590. The results of FB590 in terms of surface assessment description, fatigue performance of tensile and bending S-N curves are presented in Chapter six. Chapter seven includes a discussion of the results presented in thesis where the data is analyzed. Chapter eight outlines the conclusions and suggests directions for future work.

1.5 Project aims and objectives

The objectives of this research can be summarized as follow.

- 1- Preliminary experimental studies were performed by using mild steel fatigue specimens under tensile loading and two levels of corrosion.
- 2- The FB590 was identified as a relevant steel grade in collaboration with Tata.
- 3- Manufacture test specimens using MIG/MAG welding method.
- 4- Prepare tensile and bending specimens then expose them to different types of environments to cover typical environments encountered by the chassis in practical service.
- 5- Perform comprehensive metal and weld fatigue tests under tensile and bending loading as well as supporting tests such as surface profilometry, scanning electron microscopy and so on, in order to fully evaluate the fatigue performance of FB590.
- 6- Monitor fatigue tests using AE and DIC to identify crack initiation and propagation and other mechanisms which take place during failure.

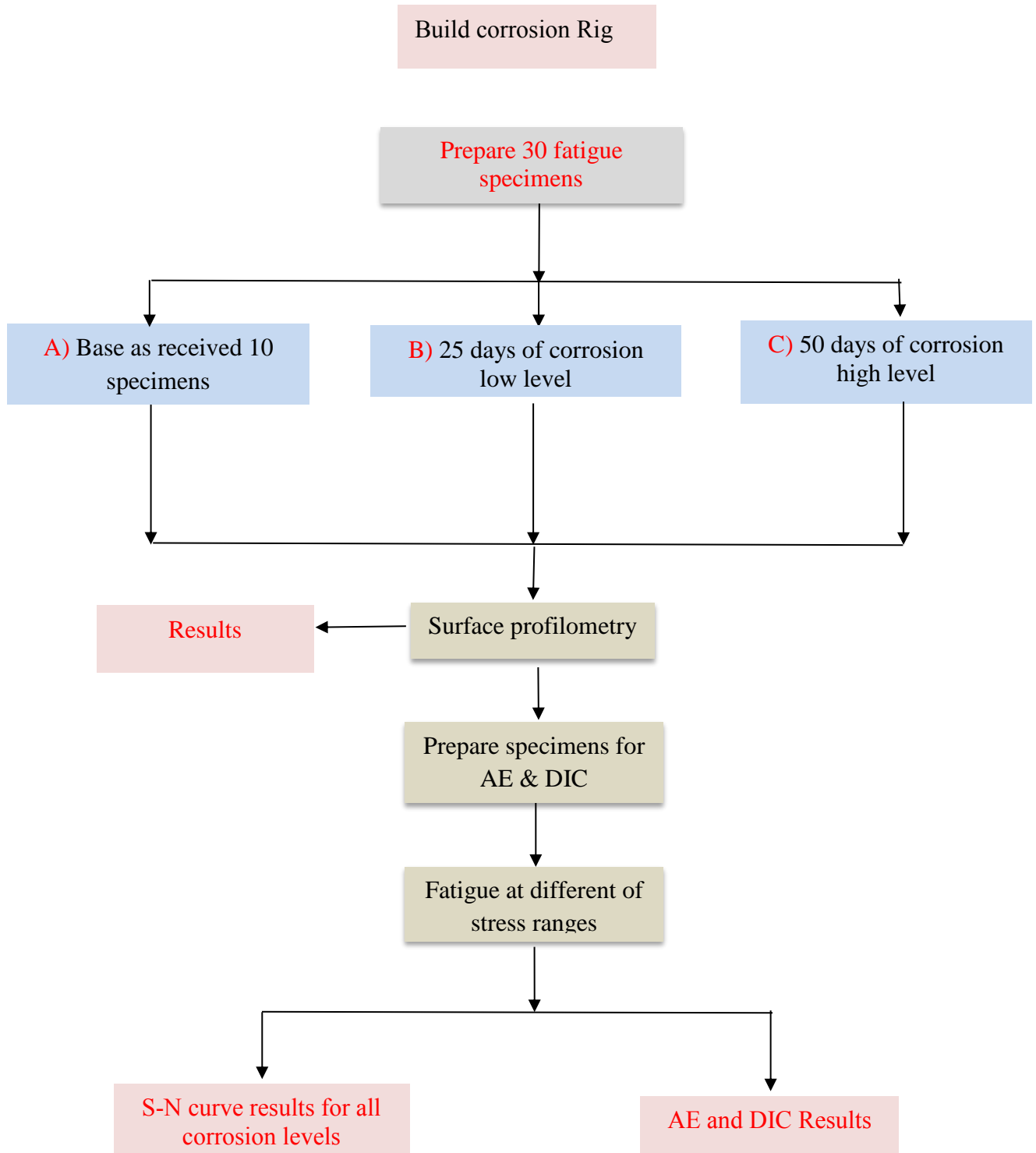


Figure 1.1: Mild steel work plan.

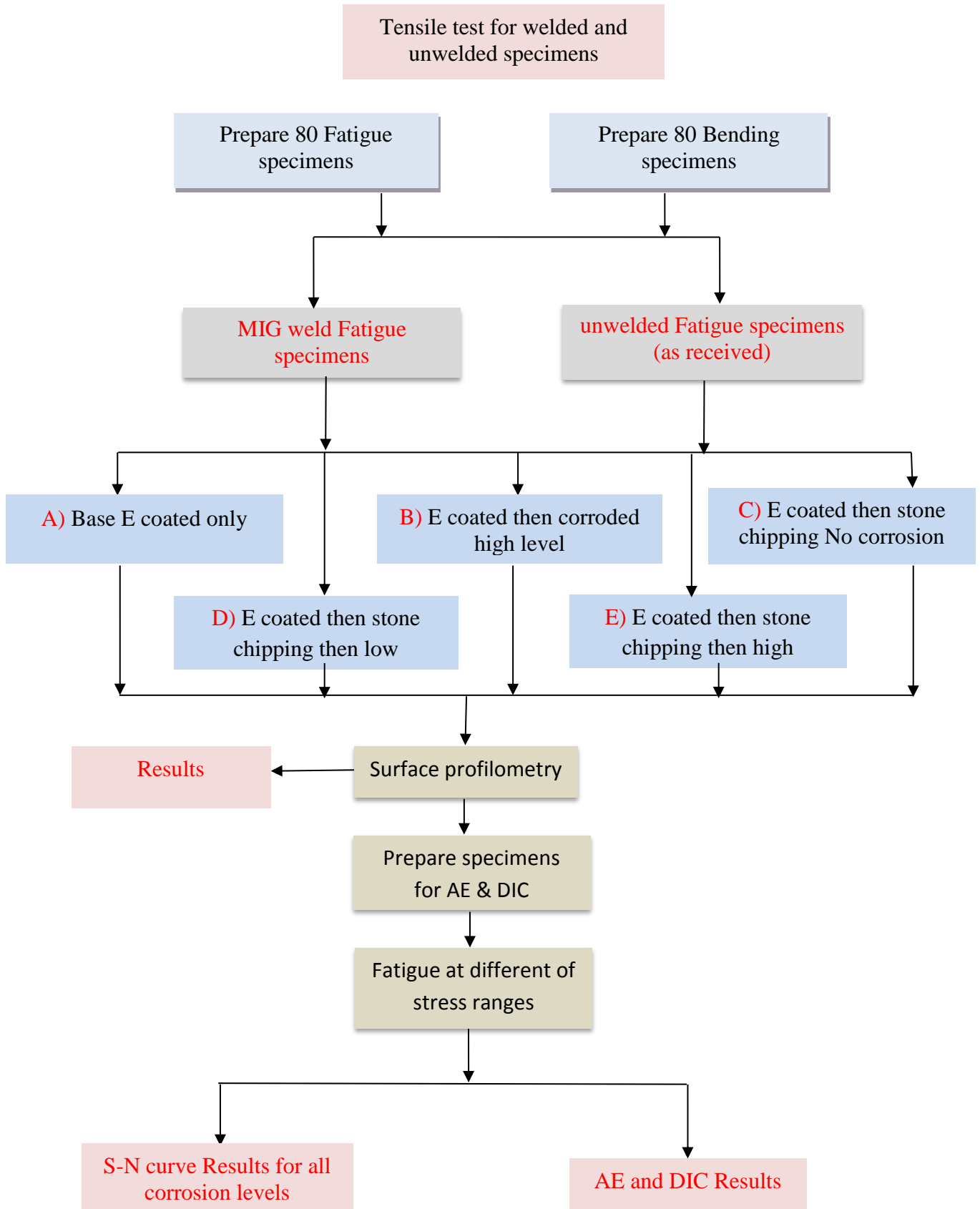


Figure 1.2: FB590 steel work plan.

2. Literature Review

2.1 Introduction

The aim of this section is to provide the reader with an overview of the relevant literature in the range of fields in which this multi-disciplinary PhD study was undertaken. This literature review covers previous investigations into the relevant materials, failure mechanisms, testing methods and failure detection techniques used in this study.

2.2 Steels for automotive chassis and suspension applications

The chassis can be defined as a structure on which a motor vehicle is erected or as the base frame of the vehicle which has to carry all the components and support all the loads. It forms the spine of the vehicle and also represents the survival cell for the passengers. Nowadays, the tyres and the steering system of the vehicle are included in the expression of chassis where the term chassis is often used with a more general meaning, including not only the frame but also the suspension. Therefore, the chassis is considered as the most important element of the vehicle and should fulfill several purposes (Genta and Morello 2009; Sampo 2011) such as:

- It holds all the parts and components together.
- connection of the suspension system;
- protection of the occupants during crash events;
- Supporting all the loads include the weight of each component and the forces generated by acceleration, deceleration and cornering.

Automotive chassis and suspension covers a wide range of components, with several types of designs and assemblies. It is important to have a well-designed chassis to ensure the safety, performance and roadworthiness of the vehicle. Besides safety aspects, a chassis must also be designed to reduce mass in order to improve fuel economy and reduce CO₂ emissions. Therefore, modern chassis designs will be optimised to accommodate both the safety and fuel efficiency requirements. Nowadays, sub-frames are usually used in modern chassis systems

compared to the vehicles of previous generations. Suspension and sub-frame assemblies are connected most often with the engine cradle as shown in Figure 2.1. Sub-frames and suspension assemblies must offer ease of vehicle assembly since they are typically assembled away from the main production line and are bolted onto the vehicle quickly and easily during assembly (Fourlaris et al. 2007; Veloso et al. 2009; Sampo 2011).

Nowadays, steel and aluminium are the predominant materials used for the mass production of automotive structures (Fourlaris et al. 2007). Steel is the most popular material used for commercial automotive chassis and suspension components. These components are very susceptible to fatigue failure within a vehicle, because of the high levels of cyclic loading they encounter during regular use. As such the chassis and suspension components need to be designed to resist various loading conditions from a range of sources. These forces can be either lateral cornering forces, longitudinal accelerating or braking forces, vertical suspension forces or combinations of these (Genta and Morello 2009; Hägele and Sonsino 2014). Steel has an advantage compared with other material since the fatigue strength usually ranges between 10^6 and 10^8 cycles, providing engineers with a confident data limit to work within as well as being relatively inexpensive when compared to other materials that offer suitable levels of fatigue resistance such as composites and aluminium. However, the usage of aluminium is increasing, especially for multi-link suspensions and for lightweight vehicle bodies (LeBozec et al. 2012; Hägele and Sonsino 2014).

Various groups of steels have been utilized for vehicle chassis and suspension systems over the years. Car makers continuously look for higher strength steels since the end goal is to down gage components, in order to decrease mass and hence enhance the fuel efficiency and reduce CO₂ emissions. Total elongation and ultimate tensile strength are frequently used to rank automotive steels (AHSS 2014). There is a general pattern that steels with high yield and ultimate tensile strengths have a tendency to be more brittle and less formable. Figure 2.2 illustrates tensile strength vs total elongation ranges of Advanced High Strength Steels (AHSS) (colour) compared to conventional automotive steels (grey), and also demonstrates how elongation values have a tendency to decrease as yield

strength increases (AHSS 2014). High strength low alloy steels (HSLA) are at present the most common family utilized in chassis and suspension applications, however there has been a late push towards Advanced High Strength Steels (AHSS), specifically Dual Phase (DP) steels (Bhole et al. 2011; Bright 2012). FB590 is a ferrite-bainite (AHSS), designed to offer high strength, ductility, and formability. It can be used in automotive chassis and suspension applications, such as, upper and lower control arms, engine sub-frames and so on. FB steels sometimes are used to achieve certain customer application demands that require Stretch Flangeable (SF) or High Hole Expansion (HHE) capabilities for improved edge stretch capability. The fundamental feature of FB steels compared with HSLA and DP steels is the improved stretchability of sheared edges as explained by the hole expansion test (AHSS 2014).

2.3 Fatigue strength of welded structures

Automotive industries implement different welding methods to join steel sheets for the production of auto bodies and different structural components (Omar 2011). Nevertheless, resistance spot welding (RSW) is currently one of the predominant procedures for assembling auto body structures (Ellwood 2003; Bhole et al. 2011), whilst MIG/MAG is the most popular technique utilized for structural chassis components such as lower control arms, sub-frames, and so on, (Ellwood 2003; Potukutchi et al. 2004). Figure 2.3 is a schematic of the MIG welding procedure, from which it is clear that numerous factors can add to the general performance of the weld and that optimising these conditions is important. These factors include the welding wire chemistry, wire size and extension, heat input, welding angle, current, voltage, nozzle speed, and shielding gas. These factors will influence the weld's performance regardless of whether the weld procedure is automated or not. The component manufactured will be less susceptible to fatigue failure and tend to be more powerful when these conditions have been optimised. The three most significant aspects listed are the nozzle control, wire speed and heat/current. The high- quality weld can be achieved by controlling the right amount of heat which is a function of welding current, the correct nozzle control and the appropriate wire speed. Defects such as porosity, lack of penetration, hot cracking, strength

reduction, distortion and residual stresses can occur if these parameters are not chosen properly.

The stress concentrations, weld defects and strength reduction lead to comprehensive static and fatigue strength decrease in comparison with the base materials. Fatigue failures usually occur at locations of high stress in either the base material or weldments. Base material failures usually take place at sharp corners, openings or at edges (Benham et al. 1996). Fatigue failure in weldments is extremely dependent on a range of factors such as material, environment, welding techniques, connection details, weld quality and the geometric profile of the weld (Harati et al. 2015). There is much available literature relating to weld geometry as this is thought to be one of the primary factors that controls the fatigue life of welded joints. The weld toe is one of the most likely fatigue crack initiation sites in welded components due to high level of stress concentration, rather than any reason caused by the original specimen microstructure, and/or properties relating to the filler material (Caccese et al. 2006; Bright 2012; Harati et al. 2015; Stenberg et al. 2015). However, the role of other factors such as microstructure effects is undeniable (Wang et al. 2016).

The presence of residual stresses in engineering components and structures can significantly affect the fatigue behaviour during external cyclic loading. The tensile residual stresses will reduce the fatigue life of the structure by increasing the growth of the fatigue crack, while compressive residual stresses will decrease fatigue crack growth rate. Pang (2013) concluded that residual stress had a relatively larger influence than the weld toe geometry on fatigue strength.

Most fatigue life improvement techniques in welded steel structures applied to date are post weld operations such as grinding, shot peening, blasting, hammering, water-jet eroding and re-melting as discussed by Kirkhope et al.(1999) . They indicated that there are special welding methods that are applied as part of the welding process in an attempt to reduce the cost of post-weld finishing. These approaches are attractive because at the production stage lower costs and the simpler quality control can be achieved than for post-weld procedures. The goal of these procedures is to produce improved weld profiles and thus reduce the stress concentration at the weld toe and thereby improve fatigue life without the need of

post-weld operations. The combination of laser welding and gas-metal-arc welding (GMAW) is one of these special welding techniques (Caccese et al. 2006).

Recently, a new method called Friction stir welding (FSW) has been proposed as an alternative for improving the fatigue behaviour of MIG welds (Costa et al. 2014). However, the FSW joints have not been yet tested for long - term service conditions, as well as the techniques suffers from a thermo-mechanically affected zone equivalent to the heat affected zone (HAZ) in fusion welding, and the FSW is limited in terms of the weld geometries and requires large clamping forces (Omar 2011).

2.4 Mechanical testing for automotive chassis

With ever increasing demand for high quality and reliable chassis components and materials, the automotive chassis components are generally designed for planned service life. As a result automotive manufacturers are committed to ensuring products do not fail within their planned lifetime. However, there is a big challenge when accurately determining the service life of a component, mainly due to inherent variations in material properties and loading histories. To solve this a more realistic assessment of component design is required via experiments under actual circumstances, in a representative environment. The purpose of durability tests (or road experiments) is to subject a component to realistic service conditions prior to mass production (Palma and dos Santos 2002).

The manufacturers check their products on public roads and on their own proving grounds because of customers' increased expectations, product complexity and competition. However, performing all these tests in this way becomes very expensive. Many of these durability tests were simulated in the laboratory due to developments in testing technology. Thus, the cost of these tests will be less where customers' service cycles could be simulated under controlled conditions in the laboratory (Palma and dos Santos 2002; Ellwood 2003).

Many authors have published papers about fatigue failures and/or fatigue design of automotive components (Ellwood 2003; Fourlaris et al. 2007; Thomas et al. 2011b; Bright 2012). Heyes (1998) studied the distribution of failures in vehicles

as presented in Figure 2.4. The most common component failures occur within the engine (41%) and chassis/body is responsible for only 7% of the reported failures. However, failures of the chassis and associated components can be catastrophic with serious consequences. In some cases, these in-service failures result in the recall of all affected vehicles with associated costs and negative publicity (Heyes 1998; Veloso et al. 2009). Therefore, many tests can be performed on strip steel to show its mechanical properties. These properties can be connected to tensile performance, fatigue performance, formability, hardness etc. However typically only three properties are determined to characterise the delivery condition of each coil, these three are the UTS, yield stress and elongation to failure (Bright 2012). Chassis components structural durability design has to be performed through a consideration of all possible types of service loadings as shown in Figure 2.5 (Hägele and Sonsino 2014). However, until now there is a lack of information for automotive chassis steel in term of fatigue performance under all possible types of service environments, which is the focus of the current study. These data and information will help engineers understand the true mechanical properties of the material and component under various environments that are anticipated.

A vital part of the design for automotive chassis structures is to guarantee that their durability targets are met. Due to manufacturers' intention to build structures that survive beyond the typical 1,000-100,000 cycles, high cycle fatigue became of particular interest, more so than low cycle fatigue. The durability (fatigue lives) of metal and welds in new chassis products can be evaluated by multiple approaches such as a combination of computer-aided fatigue analysis and practical tests in laboratories, eventually the vehicle proving grounds (Bright 2012).

2.5 Introduction to fatigue

Many industrial structures are subjected to fatigue loadings. Fatigue can be defined as the degradation of mechanical properties leading to failure of a material or a component under cyclic loading. It is estimated that 90% of service failures of metallic components result from fatigue (Pang et al. 2013). Fatigue life is referred to the number of cycles involved in the development of a crack from the scale of grain size up to final fracture of the component (Taylor 2007). This

explanation highlights that defects or in-homogeneities (inclusions, manufacturing defects or pits), which are greater than the material's inherent microstructural dimensions, are extremely harmful to fatigue life and strength. In light of this, understanding the fatigue properties of materials is an essential part of ensuring designs are both robust and reliable. However, it is very time consuming and costly to perform fatigue tests. One of the main necessities in the design of numerous mechanical components is the ability to withstand a great number of stress cycles under service loads.

There is a very beneficial way to display time to failure for a certain material with an S-N curve. The "S-N", also known as the Wöhler curve, displays stress amplitude versus cycles to failure, where the fatigue data is plotted on a semi-log or log-log scale. Usually, stress amplitude is plotted on the vertical axis and the number of cycles to failure plotted horizontally (Bathias and Pineau 2010).

The SN curve is generally a straight line when plotted with logarithmic axes, this gives the convenient relationship which is the well-known Basquin's Equation which represents the part of the S-N curve for the region where N is less than the endurance limit (Bathias and Pineau 2010).

$$\Delta\sigma = A \cdot N_f^b$$

Where:

$\Delta\sigma$ = Stress (MPa)

A = Basquin coefficient

b = Basquin exponent

N_f = Number of cycles to failure

Once the constants A and b are known, then the stress σ for any value of N (less than endurance limit) can be determined using Basquin's equation. Alternatively, for a given stress greater than the endurance limit stress, the number of stress cycles (N) after which fatigue failure will occur can be determined. In industry the Basquin relation is now the most preferred and frequently used representation of stress life fatigue data (Ellwood 2003; Bright 2012).

In order to produce realistic data for fatigue analysis, fatigue tests are performed on numerous similar specimens at different levels of maximum alternating stresses and the number of loading cycles to failure is determined. A typical S-N curve is shown in Figure 2.6 (BSI 1993), each data point being obtained from a single test. The inclined portion of the curve with negative slope constitutes the finite life region and allows prediction of fatigue strength of the material for given number of stress cycles whilst the horizontal portion represents the stress level below which a material is considered to have infinite life. The fatigue or endurance limit of a material is represented by the stress level corresponding to the horizontal portion (i.e. infinite life) which is convenient and safest for design purposes (Bathias and Pineau 2010). A cyclic loading level greater than the fatigue limit causes micro crack initiation even if the material has no initial bulk or surface defects. Fatigue specimens which are identified as having a run-out life may arise from either stress levels at which micro cracks are not initiated, or where cracks initiate but there is insufficient energy to overcome barriers during the micro structurally dominated crack growth (Bright 2012).

There are many factors that affect fatigue life of engineering structures and components such as stress state, geometry, surface finish, material type, grain size, direction of loading, environmental conditions and size and distribution of internal defects.

2.5.1 Fatigue limit (Endurance Limit)

In the automotive industry, all of the chassis and suspension components are designed for infinite life and must not fail whilst in service. The stress resulting from operating loading on such a component should be less than the material's endurance limit by an appropriate factor of safety. The component would then be expected to withstand these stress levels without fatigue failure. The fatigue limit of a smooth and polished specimen made of steel is clearly determined by a knee in the S–N curve, however, which disappears under special conditions such as periodic overloads, high levels of surface pitting, temperature and scratches, and in a corrosive environment. Commonly, a fatigue limit is frequently defined as the fatigue strength at 10^7 cycles and should be experimentally determined (Lin et al. 2001). The staircase method (or the up-and-down method) is the commonly used

method for determining of the fatigue strength at any specified life (Morrissey and Nicholas 2006). The British standard BS ISO 12107:2003 (BSI 2003), also recommends this method.

2.5.2 Staircase method

The up-and-down or staircase method involves testing specimens at a constant amplitude loading conditions approaching the fatigue limit. The test method was explained by many reports (Lin et al. 2001; Morrissey and Nicholas 2006), and the test sequence is shown schematically in Figure 2.7. Initially, the mean endurance limit is estimated. Then, a specimen is tested at a stress amplitude slightly (about 5%) higher than the expected endurance limit. In the event of survival of a specimen, the test is suspended after completion of a stipulated number of cycles (e.g. five million cycles) and the next specimen is tested at a higher amplitude of maximum alternating stress. However, if the specimen fails before completion of the stipulated number of cycles then the next specimen is tested at lower stress amplitude. Thus, the stress amplitude of each successive test is based on the outcome of the previous test. At the conclusion of this type of testing there are data containing both failures and run-outs at stress levels directly surrounding the fatigue limit stress. For a limited number of sample, the staircase method offers approximately the similar value of the fatigue limit stress as regular S-N tests at constant stress levels. On the other hand, the variance is not well predicted since most of the testing is concentrated about the mean (Morrissey and Nicholas 2006).

It is very time consuming and costly to perform fatigue tests. Therefore, many attempts have been made to determine the fatigue strength in a cost-effective way by relating fatigue strength to other mechanical properties such as yield strength, tensile strength, and so on. Some researchers (Benham et al. 1996; Fourlaris et al. 2007; Pang et al. 2013) showed that the fatigue performance of steel increases with tensile strength, whereas other researchers believe that the yield strength of the material plays a significant role in the fatigue performance (Bright 2012; Pang et al. 2013). It was highlighted the average ratio of the fatigue strength to tensile strength is approximately 0.45 (Benham et al. 1996; Fourlaris et al. 2007; Pang et al. 2013). A recent study by Tata steel (Ellwood 2003) explained from comparisons performed on low carbon steels as typically used in the automotive industry, that

the average value for the ratio of fatigue stress at 10^6 cycles to UTS is 0.54. Accordingly, the relations between fatigue strength and other mechanical properties have been of more interest. Engineers and scientists have proposed many formulae to describe the relations between fatigue strength and other mechanical properties, which are summarized by Pang et al. (2013).

2.5.3 Fatigue crack initiation and propagation

Most fatigue fractures occur with little warning, fatigue damage can take place in the initial load cycles, and surface cracks are often not visible until terminal stages of fracture are reached. It is well established that fatigue essentially consists of two stages; crack initiation and crack propagation. The crack initiation stage is dominated by the number of stress cycles required for a fatigue crack to initiate and to become a possible stress concentration. The crack propagation stage include the loading cycles required to grow the initiated crack until reaching the final failure of the structure. The total fatigue life is the sum of crack initiation life and crack propagation life. For high cycle fatigue the crack initiation period may dominate a considerable part of the total fatigue life, while for low cycle fatigue it may be covered more by stage I and II crack growth as explain below (Benham et al. 1996).

A schematic diagram of fatigue crack growth curve is shown in Figure 2.8. This provides a general overview of the stages of the fatigue damage process, which is crack initiation, stable crack proportion and unstable crack proportion as follows (Ewalds and Wanhill 1984; Benham et al. 1996).

- 1) *Crack initiation stage*, the crack in this stage may be initiated by surface scratches caused by slip bands or dislocations intersecting the surface as a result of previous load cycle or work hardening.
- 2) *Stage I crack propagation*, is micro structurally dominated crack growth, the crack and the plastic zone have the size of a few grain diameters; the crack propagates by single shear following the direction of the primary slip system making a zig-zag crack, as illustrated in Figure 2.9(a) (Rezig 2011).

- 3) *Stage II crack propagation*, the size of the crack and the plastic zone now represents several grains; a duplex slip mechanism takes place implying two slip bands, and the crack propagates in a direction normal to the direction of the applied load, as shown in Figure 2.9(b).
- 4) Final failure or fast fracture takes place when the remaining material is no longer able to support the applied load. The crack propagates rapidly and the structure fails catastrophically.

The mechanism of fatigue crack initiation changes for pristine and non-pristine specimens. The nucleation of slip planes is the main reason for fatigue crack initiation in pristine ductile material. However, in damaged specimens the failures typically take place at openings, scratches, sharp corners or at edges, where the damage causes stress concentrations, and a plastic zone ahead of the damage tip is formed. The fatigue crack initiation occurs due to plastic deformations in a direction normal to the direction of the applied load (Benham et al. 1996; Rezig 2011).

2.5.4 Influence of notches on the fatigue life

The stress concentrations provide by areas such as notches are failure critical locations that may considerably reduce the lifetime of components due to cyclic plastic deformation that may arise under service loading conditions. Thus, short fatigue cracks originated in the notch root propagate up to the total fracture of the component (Savaidis, 2010). It has been shown that there is a decrease of the fatigue limit of a notched specimen by a factor of $K_f (< K_t)$ compared with the fatigue limit of an unnotched specimen. Now, the stress concentration coefficient cause by surface roughness, K , can be calculated from equation below (Li, J. K., 1992).

$$K = 1 + \left(\frac{S_z}{S_a}\right)^{1.3} \quad (S_z/S_a < 0.15)$$

Where S_a is arithmetic average of absolute values, S_z is Average distance between the highest peak and lowest valley. A major target in the field of engineering is to develop accurate calculation tools to assess the fatigue life of such components. The study of the effect of notches on the fatigue has a fairly long history (Kerscher 2014).

2.6 Fatigue of four point bending

As previously explained, fatigue testing determines how long the product can sustain certain forces before failure and hence allows the correct design of a product. Moreover, the fatigue testing methodology is an effective and reliable way to examine fatigue properties of materials (Ellwood 2003; Fourlaris et al. 2007; Hägele and Sonsino 2014). However, fatigue data in axial loading are insufficient for evaluating high cycle fatigue which frequently happens in components that are subjected to flexural loading (Xue et al. 2007). Automotive chassis components are often subjected to various types of repeated loading such as axial, flexural and/or combinations of these loadings due to irregular bumping specially in off road conditions. Therefore, it essential to investigate the bending fatigue behaviour so as to obtain sufficient fatigue data for a meaningful fatigue strength assessment of actual components under complex loading conditions. Flexural tests have become a significant test method in both the manufacturing process and research and development to define a material's capability to withstand deformation under load.

Flexural tests simulate both tensile and compressive stresses on a specimen. The volume under stress in the case of four point bending is bigger than that of three point bending as is obvious from Figure 2.10 (Dupen 2015). In addition, the four point flexure fixture produces constant peak stresses along an extended region of the specimen hence exposing a larger length of the specimen with more potential for defects and flaws to be highlighted. This would be suitable to test large areas exposed to stone chipping, corrosion defects and large part of weldment including the weld and HAZ zones on either sides.

In general, there is very little knowledge available on the fatigue properties of steel under bending loading of unnotch specimen. Fatigue experiments are rarely performed on welded joints with pure bending loads in comparison with the fatigue experiments under axial loading and therefore fatigue strengths are not frequently seen in fatigue design specifications for welded joints subjected to pure bending loads. Design based on the fatigue strength in tension may result in inaccurate fatigue life estimation for a welded detail in bending (Xiao et al. 2012).

So far the only available four-point bending fatigue data are from experiments carried out by Miki et al. (1987) on transverse fillet welded tee joints of different dimensions to study the effect of the plate thickness on the fatigue strength. Most recent research on four-point bending fatigue of steel concerns computational studies which were validated in comparison with the experimental results of Miki et al. (1987). Xiao et.al. (2012) investigated different ways of evaluating the fatigue strength of welded joints, such as the hot spot stress (HSS) method, 1 mm stress method and linear elastic fracture mechanics (LEFM) method and the results were also compared with the fatigue experiments of Miki et al. (1987).

The boundary element method was employed to analyze the fatigue crack growth lives of welded connections under four point bending by Chen et al. (2013) due to the boundary conditions of the geometry adopted for transverse welded joint specimen was similar to the to the four point bending in the current study. The numerical results were also compared with the same experimental results in the literature of Miki et al. (1987). Therefore, it is necessary to cover this lack of information by carrying out a complete programme of experimental fatigue tests which includes both tensile and bending loading for FB590 steel and welds in order to provide comprehensive data and information that enables design engineers as well as academics to represent the damage of several environments typical of those experienced in automotive chassis applications.

There are further four-point bending fatigue tests which were carried out on other materials. For instance, Pramesti et al. (2013) predict the fatigue life of gravel asphalt concrete (GAC 2010) based on four point bending tests and compare it with observation of two accelerated pavement test sections. The result shows that the observed fatigue life is higher than that predicted, because the uncertainty of the input parameter such as stiffness and strain which are influenced by temperature, etc. Wang et al. (2006) studied the four-point bending fatigue behaviour of a laser sintered FeNiCu-alloy, the main aim of this investigation was to evaluate the fatigue properties and the crack initiation and propagation mechanisms.

The S-N curve of Cu₄₅Zr₄₅Ag₇Al₃ bulk metallic glassy alloys (BMGs) under the four-point-bend fatigue behavior was also investigated by Zhang et al. (2013) to

provide a mechanistic understanding of the fatigue and fracture mechanisms of Cu-based BMGs. This material showed a fatigue-endurance limit of 386 ± 5 MPa, the fatigue-fracture morphology indicated that Cu₄₅Zr₄₅Ag₇Al₃ has a significantly brittle fracture mode. The fracture surface was studied and can be divided into four regions: crack initiation, crack propagation, fast fracture, and melting regions.

Both three- and four-point bending tests were conducted by Zhou et.al. (2014) to investigate the bending fracture process of PMFSS produced by solid state sintering of copper fibres. It was demonstrated that three similar stages of the bending fracture process were observed for the PMFSS with 80% porosity sintered at 900 °C for 60 min. However, comparing with the three-point bending, much smaller bending force was obtained in the four-point bending test under the same displacement conditions.

There are other types of bending tests were carried out on the fillet welded joints such as plate bending (Baik and Yamada 2008; Baik et al. 2008), to study the fatigue crack initiation and propagation behaviour and in-plane bending (Mashiri and Zhao 2007). These tests illustrate different types of fatigue bending, however not similar to the four point bending in the current study.

2.7 Corrosion

Corrosion is commonly defined as the natural deterioration of a material, usually occurring due to the chemical or electro-chemical reaction of a metal with the surrounding environment. Corrosion is also very costly, besides being an undesirable process causing early and unexpected failure of structures, thereby a potential safety threat. In many cases corrosion problems are exacerbated by interactive effects caused by the conjoint action of mechanical stresses and chemical reactions. It is therefore important to understand the process of corrosion in order to choose the most appropriate designs and materials, and thus prevent or slow down its occurrence (Winston and Herbert 2008).

2.7.1 Types of corrosion

Corrosion processes may be classified as either general corrosion or localized corrosion (Fontana 2005).

General or uniform corrosion is defined as a corrosive attack dominated by uniform thinning such as atmospheric corrosion, high temperature corrosion etc., since all areas of the metal corrode at a similar rate.

Localized or pitting corrosion concerns damage which is localized rather than spreading uniformly over the exposed metal surface, and includes pitting and crevice corrosion. The rate of the metal dissolution occurring in localised corrosion is usually faster than in uniform corrosion. When localised corrosion happens in shielded areas, the term crevice corrosion is employed, whereas pitting corrosion is used to describe localised corrosion on a free surface (Winston and Herbert 2008; Rezig 2011).

2.7.2 Corrosion-Failure Mechanisms

In localized or pitting corrosion the local dissolution of the metal leads to the creation of holes or cavities at the metal surface, called pits. The surface diameter of the pits is generally small and they are very often covered by corrosion products, which makes their detection very difficult. Therefore, these forms of attack are economically important and dangerous because they can lead to premature failure of a structure by rapid penetration (Fontana 2005; Rezig 2011).

Corrosion pits can have a wide variety of shapes, as illustrated in Table 2-1. Every shape has a different level of severity, which adds more difficulties to evaluate of the damage. For example, an undercutting pit might appear to be small and shallow from the surface, but in fact spreads over a much greater area under the surface. Thus, pitting corrosion can be considered as one of the most dangerous form of corrosion due to the difficulty of detecting and assessing it (Fontana 2005; Rezig 2011).

Some studies (Burns et al. 2010; Xu and Shan-hua 2015) indicated that most pits were narrow and deep at the early stage of corrosion, with corroded specimens with such pits have relatively short fatigue lives. With increasing exposure time, primary wide pits gradually appeared as a result of neighbouring pit coalescence

at the mid-term, with a slight increase in the fatigue life with increasing corrosion time. However, this conclusion does not mean that longer exposure time leads to improved fatigue performance. Though corrosion tends to be relatively uniform with increased exposure time, the increased nominal stress caused by the reduced cross-sectional area of members due to corrosion will still significantly reduce the fatigue performance of steel components (Zahrai 2003; Xu and Shan-hua 2015). Xu and Qiu (2013) concluded that the rapid change of cross section around corrosion pits produces high stress concentrations which cause the formation and growth of the fatigue crack. The results of many studies in this area indicate that the presence of corrosion pits significantly reduces the fatigue life of corroded steel.

Formation of cracks from corrosion pits was observed by many researchers (Van der Walde and Hillberry 2008; Zhang et al. 2013; Xu and Shan-hua 2015). The study of Xin-Yan Zhang et.al. (2013) on pit corrosion showed that cracks do not necessarily initiate from the bottom of the pit, the location of crack initiation depends on the pit shape (aspect ratio), loading and the corrosive environment.

Some researchers (Xu and Qiu 2013; Xu and Shan-hua 2015) used a methodology partly based on the observations of 3D profile data to study the effects of corrosion pits on the fatigue life. 3D profile measurements were conducted to obtain the distribution and morphology characterization of corrosion pits, in order to investigate the effect of corrosion on fatigue behaviour of corroded steel. The results stated that the surface appearance affects the fatigue life greatly, and corrosion would cause the surface to become rougher, thereby rapidly declining fatigue life. Material with a fine-grained structure is more sensitive to surface appearance and becomes more adversely affected by a rough surface finish than softer, coarse grained steels (Ellwood 2003; Bright 2012). Zahrai (2003) concluded that fatigue failure of corroded steel plate can be explained by irregularities that may act as concentrators of stress and provide the local aggressive environment conducive to crack initiation.

The objective of Xu and Wang's investigation (2015) was to assess the effects of corrosion pits on the fatigue life of Q235 steel plates. The methodology was partly based on the observations from 3D profile data to obtain the distribution and morphology characterization of corrosion pits. Three types of pits were observed

and categorized such as deep-narrow pits, wide-shallow pits, and pits with secondary pits as shown in Figure 2.11, in order to carefully understanding their effects on fatigue behaviour. Results indicated that corrosion pits reduce the fatigue life significantly, particularly the sharp pits.

Over the past few years, the fatigue performance of pre-corroded aluminium alloy material was widely investigated (Chen et al. 1996; Kermanidis et al. 2005; Jones et al. 2008; Arriscorreta 2012), whilst for structural steel, there is little information on the aspects of this problem (Hao et al. 2011; Xu and Qiu 2013; Xu and Shan-hua 2015). Most studies concluded that corrosive environments accelerated fatigue crack growth rates and corrosion could dramatically reduce the fatigue failure resistance of steel materials. This due to some reasons as explained by Xu and Qiu (2013), viz: (1) generally, the principal corrosion influence (pitting or otherwise) is that of a stress raiser. Pits produced by corrosion on the surface increase the local stresses to a value more than that for crack initiation, leading to failure. (2) Pits produced by corrosion on the surface can speed up the rate of crack growth, then deteriorate the fracture toughness. Arriscorreta (2012) discussed further reasons for the reduction of fatigue life like metal dissolution, conversion of metal to metal oxides or hydroxides leading to increase volume causing metal separation. This represented new complex stress distributions not considered in early assessments.

2.7.3 Test standards for cyclic corrosion tester

The main aim of this section is to present an overview of the suitable accelerated tests which allow the simulation in the laboratory of the various corrosion processes as experienced in the field. Corrosion resistance is a significant property requirement for materials used in the automotive manufacture, particularly for vehicles that work on roads treated with highly concentrated road salts to prevent the road from icing over. Hence, automotive materials have to be tested to explore their corrosion resistance and in order to make a good selection of materials. As with fatigue testing, the most reliable method is to perform field tests, including mobile and stationary exposures which are costly and time consuming, where 2–8 years exposure is generally necessary for a full assessment of the corrosion resistance. However there are only a few studies related to field exposures in stationary sites or on vehicles. The alternative is to carry out accelerated corrosion

tests in a reasonably short time whilst providing a true ranking of materials, similar to that acquired with exposure under natural weathering conditions (LeBozec et al. 2008; LeBozec et al. 2012).

Nowadays, there are many approaches and standards for performing laboratory corrosion tests. Many of these tests are currently used by car makers and automotive suppliers in order to develop and qualify new products against corrosion, to improve new protective coating systems and choose materials. Most of the accelerated corrosion tests are cyclic in nature, and consist of intermittent exposure cycles to salt solution, elevated humidity/temperature and drying (LeBozec et al. 2008).

Accelerated corrosion methods are widely used by automotive manufacturers, for example Nissan uses the test standard CCT-I – NES M0158 , Toyota the test TSH 1555G ,Volvo Car Corporation uses the test standard VCS1027, 149, Renault the test ECC1 D172028, American producers follow the test SAE J2334 (SAE: Society of Automotive Engineers), whilst German producers use the test VDA621-415, etc.

For an example of these procedures, the Volvo indoor corrosion test, which is performed according to the standard STD 1027, 1375 (Katundi et al. 2010) is shown schematically in Figure 2.12. The test specimens are put in an enclosed chamber and exposed to a variable environment that consists of three various environmental conditions. Firstly, the specimens are immersed in a 1 % NaCl solution in order to mimic a road environment, where sodium chloride (NaCl-salt) is the predominant corrosive element. Secondly, the specimens are exposed to 90 % relative humidity for seven hours at 35 °C followed by an exposure to 45 % relative humidity for five hours. The second and third steps are repeated for seven times presenting a total exposure time of 84 hours (3.5 days).

An American standard (SAEJ2332 2002) was used in the current study and the test procedure is explained in detail in Section 3.12. When determining corrosion performance for a certain coating system, process, substrate, or design the SAE J2334 lab test method should be used since it is a field-correlated test. SAE J2334 can be used as a validation tool as well as a development tool. Field correlation must be decided when corrosion mechanisms different from cosmetic or general

corrosion are to be inspected using SAE J2334 test. SAE J2334 is a cyclic corrosion test standard commonly adopted by researchers and automotive original equipment manufacturers (OEMs) to characterize the corrosion resistance of materials in a sequence of dry and wet environments (LeBozec et al. 2008; Pang et al.). This method was recommended to predict the durability of automotive products (SAEJ2332 2002) and closely represents the exposure of the materials of interest in the current project under automotive conditions.

2.8 Automotive E-Coating

Weathering resistance is a main obligation for the coating systems which are exposed to outdoor conditions through their operating life. Coated steel plate is increasingly used for corrosively attacked components in various sectors of industry, particularly for automotive applications. Usage of automotive coatings is expected to increase by 1.8 % per year to 2.0 million metric tons by 2003, with Original Equipment Manufacturers (OEM) coatings posting 1.5 % growth per year to 1.2 million metric tons (Ramamurthy et al. 1999; Takamura and Urban 2002).

Current motor vehicle coatings are comprised of several distinct layers as shown in Figure 2.13, the coatings are either electrodeposited or spray applied. Usually the clearcoat, basecoat and primer are applied by spray whilst the electrocoat is electro-deposited by dip application. The thickness and purposes of the several coating layers are presented in Table 2.2. Current automotive passenger cars are often coated with four coating layers in addition to a 1 μm phosphate layer, as shown in Figure 2.13. Clearcoat and basecoat are considered as part of the automotive topcoat system (Ramamurthy et al. 1999; Takamura and Urban 2002).

Many underbody structural components are made from sheet steel, therefore they are typically coated to provide a first line of defence against corrosion. Corrosion protection is one of the most important tasks of automotive coatings. The barrier and galvanic protection are the two principle methods of corrosion protection for steel. Barrier coatings (organic coating, paint etc.) are design to limit the levels of oxygen and water that reach the steel surface to cause corrosion. The coating is a very powerful protection method whilst the coating remains intact, however any

break in the film during service due to, for instance, stone chipping, scratches and so on will reduce the protection which these coatings provide (Ramamurthy et al. 1999).

In such cases, galvanic protection may be used to suppress the electrochemical reaction that occurs during corrosion. One of the most widely used and cost effective method of protecting steel against atmospheric corrosion is coating with zinc. Zinc and zinc alloy coatings protect the steel in two ways - firstly, by creating a physical barrier between the steel substrate and environment and secondly, by forming and providing galvanic or sacrificial protection at cut edge and scratches. This is because zinc has a larger electro- potential than steel and therefore corrodes preferentially due to it being more electronegative than iron in the electrochemical series (Takamura and Urban 2002).

Electrophoretic deposition is a process more generally called electro-coating or E-coating. In this process electrically charged particles in a water suspension are used to coat a conductive piece. E-coat is the first pigmented coating layer, which is applied over the phosphate coating of the fabricated car steel body. Automotive parts that are E-coated are typically treated with zinc or iron phosphate prior to deposition. This treatment improves the application of the E-coat and also offers corrosion protection (Ramamurthy et al. 1999). E-coating acts as a bridge between the metal and the covering coating layers. It is a good oxygen and moisture barrier, but needs precise electrical control and expensive bath solution maintenance (Lonyuk et al. 2008). Electro coating systems are recognized as cathodic or anodic depending upon whether the component is the anode or cathode in the electrochemical method. Cathodic systems are more popular since they demand less surface preparation and provide better corrosion resistance. The coating layer is applied in a dip application by cathodic electrodeposition to the steel car body. Dip application has the advantage of being able to effectively fill the smallest recessed areas of the car body. This complete coverage guarantees excellent corrosion protection to the vehicle body. Electro coat thickness typically ranges from 10 to 30 μm (Auto/Steel 1999; Takamura and Urban 2002).

For this work, E-coating was carried out in TATA Steel IJmuiden, Figure 2.14 shows a picture of the E-coat pilot line. There are twelve separate sections; these

sections are (from left to right) listed above, which are labelled in the figure. The level of E-coat protection afforded to FB590 specimens was similar to the strategy used by all vehicle in real situation, in order to understand the level of protection needed in the likely future scenario of chassis and suspension steel down-gauging; a strategy used by all vehicle OEMs to reduce overall weight, fuel consumption and hence emissions.

2.9 Stone Chipping

Stone impact damage to painted automotive outsides is an area of important concern both to the automotive maker and the paint supplier. A common source of damage to automotive paint finishes is due to impact of small particles (stones) either thrown by tyres or from other passing vehicles. The resulting abrasion due to the great number of small impacts is called stone impact damage (also referred to in the industry as stone chipping). Stone chipping damage can result in either physical loss of paint or delamination at the metal-polymer interface (Ramamurthy et al. 1999). Physical loss of paint is a cosmetic issue while delamination at the metal-polymer interface leads to the formation of a corrosion cell beneath the coating which can ultimately lead to perforation (Ramamurthy et al. 1999). Abrasions induced by stone are sites of nucleation of corrosion affecting mainly underbody components causing mid and long term damage.

To the author's knowledge, there is no available published literature which addresses the effects of stone chipping on corrosion as well as on fatigue properties, most likely due to commercial confidentiality. Therefore, there remain important gaps of knowledge with regards actual simulation of the stone impact on corrosion as well as the consequences on fatigue life. This information is useful to the steel industry and automotive engineers in order to design both coating thickness and layout to fulfil a lifetime guarantee against failure. Most studies focussed on the determination and evaluation of coating resistance to chipping damage by stones or other flying objects (Ramamurthy et al. 1999; Lonyuk et al. 2008).

The study of stone-chip resistance needs complicated testing and analysis equipment. The SAE J400 and ASTM D3170 standard recommended practice

covers a laboratory procedure for testing and assessing the resistance of a surface coating to chipping by gravel impact. These standards introduce a method for quantitative evaluation of the changes in the strength of paint films observed when paint films are cut, as one of the means of evaluating the paint film's resistance to stone chipping, which is a paint film peeling phenomenon, by stones thrown up by a car driving ahead, or by the car itself. In this study, a commonly used method (gravelometer) has been employed for evaluation of the stone chipping resistance, explained in detail Section 3.11, which is believed to realistically simulate chipping due to stone impact (Lonyuk et al. 2008).

Figure 2.15 schematically shows the four types of failures due to the stone impact on the surface of coating (Lonyuk et al. 2008; Razin et al. 2015)– viz - (a) coating loss from the primer layer, (b) fracture at electrodeposition (ED)/primer interlayer (c) coating damage from the phosphate/ED interlayer and (d) coating separation from the steel substrate. The majority of paint and coating failures due to the stone impacts can be attributed to three main mechanisms. Firstly, the most common failure mechanism is that the coating may fail in shock compression initiating coating loss from the topcoat and/or fracture at primer/topcoat and primer/ED inter layers as shown in Types (a) and (b) in Figure 2.15. The second mechanism is that the brittle crystalline phosphate layer might fail by reflected tensile waves causing the coating separation from the steel substrate as illustrated in Type (d) in Figure 2.15. Finally, the deterioration of ED layer during weathering exposure is responsible for the reduction in inter facial adhesion between the ED and primer layers and the applied stress could easily separate the coating from the ED layer (Lonyuk et al. 2008; Razin et al. 2015).

A practical example is presented here about coating failure. Failure of these coatings takes place at the point where the projectile contacts the panel and on a small area ahead of the effect direction. This kind of damage indicates cut-through damage and is illustrated in Figure 2.16. The failure happens in the electrocoat nearby the electrocoat/phosphate layer interface, represents types (c) in Figure 2.15. The rest of the E-coat that shielded the phosphate layer are still present in the area in front of the deformed substrate (see Figure 2.16b) (Lonyuk et al. 2008).

2.10 Surface topography

For many typical kinds of loading, such as bending and torsion, the maximum stress happens at the surface. Thus, the surface condition is a very important factor in determination of fatigue life due to a high percentage of all fatigue failures originating at the surface of the component. Furthermore, the surface is often exposed to harsh environments such as corrosion, or unexpected loads such as scratch and impact. Due to the complex geometry of the scratches, machining marks and pits caused by corrosion would create stress concentrations additional to those already there. As previously discussed, high strength steels have a fine-grained structure and are therefore more harmfully affected by a rough surface finish than softer steels which have coarse grained structures (Benham et al. 1996).

As is obvious, the fatigue life is sensitive to surface finish; cracks can initiate at surface irregularities that are normal to the stress axis therefore, fatigue life decreases as surface roughness increases. Surface roughness plays an important role in determining how a real object will interact with its environment. Roughness is often a good predictor of the performance of a mechanical component, since irregularities in the surface may form nucleation sites for cracks or corrosion (Stout 1993). Xu and Qiu (2013) stated that the surface appearance affects the fatigue life greatly, and corrosion would cause the surface to become rougher, thereby rapidly decreasing fatigue life.

Alang N.A. et.al. (2011) investigated the effects of surface roughness on the fatigue life of carbon steel for rotational bending specimens, where the surface roughness was changed by using emery papers (Grit #600, #400, #100). The result showed that the number of cycles to failure of finer ground specimens was bigger than those of the coarser ground specimens. Moreover, the fracture surface observation showed the number of possible fatigue crack initiation sites to be higher on the coarser ground specimen than on the finer ground ones.

The average surface roughness, Ra, for different emery paper grit was summarized as (#600, Ra=1.778 μ m), (#400, Ra=2.885 μ m), (#100, Ra=5.484 μ m). The influence of surface roughness on fatigue limits of all machined specimens was summarized in Figure 2.17. The fatigue limit decreased almost linearly with the

increasing level of roughness. The fatigue limit of the specimen was taken when the number of cycles to failure, N is greater than $3(10^6)$. It was shown that there is little significant changes in fatigue limit with the increasing of surface roughness from $R_a = 1.778\mu\text{m}$ to $R_a = 2.885\mu\text{m}$.

The environment has an important role on the fatigue performance of a component. The surface of the metal is attacked by the corrosive environment and an oxide layer is generated that will help prevent further corrosion. However, the corrosion creates pits in the surface, which act as stress risers. The cyclic loading also creates localised cracking in this layer exposing the fresh un-corroded metal. Both these factors will accelerate the fatigue and corrosion processes (Bathias and Pineau 2010; Xu and Shan-hua 2015).

In order to conduct a detailed analysis about the influence of corrosion on fatigue life, it is necessary to acquire a quantitative two and three-dimensional evaluation of the corroded surface (Xu and Shan-hua 2015). For any quantitative assessment of corrosion severity, surface topography data is required with sufficient resolution to capture the important characteristics of the features that cause fatigue cracking. Accuracy and convenience are beneficial in the measurement of corrosion surface irregularities (Kaita et al. 2011). There are three primary methods of obtaining surface topography data that are usually non-destructive evaluation techniques (Rusk and Hoppe 2009): laser interferometry, contact stylus measurements and white-light interferometry (WLI). A profilometer (Taylor Hobson Form Talysurf) is a contact stylus technique which was recommended by previous researchers (Thomas et al. 2011a; Bryant 2013) and is available at Cardiff University. This technique is capable of easily producing two and three-dimensional maps of surface topography and was applied to pitting measurements with varying degrees of success and thus constitutes a useful way to quantify profile height distributions.

Amplitude parameters describe the surface based on the vertical deviations of the roughness profile from the mean line. Many of them are closely linked to the parameters found in statistics for characterizing population samples. For example, R_a (arithmetic average of absolute values), R_q (root mean squared average), R_{sk} (skewness or a measure of the asymmetry of the probability distribution of asperities' height), R_{ku} (kurtosis), R_v (maximum valley depth), R_p (maximum peak

height), R_z (maximum peak to valley height of the asperities) (Stout 1993). It is important to evaluate a range of parameters in order to evaluate the surface quality precisely (Deleanu et al. 2012).

The most widely used parameters to describe surface roughness in current engineering practice are R_a and R_q , these values take the average of peaks and valleys of the scanned surface. In some cases R_z , which is the average height difference between the five highest peaks and five lowest valleys, may be used to restrict any extreme behaviour in the surface profile after finishing (Taylor and Clancy 1991; Novovic et al. 2004; Thomas et al. 2011a). In addition, a skewness parameter is a measure of the symmetry of the profile about the mean line. For example, Bryant (2013) found the skewness to be an important factor to illustrate surface changes taking place predominately to the asperity tips of a surface, which became flattened where the surface has been deformed/worn during wear tests of surfaces typical of power transmission gearing. For the characterization of the surface texture Deleanu L. et.al (2012) point out that a statistical character is commonly predominated and that there is no common methodology for characterizing surfaces.

Figure 2.18 shows five different profiles characterized by the parameter set (R_q , R_{sk} , R_{ku}) (ASME 2009). The same set of parameters were investigated by Deleanu et.al (2012), but using 3D or areal measurements (S_q , S_{sk} , S_{ku}), this study underlined that a 3D investigation was more appropriate for assessing the surface quality and it reflected better the nature of the topography reality.

Wang, et.al. (2015) performed a comparison between 2D parameters (R_a and R_z) and 3D parameters (S_a and S_q) to evaluate the influence of machining parameters on the surface quality for high volume fraction SiCp/Al composites. The 3D parameters were found more accurate to describe the surface quality, with lower standard errors than 2D measurements.

Bryant (2013) demonstrated the usefulness of roughness parameters in detecting suitable changes to surface topography caused by the running-in process in mechanical components. He explained that the run and unrun profiles were obviously distinguishable by the shape of the asperity peaks. The run surface exhibited wider, flatter peaks because of plastic deformation, resulting in a more

negative skew in the surface height distribution in comparison to the unrun surface. Figure 2.19 shows the sections of the surface roughness profiles of the run and unrun surfaces. Some of surface roughness parameters are presented for each surface by R_a , R_z and R_{sk} . In industry, surfaces are usually specified using a R_a , or roughness average, value, at least partly due to its ease of measurement. In this case, the surfaces have a R_a of between nearly $0.30\ \mu\text{m}$ and $0.37\ \mu\text{m}$. It can be observed for the unrun and run surfaces that while each of these parameters differs, that they are still somewhat similar. By considering the skewness of the surface, R_{sk} , a more pronounced difference can be seen as the run surface is considerably negatively skewed as a result of running, resulting in multiple flat lands where the surface has been deformed or worn.

2.11 Acoustic Emission

Acoustic Emission (AE) can be defined as surface stress waves caused by the abrupt release of strain energy resulting in micro seismic activity within any material. The piezoelectric transducers that convert the mechanical waves to electrical signals can achieve monitoring of the micro seismic waves as shown in Figure 2.20. The detection, amplification, counting, filtering, and analysis of these signals constitutes AE technology. The technology has been extensively developed over four decades as a non-destructive assessment technique and as a valuable tool for materials research, and is a highly sensitive method for detecting active microscopic events in a material, as well as crack initiation and propagation (Miller 2005).

The AE signals generated are quantified by five basic parameters, as illustrated in Figure 2.21. These AE signal parameters are amplitude (A), rise-time (RT), duration (D), counts (C), and mean area under the rectified signal envelope (MARSE), generally known as energy (E). Other parameters, such as average frequency (counts/duration), are combinations of basic AE parameters; these are also beneficial in many cases. Cumulative absolute energy and cumulative counts are two parameters that are utilized to investigate links between AE and the fatigue crack growth process with time (Roberts and Talebzadeh 2003a).

AE is a highly sensitive technique; it includes information from both real cracks and noise. Eventually, the different types of noise hamper the reliability and accuracy of AE analysis (Fang and Berkovits 1995; Teik 2001). Generally, these noise sources are classified as environmental, internal, and special noises. Environmental noise emits from external factors, like electrical instrumentation, load train and other anonymous sources generated outside the tested materials. Internal noise originates from the reflected and retracted waves. Special noise is connected with the specific test setup, such as mechanical fretting noise in the specimen grip and friction between the specimen and loading pin or friction between bolts and specimen surfaces, these types are the hardest to exclude. To overcome this limitation, researchers (Berkovits 1993; Teik 2001) explored numerous denoising techniques such as a floating threshold, spatial filtering, and linear guard sensors to distinguish between the noise and the real AE signal. In the current study, before starting the analysis, all data files were filtered by location around the crack, using only data originating between the AE sensors and discarding other data.

The research on AE can be generally divided into two categories as traditional AE and source-function and waveform analysis. Waveform analysis is beyond the scope of the discussion in this study. Because most of the fatigue tests were very long in duration (taking up to two weeks per test) recording waveforms would create vast amounts of data which is difficult and cumbersome to process and analyse. Waveform analysis is usually used for short tests such as notched specimens or static load or low cycle fatigue.

The traditional AE technique is perfect for the cases in this study, where the main aim of this project is to identify the fatigue properties of FB590 (Barile et al. 2015; Mazal et al. 2015). Traditional AE only captures certain parameters (sometimes called AE features), including hits (emission detected by a single sensor), events (emission detected by all sensors), counts (number of threshold crossings of output signals from sensors), energy, time of the event, rise time, parametric (load) duration, etc (Huang 1998). These AE features are correlated with the defect formation and failures. These AE characteristics are only related to the captured signals and do not account for the source of the signal and wave propagation

(Barsoum et al. 2009). By correlation between these parameters, damage can be detected and located and signals from sources such as peeling of corrosion product, plastic deformation, crack initiation and crack propagation can be identified. However, it cannot classify the crack type.

RA value

An analysis method has been utilized to assess various crack types by a combination of the classical acoustic emission analysis technique and advanced analysis Rise time / Amplitude (RA) and Average Frequency (AF). This relationship between RA value and AF value can be used to classify cracks as either tensile crack type, another type (shear movement) or no crack.

The AE source can be assessed by analysis of the resultant waveform in terms of feature data such as amplitude, energy and time of arrival, the severity and location of the AE source can be assessed (Miller 2005). The waveform shape depends on the cracking mode, enabling the classification of cracks in different materials (Carpinteri et al. 2013; Behnia et al. 2014). The shape of the initial part of the waveform is examined by the RA value as defined in RILEM (Ohtsu) 2010). The shape of AE waveforms is reported to be characteristic of the fracture mode Figure 2.22 (Aggelis et al. 2011). RA and average frequency analysis are one method for analysing AE signals to define the type of cracking. RA value is the rise time (RT) divided by the amplitude (A) measured in ($\mu\text{s}/\text{v}$ or ms/v) and average frequency is defined as the ratio of threshold crossings divided by the duration of the signal and measured in kHz. Figure 2.23 shows how the classification of cracks as tensile or shear cracks is performed using the relationship between average frequency and RA value (Ohno and Ohtsu 2010; Kordatos et al. 2012; Elfergani et al. 2013; Shahidan et al. 2013). These papers report that when an AE signal has low average frequency and high RA value it is classified as a shear type crack/movement. However when it has a high average frequency and low RA value it is classified as a tensile crack.

Many researchers have conducted investigations with these two indices of average frequency and RA value for crack classification on several types of materials and under various testing conditions. For example, the classification of cracking mode in cementitious material under Four-point bending test has been studied by Aggelis

(2011) who found that this classification assists a warning against final failure. Damage assessment due to corrosion in prestressed concrete has been carried out by Elfergani et al. (2013) who observed that tensile and shear movements can be distinguished. Shahidan et al. (2013) performed laboratory experiments on a reinforced concrete RC beam tested by four point bending. They found that AE signal parameters were used in RA and intensity signal analysis (ISA) methods to indicate the type and level of damage and thereby the safety conditions and integrity of the reinforced concrete beam due to the loading process.

Ohno and Ohtsu (2010) studied the use of AE techniques on reinforced concrete under four-point bending tests, and their results showed that average frequency and RA value have a good agreement for crack classification with simplified Green's functions for moment tensor analysis (SiGMA). The first attempt to apply this technique to metallic materials under fatigue loading was carried out by Aggelis et al. (2011), where characterization for aluminium plates was performed. It was found that the RA value increases sharply about 1000-1200 cycles before final failure. Another study with metallic material under monotonic and fatigue testing has been conducted by Kordatos et al. (2012) for measuring damage propagation and dominant fracture mode. They observed that the shift of both average frequency and RA value is attributed to the shift of dominant modes of fractures.

In the current work, AE is used as an SHM technique to achieve successful characterisation of the cracking mode in FB590 steel fatigue test specimen using the RA value (ratio of rise time to amplitude of the waveforms). The results was confirmed by visual observation of the crack geometry after the experiment and the DIC measurements. This method can indicate the type of damage and enables a warning against final failure and hence the safety conditions and integrity of the structures due to the loading process.

Acoustic Emission in Fatigue Analysis

AE has long been an important tool in fatigue research, indeed the continuous monitoring of fatigue crack propagation is one of the common applications of AE. Many studies have shown that AE is capable of monitoring fatigue crack initiation

(Berkovits 1993), propagation (Roberts and Talebzadeh 2003a, b; Zhiyuan Han 2011), and crack closure phenomena (Chang et al. 2009; Zhiyuan Han 2011; Pollock 2012) in steels and other metallic alloys. Cracks and other defects will emit stress waves when load is increased, while an unflawed part in material will remain silent. Sources of acoustic emission are defect-related processes such as crack extension and plastic deformation of material in the highly stressed zone adjacent to the crack tip. Therefore, it is very important to deepen understanding of the mechanical properties and degradation processes of materials, mainly in the case of fatigue loading. Differences in material properties greatly affect AE parameters, for instance AE signals emitted from concrete are very different to those from steel. It is also important to note that AE from fatigue is not straightforward; the process of fatigue gives rise to various source mechanisms. Moorthy et al. (1996) indicated that for a ductile material the major source of AE was the plastic deformation at the tip of the crack whereas, for brittle materials, it was the crack extension at the crack tip instead. However, the authors postulated that ductile crack growth is a very weak source of AE.

Fatigue crack formation and initiation are preceded by progressive material deterioration, generated by dislocation motion and a loss of resistance in terms of life. AE has the ability to monitor this damage in real time; the measured quantities could be used as indicators of the extent of fatigue damage (Fang and Berkovits 1995).

Figure 2.24 carefully identifies possible source mechanisms when dealing with fatigue. The source mechanisms can be classified into primary and secondary sources according to Scruby (1987). The primary sources associated with crack growth are plastic zone extension, plastic opening at the crack tip, elastic crack advance as well as decohesion. Secondary events associated with fatigue crack growth are elastic response of pre crack, crack face fretting and brittle fracture of corrosion product. Secondary emissions, though not directly from crack growth, provide useful information about the movement of the crack faces.

It is beneficial to distinguish between AE signals from the plastic zone at the crack tip and AE signals from the movement of the crack itself. If the size of the plastic zone is very big, the signal released from this mechanism will not represent the

actual location of the crack tip. Growth of the plastic zone typically produces many emissions of low amplitude (Roberts and Talebzadeh 2003b).

A primary problem of AE is discriminating between particular source mechanisms, and identifying those emissions from the primary sources. Roberts and Talebzadeh (2003a, b) used a ‘load discrimination method’, where they presumed that only events happening close to the maximum or peak load are related directly with crack extension. Therefore, they used only emissions from events happening within the top 10% to 30% of peak load. Only the primary emissions will be recorded when emissions take place at the peak load. At the peak load the crack is completely open and therefore there are no connections between crack surfaces. The source location can be identified by using the source location method, and anything originating from locations away from the crack tip area can be neglected. Combining these two methods offers a precise technique to collect emissions from fatigue crack growth for analysis.

2.12 Digital Image Correlation

Over the past four decades, digital image correlation (DIC) has been developed for the measurement of displacement fields on plane surfaces. This technique provides users with full-field measurements and can be used in the determination of fracture characteristics of various materials (Sutton et al. 2008).

In general, DIC indicates a class of non-contacting methods and can be thought of as stereo vision. It is an optical-numerical full-field surface displacement and strain measurement method. One of the most generally used methods employs random patterns and compares sub-regions from deformed and un-deformed images to obtain a full-field of plane measurements (Sutton et al. 2008). The images from two calibrated cameras are processed to provide accurate three-dimensional full field measurements. The cameras are calibrated for a given test space using a calibration target of known geometry.

DIC was used to support the understanding of the detected AE signals, offering additional insight to the monitoring of crack growth with AE. The method of crack monitoring had to be non-contact so as not to produce frictional sources of AE in

the crack region, preventing the use of crack mouth opening displacement gauges. Furthermore adhesive on the specimen surface had to be avoided to eliminate the possibility that the detected AE was from adhesive cracking, thus the use of traditional methods such as strain gauges or foil crack gauges was not possible (Pullin et al. 2010a, b).

Experimental fatigue tests typically require large testing times. This testing time considerably increases when one periodically has to interrupt the fatigue test to manually measure crack lengths or specimen extension. Therefore, using DIC to periodically rapidly measure the deformation within the test sample allowed a reduction in testing time. The (DIC) technique can be applied with success to determine the initiation of cracking for comparison with the detected AE. Today, the digital image correlation technique presents the advantage of allowing fast evaluation of crack mouth opening displacement.

The DIC measurements allow the determination of plastic deformation away from the crack. This is a major advantage in materials such as mild steel, where general plastic deformation often occurs in parallel with the development of fatigue cracks. This elastic-plastic fracture process is not well understood and capturing the full deformation field during a test is potentially very valuable. DIC is a useful method for monitoring the whole area of interest and it is not limited to a specific region, therefore any damage can be detected even if the precise location is not known in advance (Shrama et al. 2014, 2015) .

The DIC measurements also allow the determination of stress intensity factors during the experiment. McNeill (1987) reports the first attempt to measure a stress intensity factor (K_I) by digital image correlation, and discussed the use of displacement data obtained by digital image correlation for the determination of stress intensity factors such as K_I . The experimental and analytical method was described with results given for different specimen geometries such as three point bending and compact tension specimen. The authors concluded that the determination of K_I through the use of DIC and least squares fitting seemed to be a viable proposition.

Risbet et al.(2010) performed a specific experimental strategy to optically track the surface of the specimen during cyclic loading. This method was also compared

to the global information obtained by more classical strain measurements devices, in order to get a correct interpretation of the phenomena. The authors recommend using AE monitoring to help to find the number of cycles for crack initiation, in addition to these optical measurements.

2.13 Combination of AE and DIC techniques

Both AE and DIC techniques have advantages and disadvantages as explained by Aggelis (2013). These techniques were utilized in monitoring fatigue tests to enable validation of the AE method and to justify the method for future damage detection applications. The complementary use of DIC and AE helps to minimise the assumptions in the interpretation of the AE trends in relation to the responsible damage mechanisms by revealing the fluctuation of the surface strain fields and other factors such as paint delamination (Shrama et al. 2014, 2015).

Few previous studies have been conducted using the combination of DIC and AE under fatigue loading. This combination of techniques has been used previously by Pullin et al. (2010a, b) under fatigue loading; the first paper reports four point bending fatigue of aerospace steel and the second concerns detection of cracking in gear teeth under fatigue loading. Other researchers have used the combination of AE and DIC but under static loading. Kovac et al. (2010) used both techniques to monitor AISI 304 stainless steel specimens subject to constant load and exposed to an aqueous solution. Aggelis et al. (2013) used both AE and DIC to monitor bending failure of concrete beams reinforced by external layers of different composite materials. The failure behaviour of thermal barrier coatings (TBCs) under tension loading was investigated by Zhou M. et al. (2014), where a coupled acoustic emission (AE) and digital image correlation (DIC) technique was used. With the help of DIC observations, the evolution of AE can specifically define the different fracture stages of a TBC system.

From what has been explained, there is still a lack of a relationship between DIC and AE results under fatigue loading. Therefore, this work aims at establishing a full understanding of using the combination of AE and DIC to monitor fatigue loading through providing valuable experimental data.

2.14 Conclusion

In summary, this literature review has shown that there is numerous research addressing the fatigue testing in general and more specifically of steels which are used for automotive chassis and suspension applications. However, there is limited research on the fatigue of steel and its weld under various environments relevant to automotive applications. Furthermore, the fatigue properties of bending loading of steel and weld are not covered well. Thus, more work is required in this area.

Moreover, there is no available published literature which addresses the effect of the stone chipping on corrosion and fatigue properties. Most of the studies concentrated on the determination and evaluation of coatings resistance to chipping damage by stones or other flying objects. The main aim of this research was to further the understanding of the effect of simulated operating environments on fatigue properties of FB590 steel and welds.

The other aim is to monitor fatigue testing using the combination of DIC and AE to identify the damage mechanisms that occur in the way of final failure. However, a few previous studies have been conducted using the combination of DIC and AE under fatigue loading. There is great potential in using the RA/AF approach for source characterisation although, there is limited research using the RA/AF applied to metallic materials.

Table 2.1: Illustrations of the different pit shapes from (corrosion-doctors.org 2016).

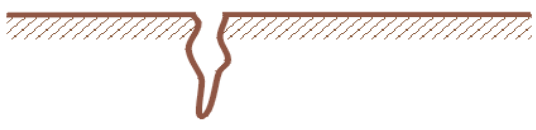
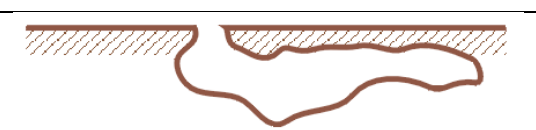
Trough Pits	Narrow and deep	
	Shallow and wide	
	Elliptical	
	Vertical grain attack	
Sideway Pits	Subsurface	
	Undercutting	
	Horizontal grain attack	

Table 2.2 Function and typical thickness of automotive coating layers (Ramamurthy et al. 1999; Takamura and Urban 2002).

Layer	Thickness	Purpose
Clearcoat	40 μm	Resist solar radiation, provide mechanical resistance to scratching and atmospheric pollution (acid rain, bird droppings, aggressive chemicals like road salts and caustic detergents)
Basecoat	15 μm	Carries all the colour pigments, long lasting colour and optimum appearance
Primer	35 μm	Cffering good adhesion and chipping resistance
Electrocoat	20 μm	Long-term corrosion protection

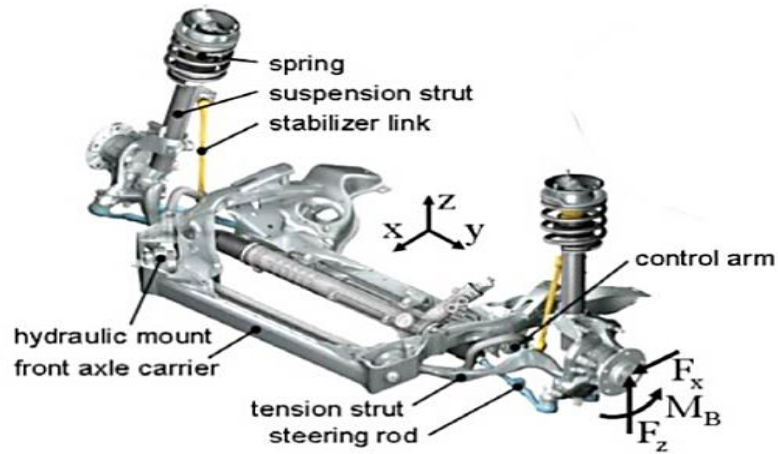


Figure 2.1 Chassis system of a BMW (3-series) adopted (Hägele and Sonsino 2014).

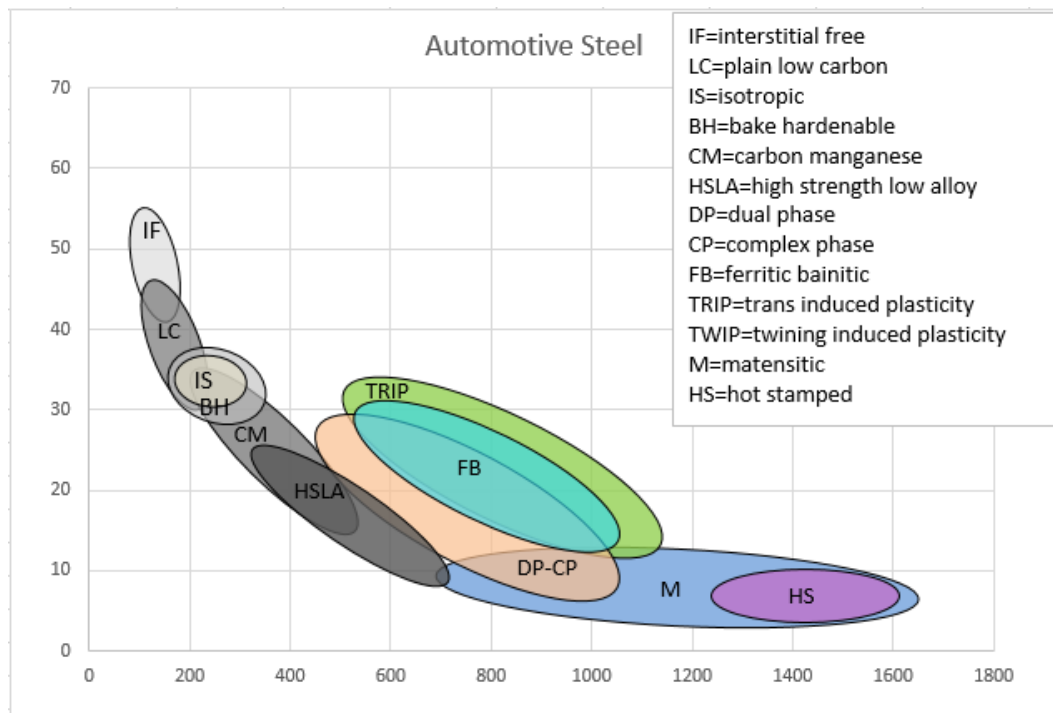


Figure 2.2. Families of Automotive steels adapted from (AHSS 2014).

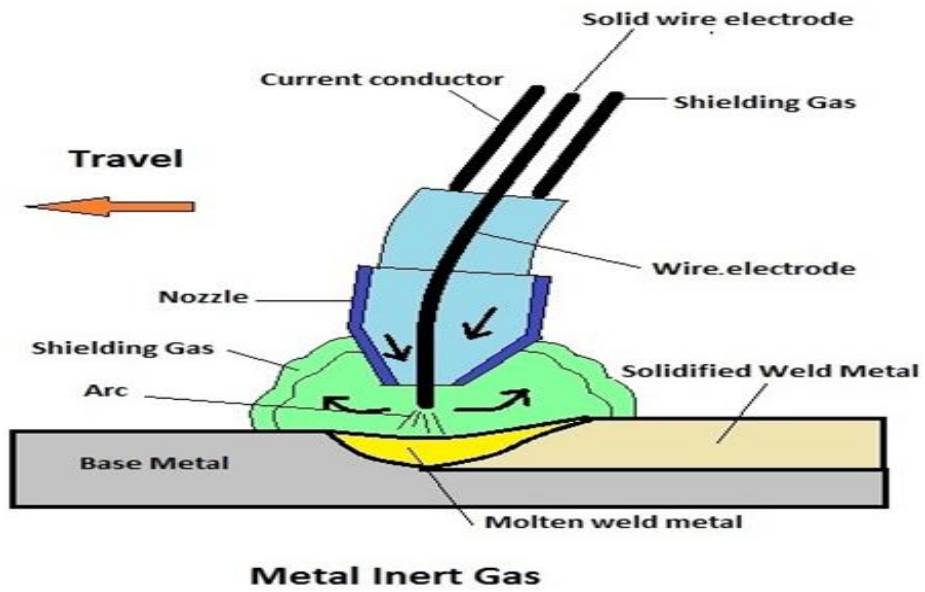


Figure 2.3 MIG/MAG welding schematic.

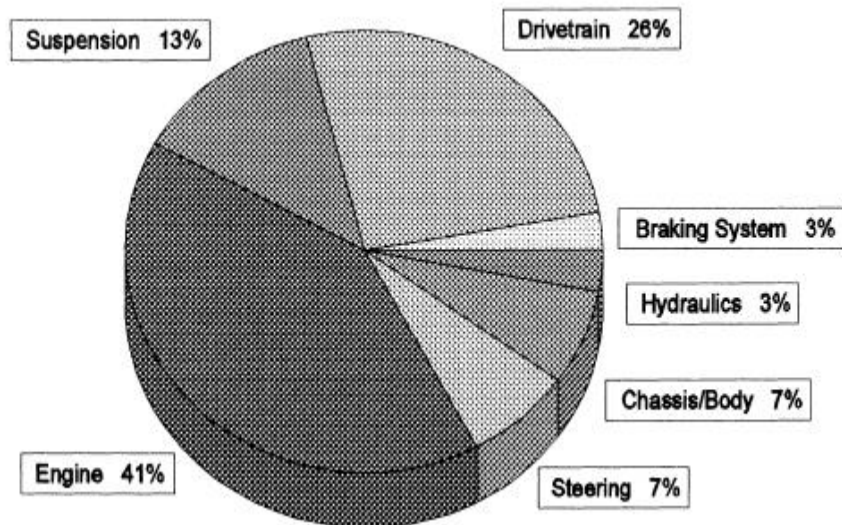


Figure 2.4: The distribution of component failures (Heyes 1998).

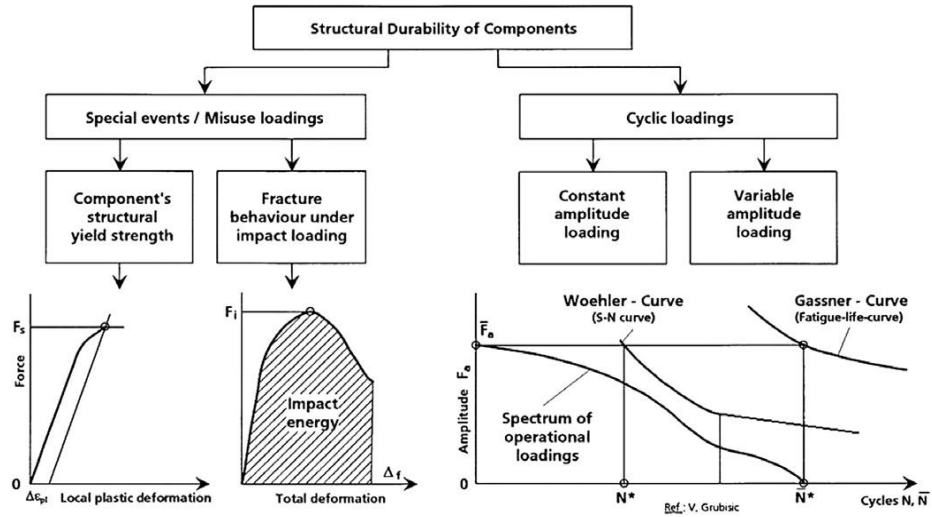


Figure 2.5: Loads determining structural durability of chassis safety components (Hägele and Sonsino 2014).

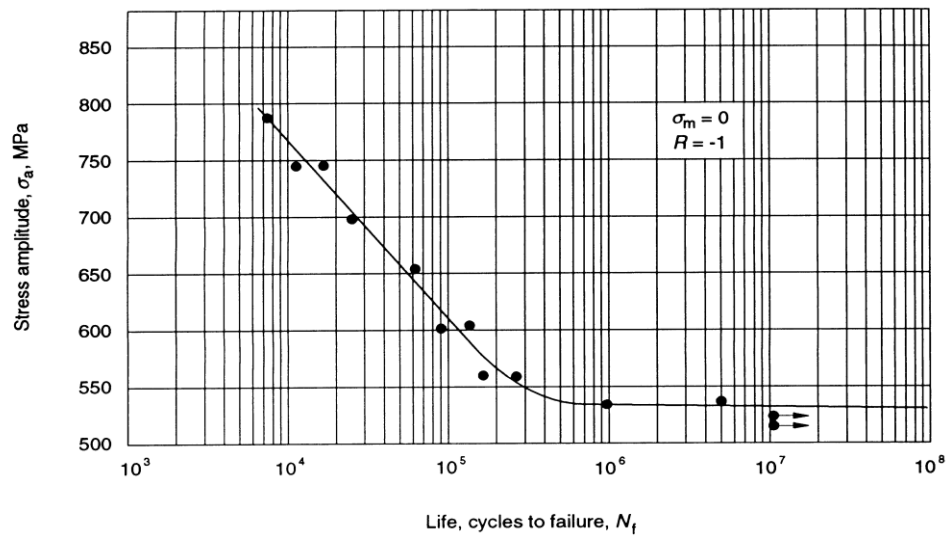


Figure 2.6: Schematic of S-N curve (linear stress scale) adopted from (BSI 1993).

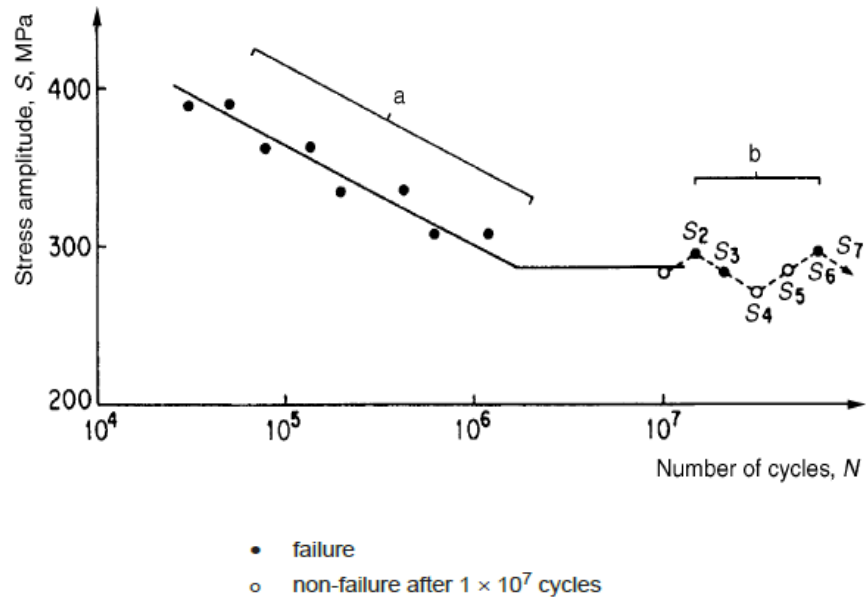


Figure 2.7: Schematic representations of S-N Curve, where part (b) shows the staircase method for determining endurance limit (BSI 2003).

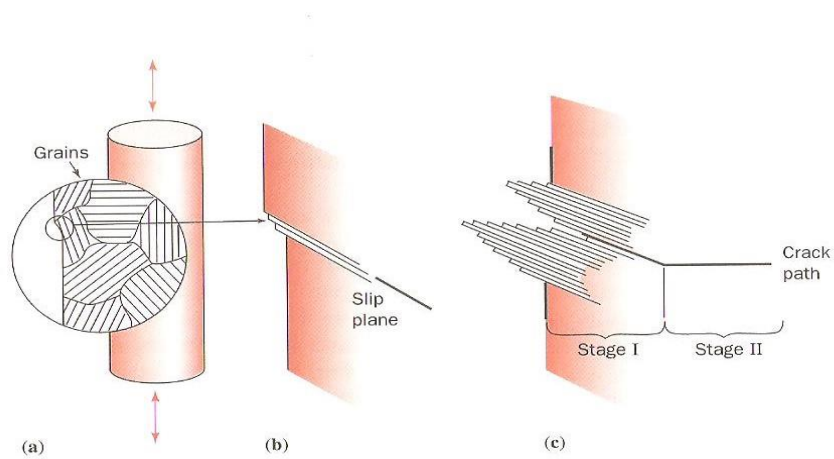


Figure 2.8 provides a general view about the stages of fatigue damage process (Benham et al. 1996).



Figure 2.9: schematic of stage (a) I crack growth (b) II crack growth (Rezig 2011).

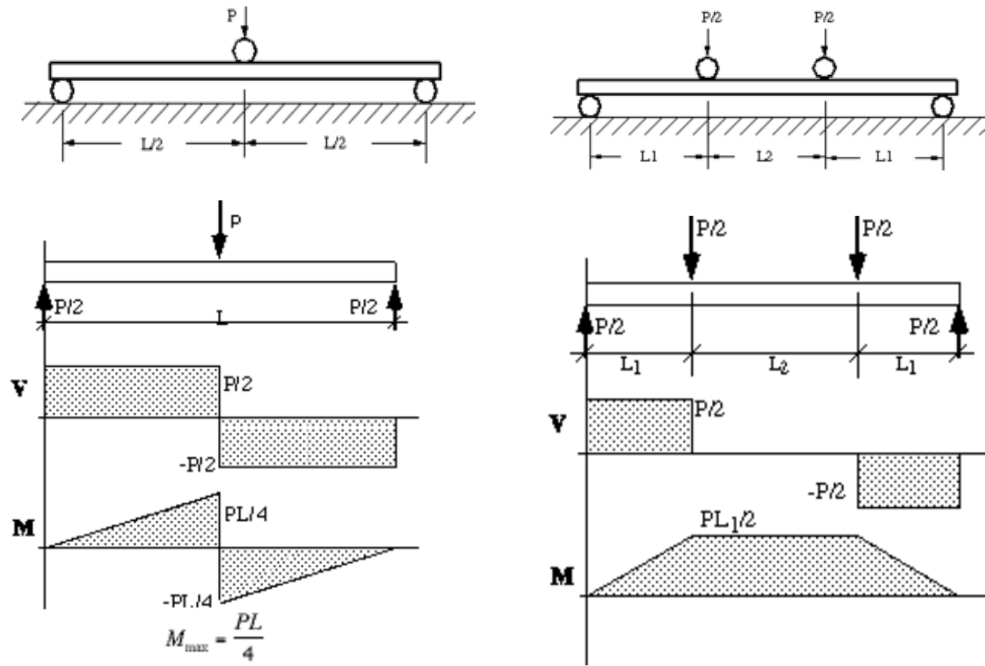


Figure 2.10 (a) Three-point bending beam (b) Four-point bending beam (Dupen 2015).

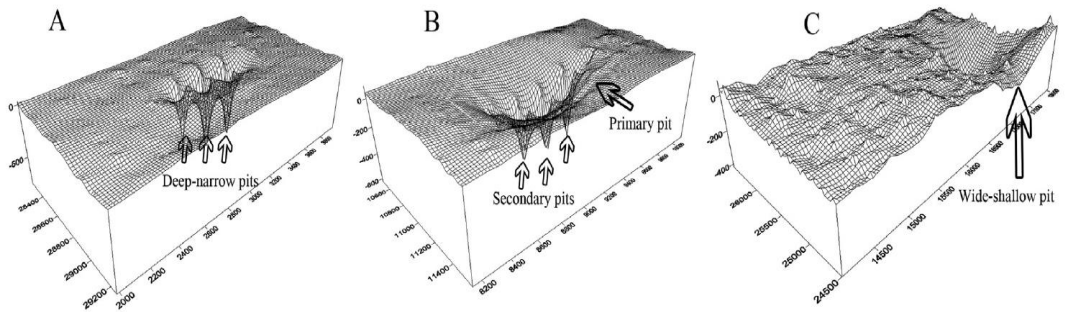


Figure 2.11: Three types of corrosion pits: (A) deep-narrow pits; (B) pits with secondary pits; (C) wide-shallow pits (Xu and Shan-hua 2015).

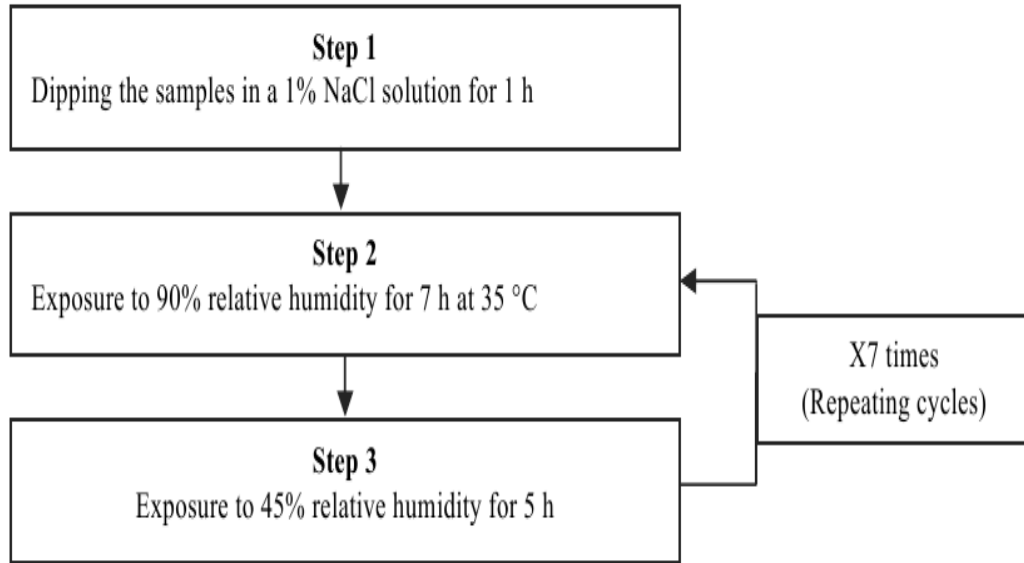


Figure. 2.12: Experimental procedure of VOLVO corrosion test (Katundi et al. 2010).

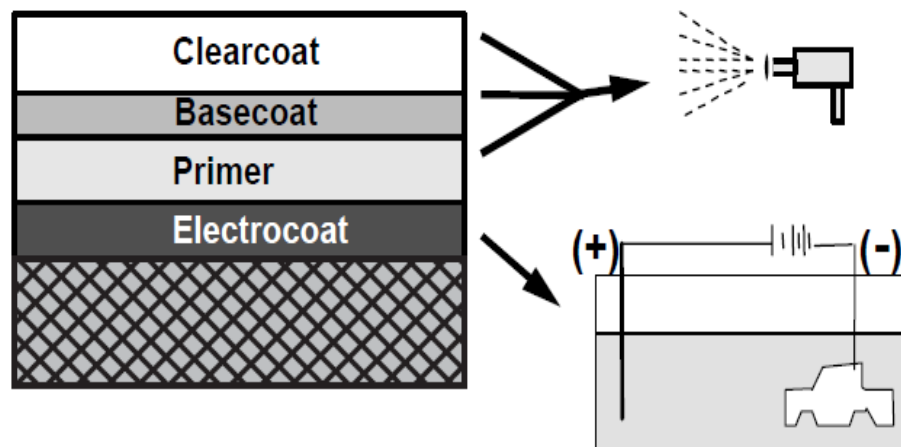


Figure 2.13 Automotive OEM coating layers (Takamura and Urban 2002).

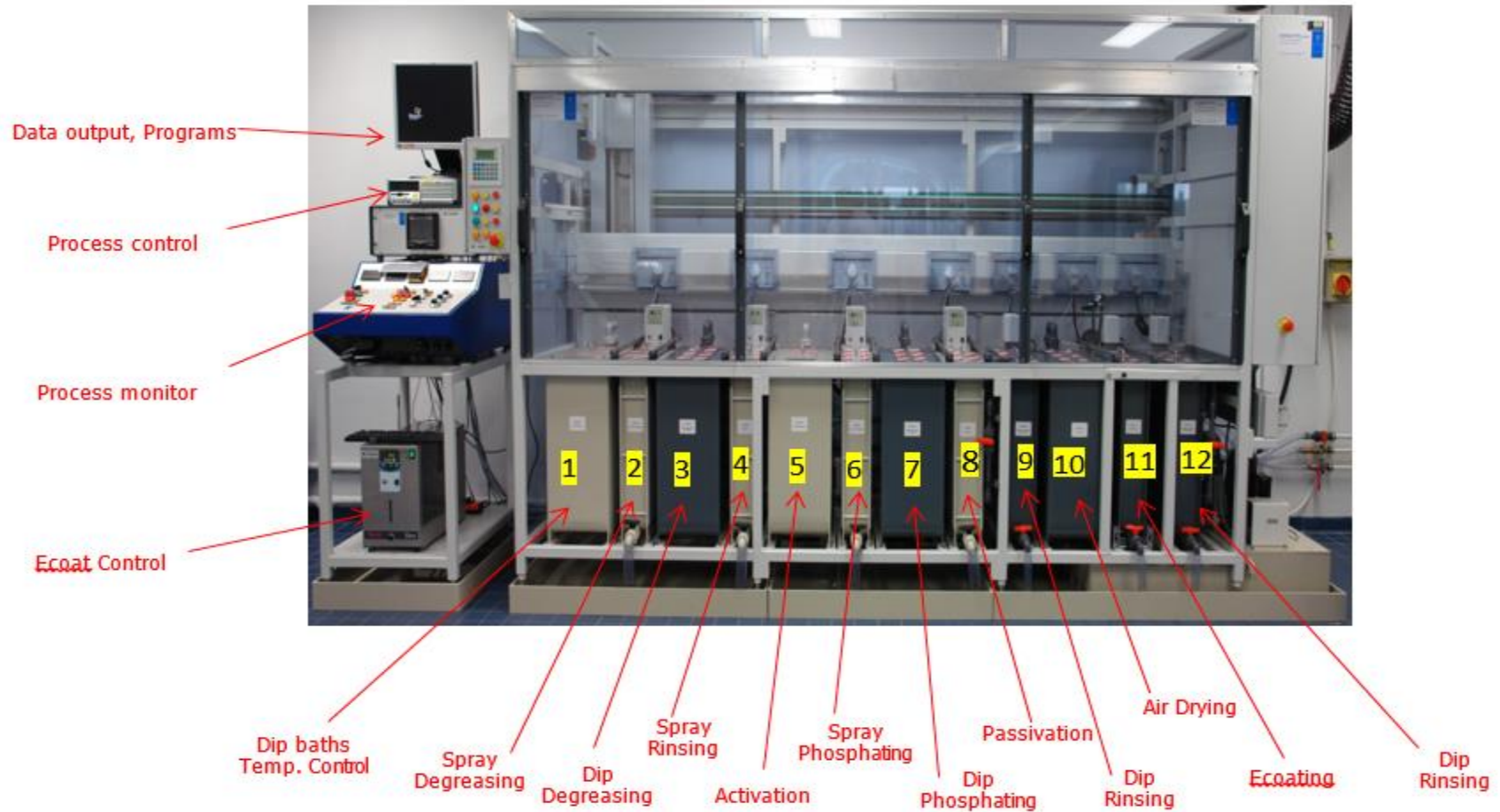


Figure 2.14: Automotive pilot coating line.

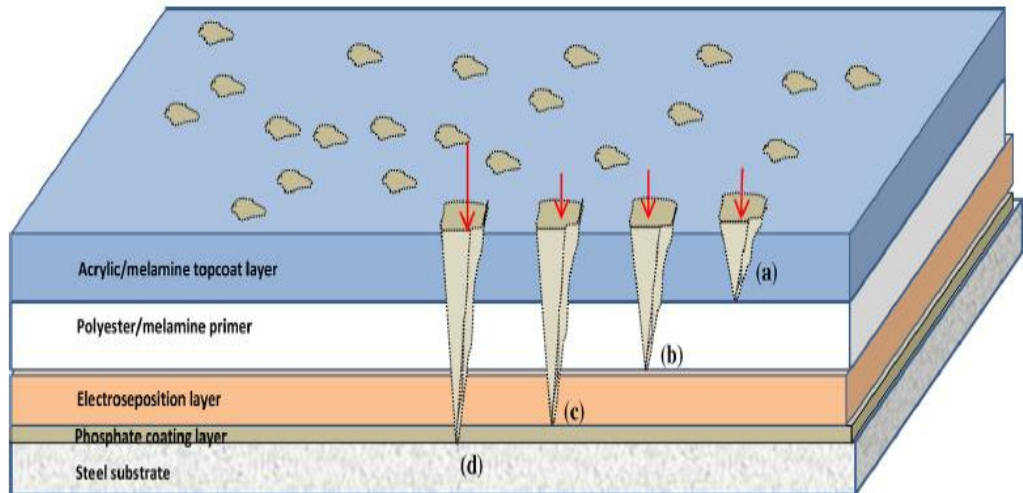


Figure 2.15: Schematic illustration of a coating system after chipping test; various types of damages including (a) topcoat layer damage, (b) primer layer damage, (c) ED layer damage and (d) phosphate layer damage (Razin et al. 2015).

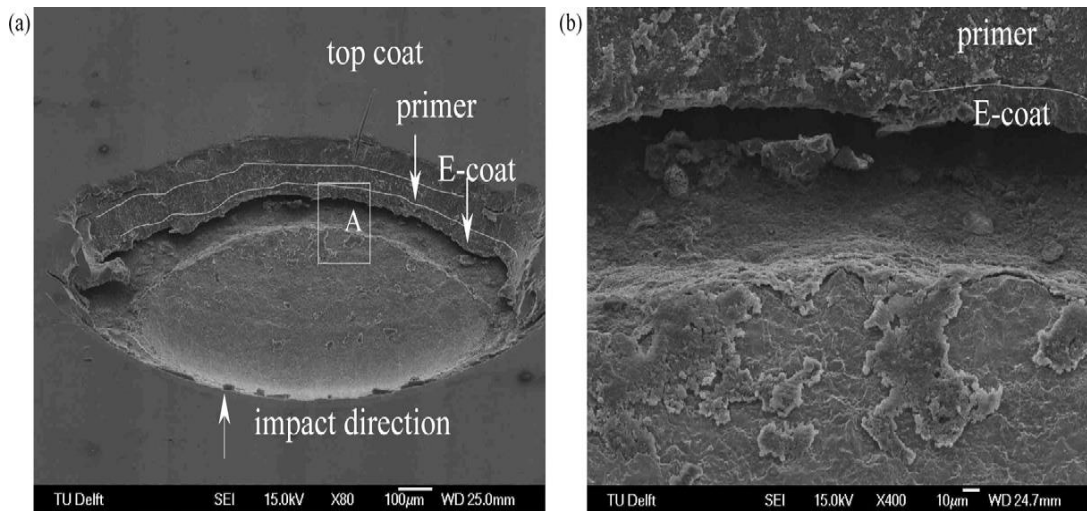


Figure 2.16: Typical damage caused by projectile impact for coating systems (a) general view, (b) magnified view of area A (Lonyuk et al. 2008).

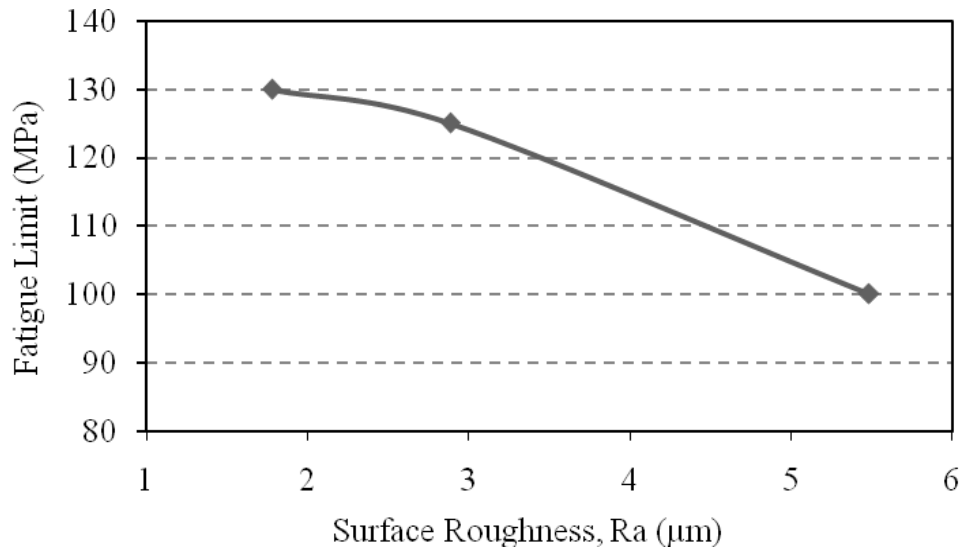


Figure 2.17. Summary of fatigue limits of analyzed specimens (Alang et al. 2011).

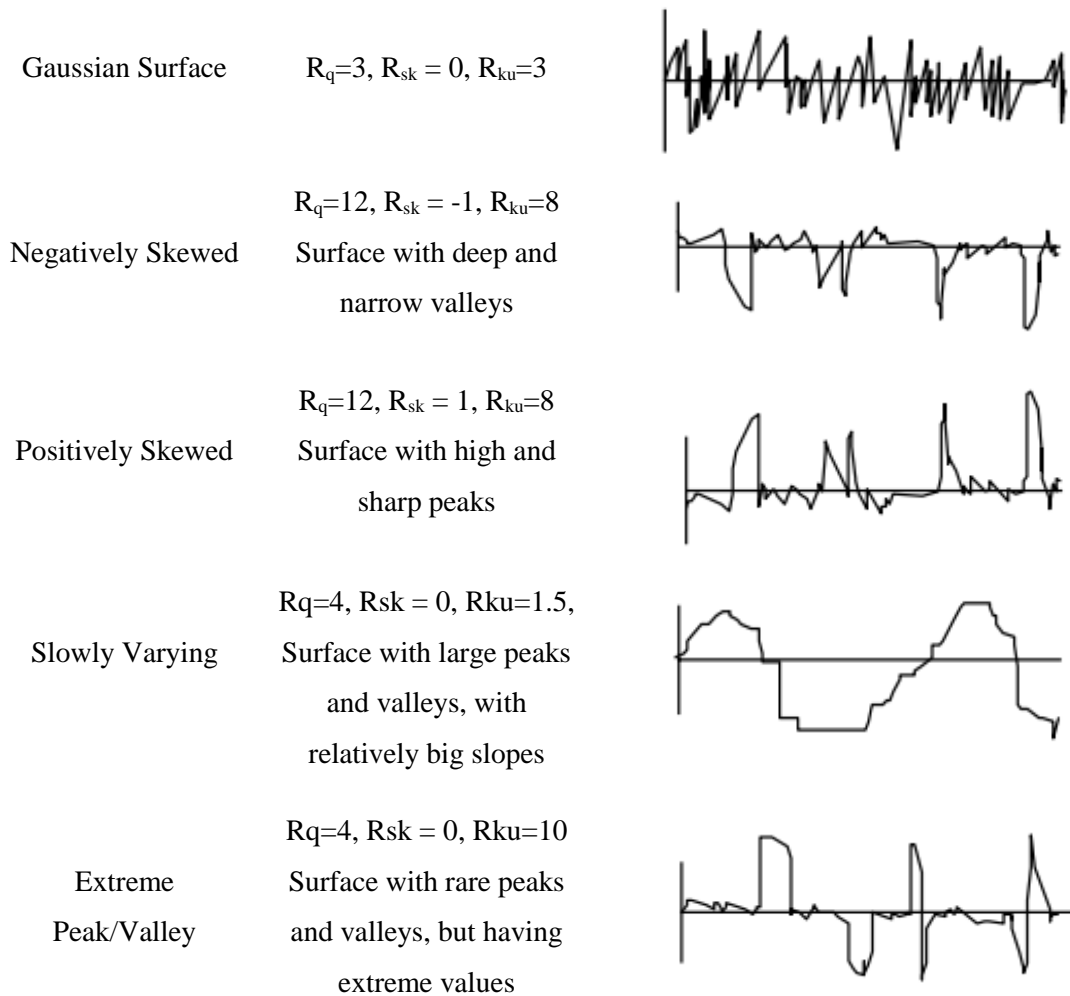


Figure 2.18: Types of surfaces and the corresponding set of parameters (R_q, R_{sk}, R_{ku}) taken from (ASME 2009).

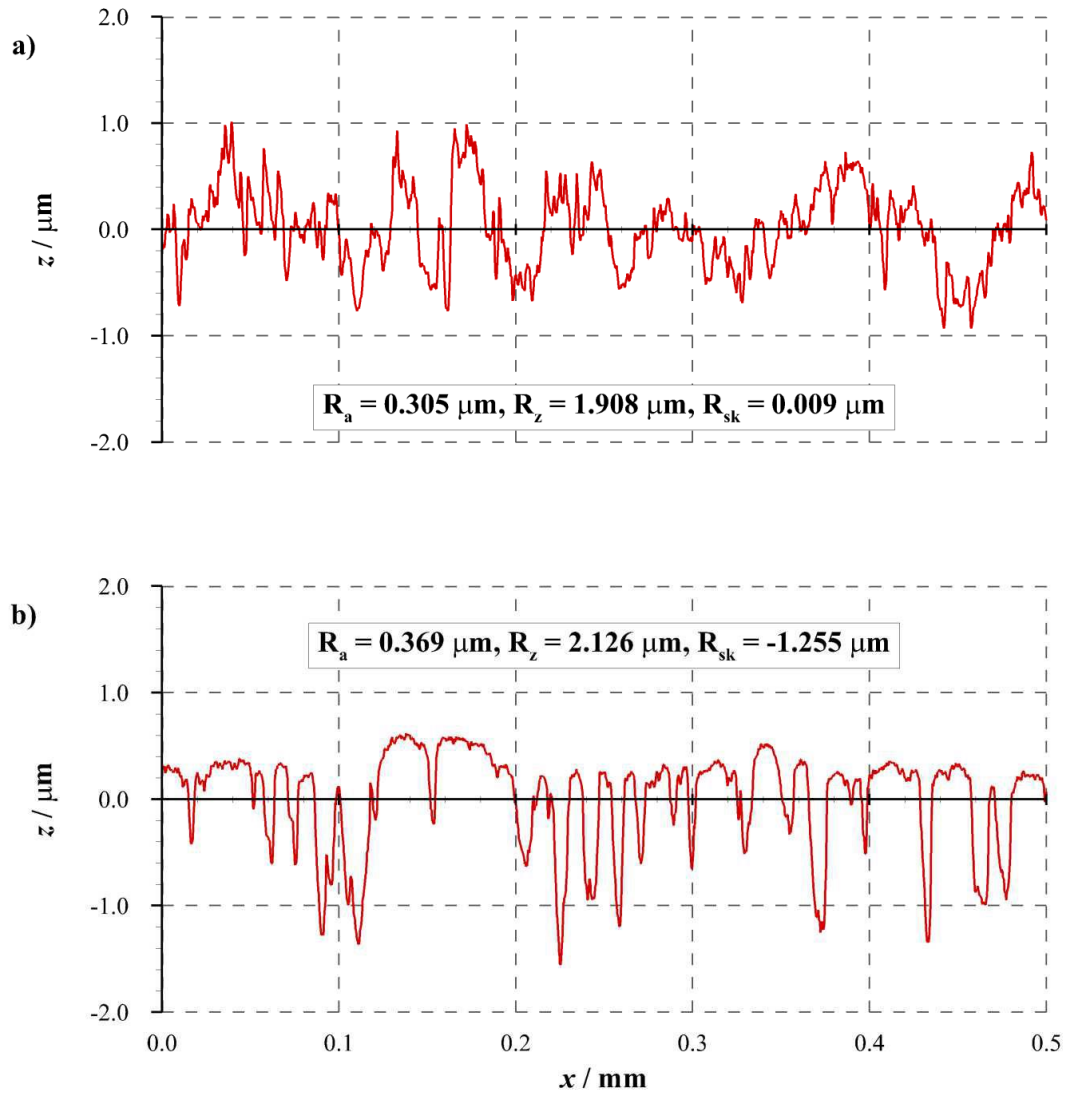


Figure 2.19: Filtered unrun (top) and run (bottom) surface roughness profiles from gear teeth adopted from (Bryant 2013).

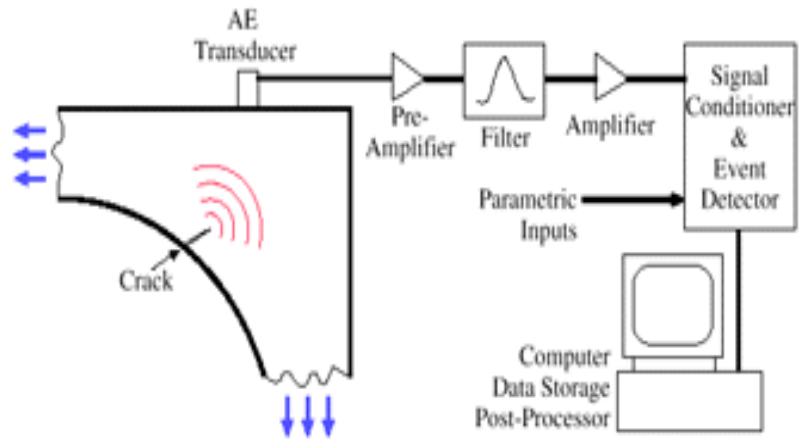


Figure 2.20 A typical acoustic emission test set-up (Huang 1998).

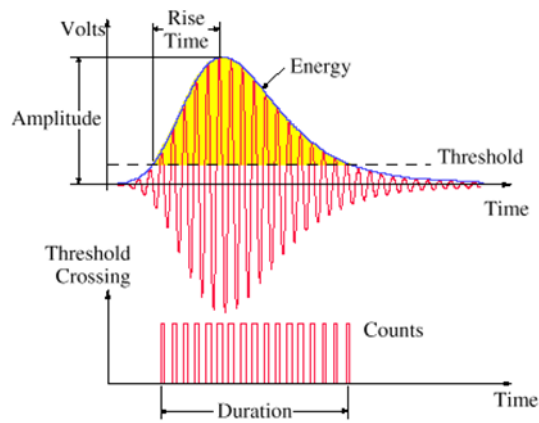


Figure 2.21: Primary acoustic-emission parameters (Barsoum et al. 2009).

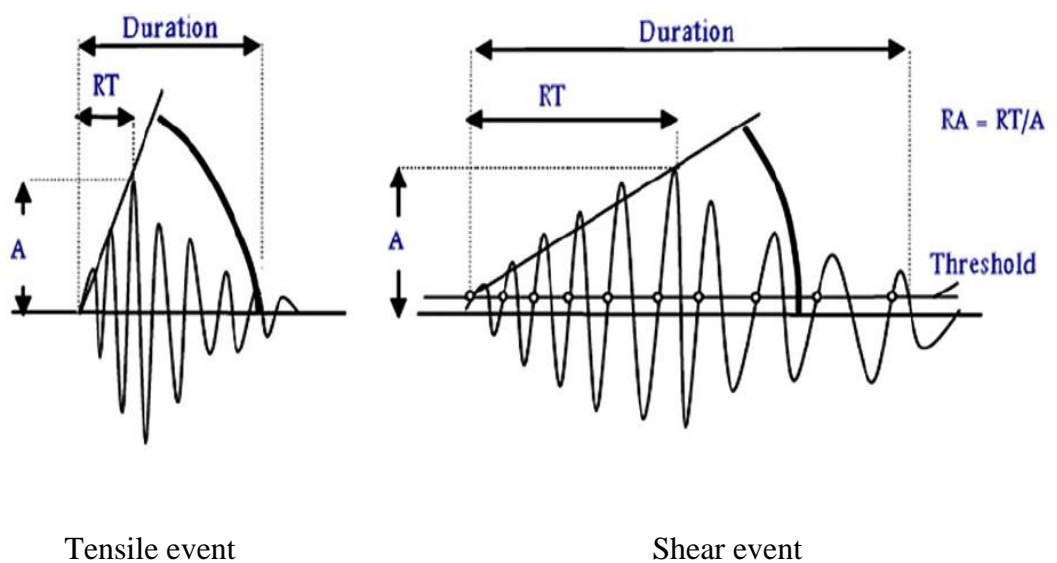


Figure 2.22: Cracking modes and corresponding AE signals (Elfergani et al. 2013).

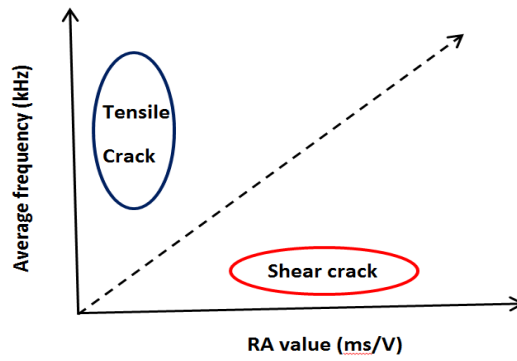


Figure 2.23: Classification type of cracking (Ohno and Ohtsu 2010)

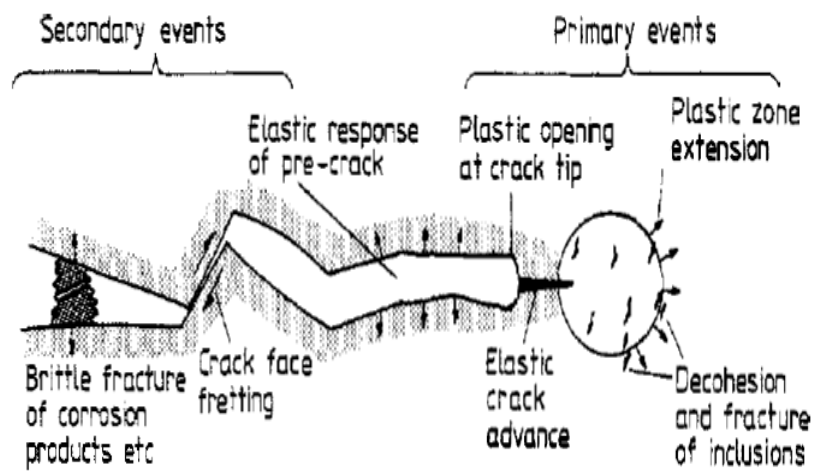


Figure 2.24 AE sources from fatigue taken from (Scruby 1987).

3. Experimental equipment, procedures and techniques

3.1 Introduction

The following chapter describes specific equipment, techniques and other systems utilised throughout this research. Experimental work detailing the stone chipping and corrosion process, the calibration and validation of monitoring techniques during the fatigue tests and the specimen surface profile measurements is also presented.

3.2 Materials and specimens preparation

3.2.1 *Welded Test specimens preparation*

It was decided that a rectangular “blank” should be made first with dimensions 120 x 140 mm, which was then subsequently welded to another such blank and cut, as shown in Figure 3.1. This blank can be machined and the specimen would then include a continuous weld in the centre, with no start/stop locations. This would eliminate the negative effects of weld start/stop regions on fatigue behaviour since the start/stop section of a weld will have different mechanical properties compared to the continuous mid-weld section as reported by (Maddox 1991; Harati et al. 2015). Thus, the entire welded samples were prepared by joining each adjacent piece together in order to obtain a blank as shown in Figure 3.1 which was then used to manufacture the standard specimens for fatigue tests in both tension and bending. The samples were butt welded from one side to guarantee acceptable penetration; moreover in order to ensure that final test specimens had approximately the same thickness and rolling properties at either side of the welded joint, the blanks were welded together such that they were originally adjacent to each other in the coil sample.

The specimens were taken from the middle of the whole sheet and sections near to the strip edges were discarded as there is inconsistency in thickness and mechanical properties near to the edges as shown in Figure 3.2 which shows data supplied by Tata Steel. The graph in Figure 3.2 shows how the thickness of a coil can vary across its width. The surfaces of the specimens were cleaned using

acetone, and then marked on the center of the upper face of the specimens in order to ensure accurate and consistent alignment between blanks before welding.

3.2.2 Welding Trials at Warwick Manufacturing Group

The welding process was carried out at the Warwick Manufacturing Group on the Warwick University campus. MIG welds were performed with the blanks in the flat position using an ABB robotic welding machine as shown in Figure 3.3. A welding jig is required to prevent clamping issues occurring when the samples spread out underneath the clamps holding the pieces to the workbench. To protect the molten weld pool during welding, the top surface of the work-piece was shielded using a mixture of argon and 18% CO₂ that was fed through the MIG nozzle at a flow rate of 18 L/min. The final welding settings are shown below.

Final settings selected for MIG butt welding:

- Wire feed speed, 6.8 m/min
- Weld speed, 20 mm/s
- Filler wire, ESAB Aristorod 13.26 Ø1.2mm diameter
- Weld programme, CMT 1184+P
- Program manufacturer Fronious
- 197 A / 22.6 V
- Gas speed, 18 L/min

Since MIG welding was done automatically, the wire feed is automatic and combined within the fusion process which ensures that samples are as consistent as possible. Thus the profiles of the MIG welds had a fairly similar appearance to that shown in Figure 3.4 also it has an almost flat profile with full penetration at other side of the welds. This image of a MIG weld can be considered to be a typical sample of this joining method. In fact the visual and geometric appearance of all welds in the collection of specimens was reasonably similar to each other, with relatively little variability in terms of distribution of filler material. However there are a few anomalies specimens which have highly raised (domed) profile or flatter in appearance when the filler material was added. There can be no doubt as to the influence of the weld geometry on the fatigue properties of this material

where it is thought that this is due to the weld toes which have high levels of stress concentration and which therefore form the main contributors to crack initiation (Lee et al. 2009; Harati et al. 2015).

All the welded samples were inspected using the dye penetrant inspection method to ensure that they were free from defects introduced at the welding position during preparation such as porosity, surface cracks, undercut, lack of weld penetration or lack of side wall fusion etc. (ASTME-165-95 2001; Tao et al. 2014).

3.3 Tensile strength measurements

Static tensile tests were performed prior to fatigue testing to determine the monotonic properties of the material at ambient conditions. Tensile test specimens were cut from the same sample of coil with the loading axis of the specimen aligned with the rolling direction. A Zwick Roll Z100 electro testing machine with load cell of 100 kN capacity was used to conduct the tensile tests of the present work. The machine is provided with special software so that the load elongation diagram can be recorded during the test.

Careful attention was applied to ensuring the gripping axis of the test specimen coincided with the centre line of the heads of the testing machine, to ensure no bending stresses were introduced. Therefore, the vertical alignment of the specimen was verified using a spirit level.

The ultimate tensile strength σ_u was defined as the maximum stress and the yield strength σ_y was obtained by using the 0.2% offset method, the elastic modulus E is defined as the slope of the elastic region of the tensile stress–strain curve.

The specimens were designed and manufactured in agreement with BS EN ISO 6892-1:2009 (BSI 2009) specifications. The geometry of the tensile test specimen is shown in Figure 3.5. The results of tensile strength measurements for both mild steel and high strength steel are presented in Chapter 4 and 5 respectively.

3.4 Specimens design

3.4.1 Mild steel fatigue specimen design

The tests were conducted on steel dog bone specimens shown in Figure 3.6 which was designed in compliance with BS 3518-3: 1963 Fatigue Testing – Part 3: Direct stress fatigue tests (BSI 1963). Fatigue test specimen geometries were designed based on an un-notched specimen with no stress raisers on the test section and included tangentially blended fillets between the test section and the gripping ends. A gentle arc was used in the specimen design to avoid failure which take place at the bottom of fillet due to the physical shape of the specimen which can also influence fatigue strength. Small radii can induce stress concentrations and are locations where cracks initiate and propagate, thus leading to failure. The specimens were aligned with the longitudinal rolling direction.

Figure 3.7 shows a Finite Element Analysis (FEA) to design a specimen with less stress concentrations, where the FEA analysis were carried out by using Solidworks. Solidworks simulation is the built-in analysis tool inside, it allows users to check a model for potential failure like excessive stress, strain and temperature. The assessment was carried out by applying a 20 kN of force at one end and proper fixture at the other end. An ASTM A36 steel which selected from material library of solidworks. Stress predictions are made for both Von-Mises and normal stress in the direction of the applied load, where the predictions for both are similar, the material and model properties as follow:

Name: ASTM A36 Steel
Model type: Linear Elastic Isotropic
Default failure criterion: Max von Mises Stress
Yield strength : 2.5e+008 N/m²
Tensile strength: 4e+008 N/m²
Elastic modulus: 2e+011 N/m²
Poisson's ratio: 0.26
Mass density: 7850 kg/m³
Shear modulus: 7.93e+010 N/m²

The screenshots of these analysis shows that there is no significant stress concentration at the bottom of the fillets. It was observed later that most of the specimens failed from the middle due to high-stress concentration in the middle of the specimens. This states why mild steel specimens were firstly chosen in order to enhance the testing procedure and overcome the problems and obstacles.

Six holes were produced at each ends of the specimen in order to hold the specimen on the testing machine. These holes were drilled though these supporting plates, one with 20mm diameter for loading pin holder and five others with a diameter 8 mm for inserting bolts and nuts to grip the specimen between supporting plates. Four supporting plates were used to grip and hold the specimen to the loading cell in the test rig during this test. These supporting plates were fabricated with the same geometry and dimensions as the specimen's ends.

3.4.2 FB590 fatigue specimen design

The FB590 fatigue specimen design is modified from the design of the mild steel specimen in order to provide a constant stress concentration in the test section area and have a sufficiently long parallel section to cater for the requirements of the corrosion study (Xu and Qiu 2013).

Figure 3.8 shows the FB590 specimen design which is compliant with BS 3518-3: 1963 Fatigue Testing – Part 3: Direct stress fatigue tests (BSI 1963). The specimens were designed to best utilise the material samples available. The specimens were aligned with the longitudinal rolling direction. The welded joint occurs at the middle section of the welded specimens.

The specimen design avoids failure which takes place at the bottom of fillet due to the physical shape of the specimen that can also affect fatigue strength. Small radii can lead to failure due stress concentrations and their locations where cracks initiate and propagate. Therefore, it is desirable to make a fatigue specimen without any geometrical stress concentration at all. This would require a large radius that would only be possible by making a specimen longer, given the desire to maintain the end width in order to use the previous clamping arrangements. Increasing the radius would then have to be done by increasing the overall specimen length, which is possible in this case due to the high sample length

capacity of the available testing machine. Designing the specimen to have large enough radiuses was not easy especially to fulfill with British and ASTM standards (BSI 1963; ASTM-E466 2002). Thus the design which is shown in Figure 3.8 was chosen after iteration of specimen design based on FEA to maintain specimen design with less stress concentration. The screenshots of these analyses is shown in Figure 3.9 which shows that there is no significant stress concentration at the bottom of the fillets.

3.4.3 FB590 four-point bending fatigue specimen design and preparation

After manufacturing tensile fatigue specimens, the remaining portion of welded rectangle (260x120) mm were cut into two pieces to manufacture bending fatigue specimens to best utilise the material available and reduce the requirement for welding new specimens, thereby reducing both effort and manufacturing costs. Figure 3.10 shows the location of the two semi rectangle geometry of the fatigue bending specimens. Specimen preparation involved cutting using the mechanical saw from the remaining blank rectangle, then milling, grinding and finally polishing the sides of interest to a 1.12 μm Ra surface finish using a surface grinding machine. The final surface appearance was mirror-like, which was assumed free of imperfections. After polishing, specimens were cleaned then e-coated. The roughness of the sides of interest was verified by using surface profilometry to measure the edge roughness prior to test. Ground method offers a desirable alternative to the wire erosion method which was used for the preparation of tensile specimens, with its high flexibility and its ability to polish sheet to high precision.

The surface profile of both cut-edges generated by using the wire erosion and surface grinding methods were measured to quantify surface roughness due to the fact that the high strength steel structures used in automotive applications are significantly influenced by the conditions of the cut-edges produced during component manufacture (Thomas et al. 2011). In order to record and quantify cut-edge surface properties of both these surfaces, a profilometer (Taylor-Hobson form 2) was employed with scans being carried out across a two-dimensional surface area providing an accurate representation of the cut-edge roughness data parameters as shown in Figure 3.11. This figure shows clearly that there is no

significant difference between the quality of surface produced using the wire erosion or grinding methods. It is evident that both surfaces which were generated using wire erosion ($R_a=3.3$) and grinding ($R_a=1.12$) showed no major difference results in terms of roughness.

Four-point bending testing was employed to study the bending fatigue properties of FB590. The bending fatigue tests were conducted in load control with a load ratio of $R = 0.1$ and a 5 Hz sinusoidal waveform. The configuration of the four-point bending test is shown in Figure 3.12, the crosshead was placed in the middle of two supporters of upper span with 32 mm, specimens with a total length of 135mm, a distance between the lower supports of 64mm, a thickness and width of 2.78 mm and 25mm respectively as shown in Figure 3.12. During each test, the applied compression load and displacement were recorded continuously by the MTS software. The specimen was considered to have failed when the specimen deflection exceeded a pre-determined maximum deflection. After failure, dye penetration was performed in order to identify the cracks which could be visible. The fracture surfaces were studied using a scanning electron microscope (SEM) in order to identify the fatigue mechanisms of the material.

3.5 Fatigue loading and test set up

3.5.1 Loading Calculation

It is evident from experimental test as explained in Chapter 4 that for a 3mm thick specimen of mild steel to reach its UTS of around 423MPa, the sample requires a force of approximately 25.3kN.

Whereas for a 2.78 mm thick specimen of FB590 with a UTS of around 600MPa, the sample requires a force of 33.4 kN. Other specimens for both mild steel and FB590 were tested at different loads and the load cycle for each specimen is reported in the following Chapters.

For corroded specimens dimensions were taken three times at different points of parallel length then, the average of width and thickness were used to calculate the cross sectional area.

3.5.2 Loading machines

A cyclic load was applied to all tensile specimens using a Losenhausen servo-hydraulic testing machine (maximum force 100kN) with an MTS FlexTest controller. The bending specimens were tested using a Dartec 20 and 5 kN dynamic testing machine. These testing machines enable displacement, load, time and cycles to be acquired, allowing analysis of cycles to failure as well as displacement characteristics to be determined.

The specimens were subjected to fatigue load ranges corresponding to specific percentages of the ultimate tensile strength. However, special consideration was paid to identify the endurance limit for each case, despite the time consuming nature of such testing. This is important as automotive chassis components are safety critical components, where failure has potentially catastrophic consequences. Crack initiation is considered a significant characteristic in automotive chassis design, particularly with the trend towards weight reduction and the increasing use of high strength steels.

The tensile fatigue cycles tested were performed with a stress ratio, $R = 0.1$. A sinusoidally varying load input at a frequency of 5 Hz ensured the specimens were subjected to constant amplitude cycling using load control. For tension fatigue tests, the failure criterion was defined as complete separation and any specimens which failed outside of the gauge test area, either in the blend fillet radius or at the ends were discarded and the results not considered. For bending fatigue tests, the failure criterion was defined when a specified maximum deflection was exceeded and the loading machine stopped. This helped to ensure consistent results with the same mode of failure and to prevent any unnecessary inconsistencies in the scatter of the fatigue data. After failure, dye penetrant was applied to bending specimens in order to identify the cracks which could be visible. The fracture surfaces were studied using an optical microscope and scanning electron microscope (SEM) in order to identify the fatigue mechanisms of the material.

The fatigue limit of the specimen was taken when the number of cycles to failure, N is greater than $5(10^6)$. The results of these tests are presented as a plot of stress range level (σ) as a function of the number of cycles to failure (N) (S–N curves).

The results of fatigue test are presented in Chapters 4 and 6 for mild steel and FB590 respectively.

3.5.3 Bending loading frame set-up and dimensions

The four point bending test set-up used the loading frame shown in Figure 3.13 test. This loading frame was built in order to guarantee sufficient precision by limiting the lateral movement of rolls or specimen during the test. Designing the loading frame to have stability was not straightforward, and the final design was arrived at following multiple iterations and physical experimentation.

One roller was fixed by welding and the other was free as shown in Figure 3.13. The free roll was surrounded by two stoppers with height which did not exceed the radius of the roll to prevent roll lateral movement and to ensure fixed dimension between supports during the test. To ensure the free roll did not bind, a 0.5 mm distance was maintained between the stoppers and the roll.

3.5.4 Fatigue test monitoring

To be able to identify the fatigue crack development, DIC and AE monitoring were used in this research. Figure 3.14 schematically shows the fatigue specimen held in a fatigue testing machine with AE and DIC equipment used to track crack growth during the fatigue test.

Figures 3.15 show two different views of the test set up. The specimen was pinned into the MTS servo-hydraulic testing machine by two 20 mm diameter pins. As with tensile testing, fatigue loads were avoided by careful alignment.

3.6 Fractographic sample preparation

Scanning electron microscopy was performed to carefully examine the corrosion defects and the fracture surface obtained after fatigue tests. The specimens for fractographic examination were sectioned to the required sizes. Then specimens were mounted on the stage of SEM device as it allowed the whole cross section sample to be prepared in the same way and analysed at once. The fractographic samples were cleaned using a solution of Nital 2% plus a tensoactive agent for a

few seconds followed by ultrasonic cleansing with acetone. The operating conditions of the SEM machine such as working distance was 7.0mm and acceleration voltage was 5.00kV. The fracture surfaces were observed using stereo Optical Microscope (Olympus) and scanning electron microscope (SEM, Model: Zeiss 1540 XB Cross Beam scanning electron microscope).

3.7 Acoustic emission instrumentation and techniques

3.7.1 Data acquisition and storage

The AE system, DiSP was used in this study. It was manufactured by Mistras Group Limited (MGL). It utilizes parallel 32 bit digital signal processor (DiSP) technology and uses Peripheral Computer Interface- Digital Signal Processor (PCI-DSP) boards. Each board carries four channels with data transfer speeds up to 20 Mb/sec assuring a wide bandwidth for multi-channel AE data acquisition and waveform processing. A more in depth description is given by the manufacturer (PAC 2005).

3.7.2 AE sensors

A sensor is a device that produces a measureable voltage signal proportional to the physical parameter it is monitoring. When the sensors are attached to an object's surface they detect surface stress waves (Lamb waves) resulting from AE events and then convert this energy into voltage-time signals that are used for all subsequent steps in the AE measurements.

A preamplifier is used to pass the electrical signal, usually located close to the sensor. The preamplifier provides a gain and low frequency filtering to remove undesirable mechanical noise, before passing to the processor for digitisation via a coaxial cable. The AE signals were amplified by a 40 dB fixed gain 2/4/6 preamplifier. A band pass filter, with a range of 100–1200 kHz, was used in the preamplifier. A threshold of 45 dB was selected, which was just above the background noise level the selection of threshold was based on previous research on isotropic materials (Baxter 2007; Barsoum 2009; Pullin et al. 2010).

The sensor selected for this study was the PAC nano 30 which at only 8mm in diameter is suitable for mounting on the relatively small fatigue specimens.

Technical details of nano 30 can be summarized as frequency range 125-750 kHz with a nominal resonant frequency in shear of 300 kHz and in compression of 140 kHz.

The smaller size of the nano 30 is very useful when identifying sensor mounting points on a fatigue specimen. Due to the surface roughness of corroded specimen, there are few flat accessible areas.

3.7.3 Sensor mounting and Couplant

The quality of the signals recorded by the AE sensors is important to the success of the test method. Poor quality of the signal will prevent the test method's ability to detect defects in the structure.

In this study, to maintain acceptable contact between the sensor and specimen surface and retain position, silicone gel was used at the interface between the sensors and the specimen surface to obtain good acoustic coupling. Initially the sensors were attached to the specimen with a U-shaped magnetic clamp shown in Figure 3.16, which was removed when the silicone was dry after 24 hours. H-N sources were conducted to verify the sensor response.

Silicone rubber compound was used because it can be applied as a fluid to achieve a thin, bubble free couplant and at the same time provide a permanent bond on the structure under test (Baxter 2007). This thin layer can provide excellent sound transmission with a relatively strong bond. Furthermore, silicone rubber compound also works very well on rough surfaces and has good resistance to bond failure if surface movement might occur during the test and therefore is suitable for vertical mounting applications. This type of bond enables easier sensor removal after use with lower risk of sensor damage compared with other commonly used methods such as cyanoacrylate bonding.

3.7.4 Hsu-Nielsen source

After the sensor is installed and connected to the monitoring equipment, before monitoring begins the system sensitivity (performance) should be checked. The first aim is to simulate the AE source and the most common technique uses the

Hsu–Nielsen source (ASTM-E976 2001), shown in Figure 3.17. This technique is a reasonable, cost effective method for sensitivity assessment and it is based on pencil lead breaks. The test is performed by breaking the lead pencil with specific dimensions against the surface of the structure being monitored.

This test consists of breaking a 0.5 mm (alternatively 0.3 mm) diameter pencil lead approximately 3 mm (+/- 0.5 mm) from its tip by pressing it against the surface of the piece. This generates an intense acoustic signal, quite similar to a natural AE source that the sensors detect as a strong burst. Hsu–Nielsen sources provide a sufficient verification of good excursion of AE events from the source to the AE sensors. Moreover they also verify the quality of the acoustic coupling between AE sensors and the surface of the structure under test. The H-N source will provide a hit with amplitude of 98 to 100 dB adjacent to AE Sensor, mounted on a specimen surface.

3.8 Preparing digital image correlation

DIC works by comparing the gauge length between two points located in a random speckle pattern and comparing the respective gauge lengths between these points across multiple images. These images are taken in succession so represent specific points or times as determined by when they were captured. This method of damage detection provides good visual analysis of events occurring in the sample (Sutton et al. 2008).

In order to use the DIC system a random speckled pattern has to be applied to the specimens prior testing. This can be done using spray paint. First the region to be measured using the DIC must be sprayed a uniform white colour. Then a fine speckle pattern is produced using a black spray paint, with only light pressure applied to the release valve such that the paint splutters out.

In addition, the DIC system must be calibrated prior to use. This calibration enables the DIC software to calculate gauge lengths and strains within the material providing data that corresponds to the images captured.

DIC images were collected every 1000 cycles using a Dantec Dynamics Q-400 system which was triggered from the MTS controller while holding briefly at maximum load. Figure 3.18 explains the load history.

The relative movement of two pixel subsets on either side of the crack was used to provide a crack mouth opening displacement (CMOD) measurement. These measurements are based on the comparison of a reference image, with images taken at different load steps. CMOD is a common engineering term /tool in this investigation CMOD refers to the distance between to pixels and includes plastic deformation.

Figure 3.19 shows a typical method of evaluation of CMOD from DIC for an uncorroded mild steel specimen under test at a peak stress of 320MPa, R=0.1. The selected region was identified by a dotted white rectangular box, and then two points around the crack edges were selected close to each other, the displacement difference between these points in the Y direction will represent crack mouth opening displacement. At the initial tests the CMOD showed a significant jump at the beginning of some tests. This because the distance between the two selected points was large and this length undergoes initial plastic deformation as illustrated in Figure 3.20.

3.9 MTS measurement and DIC comparison

As explained previously the testing machines enable displacement, load, time and cycles to be acquired. Figure 3.21 shows the consistency between behavior of both extension (MTS) and DIC results for a corroded mild steel specimen under test at 400 MPa. There is close similarity of the behavior of the results obtained from both these methods. It can be concluded that the extension MTS curve has approximately the same characteristics as the crack opening displacement curve, but with less accuracy. This is due to many contributing factors such as plastic deformation of the whole specimen as well as the extension of other connections to the actuator. Therefore, in forthcoming tests the results are presented using DIC analysis rather than MTS data.

3.10 Dye penetrant inspection

Dye penetrant is a NDT method used to aid visual inspection by enabling cracks that have broken to the surface to be readily seen. Dye penetrant testing works by capillary action where dye liquid with low surface tension penetrates inside the crack. Red dye penetrant was used in this work to ensure the indications produce a good contrast with a white developer.

The dye penetrant test was used in this work as shown in Figure 3.22 to identify the defects for bending specimens after fatigue testing. In addition it was used to identify welded joints defects such as porosity, surface cracks, undercut, lack of weld penetration or lack of side wall fusion, which are harmful to the mechanical properties, in particular, the fatigue behavior. This method was chosen because of the following;

- It is a low cost inspection method and available.
- Test is easy to complete and does not involve complicated instrumentation.
- The inspection is very quick.
- Results are easily visible.

Dye penetrant testing was carried out in accordance with (ASTME-165-95 2001) which involves six major steps which are summarized schematically in Figure 3.23; pre-cleaning, penetrant application, removal excess penetrant, application of developer, inspection and post cleaning. The inspection results showed no major weld defects.

3.11 Stone Chipping Test Method

This test method covers the determination of the resistance of coatings to chipping damage by stones or other flying objects. In this work, this method was used to simulate the actual effects of the stone chipping. The stone chipping effect is a significant source of corrosion of automotive underbodies along with undesired aesthetic effects.

The testing machine is called a gravelometer, constructed according to the design specifications shown in Figure 3.24 (ASTM-D3170-01 1996; SAE-J400 2002).

The primary usage of this test is to simulate the effects of the impact of gravel or other debris on automotive parts.

The test consists of projecting standardized road gravel by means of a controlled air blast onto a suitable test panel. The gravelometer is designed to contain road gravel, a test panel holder and a gravel projecting mechanism. The projecting mechanism, located in front of the test panel, consists of an air nozzle in the base of an inverted pipe tee. The gravel, falling into the air blast, is projected toward and impacts upon the test panel, which is usually held perpendicular to the impacting gravel. All testing is conducted under ambient temperature. After the gravel impact, the test sample is then removed and gently wiped off with a clean cloth followed by the use of tape to remove any loose paint chips remaining on the panel. Finally the degree of chipping is assessed as explained in next section.

According to ASTM D3170 and SAE 400 the recommended procedure is as follows:

- 1- The air pressure is adjusted on the gravel machine to 480 +/- 20 kPa with the air valve open.
- 2-The air valve is shut off, the lid to the gravel chamber is opened and 550 mL (one pint) of graded gravel is collected in a suitable container. The gravel is collected by scraping across the screen to allow fines to fall through.
- 3- One test specimen is placed in the panel holder with the coated side facing the front of the machine and the lid is closed to the panel chamber.
- 4- The gravel feed door is opened and gravel from the one pint container is poured into the top of the gravel hopper. The gravel should not be allowed to fall into the nozzle entrance.
- 5- The air valve is opened to allow the air to project the gravel at the specimen.
- 6- The air valve is shut; the lid to the specimen chamber is opened and then the specimen is removed.
- 7- The test specimens should be cleaned with a soft cloth to remove any dust.

Tape is used to remove all loose or damaged paint and the degree of chipping is determined

1. The test area of the specimen should be covered with a strip of tape, and then a uniform pressure is applied to ensure that the tape is firmly adhered to the specimen. There should not be any air bubbles trapped beneath the tape. Uniform pressure can be applied by using a pencil eraser or tongue depressor.
2. The tape should be removed by pulling straight up, then apply new strips of tape as specified previously.
3. Remove the latter tape by pulling straight up in the opposite direction to first one.
4. Continue this procedure using new strips of tape until all loose or damaged paint is removed.

A more complete discussion of this procedure can be found in (ASTM D3170 and SAE 400) upon which this description has been based.

There are two commonly acknowledged methods for deciding the level of chipping on the test board. In the first method, the accurate number of chips in every size extent is organized for the test range. The second technique uses a visual examination of the test panel to the Chipping Rating Standards (CRS) represented in both SAE 400 and D 3170. These standards depict various degrees of chipping severity and are arranged sequentially from best to worst according to chipping frequency. Both these methods were utilized to assess the degree of chipping on the test panel. Figure 3.25 shows some bending and tension samples after an exposed to stone chipping, the results of the chipping rating of these specimens have approximately similar degree was 5B-6A-SC (P/T), this degree would be in middle of rating ranges.

Three different kinds of specimens were prepared for the tests reported in this thesis: (260 x 115 mm) rectangular panels, tension and bending test specimens as discussed previously. The rectangular panels were mainly used to set up and calibrate the stone chipping testing facility, whereas the tension and bending test specimens were used for fatigue testing.

The gravel projecting machine was set up and calibrated before use. A typical test specimen with dimensions 260 X 115 mm was placed into the Gravelometer, then 550 mL of fresh gravel (water-worn road gravel) was projected onto the test area within 10 ± 2 s, using an air pressure 480 ± 20 kPa.

There are some unusual features (anomalies) observed during some tests such as gravel sticking in the hopper. If this occurred the test was stopped, the pipes cleaned and then the test was repeated.

3.12 Corrosion test Characterization

Corrosion tests must simulate service conditions as closely as possible. Laboratory tests may include the testing of small specimens. The indoor corrosion test was performed according to the standard (SAEJ2332 2002). This unit was manufactured from an available environmental chamber which was then modified by installing a plastic container for salt solution and a specimen hanger, plastic tubes and pump as shown schematically in Figure 3.26.

Initially, the specimens were degreased and cleaned with acetone and then hung into the rig. The corrosion area was set to 40 x 20 mm of the specimen's parallel section which was exposed to salt solution whilst all other areas were masked by using plastic tape. All specimens were subjected to alternating spraying 0.5 % NaCl concentrated solution according to (SAEJ2332 2002) and the corrosion procedure is illustrated in Figure 3.27.

A salt spray cabinet is an enclosure where solution is sprayed from a nozzle; the spray is made from a salt solution which is pumped from a water tank. All specimens for corrosion were placed in corrosion chamber individually and parallel at an angle of approximately 30° with regard to the horizontal direction. During the exposure time, all samples were regularly turned around and put in different places inside the cabinet for the same amount of time in order that they should receive similar spray deposition.

The test specimens were placed in the enclosed chamber and exposed to a changing climate that comprised of three different climate conditions. Firstly, the samples

were sprayed with a 0.5 % NaCl concentrated solution for 15 minutes in order to simulate a road environment. Secondly, the samples were exposed to 50 % relative humidity for 17 hours and 45 minutes at 60 °C. Thirdly, the samples were exposed to 100 % relative humidity for six hours at 50 °C. These steps were repeated for seven times a week as this process was automatic. When the exposure time was completed, the samples were removed from the salt spray cabinet and gently cleaned with water to remove the salt deposits.

Figure 3.27 represents schematically the experimental procedure of corrosion test. Two levels of prior-corrosion time were evaluated, two and four months. The lower level was chosen based on the ASTM and SAE standards which recommended the minimum level of corrosion of two months whereas, the higher level was chosen following discussions with Tata Steel personnel.

3.13 Surface profile measurements

The surface roughness profiles before and after any exposure or scratching process were required in order to compare experimental results. Profiles were taken using a standard stylus profilometer made by Taylor-Hobson, with the Talysurf probe highlighted in red ellipse in Figure 3.28. Profiles were recorded by moving the probe in the x -direction, as shown by the blue arrow. A moveable stage was utilised, that allowed movement perpendicular to the probe measurement direction, in the transverse, or y -direction. This allowed measurement of an array of surface roughness profiles across the specimen surface. The specimen was mounted upon a moveable stage using double sided tape. Each specimen has one measurement region from the gauge length of 40mm x 20 mm (along the directions of longitude and transverse, respectively) approximately covering the area of estimated fatigue fracture. A profilometer was used with the measurement speed set to 1.0 mm/s and the data length 40mm with the distance between lines for 3D measurements being 0.25 mm. An array of profiles ensured that the entire contact was detected; the array of profiles is shown in Figure 3.29, as presented in the TalyMap presentational software.

In order to evaluate the impact of surface characteristics on the fatigue life of the corroded specimens, it was necessary to measure the profile of the corrosion pits on the surface of all the corroded specimens, before fatigue testing.

These measurements indicated that corrosion was more severe on the upper surface, which had been more exposed in the corrosion chamber, than on the lower, less exposed surface. This led to consideration of solely the upper surface in measurements and during bending fatigue tests the specimens were oriented such that the more severely corroded surface was placed on the bottom where the maximum tensile stress occurred.

It should be noted that the profilometer characterization is a line-of-sight technique and cannot measure corrosion undercut pits where the deepest parts are hidden from view by material above it. Thus, this method is not suitable for materials with subsurface, tilted and horizontal pits. However, the final fracture surface was examined post-test by using SEM and stereo optical microscopy to cover this limitation.

3.13.1 Corrosion depth measurement

To obtain the corrosion depth of every point, roughness parameters, and pitting depth manual pre-processing of profile data was performed using the methods shown in Figure 3.30. To evaluate the extent of the corrosion when compared with the original surface, the least squares method was applied to sections of uncorroded surface in order to obtain a datum line to which the corroded surface could be compared (Stout 1993). From the profiles obtained, the depth of the deepest point and the average depth for the whole damage was recorded. The red dash line in Figure 3.30 is used to calculate the roughness parameters when the uncorroded surface is not available or far from the area interest. The red line indicates the corrosion depth which represents the difference between the original surface and the valleys. The green line indicates the pitting depth. Profiles for specimens of high level of corrosion were taken using a high range stylus profilometer gauge made by Taylor-Hobson.

For each surface, a number of surface roughness parameters are displayed; R_a , R_z and R_{sk} . In industry, surfaces are typically specified using R_a , or roughness

average, value, at least partly due to its ease of measurement (Thomas et al. 2011; Dunarea 2012). In some cases, R_z is the average height difference between the five highest peaks, and five lowest valleys, and may be used to restrict any extreme behaviour in the surface profile after finishing. Table 3.1 shows the definitions of surface roughness parameters.

To demonstrate the success of the profilometer to characterize and quantify corrosion, an experiment was performed on a mild steel specimen with dimensions 80x10 mm after it was exposed to different periods of salt spray (0,7 and 10 days). The specimen surface was divided into the corroded and uncorroded area, then nine sampling lengths were labeled with numbers (1 to 9) for each side A and B to guarantee that the entire specimen surface was scanned. The schematic of the measurement area is shown in Figure 3.31. The profilometer was employed to measure all these sampling lengths after each corrosion period. These measurements (profiles) shown in Figure 3.32 were plotted for all periods aforementioned to demonstrate corrosion increase with time of exposure, a finding which is consistent with previous work of Rokhlin et al. (1999) and Genel (2007). The measurements didn't line up in some places on the profile, because it was performed manually.

3.14 E-coating Setup and procedure

Many underbody structural components are manufactured from sheet steel with a metallic coating. E-coating is one of the main coatings used for protection of chassis and suspension components. The specimens are typically coated to provide a first line of defence against corrosion, with E-coating acting as a primer layer for subsequent paint.

Electrocoating of the FB590 specimens was carried out at TATA Steel Ijmuiden, with all of the specimens were receiving a nominal 20 μ m thick coating. The entire process takes about 15 minutes, with the samples then being cured for an extra 20 minutes as explained in the following steps.

1. Cleaning
2. Rinsing

3. Conditioning / activation
4. Phosphating
5. Rinsing
6. Post-treating/Passivation
7. Rinsing
8. E-coat (cathodic/anodic immersion painting)
9. Drying (Air)
10. Curing
11. testing

The pilot line shown in Figure 2.14 is capable of coating up to six samples at the same time. The degreasing, phosphating, activation and passivating formulas are all easily interchangeable. The E-coat section uses cathodic electro-deposition to coat the steel samples, meaning the samples act as a cathode with a negative charge and the paint is positively charged so that it is attracted to the surface of the samples. This is a self-regulating process which means the current will drop lower as the coverage of the sample becomes greater; when the sample is fully covered the current will drop to zero and the process will stop. The coated samples must then be cured for 20 minutes at 180°C to complete the process.

3.15 Metallurgy test of mild and high strength steel

The specimens for metallographic examination were sectioned to the required sizes. Then specimens were mounted in Ø40mm cold set resin mount as it allowed the whole cross section sample to be prepared in the same way and analysed at once. Polishing was carried out using different grades of emery papers to achieve a flat surface. Final polishing was done using the diamond compound (1 µm of particle size) in the disc polishing machine to achieve a scratch free surface. Specimens were etched with 5% of Nital solution (0.5 mL nitric acid in 100 mL ethanol) for 8 seconds to reveal the microstructure of specimens. The specimens were rinsed in water, and then kept in a CaO desiccator until the microstructure measurement to prevent corrosion. Microstructures were taken using a Leica optical microscope (OM) equipped with quantitative metallographic software.

Metallographic examination of as received samples of both mild steel and FB590 was carried out to determine the characteristics of the two steel grades. Metallurgy inspections were used to provide full visualization of microstructure from three different directions. Both mild steel and FB590 high strength steel specimens were sectioned to the required sizes from different directions relative to the rolling direction as shown in Figure 3.33 (parallel, perpendicular and tangential to rolling direction on the specimen surface). Specimens were then inspected with a magnification of 500 times to enable the variability in microstructure can be seen.

The micrographs for sample 2 of both types of materials shown in Figure 3.34 (a) and 3.35 (a) which is perpendicular to rolling direction. The mild steel exhibits a microstructure of almost equal axes ferrite grains approximately 22-25 μm in diameter and smaller grains of fine pearlite (a fine lamellar structure of ferrite and cementite) (Lakshminarayanan et al. 2010), while the microstructures found in the FB590 were a mix of ferrite/ bainite with consistent grain size of around 2.6 microns, consistent with Hu et al. (2014).

Longitudinal grains were observed in sample 1 (parallel to the rolling direction) in both types of materials as shown in Figure 3.34 (b) and 3.35 (b), whilst pancake-shaped grain structures were exhibited in sample 3 on the specimen surface where more variation existed to the mean grain sizes found in both types of material as shown in Figure 3.34 (c) and 3.35 (c).

In conclusion, the microstructure is consistent in terms of phase distribution for all directions of both materials. The microstructure in a direction perpendicular to the rolling direction of both materials is fairly uniform throughout, where the mean grain size is around 2.6 microns for FB590 and 22 microns for mild steel. The only difference is the slightly less consistent grain size and shape in sample 3 taken from the specimen surface for both types of material. The general shape of the grains in various directions can be seen in Figure 3.36 which is adopted from Jarman (2000).

Table 3.1 Definitions of surface roughness parameters.

Parameter	Description	Formula
S_a	arithmetic average of absolute values	$S_a = \frac{1}{n} \sum_{i=1}^n y_i $
S_q	root mean squared	$S_q = \sqrt{\frac{1}{n} \sum_{i=1}^n y_i^2}$
S_{sk}	skewness or a measure of the asymmetry of the probability distribution of asperities' height	$S_{sk} = \frac{1}{nR_q^3} \sum_{i=1}^n y_i^3$
S_{ku}	kurtosis a measure of the peakedness or sharpness of the surface height distribution	$S_{ku} = \frac{1}{nR_q^4} \sum_{i=1}^n y_i^4$
S_v	maximum valley depth	$S_v = \text{Min } y_i$
S_p	maximum peak height	$S_p = \text{Max } y_i$
S_z	Average distance between the highest peak and lowest valley	$S_z = S_p - S_v$

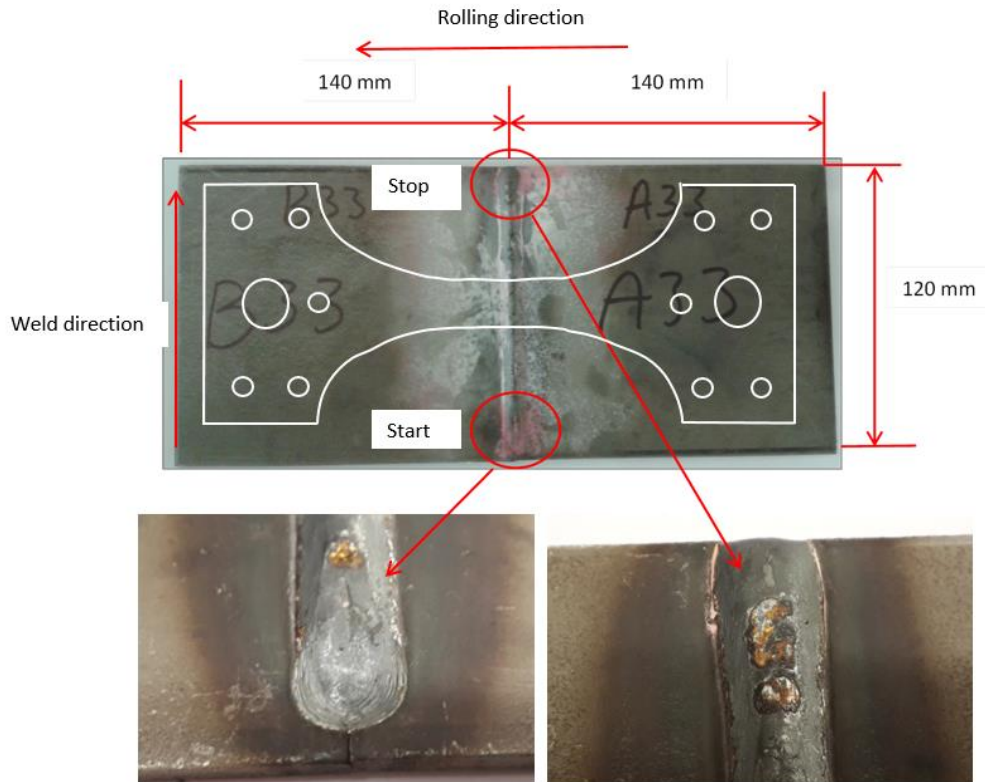
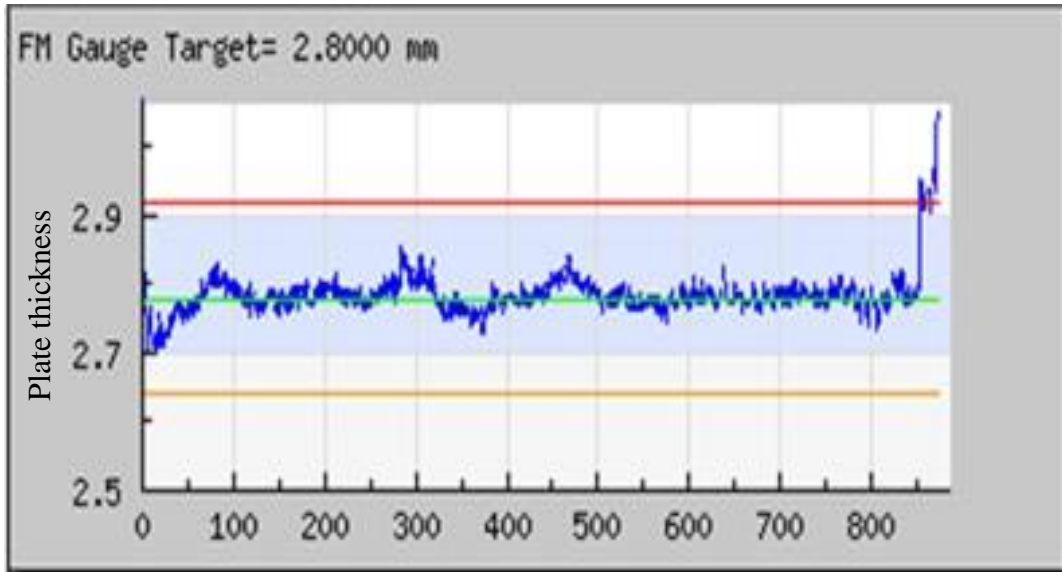


Figure 3.1: Welded “blank” with start/stop locations.



Position along coil width (mm).

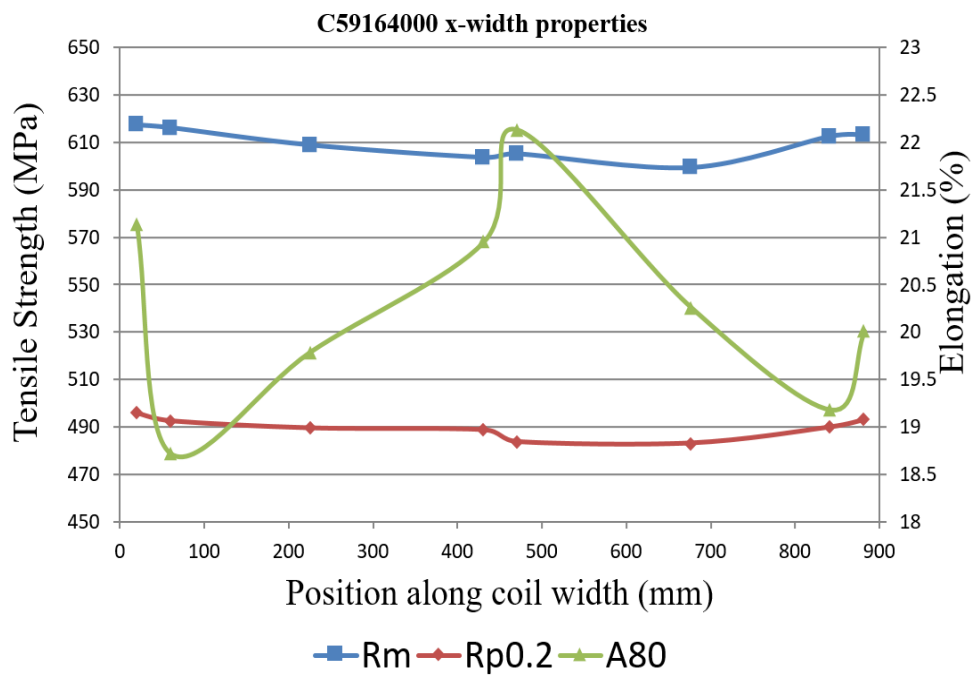


Figure 3.2: Typical thickness variability of 2.78mm for coil C59164000 FB590.

R_m: Tensile strength, R_{p0.2} Proof stress, A80: Elongation% .

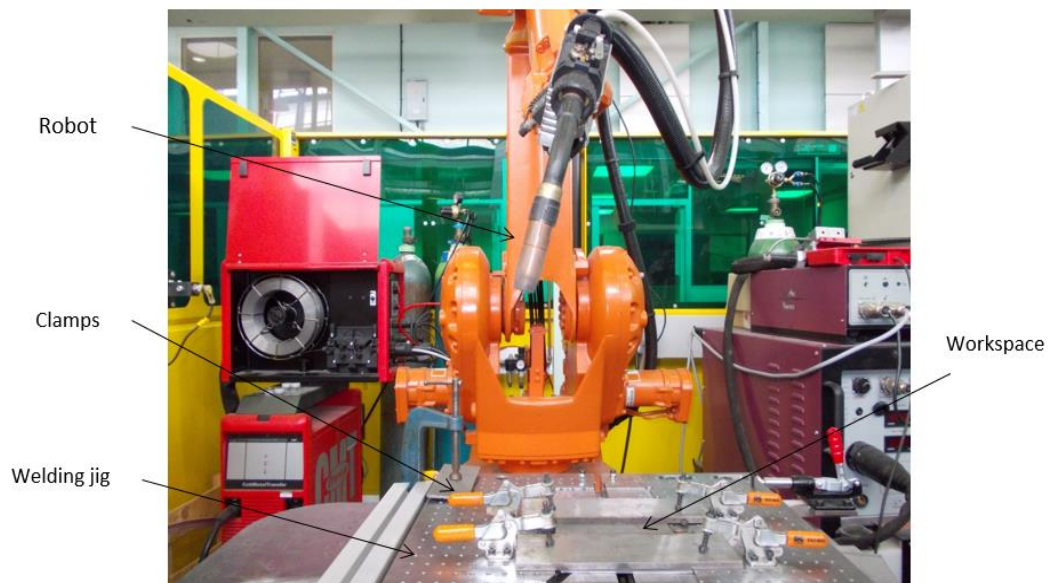


Figure 3.3: Robotic MIG welding system.

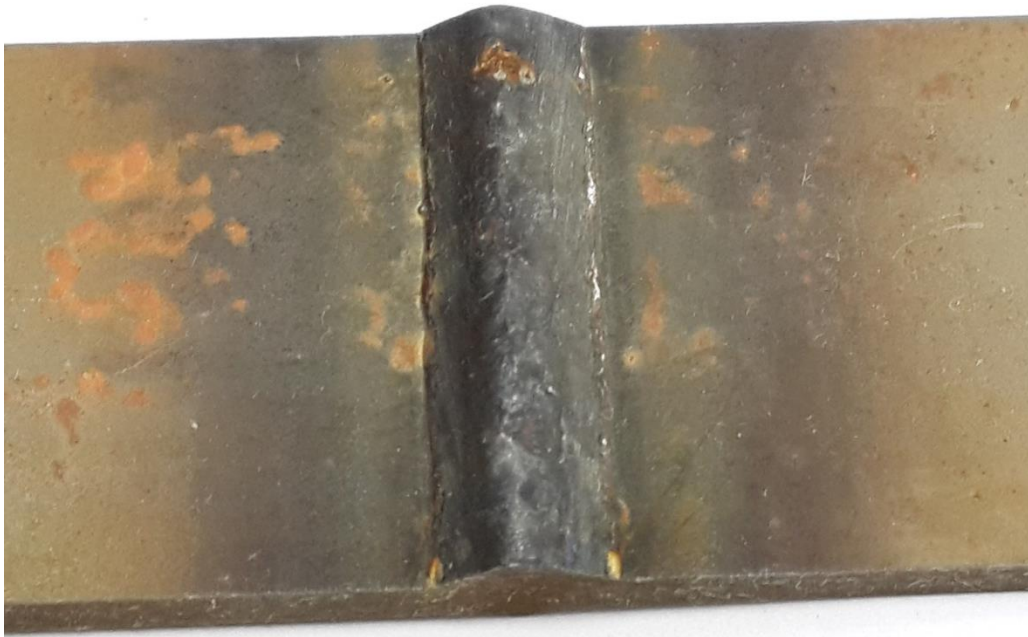


Figure 3.4: MIG weld profile.

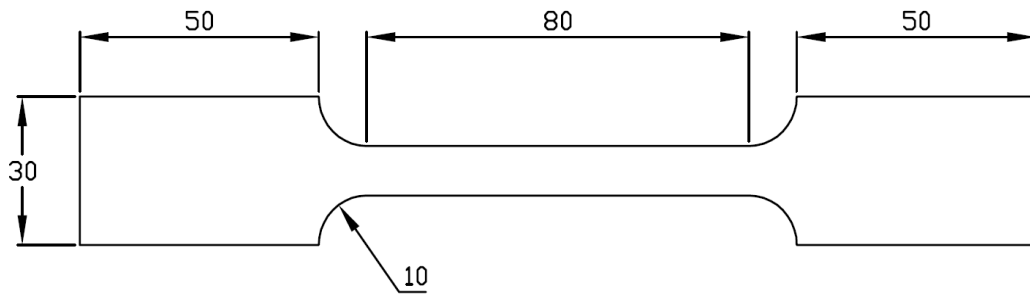


Figure 3.5: Geometry of tensile test specimen. All dimensions in mm.

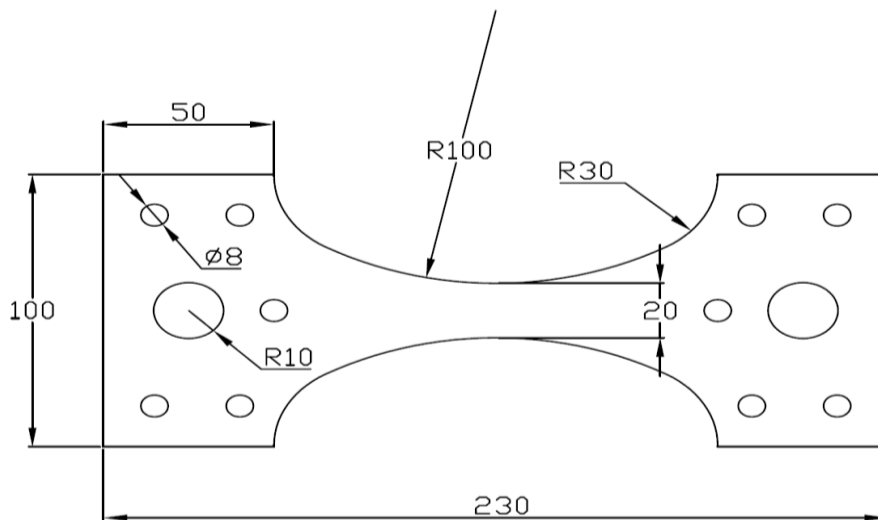


Figure 3.6: Details of mild steel fatigue specimen geometry (dimensions in mm).

Model name: weldspecimen2
 Study name: Study 2
 Plot type: Static nodal stress Stress1
 Deformation scale: 105.144

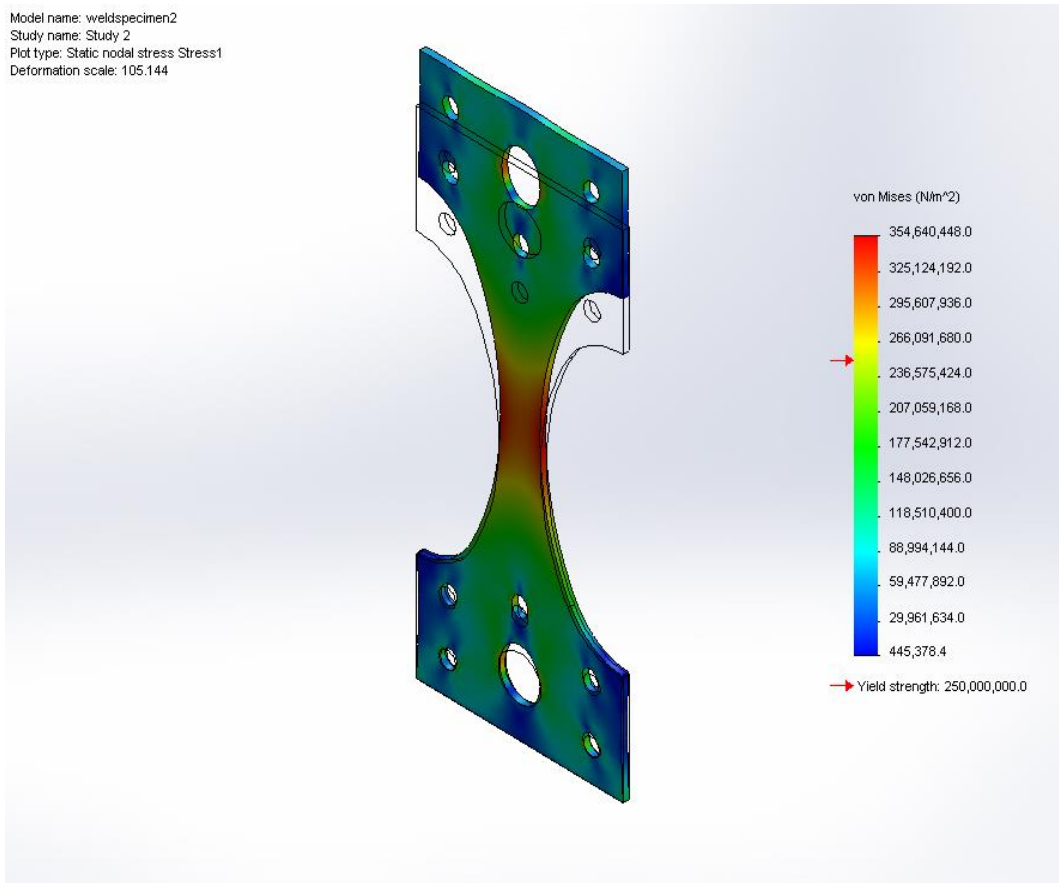


Figure 3.7: FEM stress analysis of mild steel fatigue specimen.

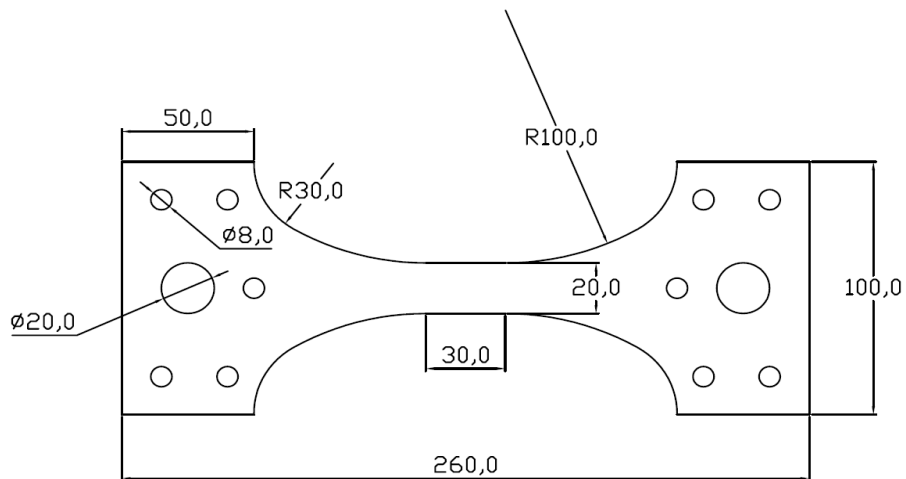


Figure 3.8: Details of FB590 fatigue specimen geometry (dimensions in mm).

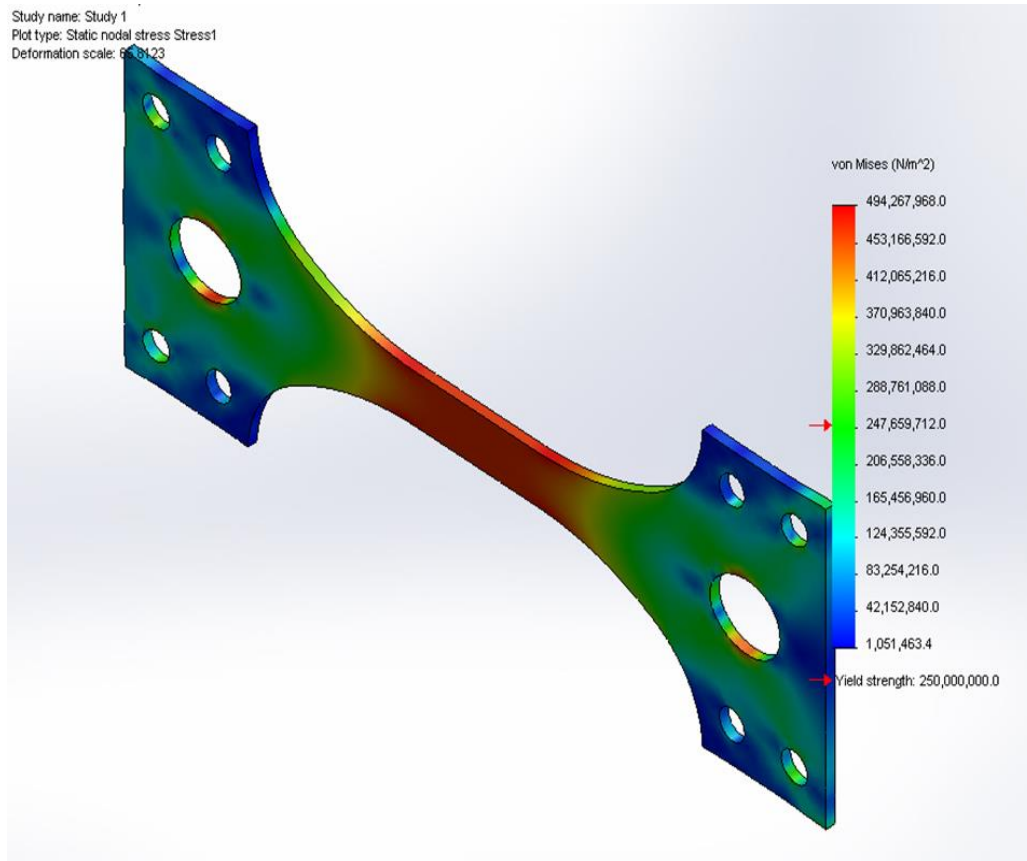


Figure 3.9: FB590 fatigue specimens with dimensions and stress analysis.

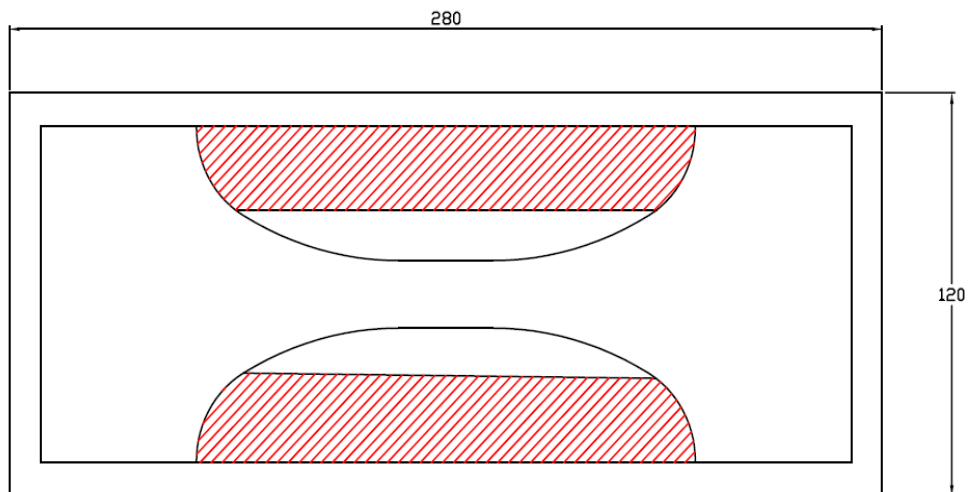


Figure 3.10: shows the location of the two semi rectangle geometry of the fatigue bending specimens.

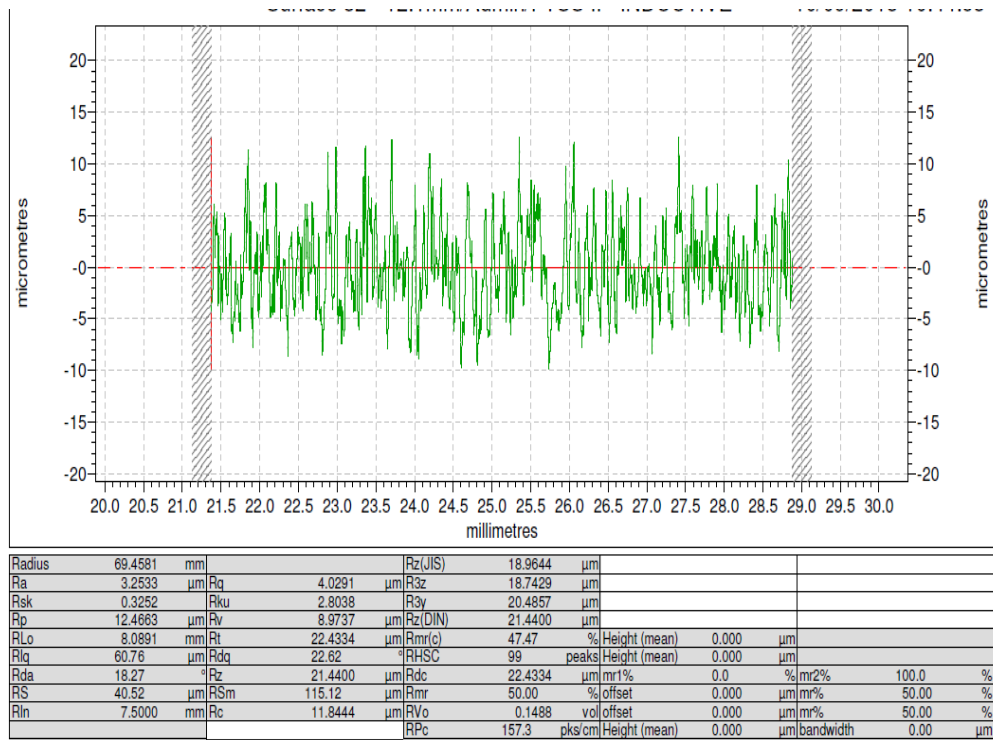
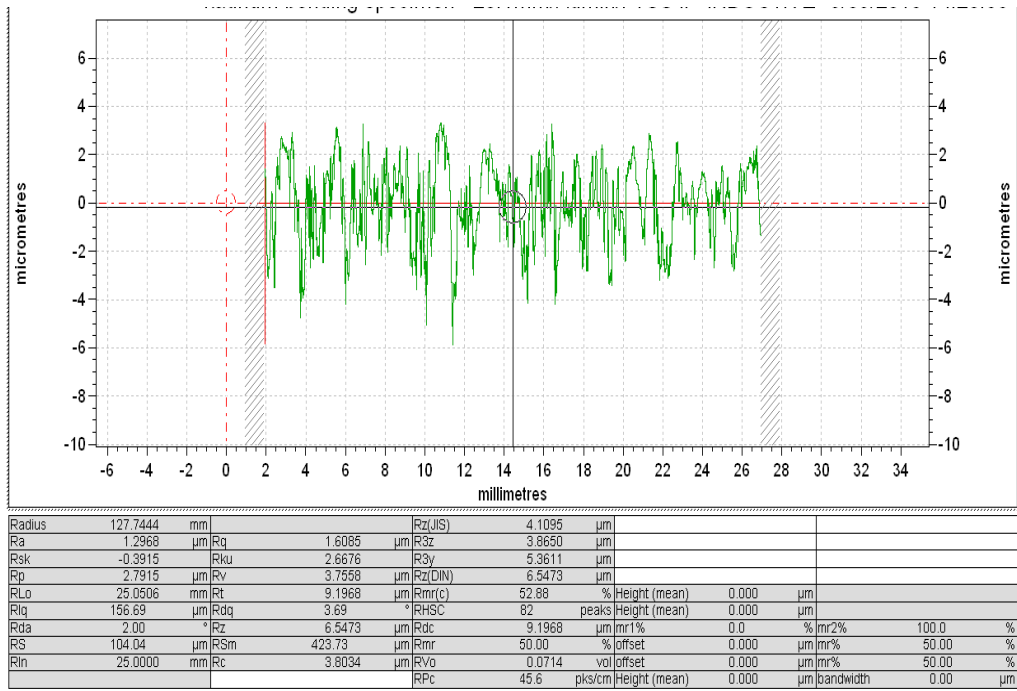


Figure 3.11: (a) cut-edges using surface grinding machine (b) cut-edges using wire erosion finish method.

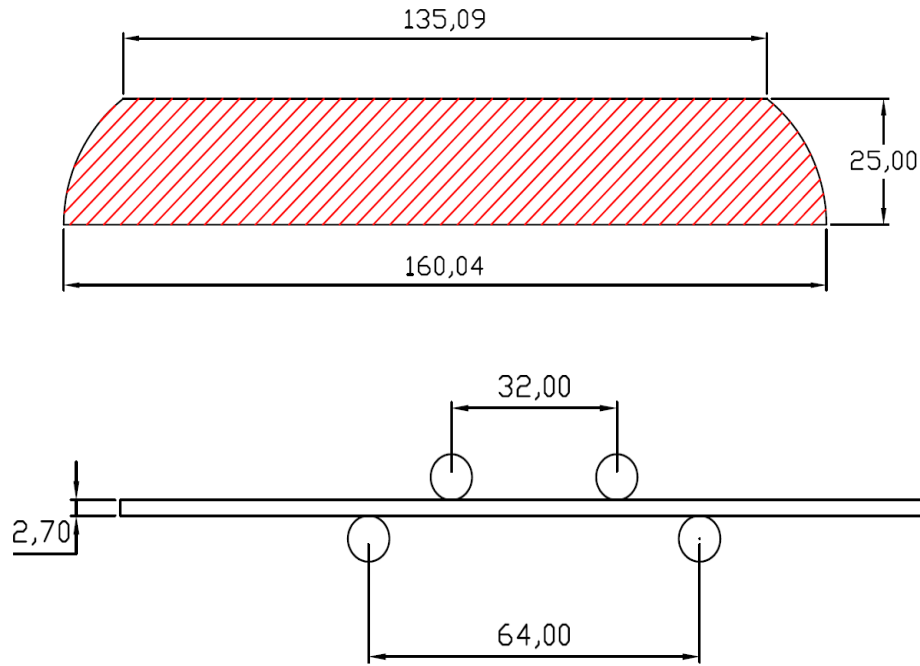


Figure 3.12: Configuration of four-point bending specimen geometry and loading frame.

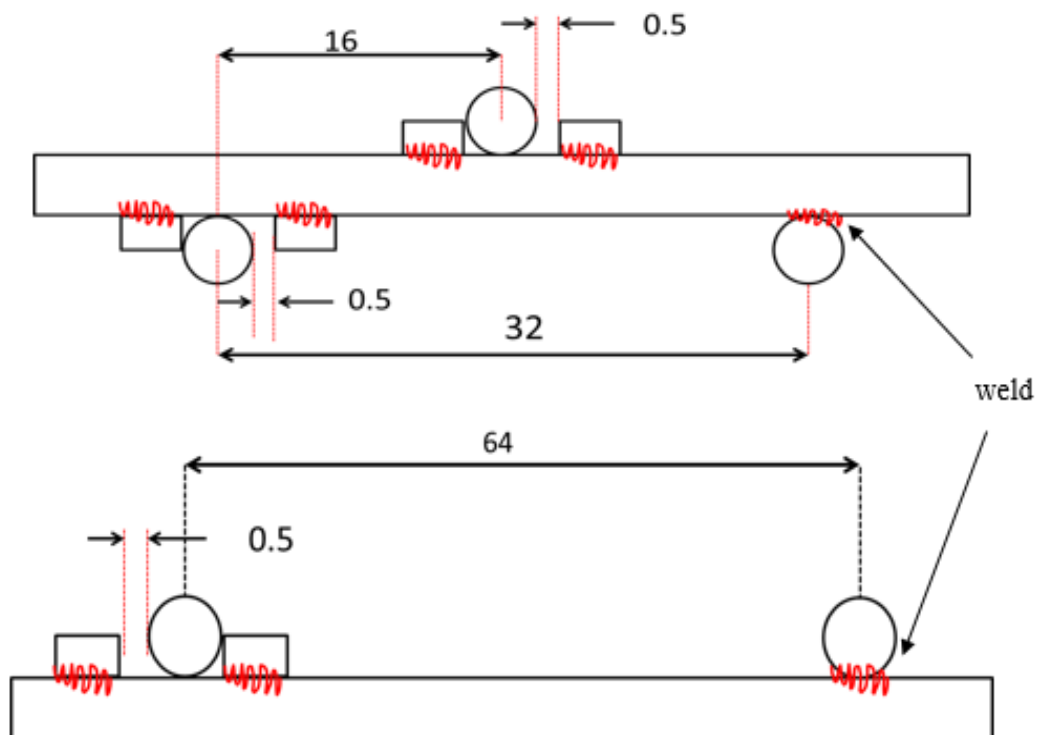


Figure 3.13: All loading frame dimensions in millimetres (a) Loading (top) piece (b) support (bottom) piece.

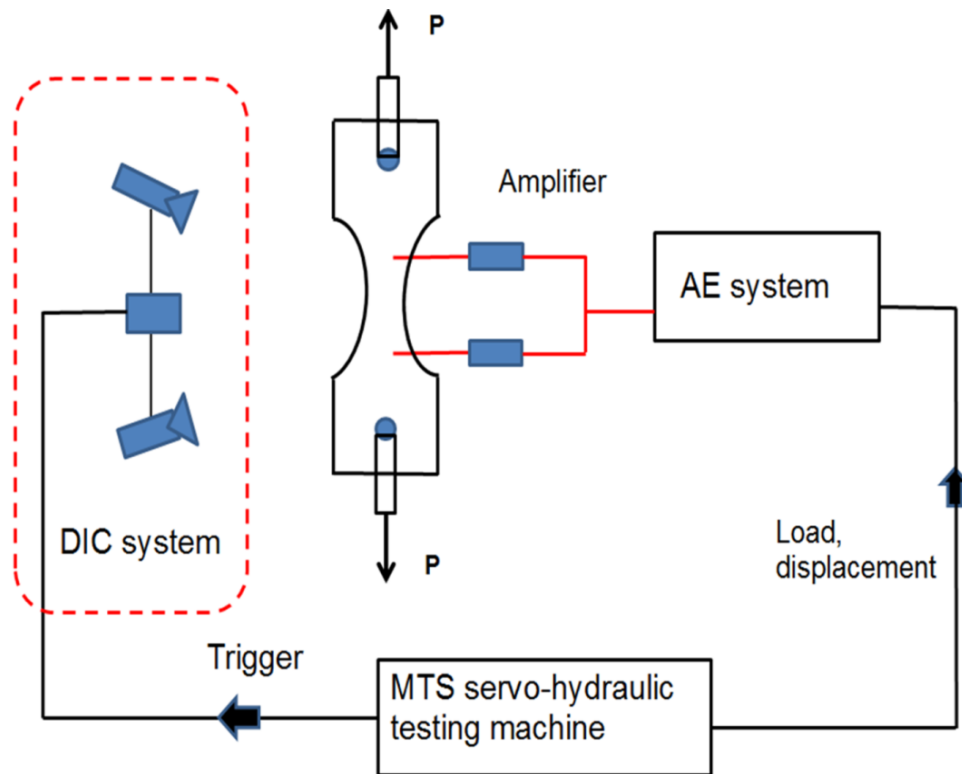
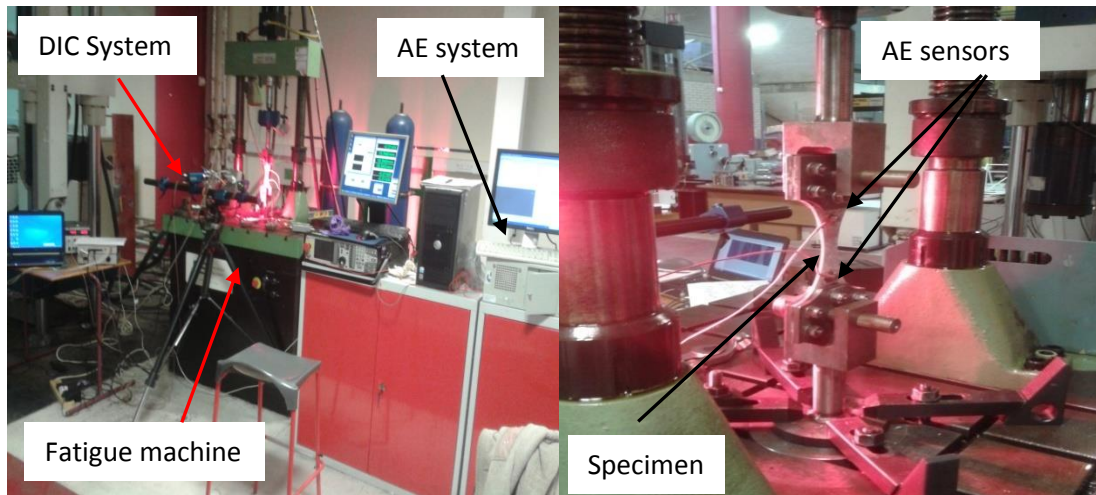


Figure 3.14: Schematic diagram of fatigue test.



Figures 3.15: Showing two different views of the test set up arrangement with both the DIC and AE systems in place.

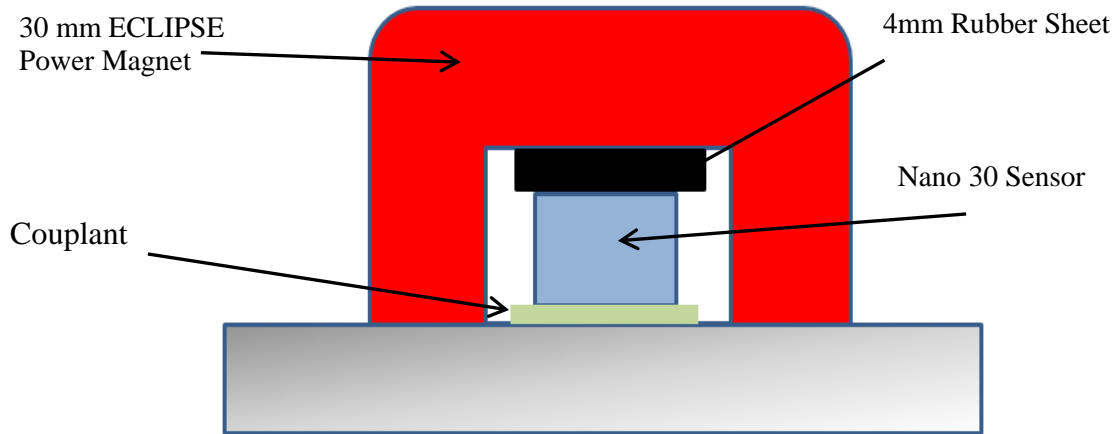
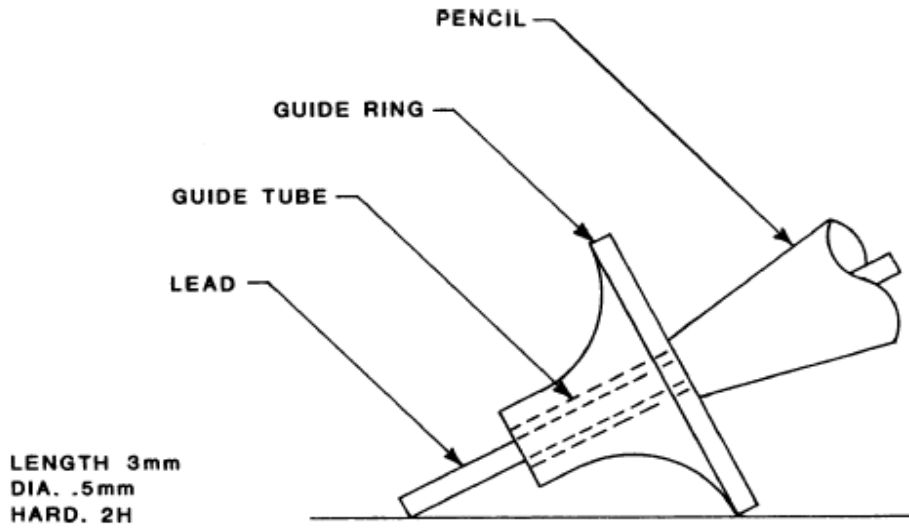
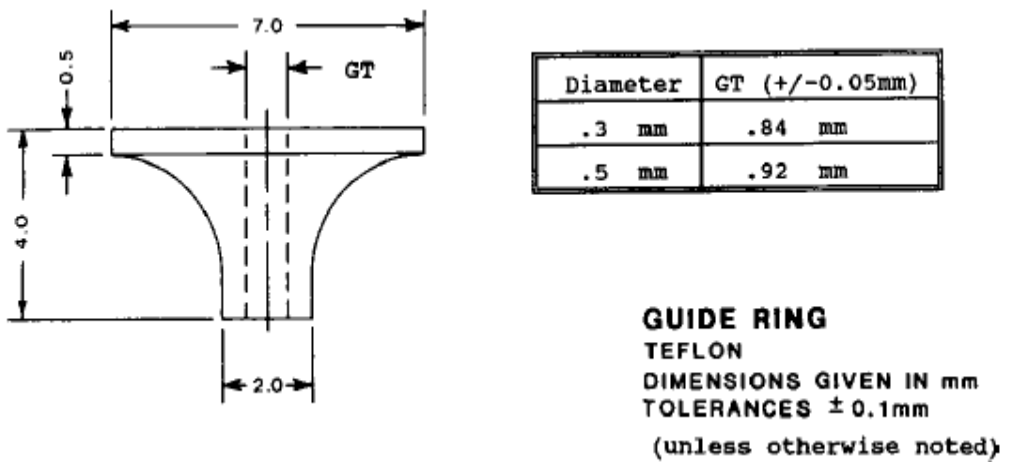


Figure 3.16: Proposed magnetic clamp.



(a) Nielsen Shoe on Hsu Pencil Source.



(b) Nielsen Shoe.

Figure 3.17: The H-N source method and guide ring (ASTME976 2001).

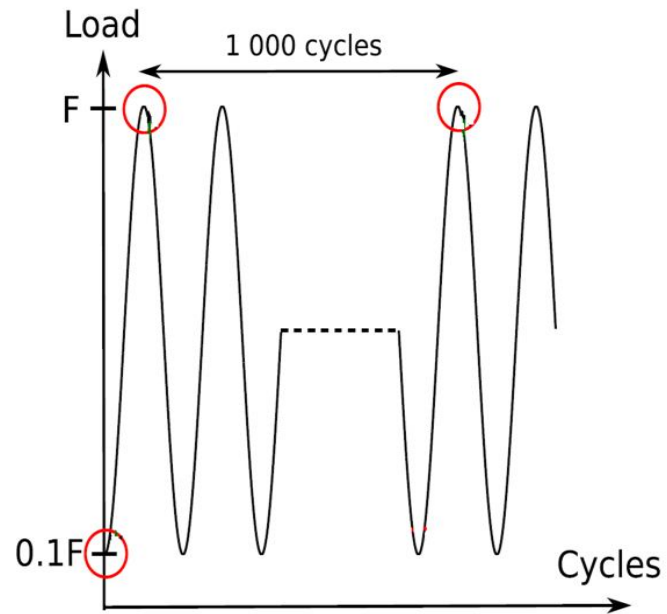


Figure 3.18: DIC Image capture during the load history.

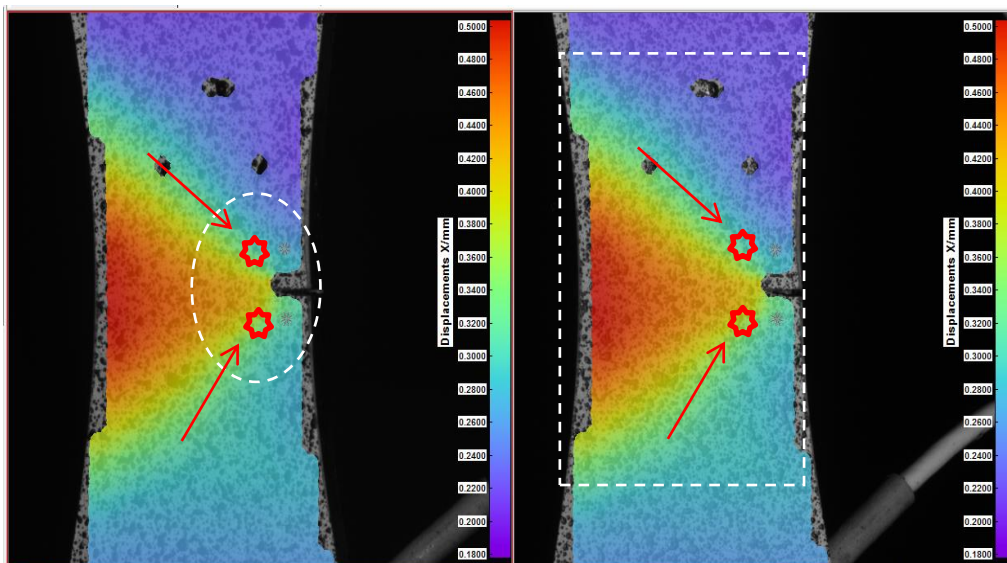


Figure 3.19: Typical results of the DIC analysis profiles for the vertical displacements measured along a line close to the edge of the sample.

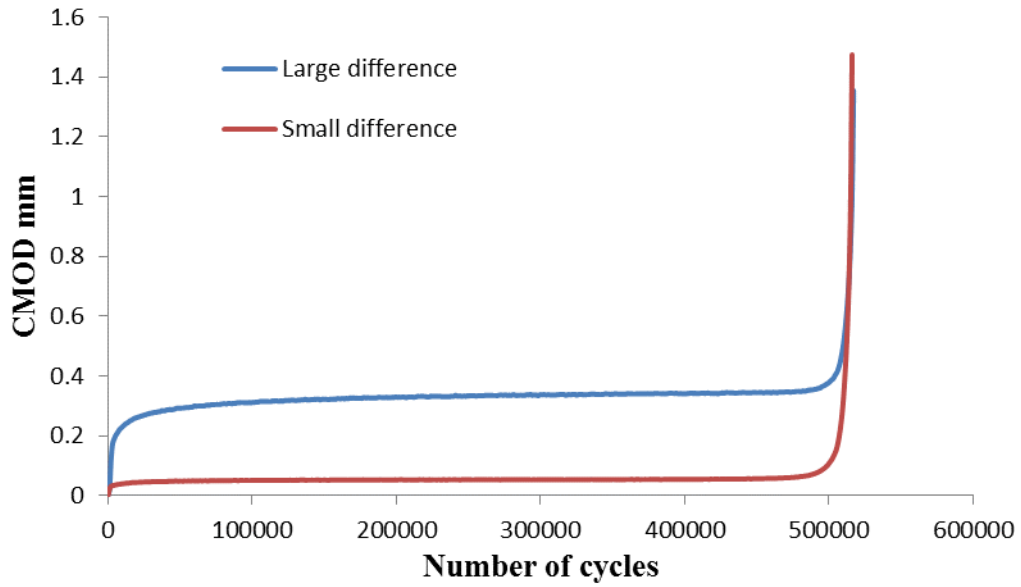


Figure 3.20: Mild steel corroded specimen under 250MPa, the blue line for the large difference between the two points (initial analysis) and red line for the points close to each other.

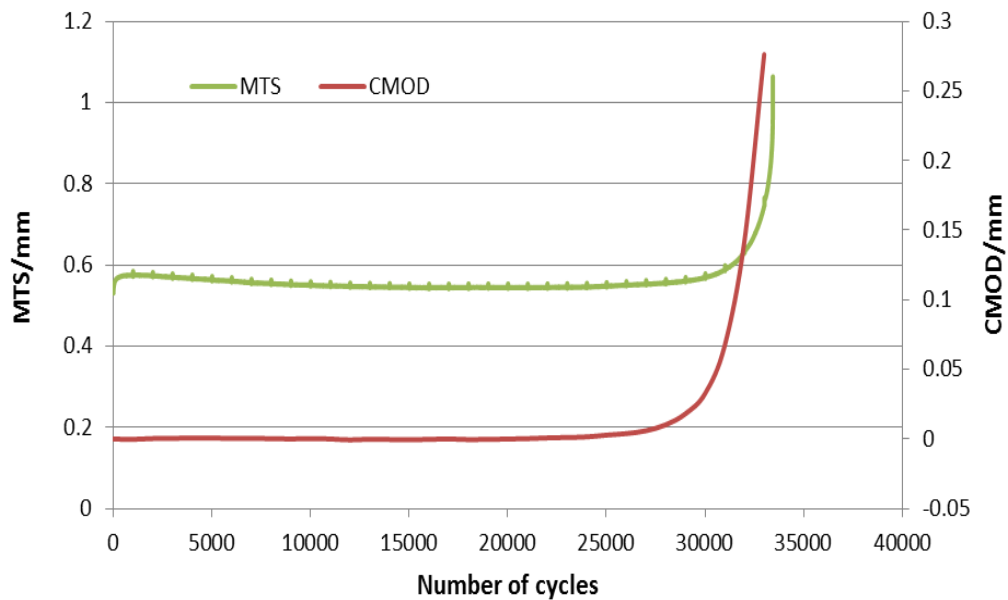


Figure 3.21: The comparison between extension (MTS) and DIC result for as received FB590 welded specimen under 400MPa.



Figure 3.22: dye penetrant method used for inspection (top images) welded joints (bottom images) bending fatigue specimens.

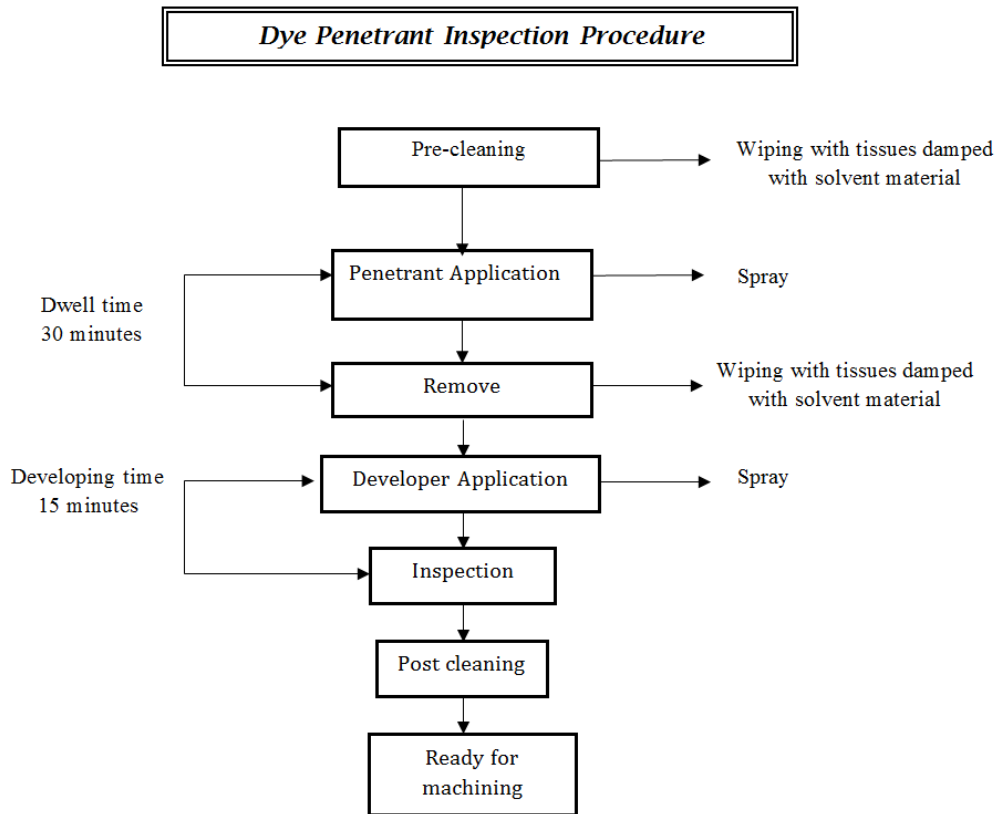


Figure 3.23: Dye penetrant inspection procedure.

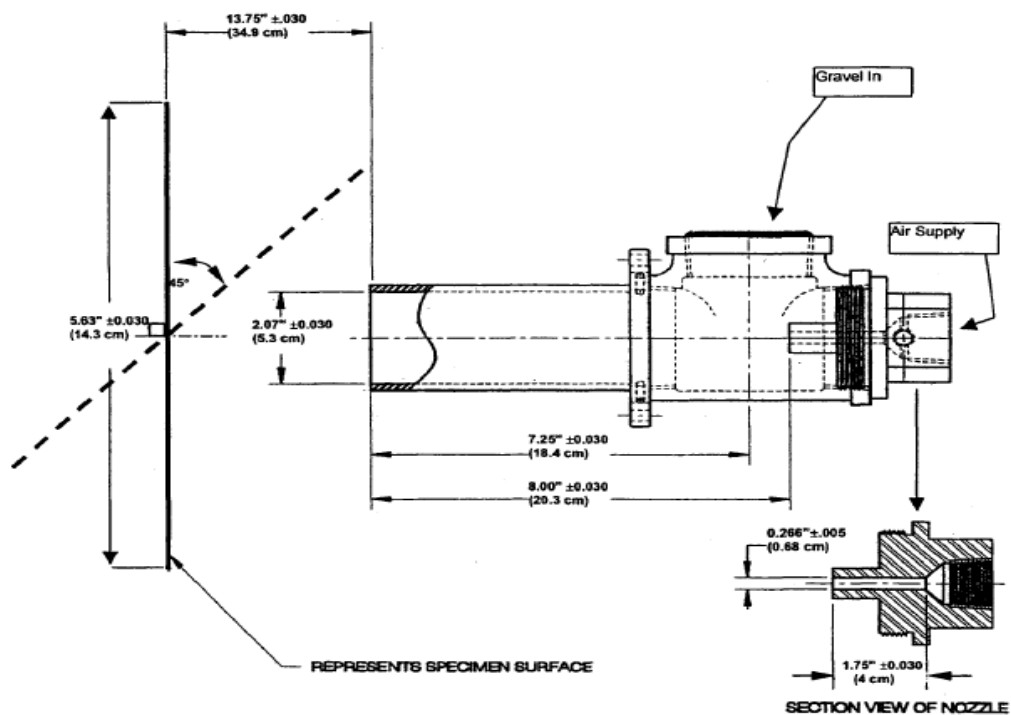


Figure 3.24: Gravel projecting machine (Gravelometer).



Figure 3.25: Different kinds of specimens after exposure to stone chipping.

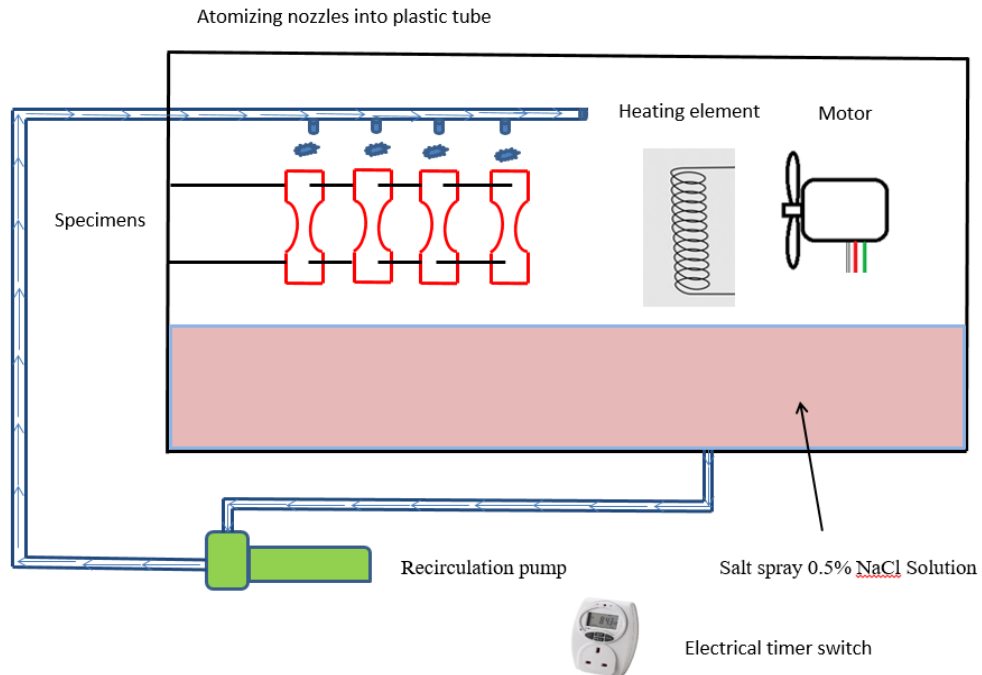


Figure 3.26: A schematic of the self-built corrosion chamber.

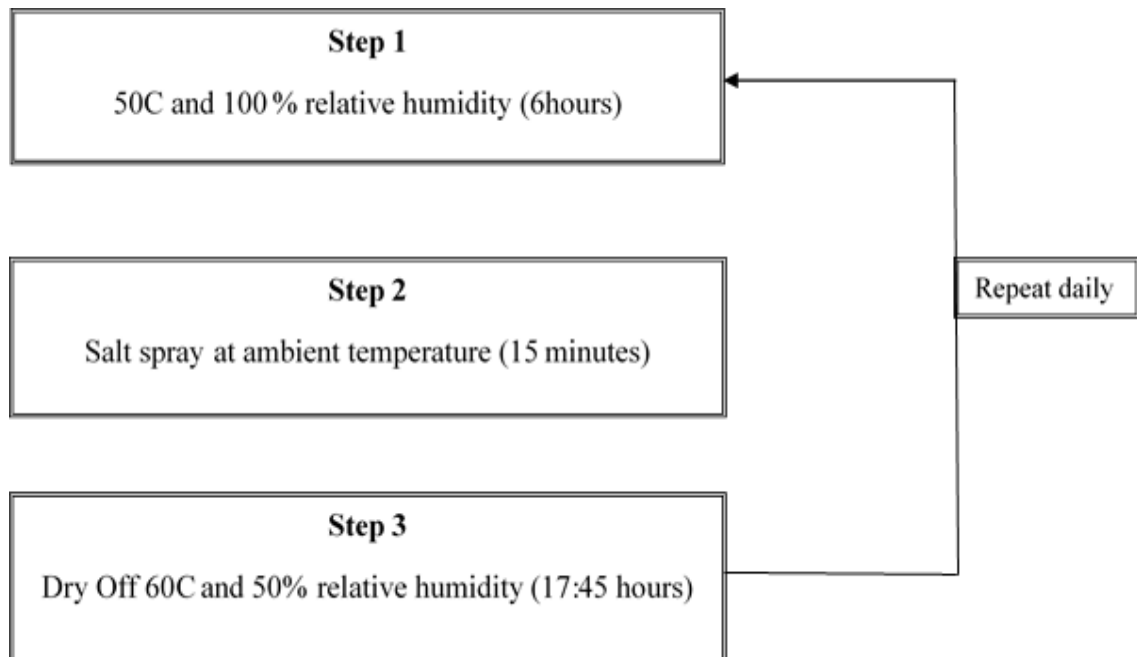


Figure 3.27: Cosmetic corrosion Laboratory test cycles 7 day/ week –automatic operation (SAEJ2332 2002).

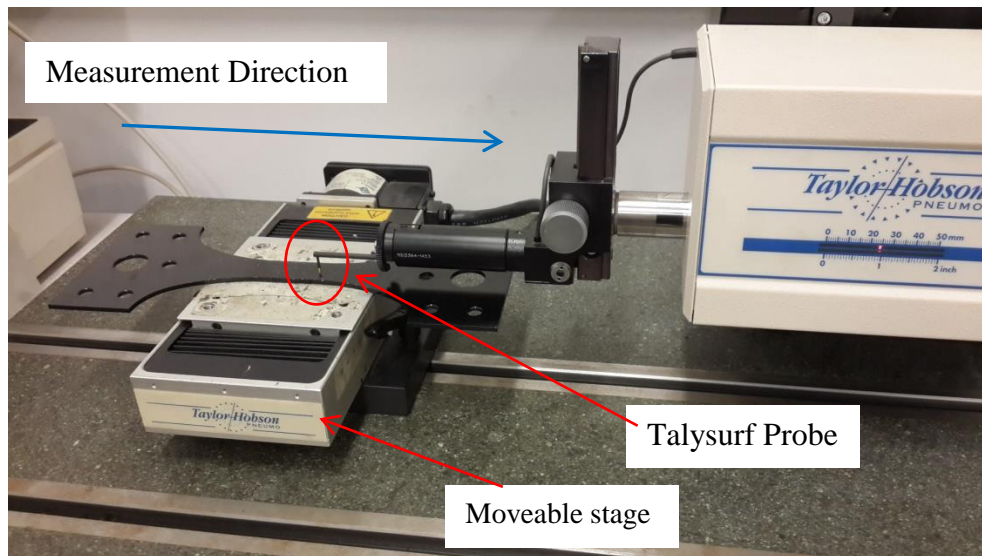


Figure 3.28: Talysurf with specimens mounted on moveable stage.

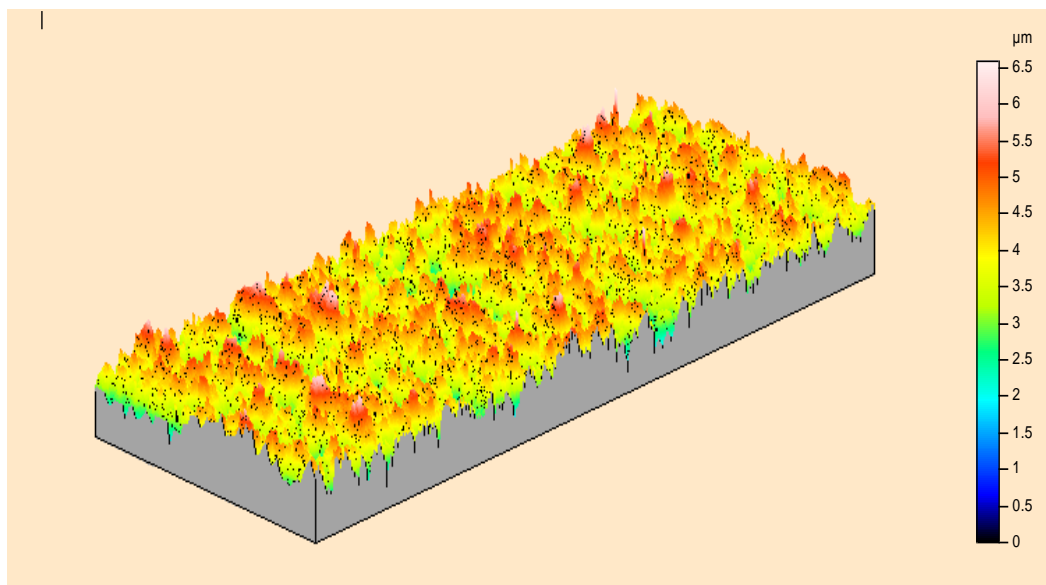


Figure 3.29: 3D representation of the array of surface roughness profiles taken from specimen surface.

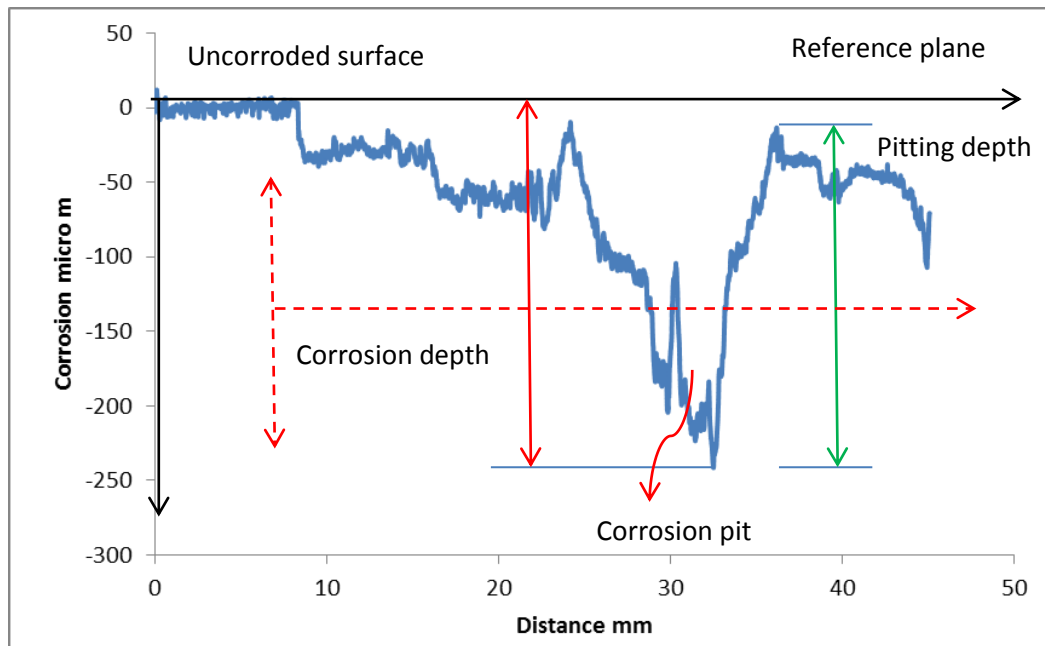


Figure 3.30: Surface profile and the principle to obtain the pitting characterization parameters (red dash line indicates 3D roughness, red indicates corrosion depth, and green indicates pitting depth).

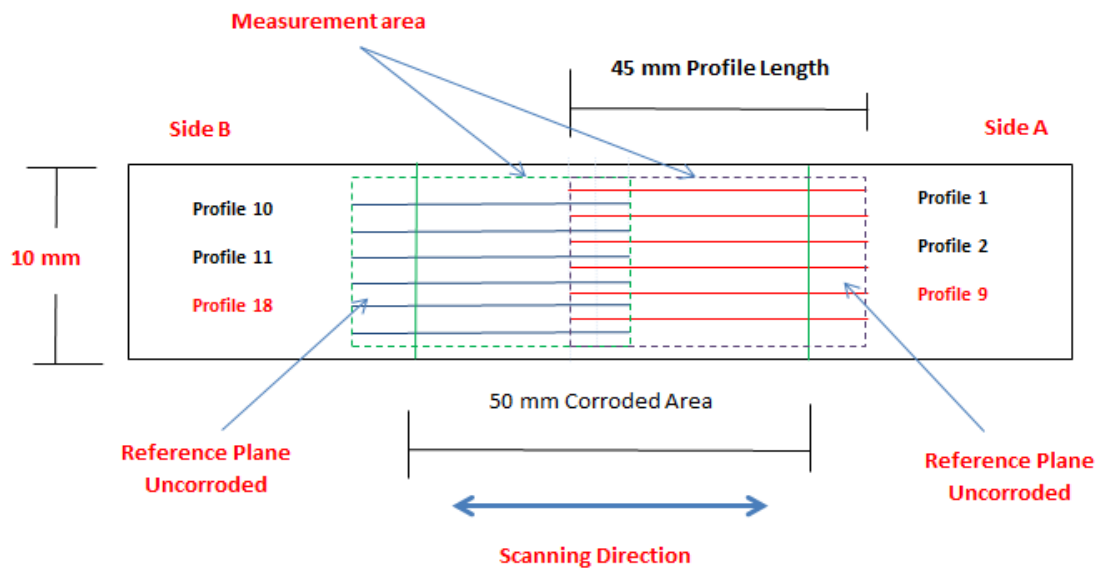


Figure 3.31: shows mild steel specimen with 18 sampling lengths of 45mm.

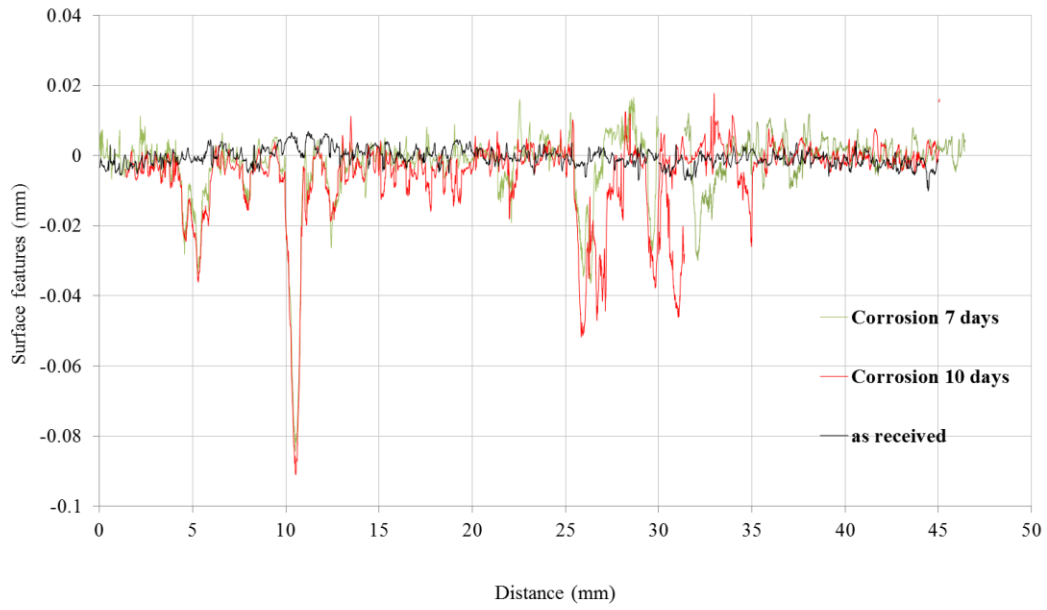


Figure 3.32: Shows corrosion depth against distance for specimen (0,7, and 10) days for side B2 p1 sample length.

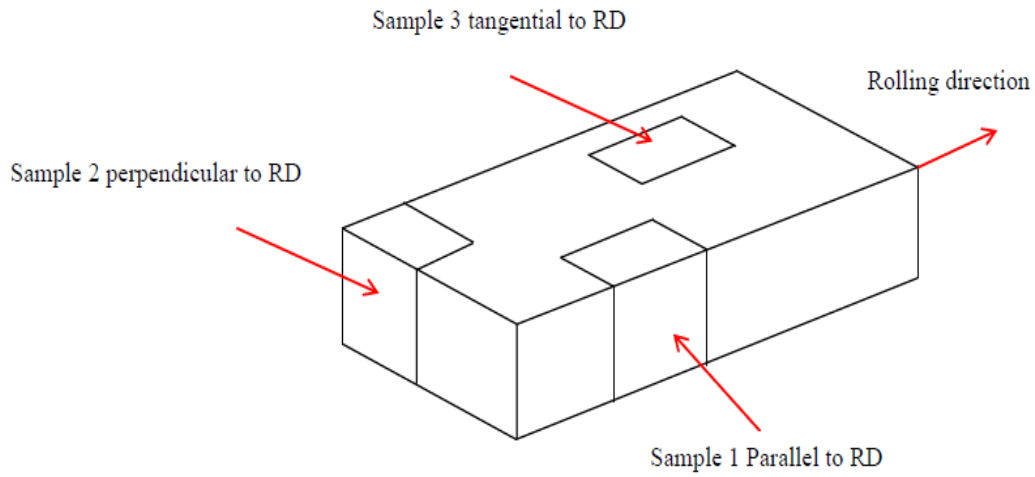


Figure 3.33: sections of specimen from different directions relative to rolling direction.

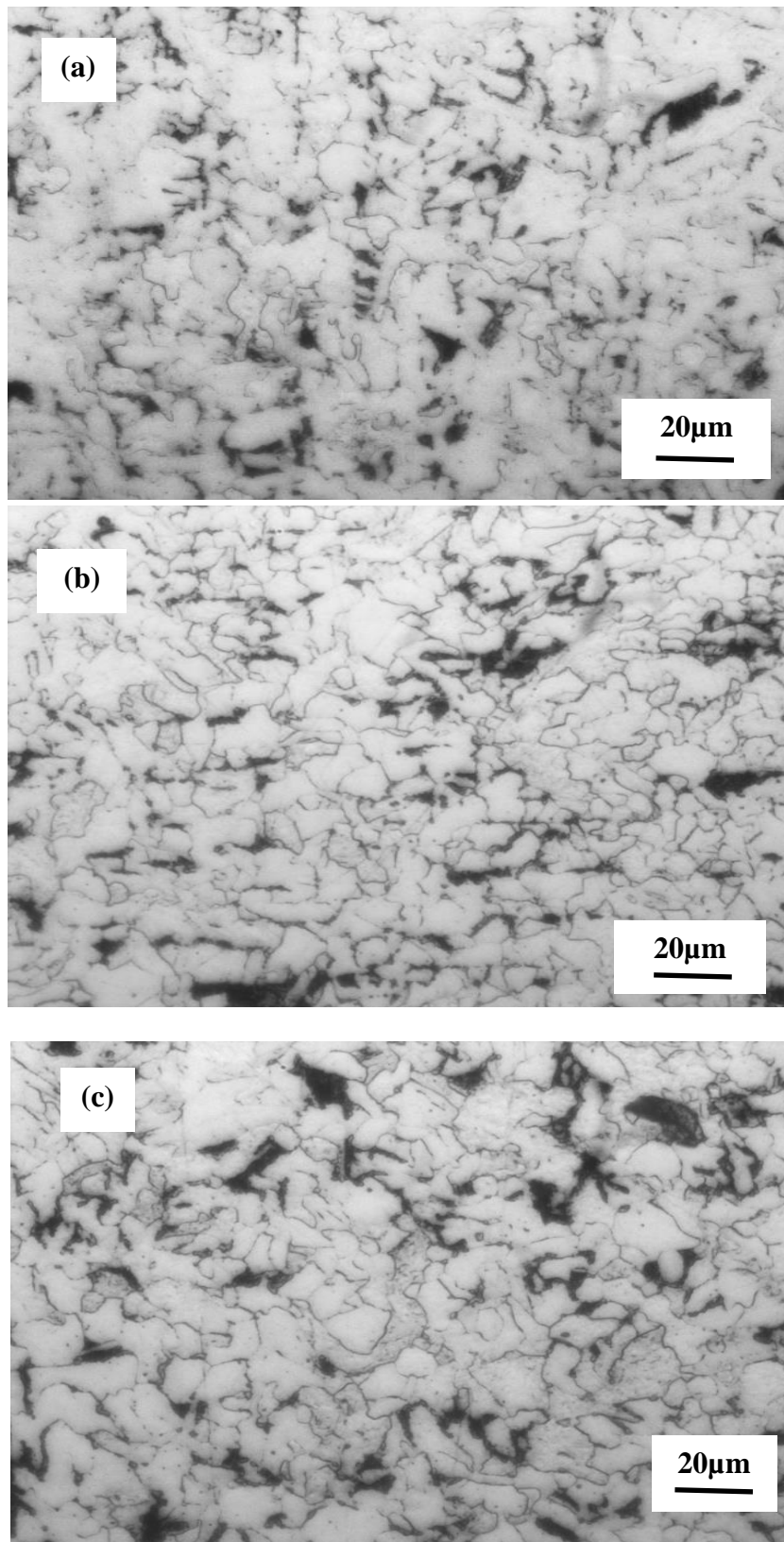


Figure 3.34: Mild steel microstructure (a) parallel to rolling direction (b) perpendicular to rolling direction (c) on the surface.

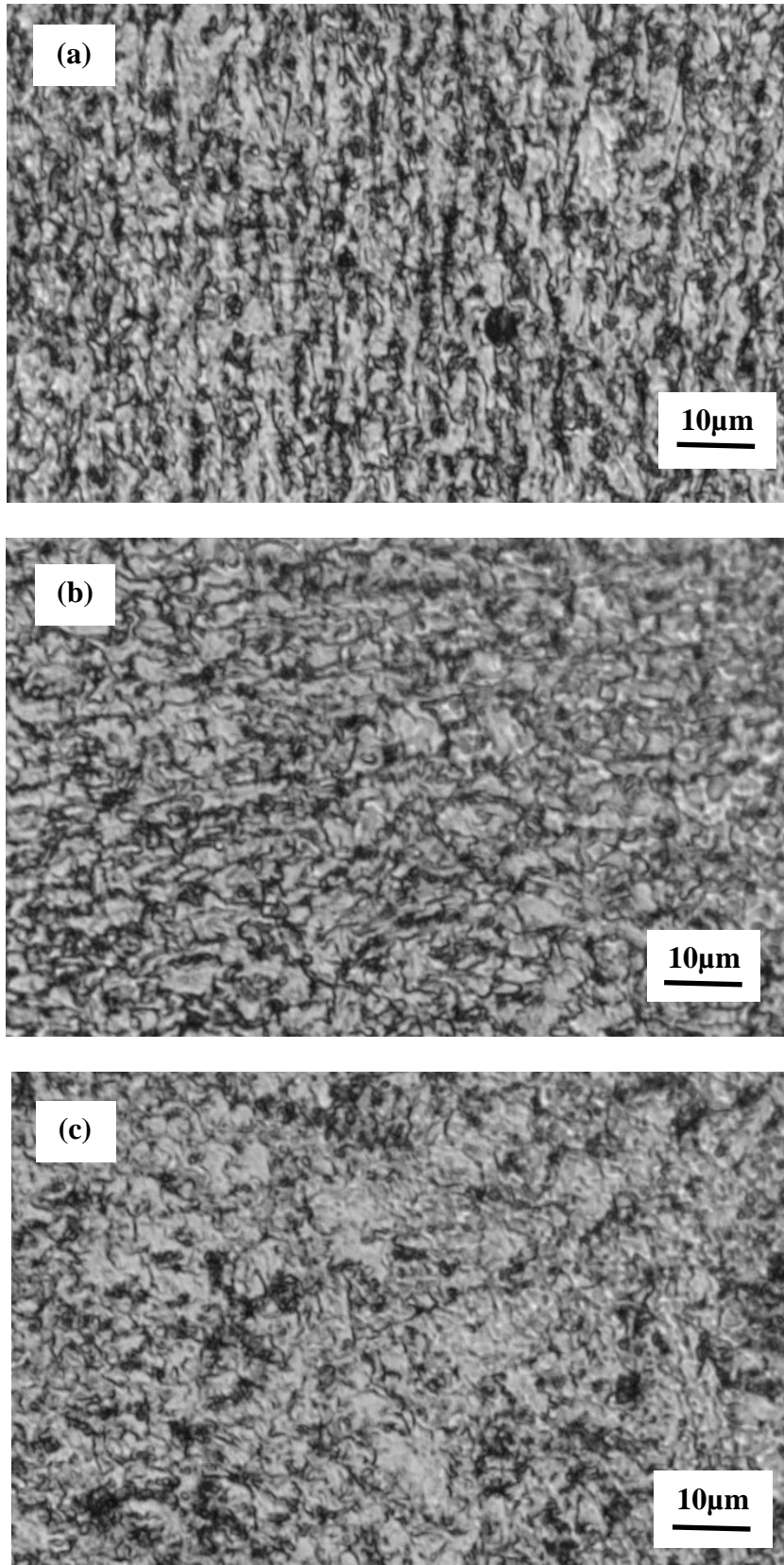


Figure 3.35: FB590 microstructure (a) parallel to rolling direction (b) perpendicular to rolling direction (c) on the surface.

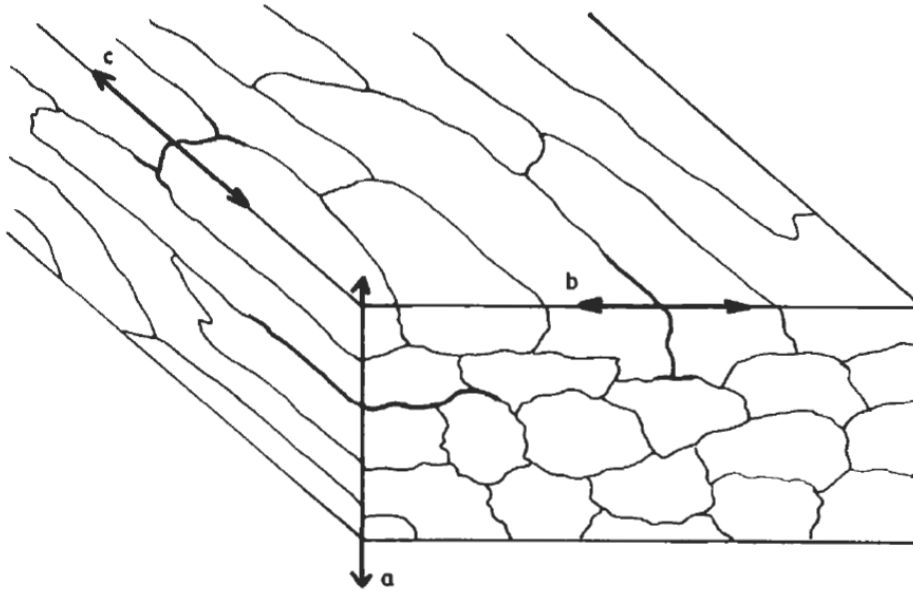


Figure 3.36: grain structure different with rolling direction (Jarman 2000).

4. Preliminary Experimental Studies with Mild Steel Samples

4.1 Introduction

It was decided to start the experimental work using mild steel due to the low cost of mild steel specimens compared with those manufactured from FB590. Moreover, training was required to utilise different techniques such as the fatigue testing machine, AE, DIC equipment, and profilometry. Using mild steel for this training prevented FB590 specimens being wasted, whilst developing the testing and monitoring procedure. Hence, the aim of this work is twofold. Firstly, to study the effect of various loading and various environmental conditions on fatigue life and, secondly, to develop a fatigue test monitoring system to identify crack initiation from background noise for mild steel at the beginning and then develop the procedure and apply it on high strength steel (FB590) and its welded structure, after overcoming the obstacles and problems such as background noise, time misalignment with cycles and so on.

Thirty fatigue specimens were prepared and tested according to the work plan shown previously in Figure 1.1. These specimens were divided into three groups where each group consisted of ten specimens and had different corrosion levels. The first group was as received, non-corroded material. The second group had undergone 25 days of corrosion and the third group 50 days of corrosion. The nomenclature for these groups is shown below. This naming convention describes and designates the surface exposed to high and low levels of corrosion attack as explained below.

Group 0 as received (**Base line**)

Group 25 low corrosion level (**25 days of corrosion**)

Group 50 high corrosion level (**50 days of corrosion**)

4.2 Tensile performance of mild steel

The tensile test was performed as explained in Section 3.3. The test specimens were manufactured from 3 mm thick mild steel plate. Figure 4.1 shows an example stress strain curve measured for this material. The results from three

tensile tests on this material are shown in Table 4.1 Mean properties are as follows: Ultimate strength 423.7 N/ mm², 0.2% proof stress 275 N/mm² and elongation 36%. The specimens were taken along rolling direction and the loading calculation was previously performed in Chapter 3.

4.3 Corrosion surface measurement and assessment

The fatigue specimens were pre-corroded following the method described in Section 3.12. A stereo optical microscope and 3D profile measurements without destruction were first conducted to obtain the distributions and characterizations of pitting corrosion, including 3D surface roughness, and topography, due to its importance in studying the effect of corrosion on the fatigue behaviour.

The measurement of the surface roughness and corrosion depth was not possible during the corrosion process as the specimen's surface needed to be cleaned from corrosion products before any measurement. This would change the conditions of the corrosion process and make it deviate from the process that was described in (SAEJ2332 2002). In addition the corrosion products play an important role in the reduction of vertical corrosion speed at the bottom of pits (Xu and Qiu 2013). Hence, it was decided to measure the surface roughness as well as the maximum and average depth of the corrosion sites at the end of the exposure time, once the experiment was finished and the specimens could be removed from the corrosion chamber. Post assessment of corrosion showed large variations in surface roughness. The test results for all cases are presented in the following sections.

The surface morphology of as received samples is clearly shown Figure 4.2. The surface was examined by profilometer, an array of profiles ensured that the entire contact was detected; the array of profiles is shown in Figures 4.2(c), as presented in the TalyMap presentational software.

The corroded specimens of Group 25 and Group 50 were exposed in the salt spray cabinet for 25 and 50 days respectively. Two types of corrosion morphology with corrosion time lapse could be observed on the specimen's surface. Most of the corrosion product was found on the gauge length of both the specimen faces, which is where the salt solution was collected during the exposure, as the specimens were

mounted at 90 degrees in the salt spray cabinet. The amount of corrosion product observed on the specimens was found to increase with the exposure period. Figure 4.3 and Figure 4.4 show the difference between the corroded specimen's surface of Group 25 and 50 respectively. It is apparent that large flaws due to corrosion effect are present and the surface becomes rougher than the surface as received (Group 0), this is consistent with observation of Xu and Qiu (2013).

The corrosive attack can produce a network of corrosion on the metal surface. The typical appearance of the specimens after removing the rust is shown in Figure 4.5. The specimens after corrosion were cleaned using a plastic brush to remove rust from the corroded specimens without causing any further damage to the surface that could potentially affect the fatigue results. Measurements were performed of the surfaces of all specimens, using a profilometer, before fatigue testing, in order to obtain the surface characteristics of the specimens. It was important to categorize the corroded surfaces in order to better understand the effects of different corrosion conditions on fatigue strength.

The corrosion was found to have almost equally affected both specimen faces. This led to considering both surfaces in measurements of corrosion depth and surface roughness. The unaffected surfaces adjacent to the corroded regions were used as an origin or reference surface as shown in Figure 4.5.

The corroded area located near the reference surface was examined with the profilometer and stereo optical microscope, as illustrated in Figure 4.6. It appears that pits were underneath the corrosion product, and the metal was superficially attacked as well as the cut edge. The damage in the corroded areas occupied the whole area of the gauge length with an arbitrary distribution of deeper and shallow corroded areas. Moreover, small corrosion flaws also developed independently on the samples at sites remote from the gauge length.

Three dimensional measurements were performed to measure surface roughness parameters of fatigue specimens. All the data was collected and analysed to calculate conventional roughness parameters for the exposed faces of the specimens such as arithmetic mean deviation (S_a), root mean square (S_q), average distance between the highest peaks and lowest valleys (S_z), maximum height of

the profile (S_t). The data was plotted using bar charts and Figure 4.7 illustrates the evolution of surface parameters with length of corrosion exposure, together with error bar representation $\pm 3S.D$. Analysis of profilometry results showed that with increasing corrosion, roughness parameter values also increased, a finding consistent with the observations of Pidaparti and Rao (2008) and Xu and Qiu (2013). By considering the skewness of the surface, S_{sk} , a more pronounced difference can be seen as the corroded surface is significantly negatively skewed (surface with more valley features than peaks) as a result of highly deforming due to the corrosion (Deleanu et al. 2012; Xu and Shan-hua 2015). Figure 4.7 also shows that there is no large difference in appearance of both Group 25 and Group 50 surfaces since the corrosion period was not large enough (SAEJ2332 2002).

After fatigue testing, the fracture surface of the failed specimens was examined by using SEM and stereo optical microscope to cover the limitation the profilometer characterization which is a line-of-sight technique and is therefore not suitable for materials with subsurface, tilted and horizontal pits. Moreover, it cannot measure corrosion undercut pits where the deepest pits are hidden from view by material above them.

4.4 Fatigue Performance of mild steel

This section's aim is not only to define the fatigue properties of mild steel under different corrosion and stress levels, but also to assess the effect of pre-corrosion during cyclic loading. The S-N behaviour of mild steel with two different environmental corrosion conditions was measured, all fatigue data within this section was collected from experimentation. The specimens were exposed to maximum loading conditions varying from 41.6%, to 85.1% of ultimate tensile strength (423 MPa), with a stress ratio of 0.1 and a frequency of 5Hz. The mild steel sheet used to produce the data used in this section was 3 mm thick, with the "as received" specimens being considered as a base line. All S-N curves displayed within this section are from longitudinally cut samples cut from the same coil as the samples used to measure the tensile behaviour of the material. The fatigue properties of corroded mild steel under tension loading are unknown previously.

Table A.1, to be found in Appendix A, shows the raw data of different stress ranges and fatigue lives for corroded and un-corroded specimens. Numerous graphical representations are generated from these data, including the fatigue curves of each specimen. The Basquin's exponents and coefficients were calculated and are listed in Table 4.2. The final S-N graphical representation shown in Figure 4.8 represents the least squares fitted Basquin curve of the failed specimen under 5×10^6 cycles with one graph showing all S-N curves for corroded and uncorroded results under tension fatigue loading on one set of axes. This allows direct visual comparison between different stress concentrations due to corrosion, as the different surface roughness resulting from corrosion will give different life cycles until failure.

As explained previously, both specimen faces were exposed to a salt solution as the specimens were vertically fixed in the corrosion chamber. This fixing is not similar to the realistic service of automotive chassis material, where the chassis material is generally exposed to a corrosive environment predominantly from one side. Moreover, the vertical fixing caused the corrosion to not be homogeneous as some specimen surfaces showed grooves perpendicular on loading direction as shown in Figure 4.9, leading to early failure. Fatigue life is sensitive to surface finish; cracks can initiate at surface irregularities that are normal to the stress axis, this is consistent with observation of Keisler and Chopra (1995), Novovic et al.(2004) and Suraratchai et al. (2008). As a result of these observations, subsequent work with FB590 horizontally fixed specimens in the corrosion chamber inclined at 30 degrees in the salt spray in order to overcome these problems and obstacles.

By analysing the SN curves there are some points above and below the reference lines. The smooth surface of uncorroded specimens shows a low fatigue life scatter due to the identical manufacturing process, whilst the data for the corroded fatigue specimens shows a larger scatter due to various surface exposure treatments. The variability in defect type and scatter of size would be the possible main factors contributing to the wide scatter of fatigue life in the non-pristine specimens (Mohd et al. 2012).

It was observed that the gradient of the corroded SN curve is slightly steeper compared with the uncorroded, and the position of the uncorroded curve would be

shifted to the right by moving from the high stress concentration of corroded specimens, to the lower stress concentration on the pristine specimens. It is clearly noticeable from these curves that the fatigue resistance of pre-corroded specimens is drastically decreased and their fatigue life reduced when compared with intact specimens. As seen from these figures the un-corroded Group 0 specimen had a higher fatigue limit and longer fatigue life compared to those of the corroded specimens. Absence of stress concentrations due to surface roughness in the intact specimen would contribute to the higher fatigue limit and the longer fatigue life. The stress raiser points increase proportionally with the surface roughness. Therefore, the crack can start propagate at any point where there is the highest stress raiser.

These results further supported the general conclusions that the increase in corrosion exposure decreased the fatigue life. At the higher applied stress levels, the differences in fatigue lives from the low corrosion level to the high corrosion level became less pronounced. With the decreasing of the fatigue load, the difference of the fatigue lives became noticeable and the scatter is larger. The analysis suggests that stress magnitude has a higher detrimental impact on the fatigue life of the specimens as compared with stress concentration due to different corrosion time showing a good agreement with the previous work of Hao et al. (2011).

There was a special attention devoted to identify fatigue endurance limits, the fatigue limit of the specimen was taken when the number of cycles to failure, N , is greater than 5×10^6 cycles. The horizontal arrows in Figure 4.8 indicate a run-out, for example a fatigue test is suspended at a very high number of cycles, without evidence of fatigue damage. It was also found that the base line specimen had the highest fatigue limit. It can be observed that the endurance limit decreases with increased surface roughness due to the corrosion exposure. It is important to note that the surface appearance affects the fatigue life greatly, and corrosion would cause the surface to become rougher, thereby rapidly decreasing fatigue life and endurance limit. This finding agrees with the recent investigations which confirm the reduction in fatigue life and endurance limit notably with time of corrosion attack (Wang et al. 2003; Wasekar et al. 2011).

4.5 Acoustic Emission analysis for mild steel fatigue tests

This section shows investigations performed on mild steel fatigue specimens to identify sources of AE in mild steel and relate them to damage mechanisms, this subject was extensively explained in previous work (Shrama et al. 2014, 2015). DIC, a full-field strain measurement technique, was used to validate the findings and provide a clear depiction of the surface strain field evolution. This section describes in detail the results of three ‘dog bone’ style specimens undergoing uni-axial fatigue loading.

Crack growth was monitored in the test using two AE sensors and, to allow a comparison with the detected and located signals, DIC images were captured periodically at peak loads to provide a clear depiction of the surface strain field evolution. As part of the initial analysis, located signals were compared with areas of high deformation and crack growth as identified by the DIC system. SEM fractography was used to investigate crack initiation and growth. Results demonstrated that the combination of AE and DIC can provide much useful information to help to distinguish the different AE signals originating from various possible failure mechanisms such as plastic deformation, delamination of DIC paint and crack initiation and propagation. This might be utilized for an effective and powerful approach to monitor multiple failure mechanisms; this has significant applications in automotive chassis testing.

4.5.1. Results and acoustic emission analysis

AE is a sensitive technique which acquires AE information from both real cracks and noise. Eventually, the different types of noise obstruct the reliability and accuracy of AE analysis (Berkovits 1993; Teik 2001). To remove AE noise data related to surface rubbing at the pins, environmental noise and other unknown sources generated outside the test specimens, data files were filtered by location around the crack, using only data originating between the AE sensors and discarding other data. This region included the fatigue crack growth and crack closure, but also plastic deformation of the material around the crack tip and elsewhere. The AE parameters were compared with DIC measurements and plotted against number of cycles (N) under various stress levels. In general the

cumulative energy and count followed the crack growth for the duration of the test; this confirms that the AE is detecting the crack growth. The rate of events varies during the test and did not increase continuously with crack length, this variation in the rate of events is due to a variety of source mechanisms.

In this study two experimental cases are presented in detail that reflect the general observations associated with other experimental tests at loads 320 and 230 MPa. Case I is for a load condition of 230 MPa with an un-corroded specimen whilst Case II presents results for a test load of 320 MPa for a specimen previously subjected to 25 days of corrosion.

4.5.2 Fractography characterization

Fractography can provide information as to the location and nature of the critical discontinuity, as well as any apparent trends in the corrosion features, shapes, and severity of damage. The scanning electron micrographs of the fracture surface of the two fatigue specimens are shown in Figures 4.10 and 4.11. The fatigue crack of specimen I (Figure 4.10a) was almost flat with a length of 5.114 mm. The fatigue crack of Case II, Figure 4.11a, shows typical features under high axial loading fatigue, it consists of a 45° chamfer at the left end of Figure 4.11b, where the crack initiated in stage I, then it is followed by a granular area of fatigue crack growth. The fatigue crack propagation region for case II was rougher and shorter than in case I with a length of 1.122 mm. The reduction in specimen cross section area is obvious; it occurred before quasi-cleavage, suggesting plastic deformation as shown in Figure 4.11a.

In both cases, the fatigue fracture surface can be divided into two parts, fatigue crack propagation and fast fracture. The first part is characterized by a granular area close to the crack initiation zone but there was a difference in the length of the first part between the two cases. The remaining surface, the second part, is the ductile fracture surface, as shown in Figure 4.10d, caused by overloading of the specimen because of the reduction in cross-section area (Kovac 2010). This part is similar to the tensile fracture surface mechanism, like the classic cup and cone type. The transition from the stable to unstable crack propagation is characterized by the change in fracture mode from fatigue crack growth to a ductile fracture. Figures 4.11c and d shows average dimple sizes (diameters) of micrographs for

the specimen Case II. Also it shows the presence of non-uniform small and large dimples, indicating considerable plastic deformation ahead of the fatigue crack. The elongated shape of some voids may indicate that there were localized shear stresses. Figure 4.11d shows dimple coalescence, there is a direct relationship between dimples coalescence and necking (Zare and Ekrami 2011). The dimple coalescence and necking is not obvious in Case I as shown in Figure 4.10c where less plastic deformation occurred and the fracture surface is more characteristic of pure fatigue failure. The fracture surfaces for the specimen in Case I shows a higher amount of fatigue damage and a significantly longer crack length before fast fracture occurs.

4.5.3 Plastic deformation

The plastic deformation effect took place through the fatigue process, especially at an early stage of the test, and significant AE occurred during this deformation. It was obvious in Case II (the tests under high load), however it also occurs under lower load (Case I) (Lepisto 2003).

It was observed that the plastic deformation was accompanied by pronounced AE activity. This may have been due to dislocation glide and deformation twinning (Janeček 2007; Vinogradov 2013) although these typically have much lower amplitudes; other possible sources include fracture of surface oxides and cracking or delamination of the paint from the surface. Figure 4.12 and Figure 4.13 show AE parameters such as cumulative counts, amplitude and load vs number of cycles for Case I and case II. This activity is shown by group A (dashed line rectangle) in both Figures 4.12 and 4.13. It can be seen from these figures that these signals had an amplitude range of around 45-50 dB; this agrees with the findings of Barsoum (2009).

Figure 4.14 shows the test results for an uncorroded specimen under similar loading conditions to Case II. In this test the specimen was reused for a second time. Firstly this specimen was loaded to 211MPa for around 5.6 million cycles then re-loaded at 320MPa until failure at 104247 cycles. Figure 4.14 (b) shows that there was no significant AE activity at early stages of the test when compared with Case II. The possible reason for this is that the damage that generated the AE happened in the first loading at a lower load; this tends to suggest that some other

mechanism such as fracture of brittle surface oxides during plastic deformation may have been responsible for this AE. Since there was significantly more plastic deformation when the specimen was first loaded to 320 MPa, one would expect significant AE during the second test if the AE was due to plastic deformation alone.

DIC provides a clear depiction of the surface strain field and its transient changes according to stress redistribution which occurs during crack propagation and is a good measuring tool to analyse and quantify the growth of the crack and plastic zone changes. The region of interest for correlation was chosen as (20x60) mm centred on the parallel section so as to observe the damage evolution until final failure. Figures 4.15 and 4.16 show the DIC images which were captured sequentially and show the development of the strain distribution during fatigue loading for cases I and II. The grey area highlights the plastic zone in the wake of the crack tip, where correlation is lost due to the crack growth. The majority of damage initiation happened at the periphery of specimen towards the middle. The maximum strain was observed around the edge of the crack tip perpendicular to the loading direction. A key to the strain contours is provided but should not be considered to be a true representation of the actual magnitude of the strain values around the crack position (Pullin et al. 2010), due to the calculation method employed by the image correlation software. The displacement is calculated over a subset of pixels which has a finite size, and then the strain is calculated assuming a continuous displacement field over several subsets. The spatial resolution of the strain measurement is therefore limited, and will be less accurate near the crack.

Case I

Figure 4.12 shows a large number of signals (group B) which occurred during crack initiation and early growth. Generation of AE during high cycle fatigue has previously been attributed to crack initiation (Berkovits and Fang 1995; Elforjani and Mba 2009; Mukhopadhyay 2014), but this seems unlikely. This stage involves the growth of microstructurally small cracks (MSCs); this could constitute stage I (shear cracking). In this stage crack initiation stems from dislocations in the structure that accumulate due to high stress concentrations at grain boundaries,

notches, or surface irregularities. These begin to form fine slip line systems within the structure along the shear plane. As the slip lines increase in density they broaden into bands, which ultimately form micro cracks (Wanhill 1984; Chopra 2002). It is difficult to explain how this activity, predominantly consisting of very localised dislocation movement, could generate AE with an amplitude that could be detected, although other researchers have observed AE from fatigue crack initiation that generated low amplitudes signals (Pollock 2012). The visualisation of the crack at this stage is difficult using DIC due to its very small size in comparison to the resolution of the DIC measurement. In addition in this case the crack started from the opposite face of the specimen to the DIC camera. Other possible mechanisms could include cracking of brittle surface oxides or of the paint on the surface during plastic deformation and crack initiation. Examination of traditional AE parameters such as rise time and duration was not particularly helpful in determining the source(s) of these emissions.

The signals that occurred during the propagation stage of fatigue life have been divided into groups C (rounded rectangle) and D (rectangle) which involves growth of mechanically small cracks. Mechanically small cracks correspond to Stage II (tensile) cracks, which are characterised by striated crack growth, with a fracture surface normal to the maximum principal stress (Chopra 2002).

The amplitudes of the AE signals detected at peak load (group D) is less than 50dB while the amplitude of AE signal released at low load (group C) have various amplitudes. Most of the high amplitude signals (above 56 dB) were released at this load level. The increasing amounts of fretting emission were observed as the crack advanced from Stage II towards Stage III (final fast fracture stage which may not appear here because the AE system could not locate it). Along with this, the fracture surface became rougher (Pollock 2012), as may be seen in the fractography results shown in Figure 4.10a.

The low amplitude and relatively small numbers of detected signals at peak load, suggest that the primary source associated with the crack growth is difficult to detect in mild steel plate (Jun 1990). Moreover the result may suggest that the crack growth mechanism at the crack tip may be dominated by plastic tearing as this is obvious from SEM results and agrees with Scruby (1987). A few signals

with amplitude above the detection threshold (45 dB) detected at peak load may have been generated by a ductile crack extension mechanism which is a very weak source of AE (Scruby 1987; Moorthy et al. 1996) or more likely, from cracking of surface oxides, paint, etc.

All high amplitude signals were detected at a relatively low load level (around 2.5 kN in Case I) which suggests that the signals were caused by the rubbing of the two crack surface during crack closure (Scruby 1987; Pollock 2012). Crack closure usually takes place just after the crack opening at crack tip (crack advancement) due to the sudden change of stress level associated with the stress relief during crack growth.

The closure effect is not clear in Case II (Figure 4.12), because the specimen was considerably elongated, as is obvious from the DIC results, such that the crack faces did not contact each other. In addition the first part of fatigue crack was very short compared with the previous case I as shown in Figure 4.10b.

Case II

This case presented different trends to those noted in the earlier case. Referring to Figure 4.13(a), there was a slight increase in AE activity at around 8000 cycles. This is not obvious in this figure; however an increase can be seen in the enlarged view shown in Figure 4.17(a). The increased AE activity which is represented by group C (rounded rectangle) was thought to be generated from one of two mechanisms. The first one is crack initiation, and the second one is most likely considered as noise due to rubbing of the damaged corrosion product under DIC paint with specimen surfaces around the crack path as shown in Figure 4.18. The amplitude of these signals could be higher due to the brittleness of the corrosion products and the friction between the delaminated paint and the specimen surface. Figure 4.17 (b) shows out of plane displacement measured using the DIC system which reveals that the DIC paint had flaked due to the crack initiation underneath it. Figure 4.17 (c) shows another significant increase in AE activity around 16k cycles accompanied by a similar increase in DIC displacement pattern. This increase may have resulted from crack extension and other signals related to these mechanisms such as plastic opening at the crack tip, plastic zone extension and

crack advance (Scruby 1987; Barsoum 2009). This increase demonstrates that the crack has started and was consistent between both techniques. This increase was largely caused by crack growth as opposed to plastic deformation away from the crack tip, observations which are consistent with those of (Pullin et al. 2010).

Returning to Figure 4.13(b), it may be seen that there was a group of signals (group B) having high amplitudes above 94dB. Consideration of both AE and DIC data allows these signals to be identified as resulting from the mechanism of brittle fracture or delamination of corrosion products from the underlying substrate material. Consideration of the location of signals, identified by the time of arrival method using commercial software (AEwin), identifies these signals as being generated by a source at an “X” location (along the test specimen’s reduced section) of 0.01-0.02 m, as shown in Figure 4.19(a). Inspection of the corresponding DIC image in Figure 4.19(b) shows a high level of out-of-plane displacement at this location, highlighted in Figure 4.19(b). The out of plane displacement at this location was compared to that at surrounding points (Figure 4.20) and shown to have a higher level, increasing with loading cycle, indicating the gradual flaking of corrosion product. Post-test visual inspection of the specimen confirmed the presence of flaking corrosion product at this location.

4.6 Conclusions

From these laboratory investigations the following conclusions and observations may be drawn:

Good training on equipment and devices used in these tests, such as the fatigue test machine, surface profilometer DIC and AE, will help to avoid and reduce specimen loss to complete the tests on FB590 material more precisely.

The specimen design was changed for FB590 Specimens with larger radii and a longer parallel sections were used in order to be more suitable for corrosion studies.

The mild steel specimens were fixed vertically in corrosion chamber whereas in the subsequent FB590 investigations, specimens were inclined at 30 degrees in the

salt spray cabinet. The latter setup was more realistic and similar to chassis in service.

The monitoring procedure of fatigue tests using DIC and AE was developed, and associated problems were overcome, such as time misalignment between DIC and AE results.

These results showed in general that the increase in corrosion exposure decreased the fatigue life. In addition, the analysis suggests that stress magnitude has a higher detrimental impact on the fatigue life of the specimens as compared with stress concentration due to different corrosion time.

The investigation stated well the capabilities of AE for detecting fatigue fractures, and its potential for distinguishing the different AE signals from various possible failure mechanisms. Plastic deformation, delamination of corrosion product and DIC paint as well as crack initiation, propagation and closure are all involved in this process and AE monitoring provides valuable information to help to distinguish between them.

DIC allows a clear depiction of the surface strain field evolution and its transient changes according to stress redistribution which occurs as the crack propagates. It is a useful method for monitoring the whole area of interest and it is not limited to a specific region, therefore any damage can be detected even if the precise location is not known in advance. DIC was used to support the understanding of the detected AE signals. The complementary use of DIC and AE helps to minimise the assumptions in the interpretation of the AE trends in relation to the responsible damage mechanisms by revealing the fluctuation of the surface strain fields and other factors such as paint delamination. Additionally, SEM was also used to verify and support the relationship between various phenomena occurring in fatigue failure and the AE signals.

The combination of AE and DIC was also helpful in distinguishing between crack initiation and early propagation and background noise, which is otherwise difficult using AE. Early growth of cracks in steel typically generates only very low level AE which is difficult to distinguish from rubbing or fretting, for example of loose paint or corrosion products. The use of DIC allowed significant cracks to be

identified well before failure. This could have numerous applications in testing more complex structures, for example in automotive chassis or aerospace applications.

Table 4.1: shows mechanical properties of mild steel plate.

Ident. Mark	Width mm	Thickness mm	Area mm ²	0.2% Proof.	Ultimate	Elongation		Elastic Modulus kN/mm ²
				Stress N/mm. ²	Stress N/mm. ²	mm.	%	
1	9.96	3.02	30.17	268.5	412.0	18.0	36.0	206.7
2	9.99	3.03	30.27	281.5	431.1	17.9	35.8	234.68
3	9.96	3.03	30.27	277.5	428.1	18.2	36.4	250.26
Average				275.83	423.73		36.1	230.54

Table 4.2: Processed mild steel S-N data.

Mild Steel Data Set	Basquin Coefficient (A), (MPa)	Basquin Exponent (b)
As received	1161.4	-0.112
Low level of corrosion	1589.5	-0.142
high level of corrosion	1677.5	-0.154

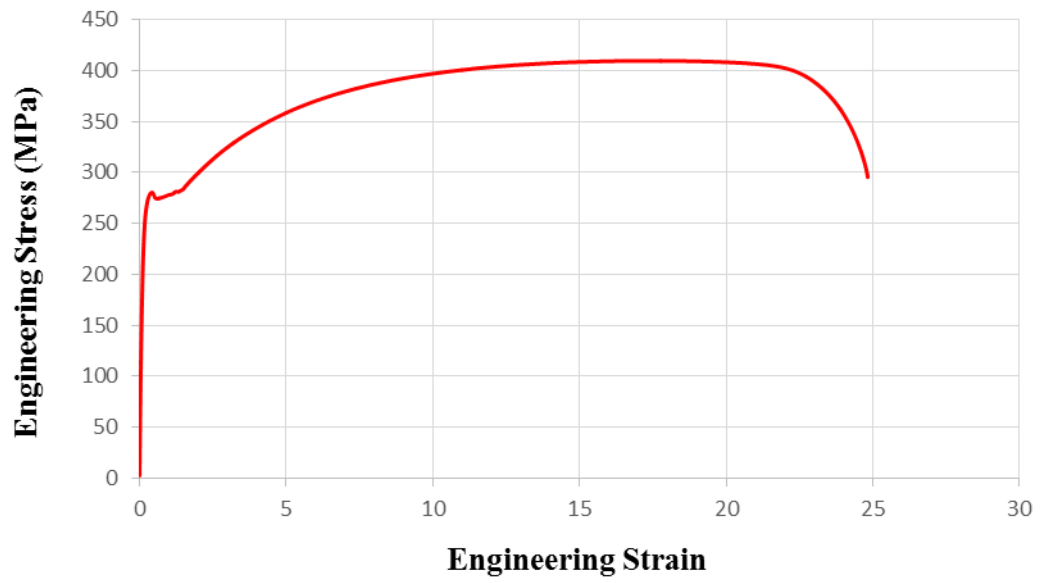
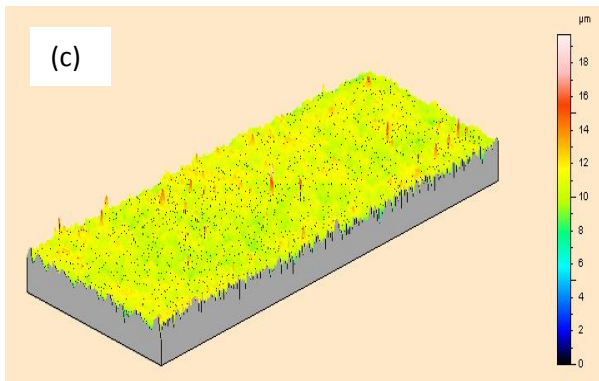
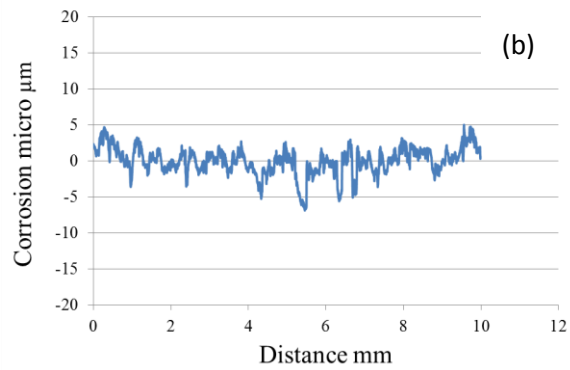
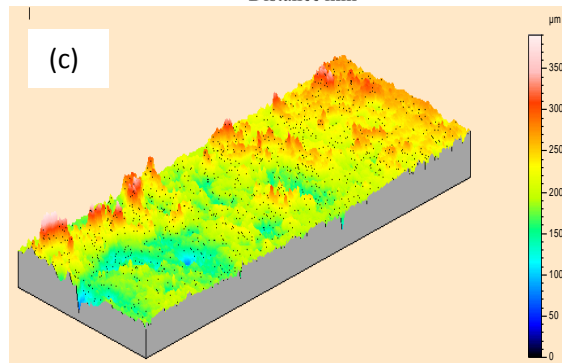
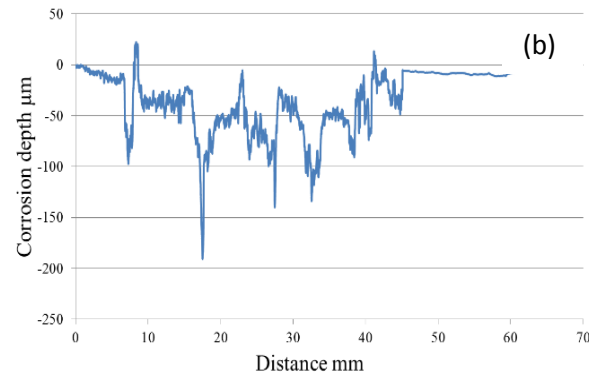


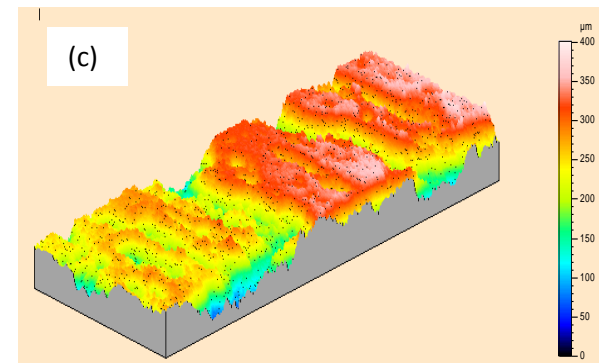
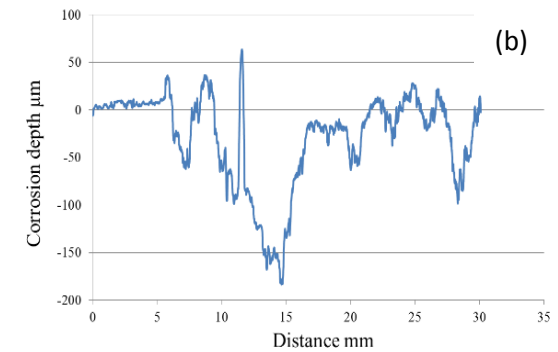
Figure 4.1: Stress strain curve of mild steel.



Figures 4.2: (a) The typical appearance of the as received specimen (b) 2D profile (c) 3D image of as received specimen.



Figures 4.3: (a) The typical appearance of the Corroded 25 days (b) 2D profile (c) 3D image.



Figures 4.4: (a) The typical appearance of the Corroded 50 days (b) 2D profile (c) 3D image.

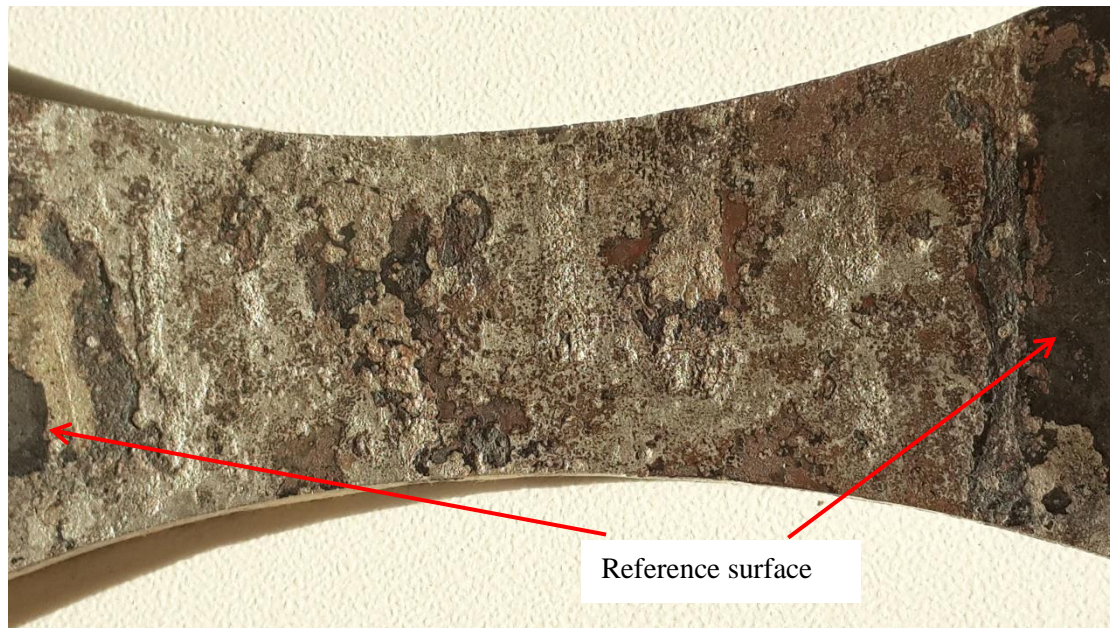
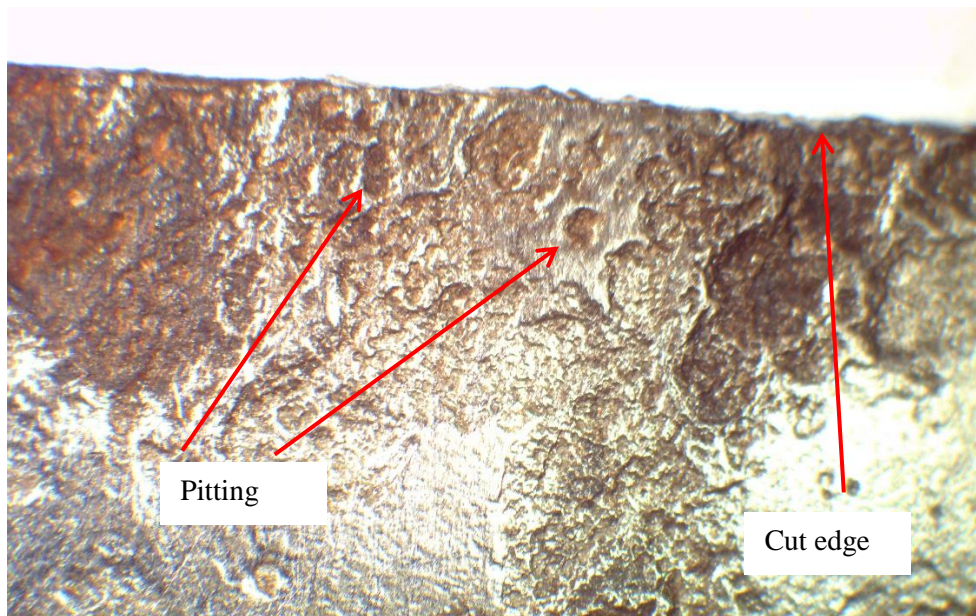


Figure 4.5: The typical appearance of the specimens after removing the rust.



Figures 4.6: Stereo optical microscope image of corroded surface.

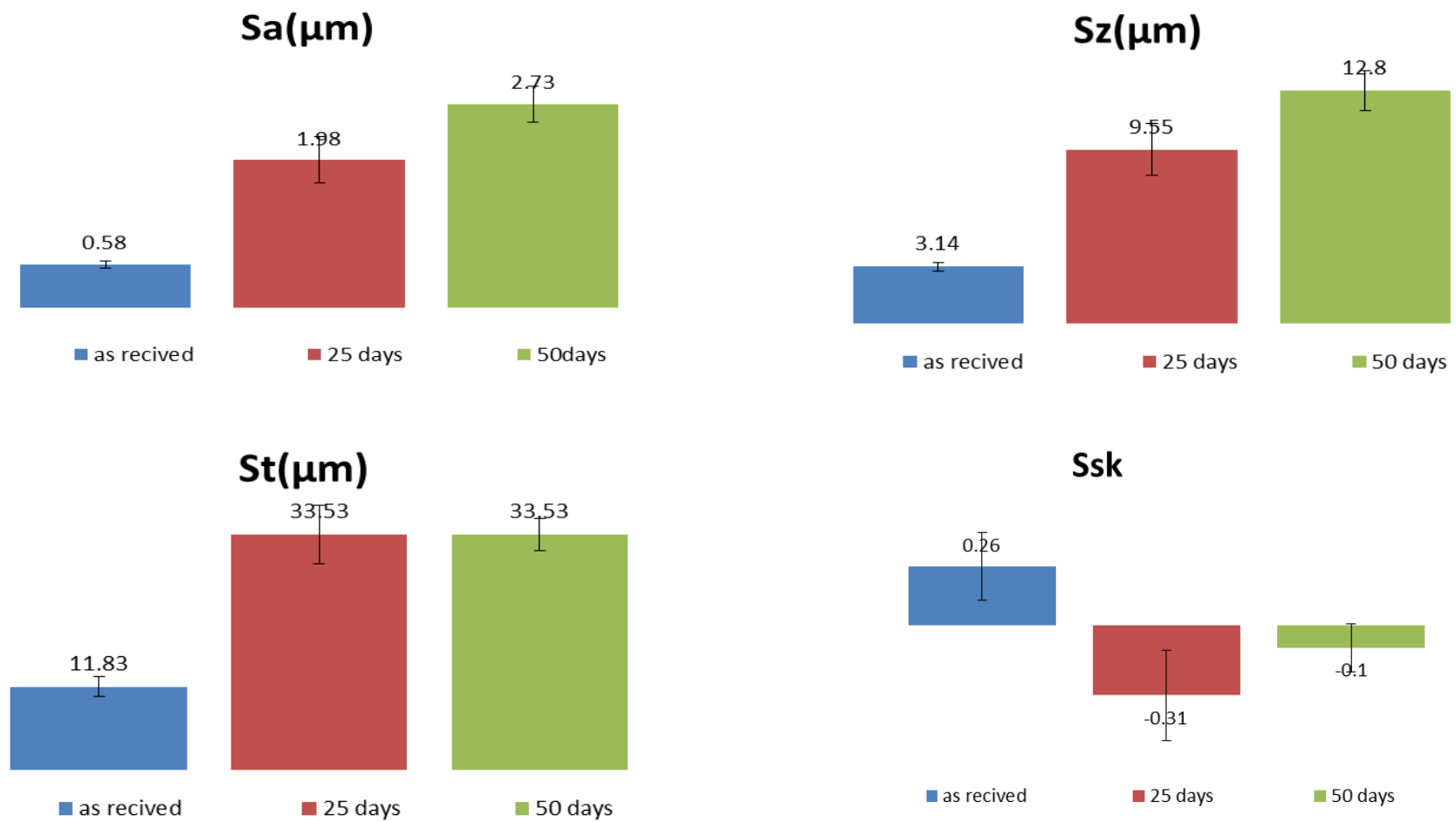


Figure 4.7: Roughness parameters increasing with time of corrosion.

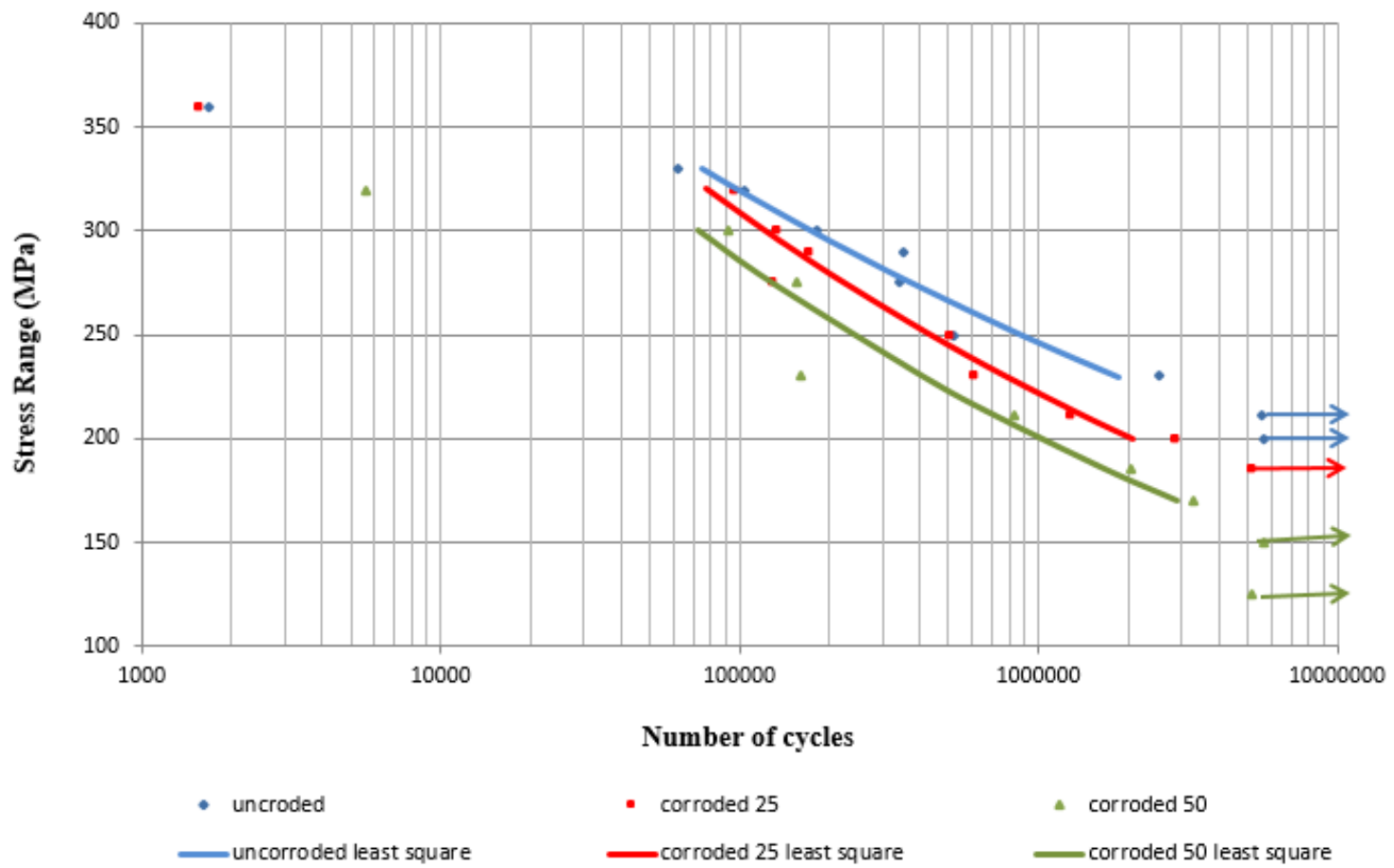


Figure 4.8. shows S-N curve comparison of the uncorroded and corroded specimen.

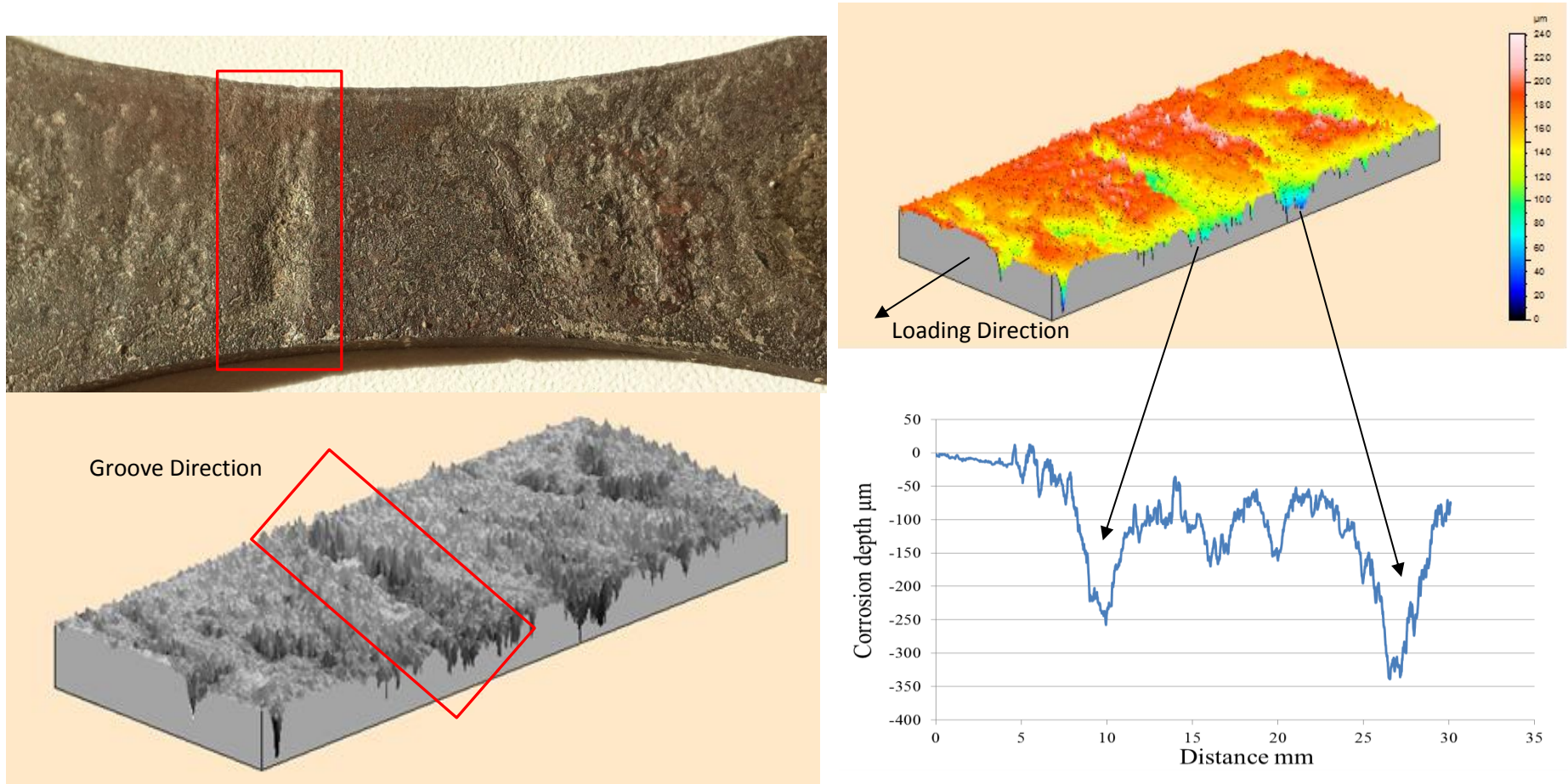


Figure 4.9 Grooves perpendicular to direction of the loading.

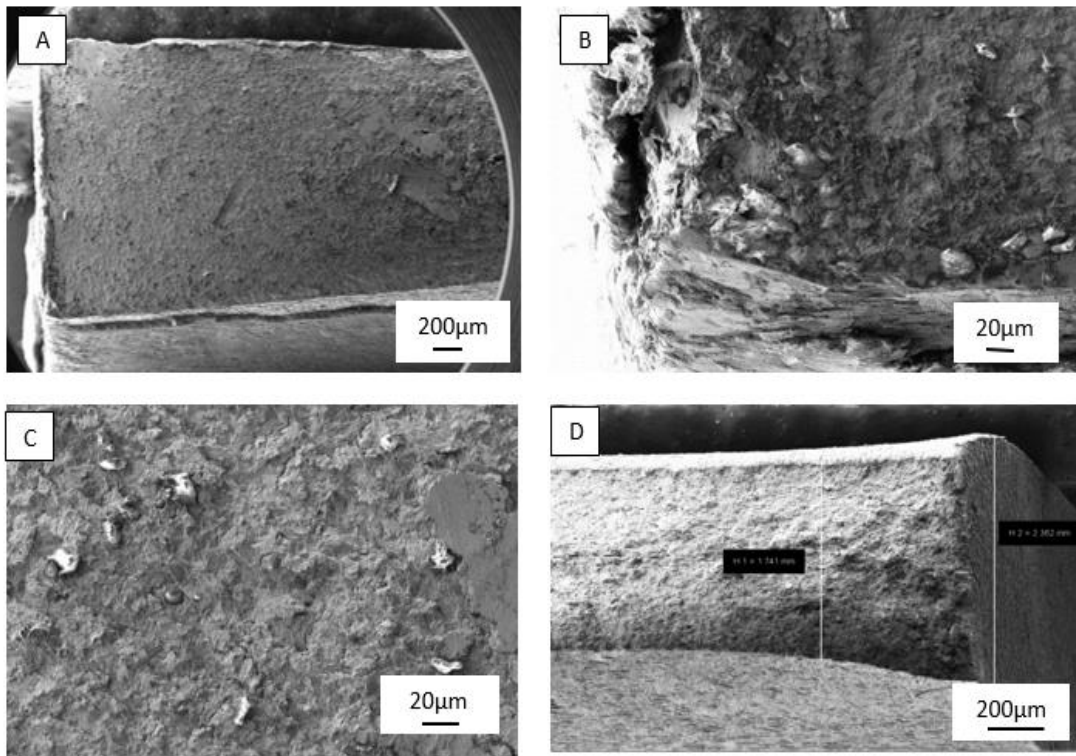


Figure 4.10: SEM micrographs taken from fracture surfaces of fatigue tested specimens Case I (a) showing the general appearance and no necking (b) indicates the crack initiation corner opposite to DIC cameras, (c) shows that dimple coalescence was not obvious in the specimen tested at 230MPa (d) indicates ductile fracture and reduction in cross-section.

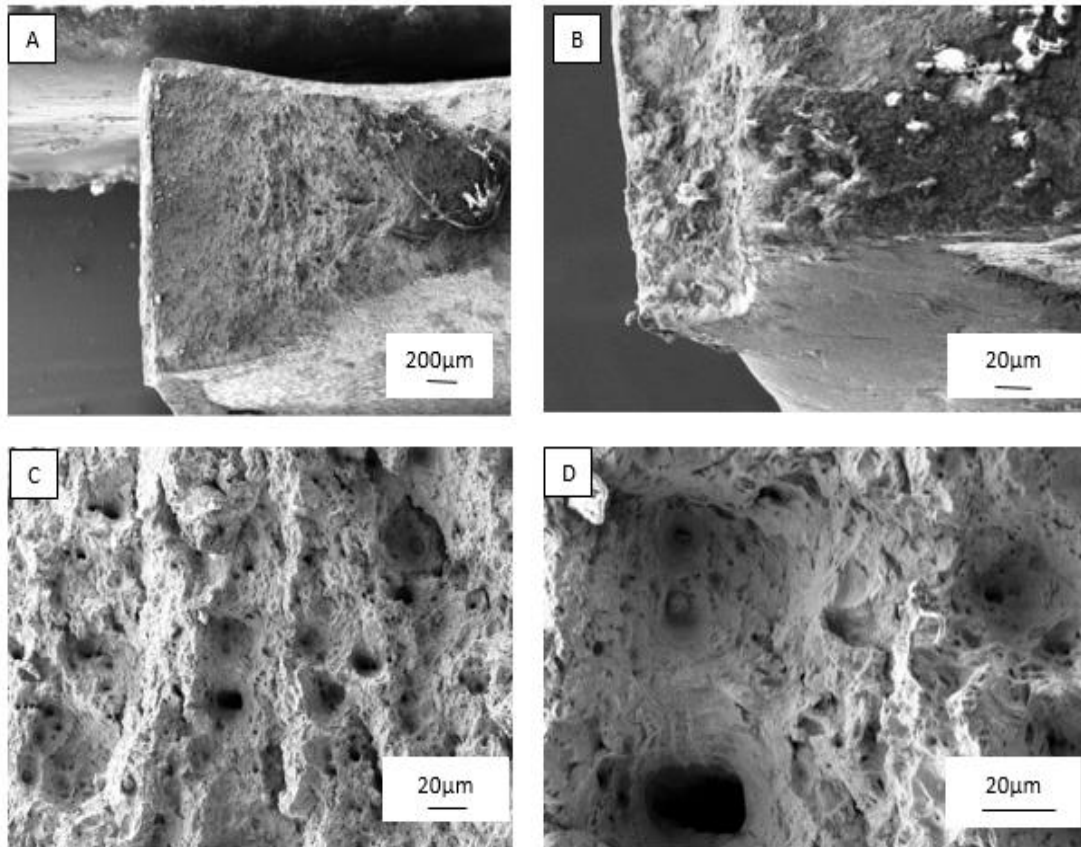


Figure 4.11: SEM micrographs taken from fracture surfaces of fatigue tested specimens Case II (a) showing general appearance and necking, (b) site of crack initiation (c and d) indicates elongated shape of some voids and dimple coalescence.

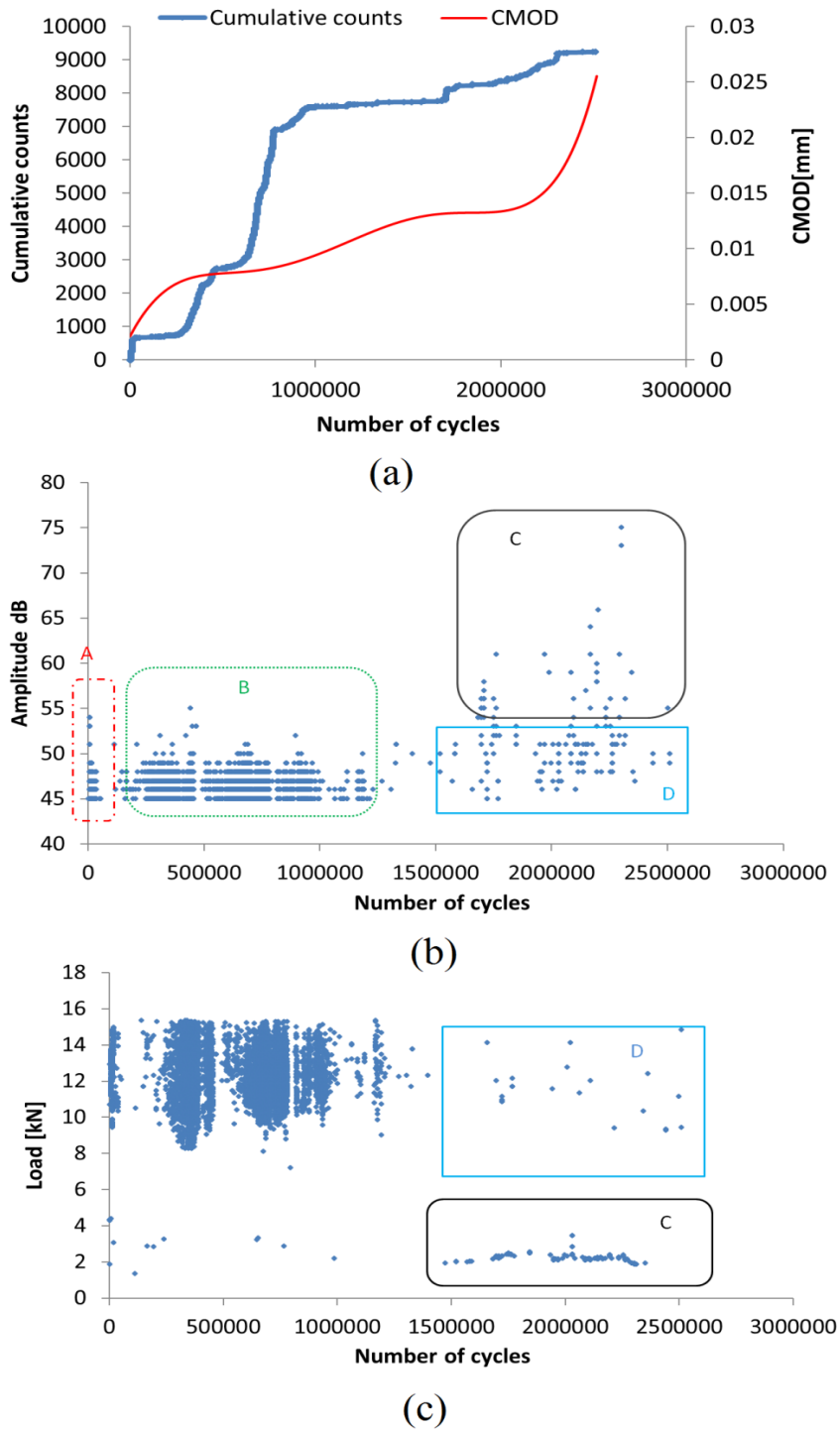
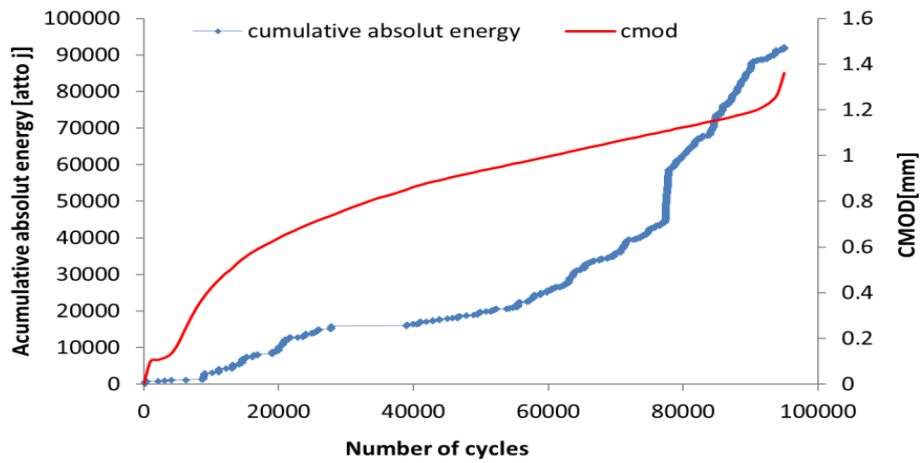
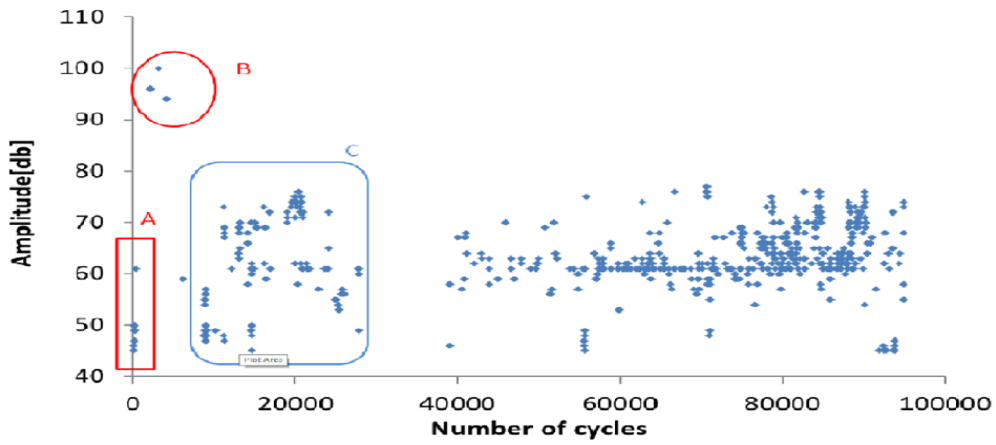


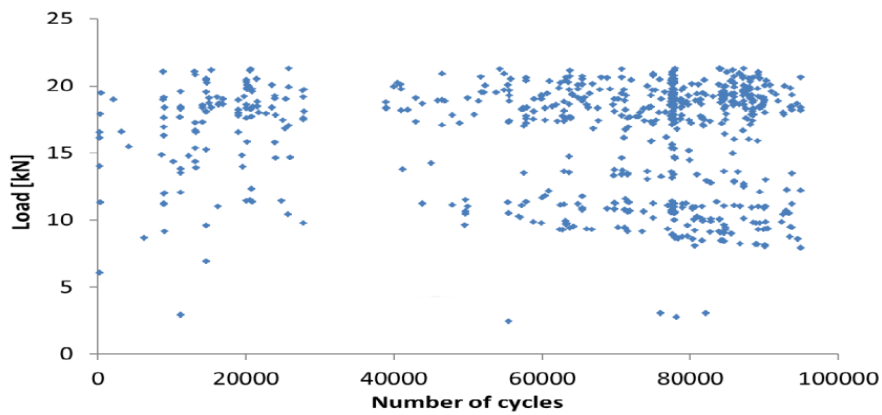
Figure 4.12: (a) Cumulative counts on primary axis and CMOD on secondary (b) Amplitude (c) Load vs Number of cycles for uncorroded specimen under 230MPa Case I.



(a)



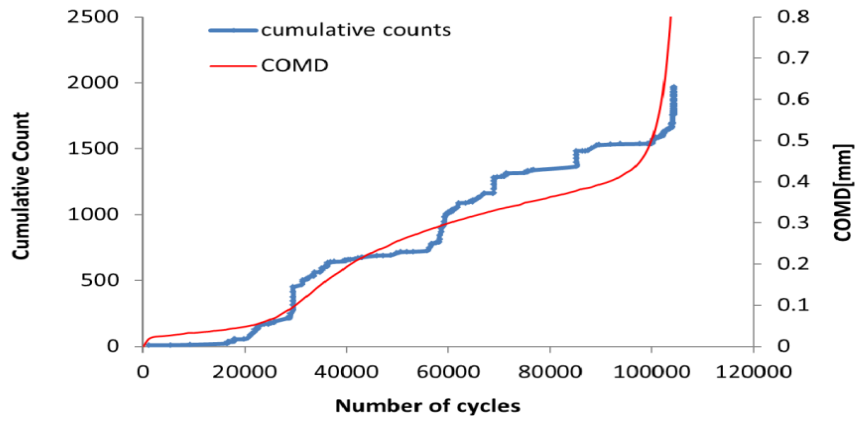
(b)



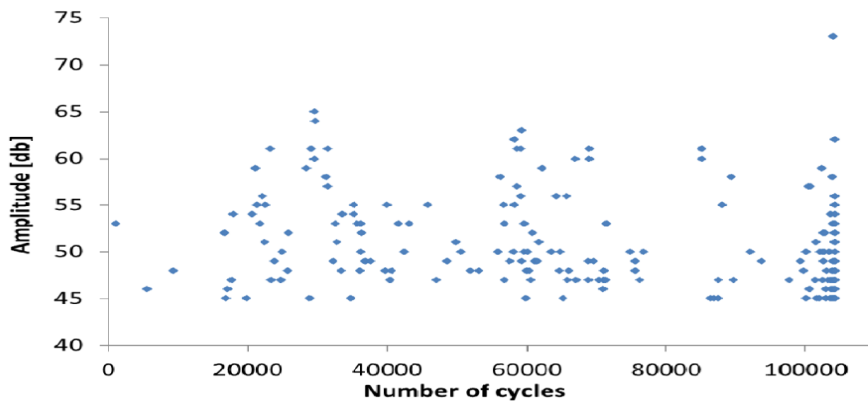
(c)

Figure 4.13: (a) Cumulative absolute energy on primary axis and CMOD on secondary (b) Amplitude (c) Load vs Number of cycles for corroded 25 days specimen under 320MPa case

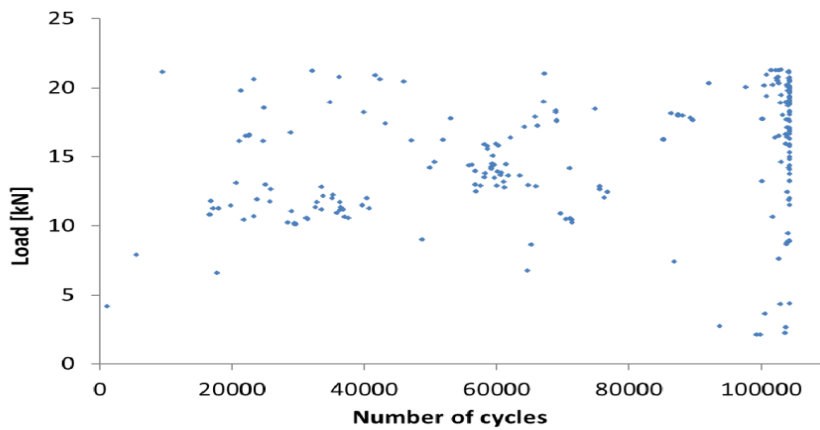
II.



(a)



(b)



(c)

Figure 4.14: (a) Cumulative absolute energy on primary axis and COMD on secondary (b) Amplitude (c) Load vs Number of cycles for corroded 25 days specimen under 320MPa case

II.

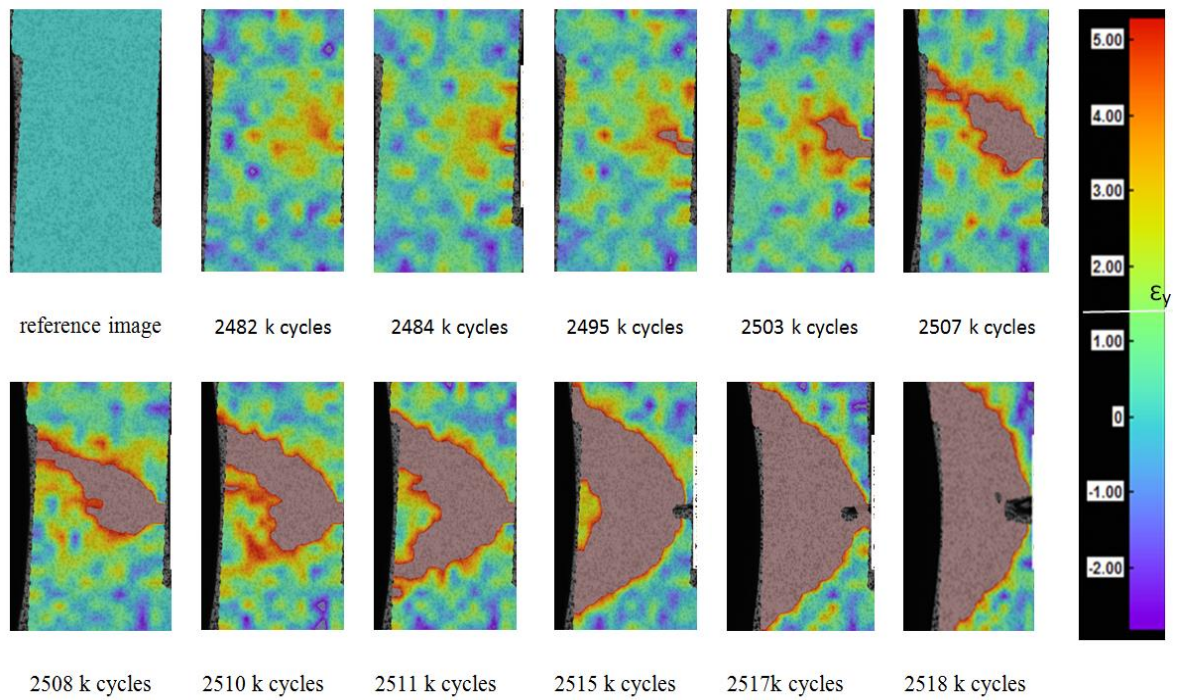


Figure 4.15. Development of microstrain during fatigue loading for case I.

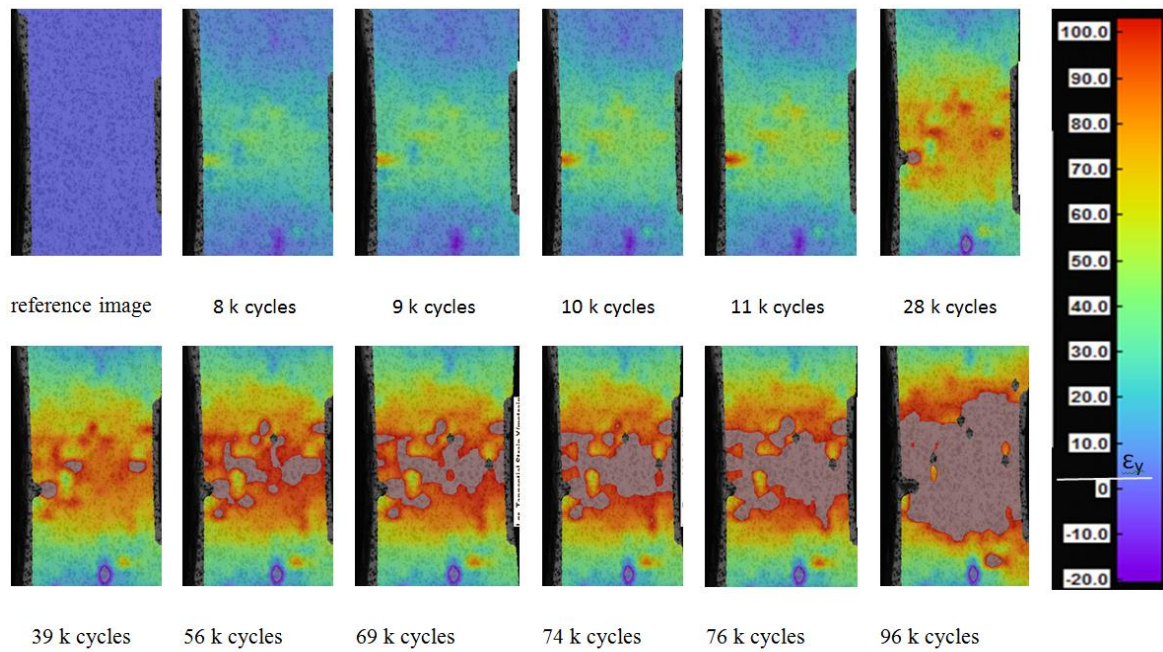


Figure 4.16. Development of microstrain during fatigue loading for case II.

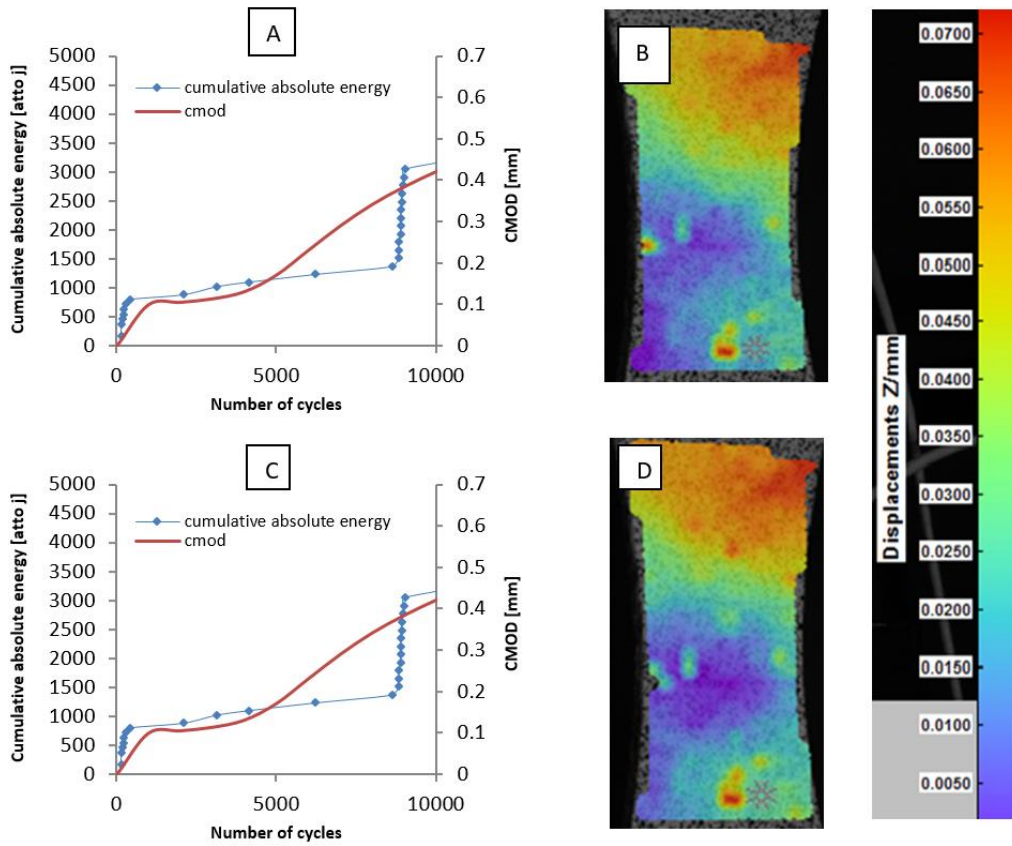


Figure 4.17. (a) Focused view of Figure 4.13 at 8 k cycle and (b) corresponding DIC images (c) focused view at 16 k cycle (d) DIC images at 16 k cycle.

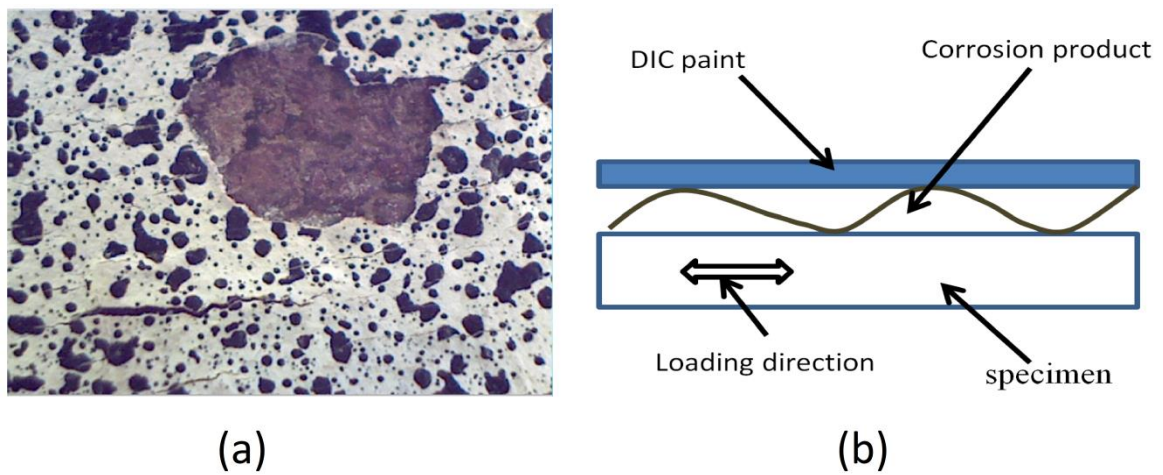


Figure 4.18. Schematic explain the rubbing of the damaged corrosion product underneath DIC paint with specimen surfaces around the crack path.

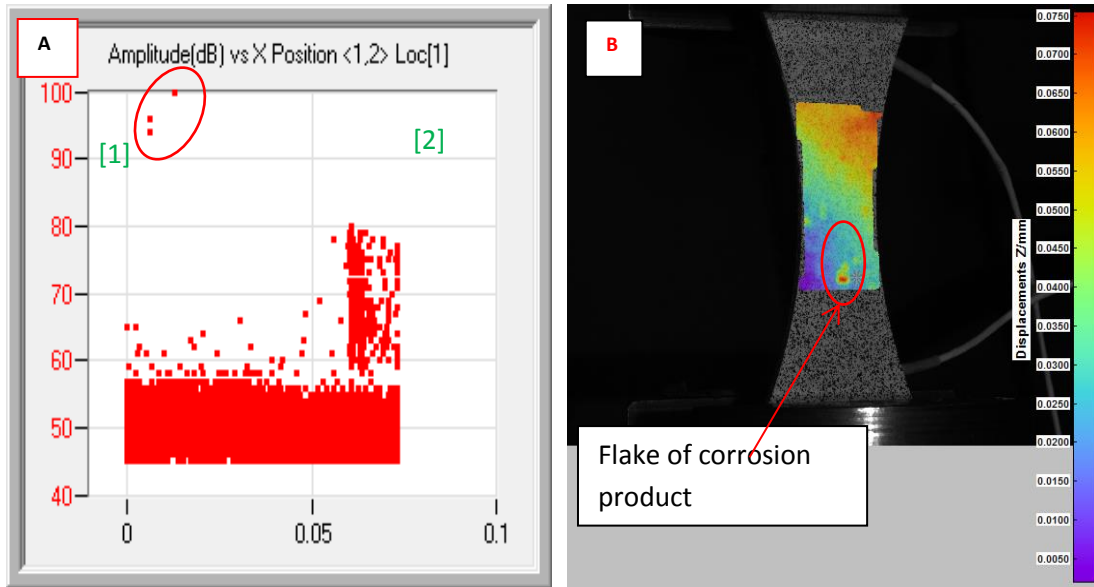


Figure 4.19: reveals the flake in the corrosion product by DIC and AE methods.

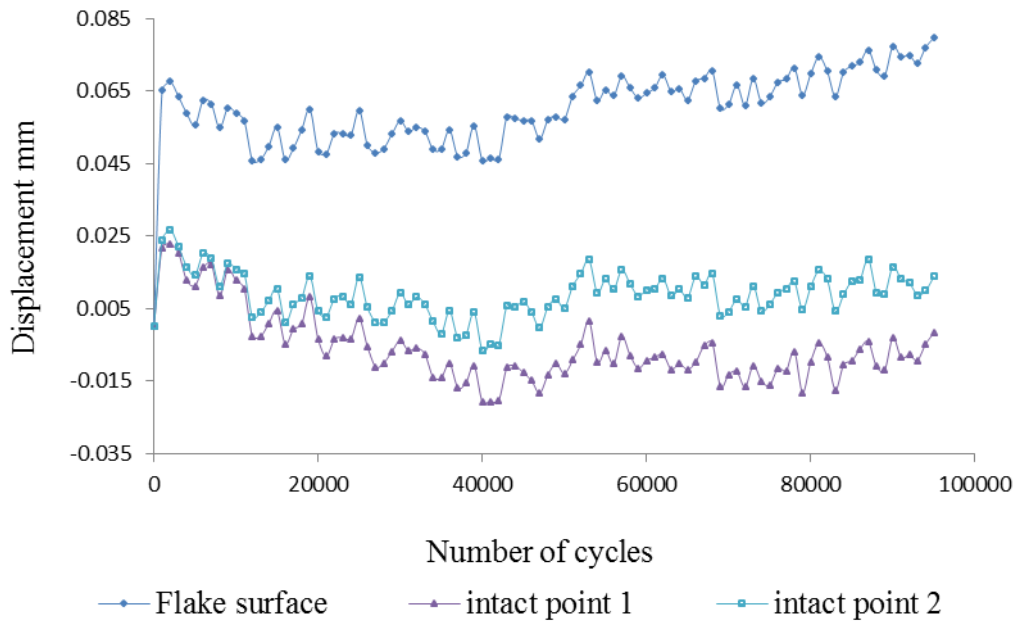


Figure 4.20. Out of plane displacement for intact and flake surface.

5. The Preparation of Experimental Studies for FB590

5.1 Introduction

This chapter focuses initially on the material properties of FB590 and specimen preparation and then goes on to address the monitoring of fatigue tests using AE and DIC. The main aim of this work is to provide FB590 S-N curves data for tension and bending fatigue loading, for both welded and unwelded specimens. The FB590 work plan was made to simulate and cover all possibilities of environmental conditions which are encountered by a practical vehicle chassis. Eighty fatigue specimens each for tension and bending were prepared according to the work plan shown Figure 1.2. These eighty specimens were divided into five different main groups; each group consisting of eight specimens. For nomenclature purposes the different test configurations were designated as either Group 1, Group 2, Group 3, Group 4, or Group 5 type configuration as shown in Figure. 1.2. This naming convention describes and designates the surface exposure to stone chipping and corrosion attack as explained below. High and low corrosion refers to the exposure time of the samples in the corrosion chamber.

Group 1 Base E coated only (**G1-Base**)

Group 2 E coated, stone chipping, no corrosion (**G2-Stone**)

Group 3 E coated, stone chipping, low corrosion (**G3-SLC**)

Group 4 E coated, stone chipping, high corrosion (**G4-SHC**)

Group 5 E coated, no stone chipping, high corrosion (**G5-HC**)

5.2 Material properties

Advanced High-strength steels (AHSS) are one of the most popular alternative materials for weight reduction in next-generation vehicles. Their use is extremely promising in automotive industries to meet the increasing requirements of crashworthiness and fuel efficiency. Hot rolled FB590 HR is a ferrite-bainite AHSS which has been developed to meet weight reduction requirements. It can be used in automotive chassis and suspension applications, such as, upper and lower control arms, engine sub-frames and road wheels (specifically wheel discs).

Substitution of standard grades with FB590 HR provides opportunities to reduce gauge whilst maintaining the in-service performance and potential cost and weight savings. In the following sections the preparations for testing of FB590 will be explained.

5.3 Tensile performance of FB590

The tensile tests were performed as explained in Section 3.3. The tensile FB590 welded specimens were prepared from the same manufacturing process as the fatigue specimens using two welded rectangular pieces of (120 x 140) cm, with the specimens aligned with the rolling direction. The low alloy steel filler wire ESAB Aristorod 13.26 Ø1.2mm was used, the details of which are listed below in Table 5.1. The nominal composition of FB590 is listed in Table 5.2 as received from Tata Steel. Tables 5.3 and 5.4 show the measured mechanical properties of un-welded and welded FB590 specimens respectively obtained during this research. To obtain the accurate tensile strength in each condition, three specimens were tested and the average of the three results is presented in the bottom row of each table. Tata Steel measurements for longitudinal direction are shown in Table 5.5 and show good agreement with these measurements except for the modulus of elasticity. In the current measurements more realistic values of a mean elastic modulus of 203 GPa compared with the Tata measurements of 160 GPa was found. The mechanical properties of the welding consumable are significantly greater than the base material, and as such, the tensile specimens did not fail at the welds. Figure 5.1 shows tensile test specimens after failure and it was found that all the welded specimens failed in the base metal. The main difference between welded tensile specimens and un-welded can be seen in the elongation properties, which are shown in Figure 5.2. The ductility (elongation) of weld was lower than that of the base metal. However, yield and tensile strengths are higher than those of the base metal. It is thought the difference in extension is potentially due to the extra material that is deposited in the weld that could resist the necking that normally occurs in the centre of the work piece.

5.4 Hand calculation for four-point bending tests

Before starting four-point bending fatigue tests it is essential to carry out hand calculations to find out the maximum stress and deflection experienced in the sample. This type of calculation helps ensure correct data is fed into the fatigue testing machine as well as to determine the appropriate dimensions for loading frame. Physical testing may involve measuring time, load, stresses and deflection derived from material testing machine data.

By considering a simple four-point bending beam being loaded as shown in Figure 5.3, the maximum stress in this beam is at the point where the bending moment is greatest i.e. at the middle point under the applied load. The equation for this maximum stress is given by the equation (3) shown below, where M represents the applied moment, F represents applied load, y represents half the thickness, I is the second moment of area and δ represents the deflection (Dupen 2015).

$$M = \frac{L}{4} \times \frac{F}{2} = \frac{FL}{8} \quad \dots\dots\dots (1)$$

The second moment of area for a rectangular beam is given by equation (2).

$$I = \frac{b \times d^3}{12} \quad \dots\dots\dots (2)$$

Where, b is beam width and d is beam thickness.

$$\sigma_{MAX} = \frac{M \times y}{I} \quad \dots\dots\dots (3)$$

Inserting equations 1 and 2 into the equation 3 gives:

$$F = \frac{4bd^2}{3L} \sigma \quad \dots\dots\dots (4)$$

According to (ASTM-E855 2002) the modulus of elasticity for four points bending is obtained as follows:

$$E = \frac{Fa(3L^2 - 4a^2)}{4bd^3\delta} \quad \dots\dots\dots (5)$$

By simplifying equation 5 and substituting $a=L/4$ for the current case the deflection can be obtained as:

$$\delta = \frac{11FL^3}{64bEd^3} \dots\dots\dots (6)$$

Inserting equation 4 into the equation 6 gives:

$$\delta = 0.22916 \frac{L^2}{Ed} \sigma \dots\dots\dots (7)$$

In the current work four-point bending specimens with a total length of 135mm, made of rectangular section with dimensions of b =25 mm, d=2.78mm were used, and the distance between the lower supports L was calculated from Equation (7) by considering the maximum deflection is 1 mm and ultimate stress 600Mpa. These values were determined in order to minimise plastic deformation. The distance between the lower supports was calculated to be 64mm and this greater than 10 times specimen thickness, as required by ASTM E855.

5.5 Fatigue performance of FB590

The tensile fatigue testing was completed on a Servocon machine at Cardiff University. The Servocon has a maximum permissible load of 100kN, whereas the maximum load used as part of this project stood at around one third of that value. Given the large number of tests (more than 160 specimens) and the desire to identify the endurance limit of the material (resulting in tests taking more than 12 days to complete), the overall tensile fatigue testing programme took a considerable amount of time and effort to complete. The bending specimens were tested using a Dartec 20 and 5 kN dynamic testing machine due to the availability of the testing machine at the time of the testing. Some of the challenges encountered along the way included failure of a 20mm pin as well as failure from weld of base grip holder as can be seen in Figure 5.4.

5.6 Metallurgy test of MIG Welds of FB590

In order to show full microstructure visualization of welded specimen, a cross section was taken across the full width of the welded sample to include the parent material, heat affected zone, and the weld bead itself. The microstructure of the base material shown in Figure 5.5 is fairly uniform throughout, where the mean

grain size is around 2.6 microns. The Heat Affected Zone (HAZ) can be found immediately to either side of the welded filler material and shows a microstructure similar to the base material prior to welding; suggesting minimal damage was inflicted to the material from the large amount of heat applied during welding as stated in Figure 5.6. This is especially true of MIG welds, where the HAZ was relatively small (Bright 2012). The microstructures found in the HAZ were a mix of ferrite/ bainite, identical to the base metal. The only difference was the slightly less consistent grain size, where more variation existed to the mean 2.6 micron grains found in the base material.

Even though similar consumables (AristoRod 13.26) were used for this welding method, in terms of chemical and mechanical properties, the microstructures of weld were shown to be significantly different from other areas as shown in Figure 5.7. Figure 5.8 shows the transition line from weld material to HAZ. The MIG weld has a very irregular pattern of large and smaller grains of ferrite, along with bainite and martensite. MIG welds include numerous forms of ferrite; these include fine grains of acicular ferrite, as well as inconsistent patterns of large and small ferrite grains, widmanstatten ferrite. These observations are consistent with those of Nayak et al. (2012) and Hu et al. (2014).

5.7 Micro hardness measurements

Figure 5.9 shows the overall cross-sectional views of both weld and base metals. To evaluate the effects of heating and cooling during the welding cycle on the properties of the welds; micro hardness profiles were measured across them. A hardness profile was taken across the FB590 weld specimen with an indent interval of 0.2 mm, and extended into the parent material as shown in Figure 5.9. The hardness of the specimens was measured using a Zwick microhardness testing machine, shown in Figure 5.10. The hardness test was performed using a diamond indenter with a 200-g load and approximately 15 seconds dwell time. The two diagonals of the indentation left in the surface of the material after removal of the load were measured using a POLYVAR optical microscope with an objective lens of 20x as illustrated in Figure 5.11.

The results are presented in graphical form as shown in Figure 5.12. The average hardness value measured for the as-received FB590 steel plates (200 HV), and the fusion zone (FZ) hardness was observed to be somewhat higher for the welding process examined in this work, which can be related to the increase of the harder martensite phase. The difference in the hardness of the FZ relative to that of the as received FB590 steel indicates an evolution in the metallurgical phase constituents. The highest FZ hardness that was observed for the MIG weld is 306 HV, this could result from the formation of a multi-phase microstructure which consists of acicular ferrite, bainite and martensite, as explained previously in Figure 5.7. This is suggested on the basis of the relatively high cooling rate promoting the formation of bainite and martensite (Nayak et al. 2012). In addition, the filler material contains relatively high amounts of manganese, which additionally contributes to increased toughness of the weld and which in turn increases the hardness (Tušek et al. 2001). In general, the increase in hardness results in increased strength whilst decreasing formability or ductility. Some measurement points were discarded due to being located on scratches as shown Figure 5.13.

5.8 Acoustic Emission for FB590 fatigue tests

This section focus on the characterization of FB590 fatigue damage in welded plates using AE and DIC and utilizes the developed procedure of monitoring fatigue testing of mild steel using DIC and AE systems to identify crack initiation and other mechanisms taking place during final failure. AE is a non-destructive testing technique which has been previously used to identify the nature of damage such as tensile cracks and shear movements within a structure (Aggelis 2011) and (Elfergani et al. 2013). DIC, a full field strain measurement technique, was also used to provide a clear depiction of the surface strain field evolution.

The fracture mode of cracking in thin plates normally changes from a tensile mode to a shear mode close to failure. In the presented work, the AE parameters of amplitude, rise time and average frequency were used with RA (ratio of rise time to amplitude of the waveforms) to classify the damage. The behaviour of the RA value which describes the shape of the first part of the AE signal has been used for

characterization of the cracking mode. This was confirmed by visual observation of the crack geometry after the experiment and the DIC measurements. The method described indicates the type of damage and enables a warning against final failure and hence the safety conditions and integrity of the structures due to the loading process.

This investigation considers the use of the RA value for damage identification and classification. This method has been extensively utilised for numerous AE applications in concrete but there has been little research into the relationship between tensile and shear movement or into the classification of damage of metal plates. In Chapter 2 there are further details regarding the RA value. AE results were correlated with the strain field measured using DIC, giving valuable insight into possible mechanisms of damage and AE generation.

5.8.1 Results and Acoustic Emission analysis

The response of the nano 30 sensor to a H-N source was above 98 dB demonstrating that both sensors were mounted correctly as explained in Section 3.6. In order to remove AE noise data related to surface rubbing at the pins, environmental noise and other unknown sources generated outside the test specimens, as well as to ensure that only the signals released from the fatigue crack growth were used for analysis, all data files were filtered by location around the crack, using only data between the AE sensors and discarding other data.

Figure 5.14 shows the failed test specimen; Figure 5.15 shows a photograph of the fracture surface after the end of the experiment. The crack propagates horizontally, creating a straight fracture surface (SFS) for an additional 2-3mm away from the one edge. Later, the fracture surface becomes curved. This is attributed to the local plane stress field due to the small thickness of the plate. Therefore, although the crack starts to propagate horizontally, under the application of the tensile stress final fracture occurs due to the shear stresses, which are at 45°.

Figure 5.16 shows cumulative AE energy compared with crack mouth opening displacement (CMOD) as a function of time. As is typically expected in metal

fatigue, the rate increases exponentially with the final failure of the specimen occurred at 33444 cycles.

Analysis was carried out on the AE signals detected during the whole fatigue test as shown in Figure 5.17. The detected amplitude is attributed to a number of sources such as corrosion product, microcracking, macrocracking, crack propagation, and separation of the e-coating layer and DIC paint from the specimen surface. From Figure 5.17, three zones have been highlighted; these zones are highlighted based on visual inspection of the specimen and its fracture surface, DIC measurements and previous investigations.

The high amplitude at early stage of the test in **zone 1** is attributed to the signals released due to stretching and loading of the specimen. The following highlighted zone is **zone 2** which could correspond to various mechanisms such as flaking in the e-coating layer or DIC paint near to the weld due to high stress concentrations at this area (weld toe) and the difference between the modulus of elasticity of the specimen, e-coating layer and DIC paint as shown in Figure 5.18. In addition, the DIC visualization shown in Figure 5.19 shows the difference in z displacement between two points on the weld metal and the base metal. As the specimen stretches due to the loading, the delamination of e-coating at the weld area starts to initiate and this increases with loading cycles. This increase then leads to movement of both the e-coating layer and DIC paint causing a surface crack to form in both of them. This is obvious from visual inspection for both specimen's faces (rear and front face). Flaking occurred in the e-coating layer on the rear side which is on the face not monitored by the DIC system Figure 5.18b.

The last highest amplitudes located in **zone 3** correspond to a combination of macrocrack propagation and shift of the cracking mode from tensile to shear as it clear from the fracture surface Figure 5.15. At this time the CMOD reading suddenly increased to it is maximum value.

In order to gain a more in-depth understanding of the features of AE signals from the fatigue crack growth mechanism, the located AE events were further investigated. In order to explain the transition between different cracking modes the RA value may be considered, which also takes into account the signals'

amplitude (Rilem, 2009). The sequence of the cracking modes within a typical fatigue specimen of this kind. This cracking mode sequence may well be one reason behind the shifting behavior of the AE parameters.

The three zones have been also chosen as examples to distinguish between the crack stages, and to classify mode types. Figure 5.20 a–c shows the AF vs. RA values for different periods of the test.

Figure 5.20 a shows the AF vs. RA for zone 1 (associated with the specimen being stretched and could be also from plastic deformation). It can be seen that the most of data points have various AF and low RA value (less than 2 ms/v). Therefore, this indicates that the type of the signal is associated with tensile damage (Aggelis 2011) and (Elfergani et al. 2013). It can be noted from Figure 5.20 b that in this area the RA value has a wide distribution (RA values 0–15 ms/v and AF values 0–50). This is attributed to delamination in e-coating layer and DIC paint, possibly due to macrocrack formation, which leads to material volume increase thereby expansion and cracking for the outer layer of e-coating and DIC paint.

The Figure 5.20 c shows the relationship between RA value and AF associated with the crack region in the last stage of the test in which the transition between different cracking modes occurs from a straight fracture surface to a curved surface shape. Therefore, this indicates that the crack type is mixed between two modes; tensile cracking and shear mode movement during the final cycles of the test, consistent with the findings of (Elfergani et al. 2013) and (Aggelis 2011).

Figure 5.20 shows different mechanisms related to different RA/AF value, the zone 3 is a mixed mode area of both tensile and shear movement whilst zone 1 is purely tensile and zone 2 is almost purely shear. It has been shown that by using AE and the relationship between RA and AF value, the crack area can be located and identified. The small specimen size and the sensitivity of the sensors enables the capturing of these changes accurately as the crack develops (Aggelis et al. 2011). Hence, it could be possible to provide a failure alarm and location to the structure prior to any significant deformation. Furthermore, by knowing the crack type it is possible to identify its severity level, and therefore it is possible to identify

whether maintenance is needed. This issue has great demand and is vital to maintain the structure both for safety and economic considerations.

The AE behavior is repeatable for other specimens tested in this experimental series. Figure 5.21 shows the cumulative AE energy and RA value for three interesting zones for another welded specimen. In this case the AE rate remains constant as well, while the other shape parameters exhibit the same behaviour trend. The specimen failed at 38724 cycles, while the parameters undergo an increase from about 35147 cycles.

The above results imply that for a similar experimental procedure (material, specimen geometry, fatigue parameters) when RA exhibits a sharp increase this would indicate a remaining life of approximately less than 2000 cycles. This results are consistent with (Aggelis et al. 2011) although the author applied this technique using different material and specimen design.

5.9 Conclusions

The work presented in this chapter followed two main sections of research. The first section focussed on the material properties of FB590 and the specimens preparation in order to provide S-N curves data for tensile and bending loading, for both welded and unwelded specimens. The second part addressed the monitoring of the fatigue test using AE and DIC techniques. The AE analysis was successfully used to determine crack movements and classify it in accordance with the observations made during fatigue testing. The AE method can not only detect the e-coating layer and DIC paint cracking but evidence of the fatigue process can be observed. Therefore this technique was successfully used to assess the damage of high strength steel samples, where it was shown that microcracks and crack propagation could be detected. The correlation of AE parameters with damage accumulation and the fracture mode has been used to evaluate differing crack types. The results have demonstrated that the AE technique is valid in monitoring and hence the potential for monitoring real structures under test such as automobile chassis structures. Thereby the results offer encouragement to the use of the AE

technique to detect the remaining life in fatigue test and also enables a warning against final failure.

Table 5.1: welding consumable data.

Welding Consumable	Chemical Composition (Typical - Wt%)				
	C	Si	Mn	Ni	S
ESAB Aristorod 13.26 Ø1.2mm	0.095	0.8	1.40	0.8	0.025

Welding Consumable	Mechanical Properties (As-welded argon shielded)		
	Yield stress R _e (MPa)	Tensile strength R _m (MPa)	Elongation A (%)
ESAB Aristorod 13.26 Ø1.2mm	540	625	26

Welding Consumable	Welding parameters (As-welded argon shielded)			
	Arc voltage, V	Welding current, A	Wire feed, m/min	Deposition rate kg weld metal/hour
ESAB Aristorod 13.26 Ø1.2mm	20-33	120-350	2,7-12,4	1,5-6,6

Table 5.2: chemical composition of FB590 plate as received from TATA steel.

FB590 Chemical Composition (Typical - Wt%)						
C	Si	Mn	Ni	S	Ti	V
0.074	0.176	1.31	0.0044	0.0018	0.014	0.002

Table 5.3: mechanical properties of FB590 unwelded plate.

Ident . Mark	Width mm	Thicknes s mm	Area mm ²	0.2% Proof.	Ultimate	Elongation		Elastic Modulus kN/mm ²
				Stress N/mm. ²	Stress N/mm. ²	mm.	%	
1	9.96	2.69	26.79	480	590.51	-	-	208.0
2	9.99	2.66	26.79	474.8	592.38	12.23	24.5	195.2
3	9.96	2.67	26.79	482.3	589.15	10.35	20.2	208.2
Average				479	590.68		22.3	203.8

Table 5.4: mechanical properties of welded FB590 plate.

Ident. Mark	Width mm	Thickn ess mm	Area mm.2	0.2% Proof.	Ultimate	Elongation		Elastic Modulus kN/mm2
				Stress N/mm.2	Stress N/mm.2	mm.	%	
1	9.98	2.7	26.95	525.0	602.2	-	-	185.4
2	9.98	2.7	26.95	525.42	603.7	-	-	212.3
3	9.99	2.7	26.95	539.87	604.1	-	-	196.0
Average				530.1	603.3			197.9

Table 5.5: TATA steel measurements for longitudinal direction.

Ident. Mark	Width mm	Thickness mm	Area mm.2	0.2% Proof.	Ultimate	Elongation	Elastic Modulus kN/mm2
				Stress N/mm.2	Stress N/mm.2	%	
1	19.32	2.678	51.73896	495.62	617.6	21.13	155.2
2	19.313	2.696	52.06785	492.43	616.4	18.72	167.3
3	19.313	2.738	52.87899	489.49	608.98	19.79	169.2
4	19.321	2.746	53.05547	488.71	603.67	20.95	139
5	19.351	2.748	53.17655	483.79	605.18	22.13	171.9
6	19.365	2.755	53.35058	483.23	599.3	20.26	155.1
7	19.37	2.682	51.95034	489.94	612.76	19.18	166.8
8	19.382	2.656	51.47859	492.92	6013.41	20.01	155.5
Average				489.51	609.66	20.27	160

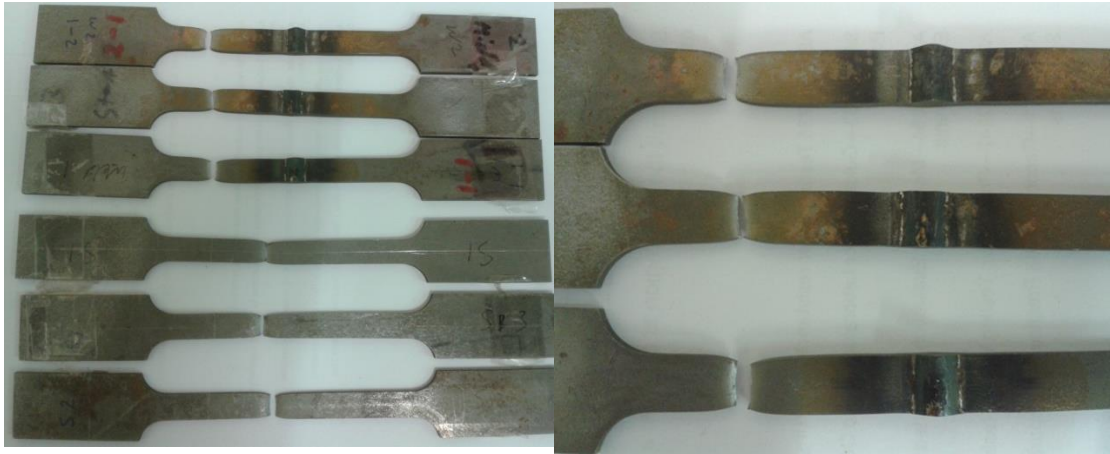


Figure 5.1: (a) Failed un-welded and welded tensile specimens after test (b) welded specimens failed in base metal region.

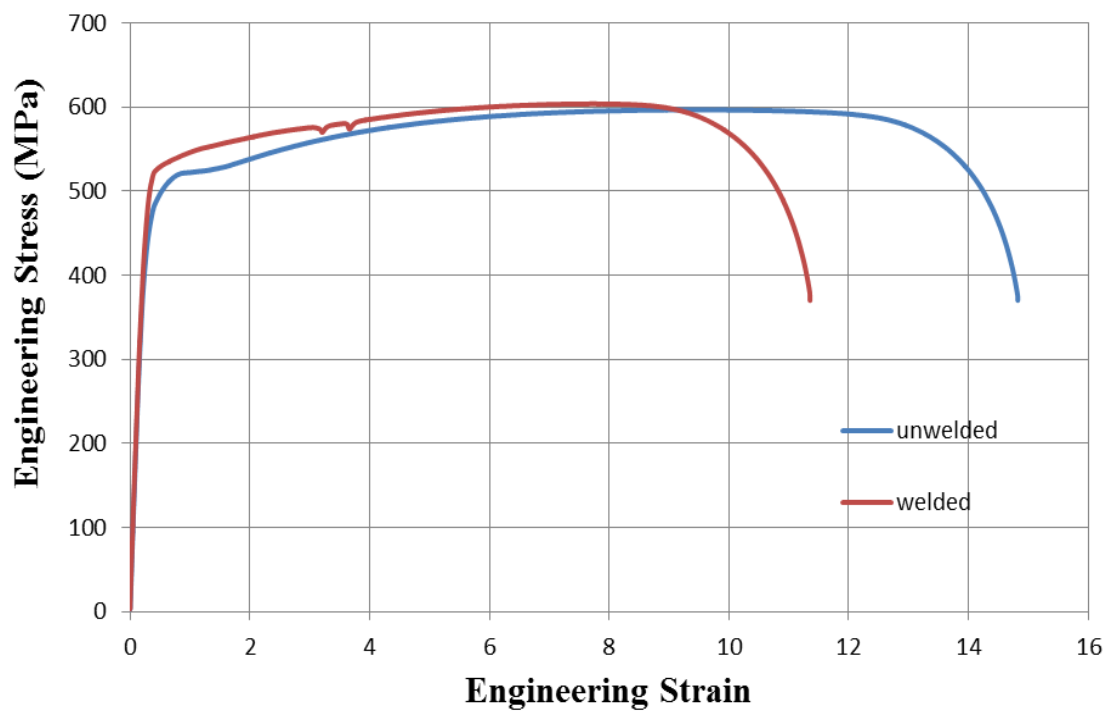


Figure 5.2: Tensile performance of MIG welded FB590.

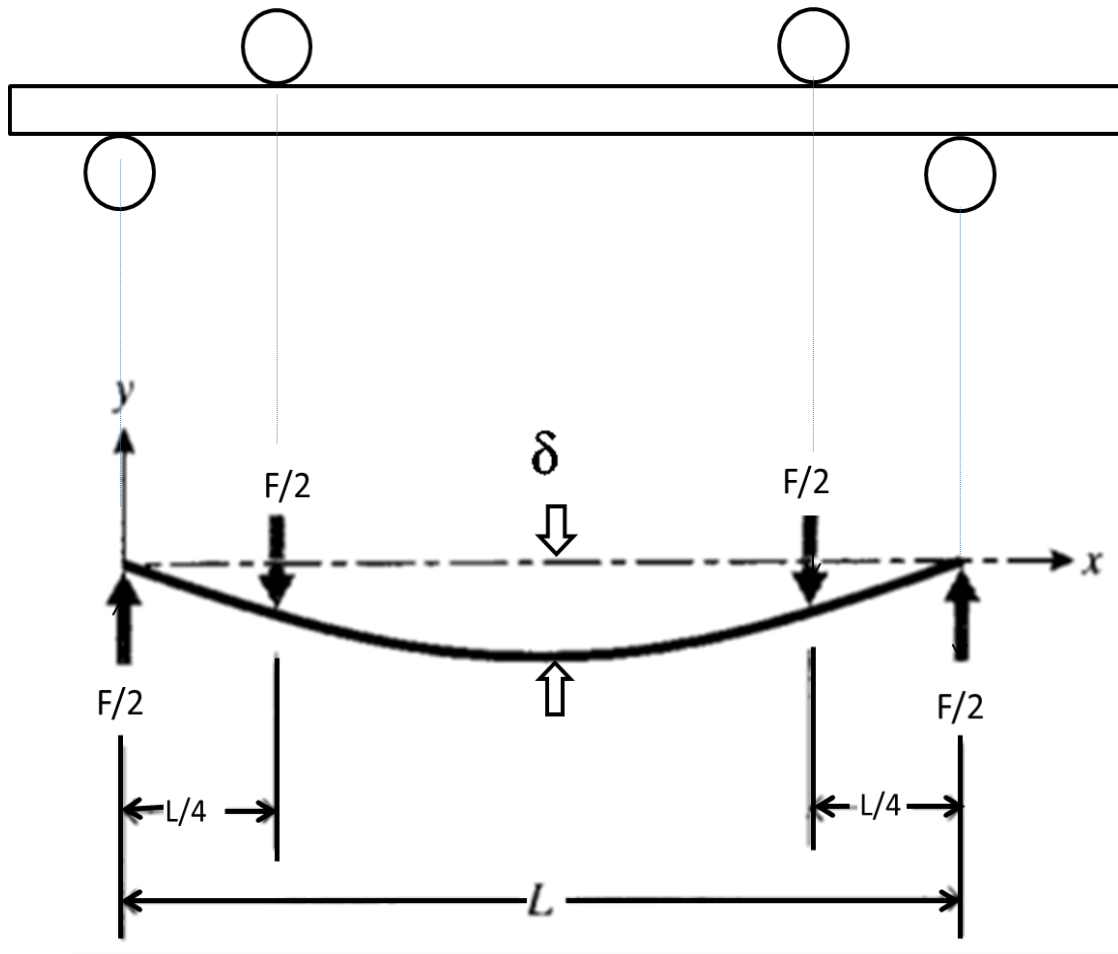


Figure 5.3: Four points bending.



Figure 5.4: Failed connection pins and weld of base grip holder.

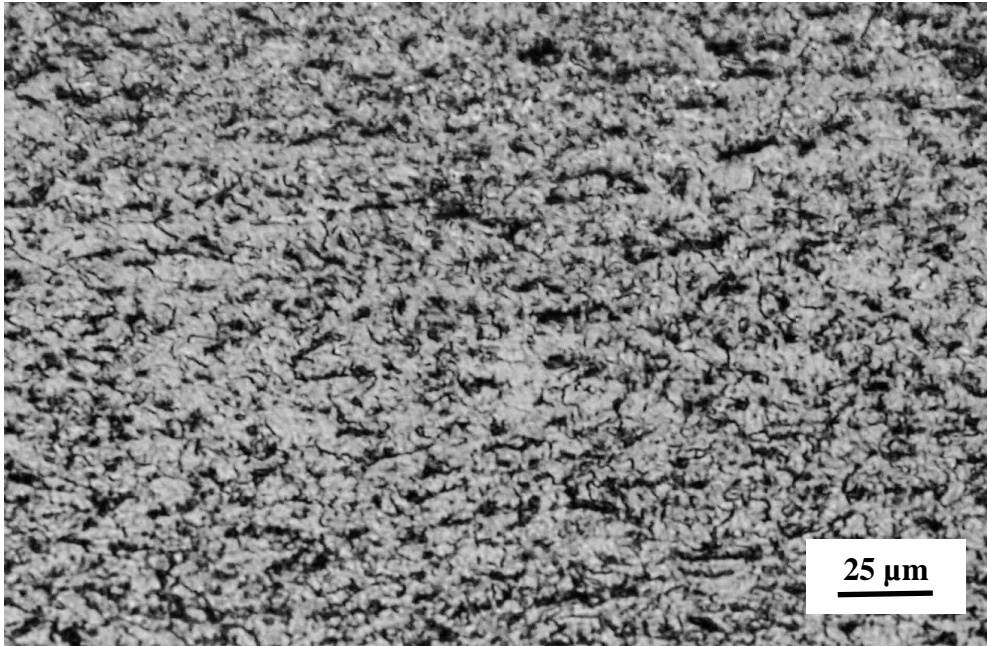


Figure 5.5: Base material micrograph (FB590).

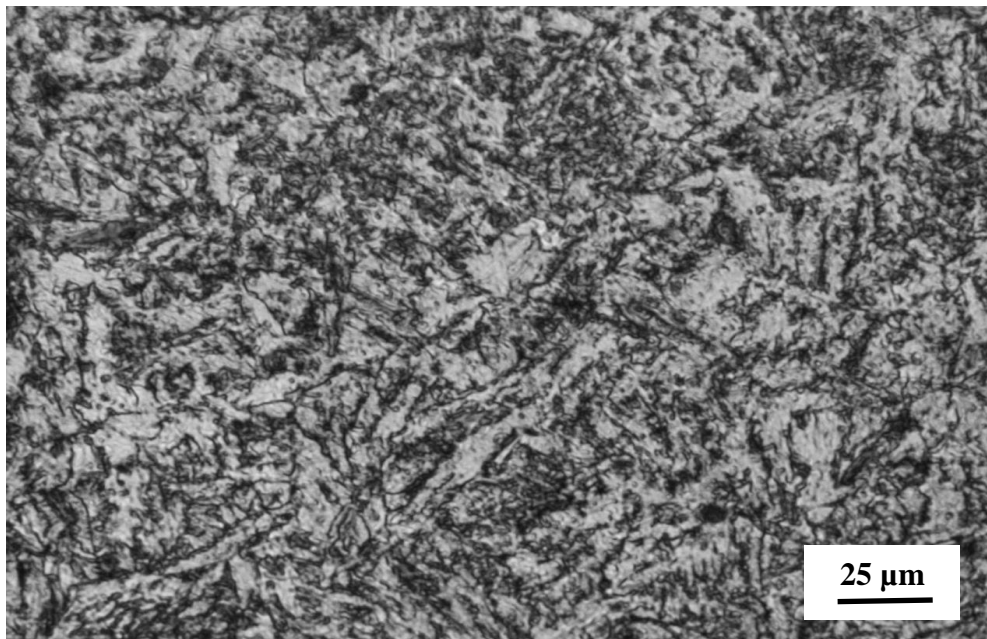


Figure 5.6: HAZ material micrograph (FB590).

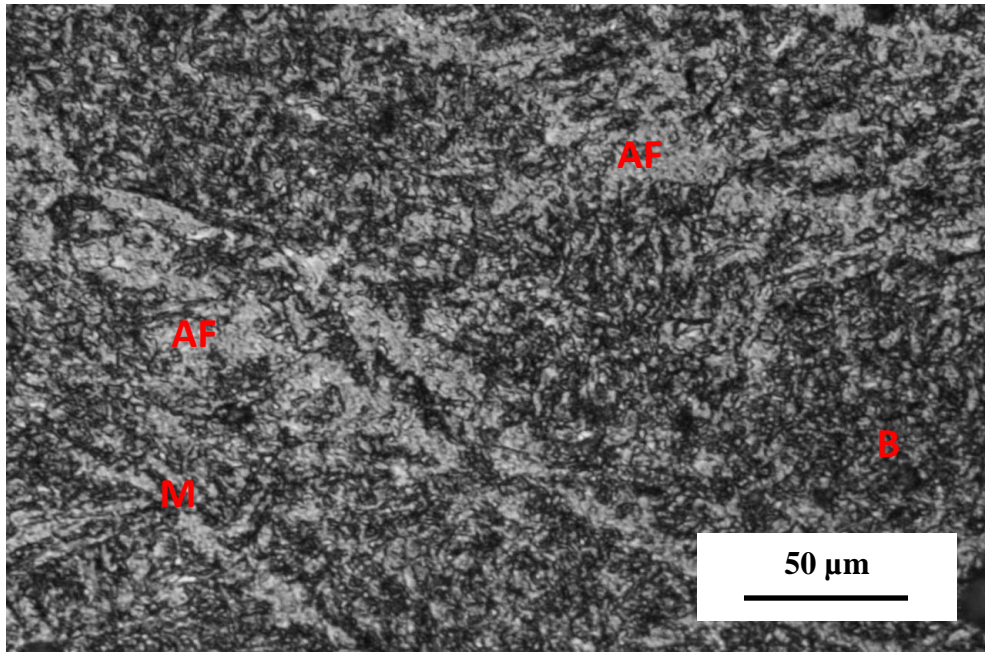


Figure 5.7: MIG weld material micrograph (FB590) AF: Acicular Ferrite , B :Bainite M: martensite.

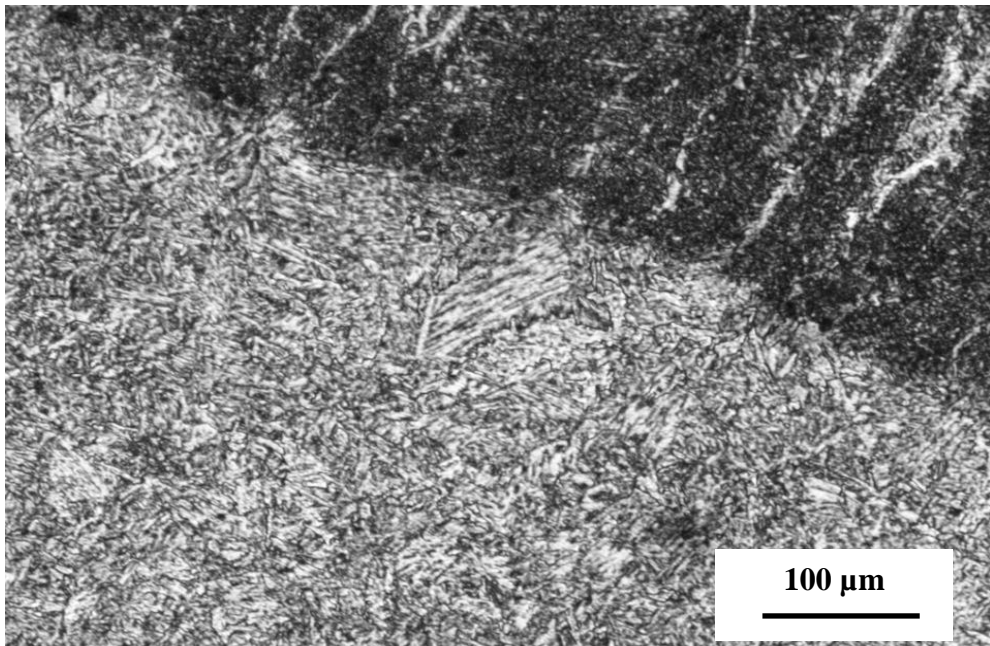


Figure 5.8 : show transient line from weld material to HAZ (FB590).

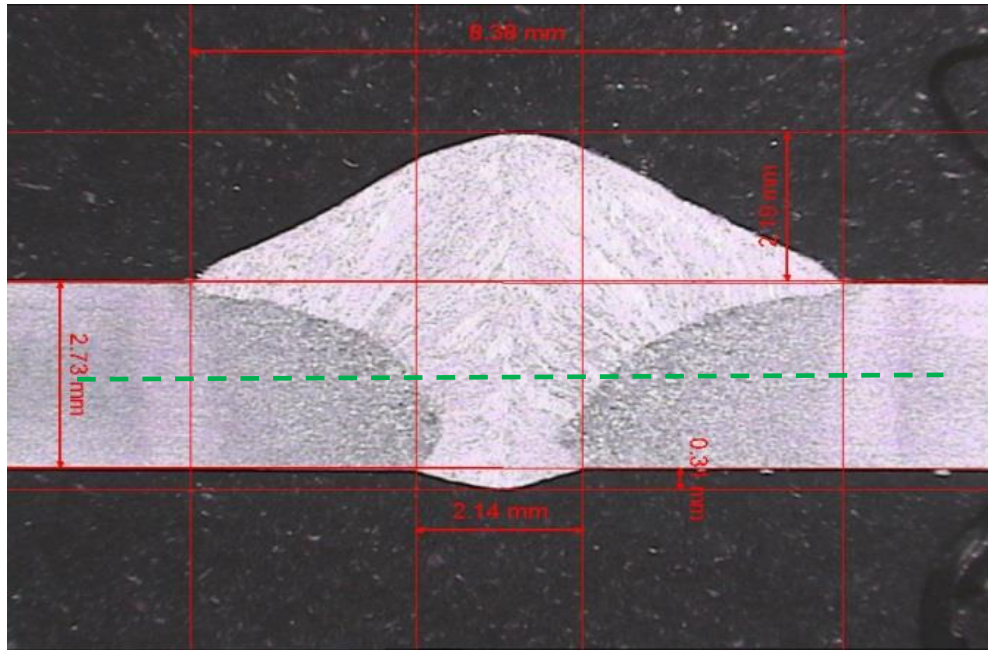


Figure 5.9 : selected spots on the top surface of the specimen.



Figure 5.10: photograph Micro hardness tester.

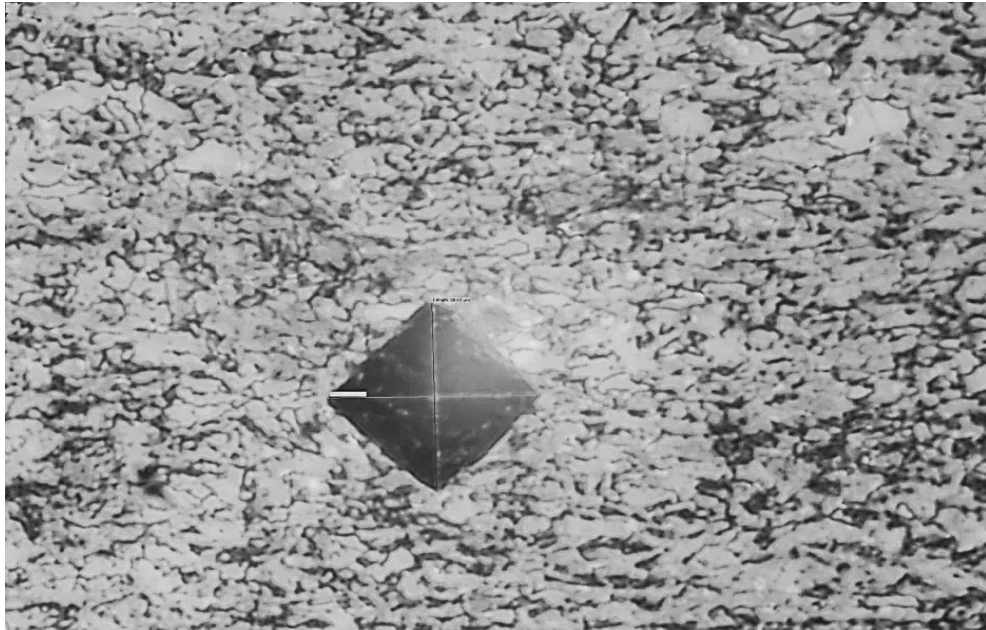


Figure 5.11: The two diagonals of the indentation.

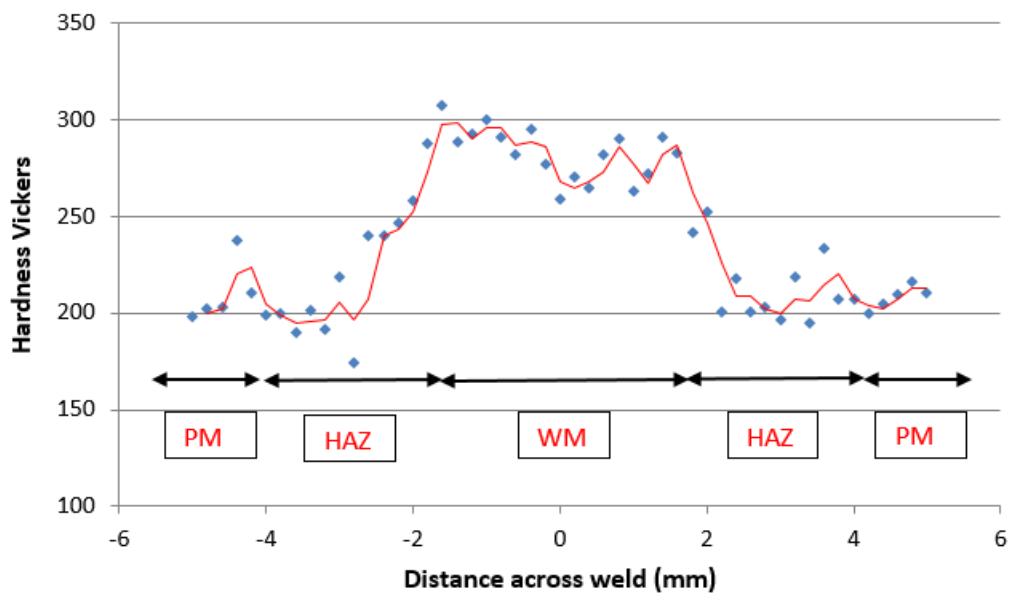


Figure 5.12: Hardness measurements every 0.2mm.

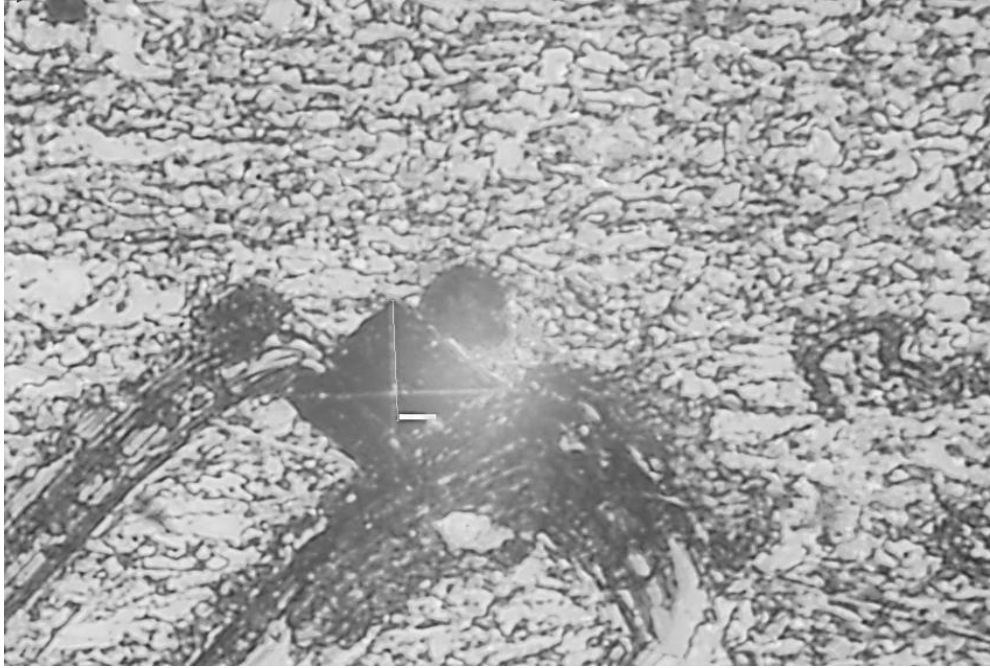


Figure 5.13: Shows the points were discarded.

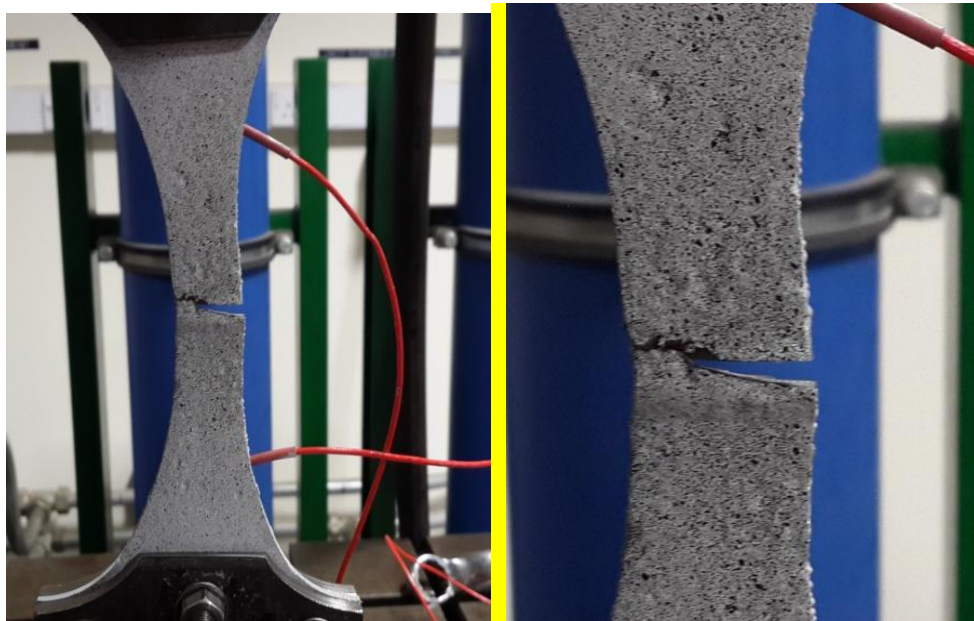


Figure 5.14: Photo of failed test specimen.



Figure 5.15: Part of the specimen after fatigue failure, plane stress fracture.

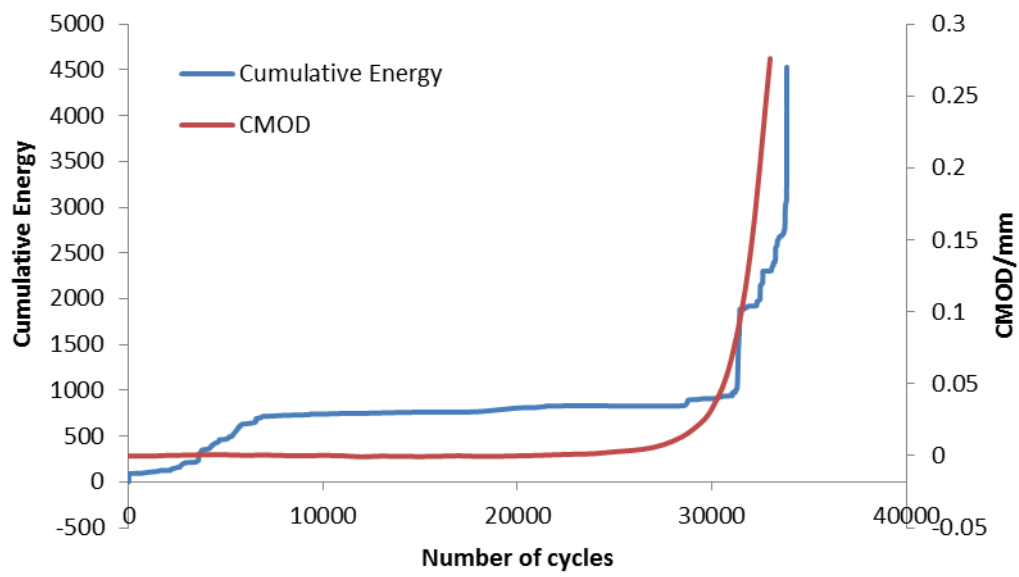


Figure 5.16: Trend of event rate for fatigue test and CMOD.

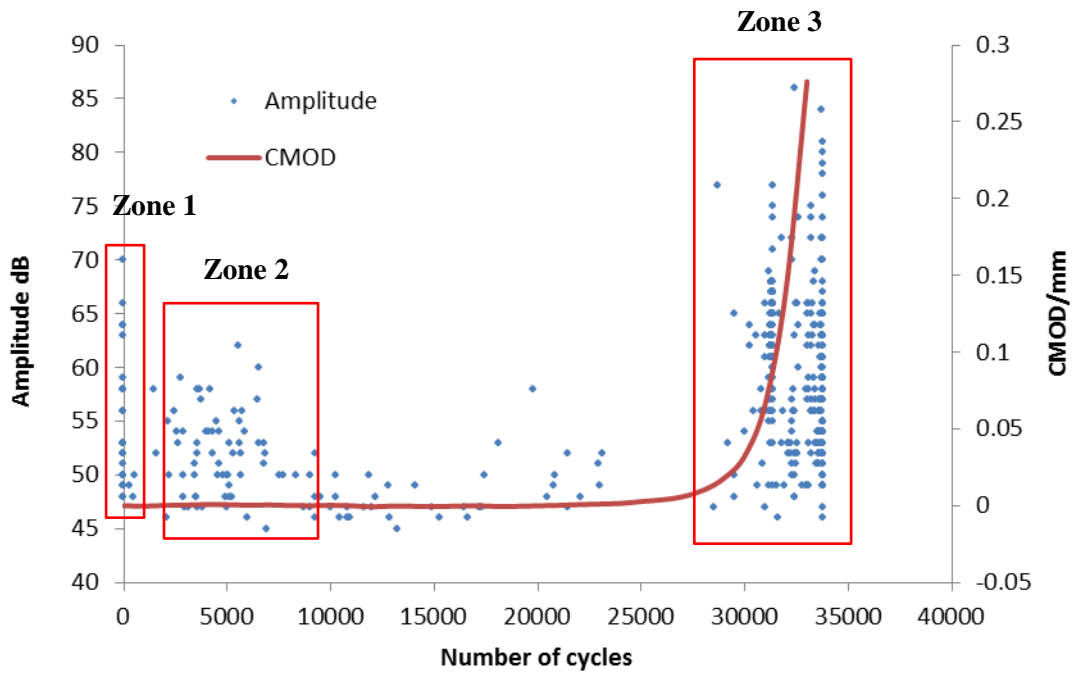


Figure 5.17: Amplitude of detected signals for duration of investigation.

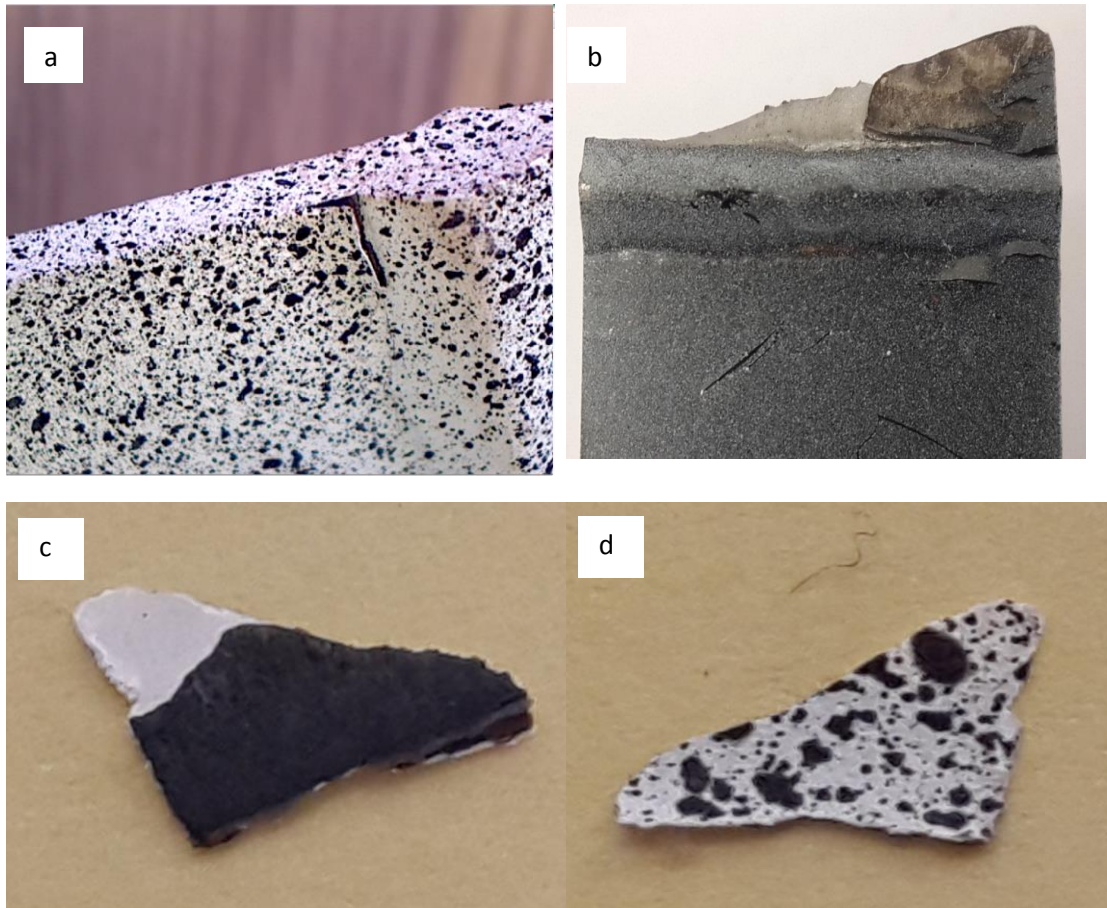


Figure 5.18: specimen after fracture (a) front side (b) rear side which is opposite side to DIC cameras (c,d) reveals the flake in the ecoating layer and DIC paint.

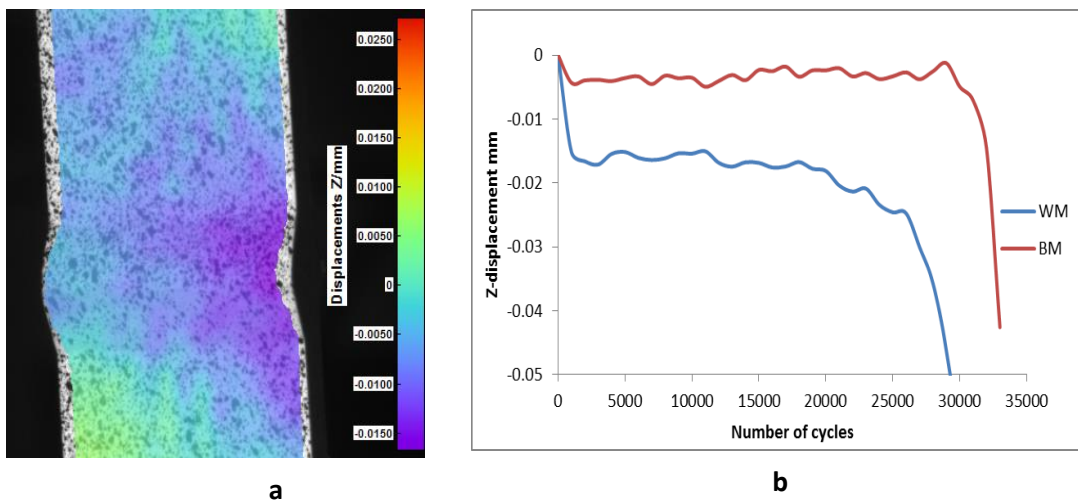


Figure 5.19: (a) reveals the flake in the DIC paint (b) Out of plane displacement for base metal and weld surface.

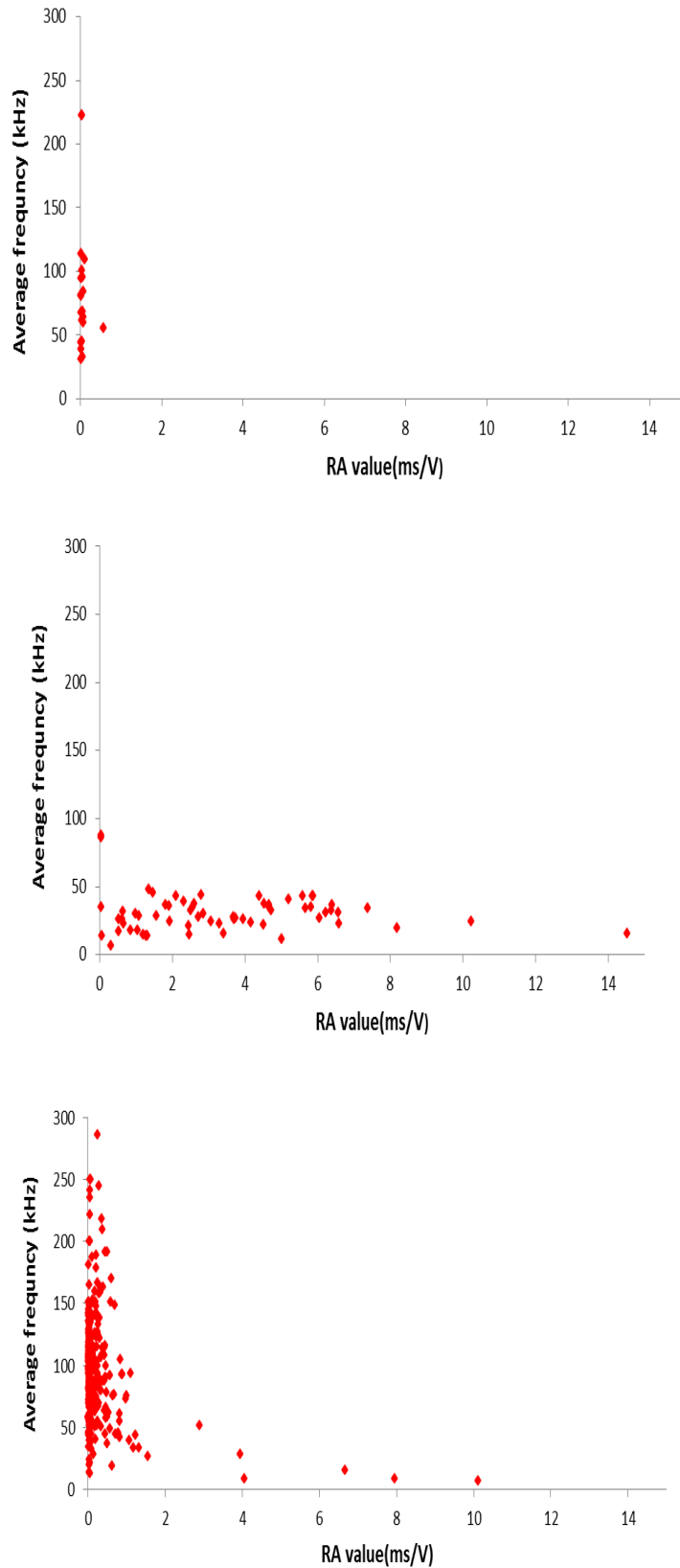


Figure 5.20: Relation between the RA value and average frequency of (a) zone 1, (b) zone 2 and (c) zone 3.

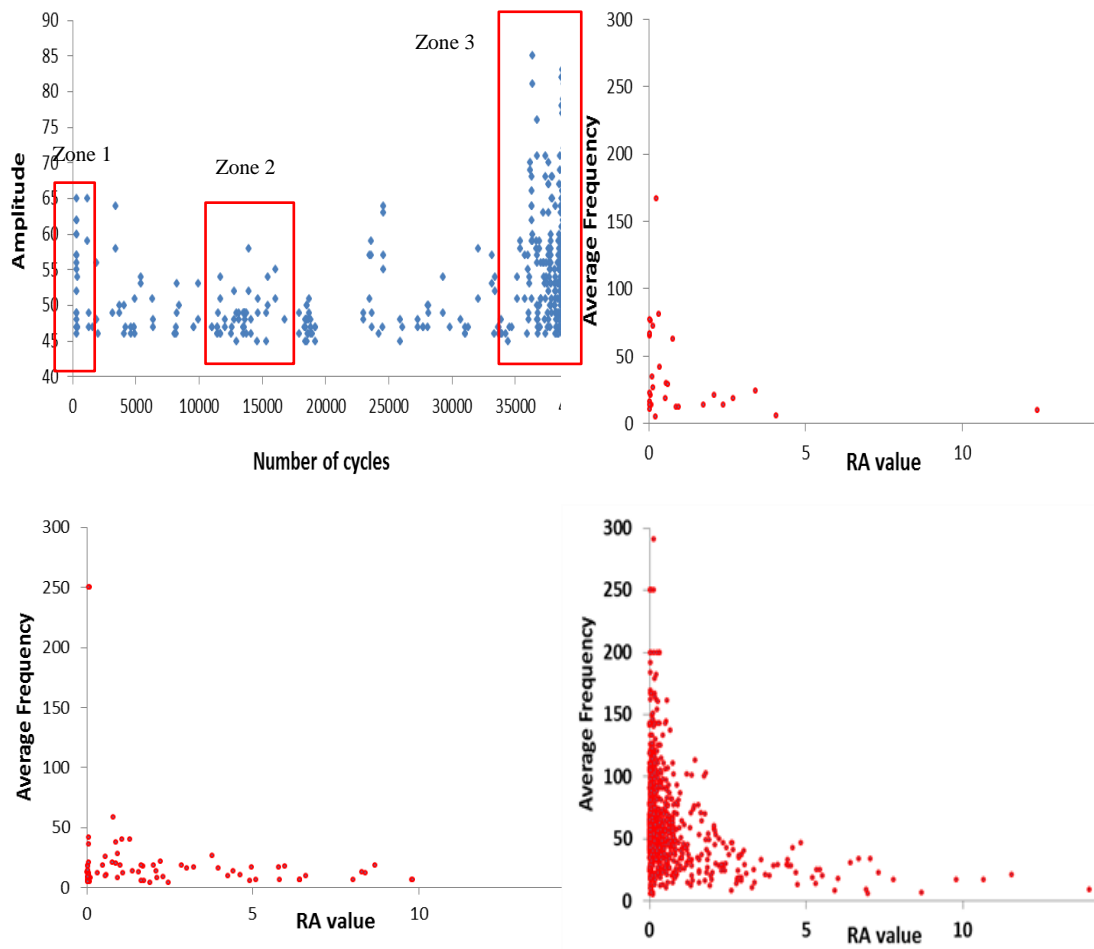


Figure 5.21: (a) Amplitude of detected signals for duration of investigation and relation between the RA value and average frequency of (a) zone 1, (b) zone 2 and (c) zone 3.

6. Fatigue properties of FB590

6.1 Introduction

The main aim of this chapter is to show the behaviour of the FB590 steel grade under various loading and environmental conditions which are typically encountered in the chassis in practical use. This behaviour is important for automotive engineers in order to be able to predict the performance of chassis components under a range of various loading and environmental conditions. The fatigue properties of this grade are unavailable in the TSSP-UK brochure and therefore it is essential to carry out these experiments in order to determine fatigue performance properties under various environmental conditions which can be obtained for use by design engineers. Finally, the failure mechanisms of each surface treatment were also investigated by using SEM.

6.2 Evaluation of surface quality

As explained in Section 4.3, the measurement of the surface roughness and corrosion depth were performed after completing the corrosion process. The current study is performed as a first step towards quantitatively investigating the effects of corrosion on the fatigue behaviour of steel plate based on the 2D and 3D surface profiles. In this work, stereo optical microscope and 3D surface profile measurements were first conducted to obtain the distributions and characterizations of pitting corrosion, including 3D surface roughness and topography. Assessment of corrosion showed large variations in surface roughness of corroded steel specimens. The test results for all cases are presented in the following sections.

Surface assessment of as received and Ecoated samples

The surface morphology of as-received and ecoated samples are clearly shown in Figures 6.1 and 6.2 respectively. It appeared that surface of the ecoated specimens became finer than the as received surface. The surfaces were examined with a stylus profilometer, an array of profiles were measured using a y-stage to ensure that a three-dimension representative are of the specimen was measured; the three

dimensional measurements are shown in Figures 6.1(c) and 6.2(c), as presented in the TalyMap analysis software.

Surface assessment of stone chipping specimens Group 2

The specimens of Group 2 were exposed to stone chipping following ecoating according to the procedure explained in section 3.11. Indeed, most of the stone chipping effect was found on the gauge length, with the stone chipping marks visible in the specimen's surfaces as shown in Figure 6.3. It appeared that large flaws due to stone chipping effect were present and the surface became rougher than surface of the specimens which had been ecoated only (Group 1).

Surface assessment of Group 3 and 4

The specimens of Group 3 and 4 were exposed in the salt spray cabinet for two and four months respectively after previous ecoating and exposure to stone chipping. Two types of surface morphology can be observed with corrosion time lapse on the surface of specimens. Most of the corrosion product was found on the gauge length, which is where the salt solution had collected during the exposure, as the specimens were inclined at 30 degrees in the salt spray cabinet. The amount of corrosion product observed on the specimens was found to increase with the exposure period. Figures 6.4 and 6.5 show corroded specimen's surface, 2D profile and 3D image of Group 3 and 4 respectively. It can be noted that in all cases in Group 3 the profiles were taken using a standard stylus profilometer made by Taylor-Hobson, whereas in Group 4 there were some difficulties in measuring surface topography since the corrosion depth was larger than profilometer gauge range, entailing the use of another stylus and gauge with larger range. However, for the purposes of this work, the results are comparable.

Surface assessment of Group 5

In this case the specimens were exposed in the salt spray cabinet for four months without previously being exposed to stone chipping. The corrosion product ran in marks along the specimen edges, the damage in the corroded areas occupied a strip area of approximately 2-4 mm along the specimen edges with both deeper and shallow corroded areas towards the edges. The centre of the specimen was nearly pristine, there were no corrosion marks visible in the middle of the specimen,

clearly showing that the metal was attacked from the cut edges, as illustrated in Figure 6.6.

Measuring surface roughness parameters

Three dimensional measurements were performed to measure surface roughness parameters of fatigue specimens. All the data were collected and analyzed to calculate conventional roughness parameters for the exposed faces of the specimens such as (S_a), (S_q), (S_z), and (S_t). These data were plotted using histograms, Figure 6.7 illustrates a full surface parameters analysis with error bar representation $\pm 3S.D$, was calculated across each group. Analysis of profilometry results shows that with increasing corrosion, roughness parameter values also increased, roughness of the surface increases as a function of exposure time and this is consistent with the observations of Pidaparti and Patel (2008), Pidaparti and Rao (2008) and Xu and Qiu (2013). By considering the skewness of the surface, R_{sk} , a more pronounced difference can be seen as the run surface is significantly negatively skewed (surface with deep and narrow pits) as a result of highly deforming due to the corrosion (Deleanu et al. 2012; Xu and Shan-hua 2015).

6.3 Surface assessment description

The fatigue specimens were pre-corroded following the method described in Section 3.12. The corrosive attack can produce a network of corrosion pits on the metal surface. The typical appearance of the specimens before and after removing the loose corrosion product is shown in Figure 6.8. The specimens after corrosion was cleaned using a plastic brush to remove loose rust from the corroded specimens without causing any further damage that could potentially affect the fatigue results. Before fatigue testing, the surface of all the specimens was measured using a profilometer, in order to obtain the surface characteristics of the specimens, as well as the maximum and average depth of the corrosion sites. There are various types of corrosion conditions in steel specimens and it can be seen that the corrosion damage can take place in many shapes and forms, however it is important to categorize these different corrosion conditions for better understanding of their effect on fatigue strength.

The upper surface (as installed in the salt spray cabinet) was more exposed to salt solution, whilst the lower surface was less exposed as the specimens were inclined at 30 degrees in the salt spray cabinet. The number of active corrosion sites recorded was much lower than on the upper surface. Therefore the upper surface was considered in measurements of corrosion depth and surface roughness. The unaffected regions of the ecoated surfaces were considered as a reference surface adjacent to each area of corrosion on the specimen as shown in Figure 6.9(a). The area located near the reference surface was examined with the profilometer and stereo optical microscope, as illustrated in Figure 6.9(b). It appeared from optical microscope and visual inspection that the pits were underneath the corrosion product, in addition to corrosion pits, larger flaws due to uniform corrosion were present on the specimen's surfaces, which clearly shows the metal was superficially attacked as well as the cut edges attacking. The damage in the corroded areas occupied the whole area of the gauge length with an arbitrary distribution of deeper and shallow corroded areas. Moreover, small corrosion flaws were also developed independently on the samples at sites remote from the gauge length. These damages originated at sites where the salt solution had penetrated beneath the stone chipping sites as clearly shown in Figure 6.9(a), the stone chipping marks were still visible in the corroded area for Groups 3 and 4.

In the initial stage of corrosion, severe corrosion happened only on some particular locations on the surface of corroded specimens, because the specimens were prepared to initiate pitting corrosion in the gauge length of the specimen. However, with the progress of corrosion time, the corrosion damage which took place on the surface of corroded specimens tends to be uniform due to neighbouring pits coalescing to form the general corrosion and this is consistent with Jones et al.(2008) and Xu and Qiu (2015). Therefore; several areas of damage due to general corrosion were present on the specimen surface as well as irregular corrosion flaws which were detected in the parallel section after removing the specimen from the salt spray cabinet.

Figure 6.4 clearly shows the surface morphology of low level of corrosion (Group 3). There are clean metal areas which were distributed irregularly in the centre, surrounded by corroded zones. The damage occupied scattered areas, acircular pits

(narrow and deep) distributed densely on the surface at the early stage of corrosion for Group 3. The average depth was approximately 200 μm and the maximum depth approximately 350 μm . However, uniform corrosion morphology (wide and shallow pits) tended to appear at the late stage of corrosion in Group 4 as shown in Figure 6.5. The reduced pit density and uniform corrosion morphology are thought to be related to the joining of adjacent pits during long exposure times. The damage had irregular dimensions and appeared shallow except at some points large pits reached to 500 μm . The bottom surface of the damage was not a regular shape with the presence of significantly deeper local areas than the rest of the damage. It is interesting to note that the pit profiles change from sharp to blunt as the corrosion time increases and this is consistent with observation of Pidaparti and Rao (2008) , Arriscorreta (2012) and Xu and Shan-hua (2015). The pits depth was measured by the profilometer, was below 50% of specimen's thickness, and according to (Kaita et al. 2011) the overall corrosion can be considered when the corrosion depth is greater than 50% of specimen's thickness.

Figure 6.6 clearly shows the different areas which were observed in the corroded damage zone of Group 5 - an ecoated area in the centre, surrounded by corrosion product. Around that zone, the conditions were active corrosion initiated, which clearly shows the metal was attacked from the cut edges. This damage was expected to initiate a fatigue crack which would ultimately cause the failure of the specimen. The average depth was 175 μm and the maximum depth approximately 300 μm .

It should be noted that the profilometer characterization is a line-of-sight technique and cannot measure corrosion undercut pits where the deepest pits are hidden from view by material above it. Thus, this method is not suitable for materials with subsurface, tilted and horizontal pits. However, the fracture surfaces were examined by using SEM and stereo optical microscopy to cover this limitation.

6.4 Performance of FB590 Products

This section's aim is not only to define the fatigue properties of this grade of steel under different environmental conditions, but also to assess the effect of stone

chipping and different levels of pre-corrosion under different cyclic loading. This section contains S-N data of FB590 specimens prepared with five different environmental conditions, all fatigue data within this section were collected from experimentation.

The results can be compared to the base line group 1 (uncorroded and unwelded samples), as well as to other materials used for chassis manufacture. All S-N curves displayed within this section are from longitudinally cut samples which, along with specimens used to measure the tensile behaviour of samples, were cut from the same coil.

6.4.1 Base line E coated only (Group 1) S-N Curves

The FB590 steel sheet used to produce the data for the following graphs were all 2.7 mm thick, and the specimens in this group were only ecoated and therefore were considered as a base line. The fatigue properties of this grade of steel under tension and bending loading are not available in any TSSP-UK literature.

Numerous graphical representations are generated from the data in Appendix A.2, these include the fatigue curves of each. The Basquin exponents and coefficients were calculated and listed in Table 6.1. These results are of particular interest for automotive users.

The final S-N graphical representation shown in Figure 6.10 is a plot of the least square of the failed specimen under 5×10^6 cycles with one graph showing all S-N curves for the tension and bending fatigue loading and for welded and unwelded on one set of axes. This allows direct visual comparison between welded and unwelded condition on one hand and the bending and tensile loading on the other hand, which will be discussed in greater depth in subsequent sections.

6.4.2 Tension and Bending S-N Curves for Group 2

In this group the ecoated specimens were exposed to stone chipping, as explained previously in Section 3.11. The fatigue properties of this grade of steel following exposure to stone chipping were not previously available. Appendix A.3 shows the raw data for tension and bending loading following SN curves on this material. All

S-N curves displayed within this section are from longitudinally cut samples and are shown in Figures 6.11.

The S-N curves are displayed in the same fashion as the Group 1 data in the previous section, one graph showing all S-N graphs for the tensile and bending fatigue for welded and unwelded specimens as well as analysis of the Basquin properties as shown in Table 6.2.

6.4.3 Tension and Bending S-N Curves for Group 3

In this Group the ecoated specimens were exposed firstly to stone chipping followed by a low level of corrosion, as explained previously. Appendix A.4 shows the raw data for tension and bending loading following SN curves on this material. All S-N curves displayed within this section are from longitudinally cut samples and are shown in Figures 6.12.

The S-N graphs are displayed in the same fashion as the Group 1 data in the previous section, one graph showing all S-N curves for the tensile and bending fatigue for both welded and unwelded specimens as well as analysing of the Basquin properties as shown in Table 6.3.

6.4.4 Tension and Bending S-N Curves for Group 4

In this group the ecoated specimens were exposed firstly to stone chipping then a high level of corrosion, as explained previously. Appendix A.5 shows the raw data following S-N curves on this material. All S-N curves displayed within this section are from longitudinally cut samples and are shown in Figures 6.13.

The S-N graphs are displayed in the same fashion as the Group 1 data in the previous section, showing all S-N graphs for both the tensile and bending fatigue for welded and unwelded specimens on one graph as well as analysing of the Basquin properties in Table 6.4.

6.4.5 Tension and Bending S-N Curves for Group 5

In this Group the ecoated specimens were exposed directly to a high level of corrosion, but without prior stone chipping as explained previously. Appendix A.6 shows the raw data following SN curves on this material. All S-N curves displayed

within this section are from longitudinally cut samples and are shown in Figures 6.14.

The S-N graphs are displayed in the same fashion as the Group 1 data in the previous section, showing all S-N curves for the tension and bending fatigue for welded and unwelded on a single figure as well as analysis of the Basquin properties as shown in Table 6.5.

Figures 6.15- 6.18 show relationships between stress range and number of cycles to failure for the welded and unwelded specimens under different surface treatments. These figures include the least square fitting of the failed specimens under 5×10^6 cycles as well as raw data points for each group. The comparison among S-N curves of all groups is presented in these figures for bending and tensile loading and for welded and unwelded specimens. These figures show comparison among different stress concentration.

6.5 S-N curves

By analysing the SN curves there are some points above the reference lines, whereas others below the reference lines. The smooth surface of pristine specimens Group1 (uncorroded and unwelded) showed low fatigue life scatter due to the identical manufacturing process, while the data for other fatigue specimens showed a large scatter due to various surface exposure treatments and variation in weld geometry.

To summarise, the S-N curves shown in Figures 6.10-6.14 provide much information which is fundamental for developing robust designs. Each graph on its own provides automotive users with essential information that is required for engineers, however by breaking down them at the same time bigger types of interest show up.

In the current study, the fatigue tests were performed under high mean stresses (load ratio 0.1) which is more dangerous than those of low mean stresses (load ratio < 0.1). The higher mean stresses have a detrimental effect of reducing the stress range materials can withstand (Benham et al. 1996; Bathias and Pineau

2010; Bright 2012). Therefore the current study can be considered more extreme than the studies which were conducted under lower mean loads due to real components usually failing at higher loads.

The impact of different levels of stress magnitude, welding and stress concentration due to surface exposure to stone chipping and to saline solution on the fatigue life of the specimens will be discussed in more detail in Chapter 7.

6.6 Stress concentration due to weld geometry and stone chipping

The failure of bending specimens can occur anywhere, but most probably at the centre between the loading supports on the bottom side, because there is the location with the highest value of tensile stresses. In this study all bending specimens were tested by putting the high stress concentration side for instance welding cap or stone chipping side on the bottom side where maximum tensile stress was found. The opposite face of the specimen, which contained welding root or intact or non-stone chipped face was therefore loaded in compression. From observation, no significant difference was observed between specimen faces for the plain bending specimen, thus there was little importance to which face was placed in the lower or upper position. However, this issue is different for welded and stone chipping specimens where their faces containing significant high stress concentrations on the bottom were exposed to tension as displayed in Figure 6.19, which shows an example of a bending fatigue specimen failed from stone chipping site.

To explain this issue in more detail, a comparison was performed for two welded bending specimens from Group 1 under same stress of 450 MPa, the first specimen had the welded cap on the top face during testing, and failed at 537931 cycles. The second specimen was tested with the welding cap on the bottom face and failed more rapidly at 67377 cycles, suggesting that the specimen fails more rapidly when the weld cap is located on the bottom face. A similar experiment was performed on another two stone chipped, unwelded specimens from Group 2. These specimens were tested under same stress of 450 MPa. The first specimen with the stone chipped surface was on the top failed at 3012554 cycles whereas the other specimen with the stone chipped face on the bottom failed at 1188966 cycles,

suggesting that the specimen fails more rapidly when the stone chipping face is on the bottom.

Further investigation was carried out on the fracture surface of failed bending specimens by using scanning electron microscopy SEM, explained in detail in the next section.

6.7 Fractography of fatigue bending specimens

Typical SEM fractographs of different bending fatigue specimens are shown in Figures 6.20 and 6.21 to explain the effect of stone chipping on crack initiation and to show the fracture surface of the bending specimens. All figures revealed the cleavage features of flat facets and fatigue striations. Figure 6.20 and 6.21 show fracture surfaces of two stone chipping bending fatigue specimens under 450MPa. In the first specimen the stone chipping was on the top surface during bending fatigue test whereas the second specimen the stone chipping face was on the bottom surface.

The fracture surface of first specimen Figure 6.20 (a,b), is almost flat with approximately 9.2mm length. Shear lip lines were observed starting from the bottom right hand corner where the maximum tensile stress occurs toward the top surface where the stone chipping marks are. This indicates that crack initiation happened at the corner where the grains have two free surfaces, and hence these grains have little support compared to the grains in the middle thickness of the material as explained by Maddox (1991). Figure 6.20 (d-f) also shows that the ductile overload fracture was predominant in the last stage of the test; this part is almost rough and short.

Frontal fracture surface of the second specimen showed the crack initiated from some tiny scratches on the bottom surface where the stone chipping marks are, as shown from Figures 6.21 (b-f).

It can be also observed that, in both cases, the fracture surface consists of two parts, fatigue crack and fast fatigue fracture. The first part is characterized by granular area close to the crack initiation zone. The presence of dimples is not obvious in this part of fracture. The remaining surface, the second part, is ductile fracture,

6.20 (c,d) and 6.21 (g), caused by overloading of the specimen because of its reduced cross-section (Kovac 2010). It is classic cup and cone type, similar to the tensile fracture surface mechanism. The presence of non-uniform small and large dimples indicates a typical ductile mode of fracture (indicating considerable plastic deformation ahead of the fatigue crack). The elongated shape of some voids may indicate that localized shear stresses are present. The transition from the stable to unstable crack propagation is characterized by the change in fracture mode from fatigue crack growth to a ductile fracture.

Note that this information may lead to the conclusion that the failure will occur where the combination of the local stress and the size of the local flaw results in the condition of rupture. Therefore all bending specimens were tested by putting the stress concentration sites (welding cap and stone chipping faces) on the bottom in order to test the material on the worst potential failure.

6.8 Fractography of fatigue tension specimens

Profilometer characterization is a line-of-sight technique and cannot measure corrosion undercut pits where the deepest pits are hidden from view by material above. Thus, this method has some limitations for corroded materials with subsurface, tilted and horizontal pits. However, the fracture surface was examined by using stereo optical microscope and SEM to cover this limitation.

Examination of fracture surfaces of failed specimens helps in determining the controlling mechanisms of failure. Numerous information can be provided by fractography such as the location and nature of the critical discontinuity as well as any apparent trends in the corrosion features, shapes, and severity of damage.

Figure 6.22 shows the fracture surface micrograph of the uncorroded specimens that has been analysed. The fatigue crack origin could be found in the top right - hand corner of Figure 6.22 (a), and there were obvious radial lines towards the bottom left corner, which indicated the crack extension direction Figure 6.22 (b). There was no doubt that the fatigue crack origin of the uncorroded specimen was at the point of stress concentration. It is clearly shown that the fracture of each fatigue specimens consists of fatigue crack initiation zone which is a near surface,

fatigue crack growth zone which is an inner-core occurrence (Kovac 2010). The fracture surface consists of two parts, the stable crack propagation region (fatigue crack) and after certain length of propagation the specimen cannot withstand with the applied stress anymore. Therefore, it fails rapidly when entering the second region which is sometimes known as fast fatigue fracture. The result also show that the crack starts to propagate almost equally from the machined edge for the as received specimen (Group1) because the stress raiser is eliminated by reducing the specimen surface roughness. This appearance is different for specimens exposed to stone chipping (Group 2), where the crack initiated from stone chipping sites as shown in Figure 6.23. Figures 6.20 and 6.21 show more details about the fracture surface as well as explaining the effect of stone chipping on crack initiation of the bending specimens.

Examination of the fracture surface of corroded specimen showed that remaining cross sectional area declined rapidly with the increase of corrosion time and the corrosion flaw had a complicated shape, as previously explained in table 2.1 and Figure 2.11. SEM and optical microscope analysis revealed that pre-corroded specimens tested in this study fractured from fatigue cracks that formed from corrosion induced pits and metal dissolution locations at the corroded areas Figure 6.24. A typical fracture surface of the corroded specimens showed that cracks started to fail from corrosion pits which could became the fatigue crack extension source, and the crack could originate from several corrosion pits. It could be found obviously from Figure 6.24 that the fatigue crack extension presented an elliptic shape. There were evident corrosion traces on the surfaces of the specimens. Figure 6.25 showed that subsurface pitting and tunnelling were detected as a manner by which propagation of these developing discontinuity states evolved during the experiments, these played a significant role in the both the formation and propagation of the pits and also the nucleation of fatigue cracks.

6.9 Conclusions

It could be deduced from the fatigue life curves that the pre-corrosion and welded specimens ruptured sooner than the pristine specimens, however, fatigue limits were determined for the pre-corrosion and welded specimens, while previous

studies showed the fatigue limits did not exist for these specimens since they used stress levels insufficiently low. Furthermore, the scatter of the fatigue strength of pre-corroded and welded specimens is larger than of virgin ones. In addition, it can be seen from the fatigue life curves that the fatigue strength of the bending loading is much higher than that tensile loading, because in bending loading the stress would be tensile in the bottom surface and compressive in the top surface while in tensile loading specimen the whole cross section would be under tensile stress.

It could be also deduced from the profilometry measurements the overall corrosion did not exist for the pre-corrosion specimens, due to the corrosion depth not exceeding 50% of specimen thickness.

Following fatigue testing, the fracture surface was examined using a scanning electron microscope (SEM) to determine the failure mechanisms of each surface treatment. The results of the fractography comparisons support the general conclusions as the crack starts to propagate almost equally from the machined edge in Group 1, while the crack initiated from stone chipping sites in Group 2. Surface roughness due to corrosion defects serve as a high stress concentration point which can enhance crack nucleation. The stress raiser points increase proportionally with the surface roughness. Therefore, the crack can start to propagate at any point where the highest stress raiser is located. The results showed that most of the corroded specimens failed from pitting, therefore, the pitting would be the most harmful defect to fatigue life of the corroded specimens. In addition, SEM analysis revealed metal dissolution and subsurface failure modes including tunneling, subsurface cracking (which cannot be detected by profilometry) in addition to pitting. What is clearly noticeable is that corrosion has a huge detrimental effect on the fatigue performance of the steel strip.

Table 6.1: Processed FB590 S-N data of Group1.

FB590 Data Set	Basquin Coefficient (A), (MPa)	Basquin Exponent (b)
Bending unwelded	886.71	-0.034
Bending welded	5425.6	-0.185
Tension unwelded	991.46	-0.059
Tension welded	3069.6	-0.195

Table 6.2: Processed FB590 S-N data of Group 2.

FB590 Data Set	Basquin Coefficient (A), (MPa)	Basquin Exponent (b)
Bending unwelded	1944.8	-0.107
Bending welded	9537.1	-0.246
Tension unwelded	1260.3	-0.088
Tension welded	4301.4	-0.224

Table 6.3: Processed FB590 S-N data of Group 3.

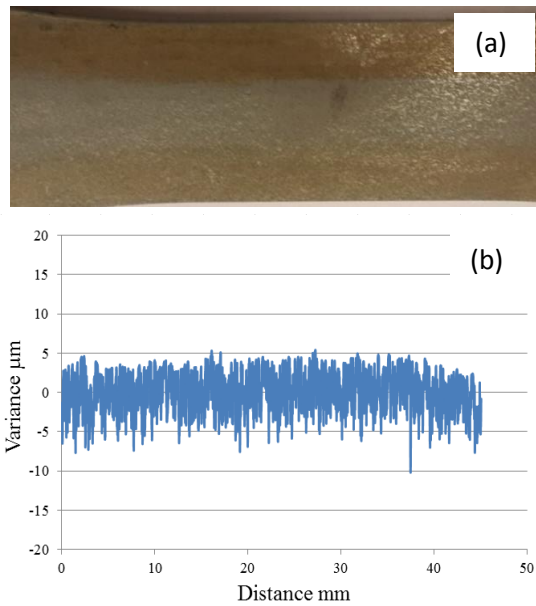
FB590 Data Set	Basquin Coefficient (A), (MPa)	Basquin Exponent (b)
Bending unwelded	1948.6	-0.125
Bending welded	2122.3	-0.146
Tension unwelded	3113.1	-0.185
Tension welded	3936.5	-0.248

Table 6.4: Processed FB590 S-N data of Group 4.

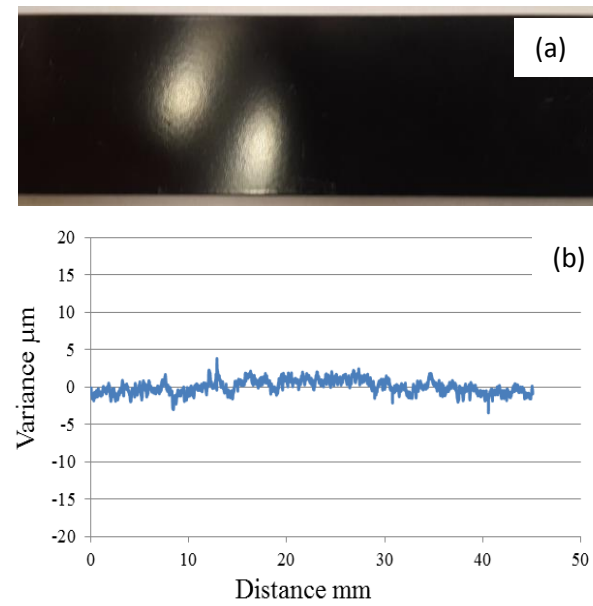
FB590 Data Set	Basquin Coefficient (A), (MPa)	Basquin Exponent (b)
Bending unwelded	2653.1	-0.182
Bending welded	2888.5	-0.193
Tension unwelded	2860.6	-0.212
Tension welded	8573.1	-0.307

Table 6.5: Processed FB590 S-N data of Group 5.

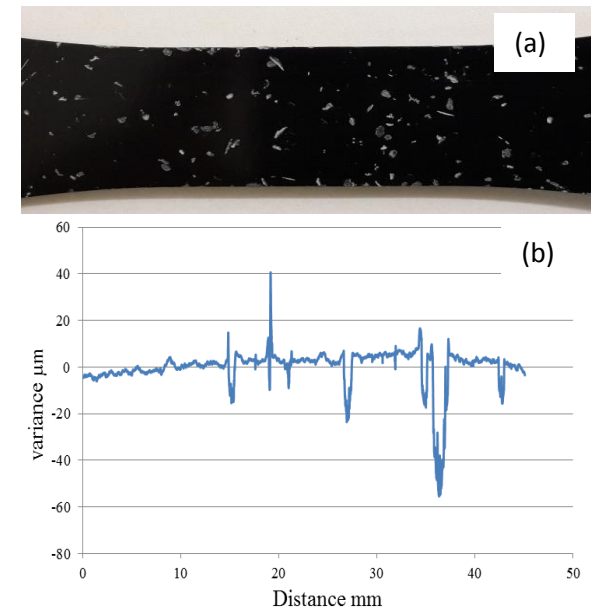
FB590 Data Set	Basquin Coefficient (A), (MPa)	Basquin Exponent (b)
Bending unwelded	2087.8	-0.127
Bending welded	3320	-0.184
Tension unwelded	1743.1	-0.138
Tension welded	9394	-0.302



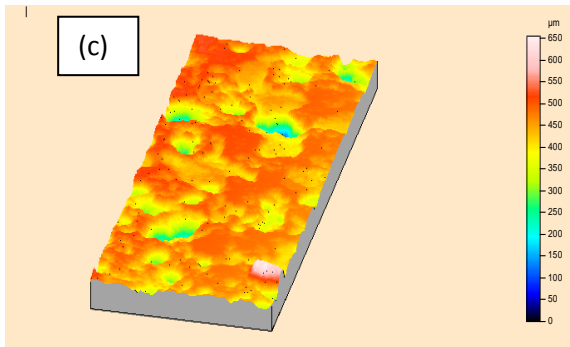
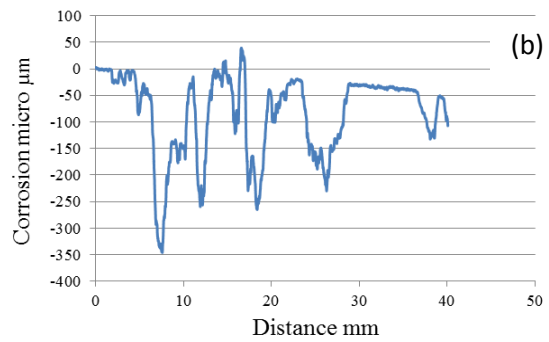
Figures 6.1: (a) The typical appearance of the as received specimen (b) 2D profile (c) 3D image of as received specimen.



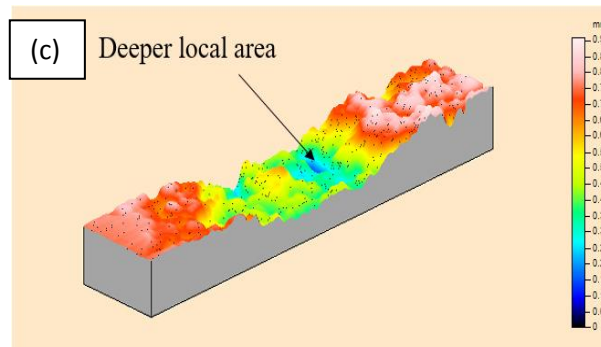
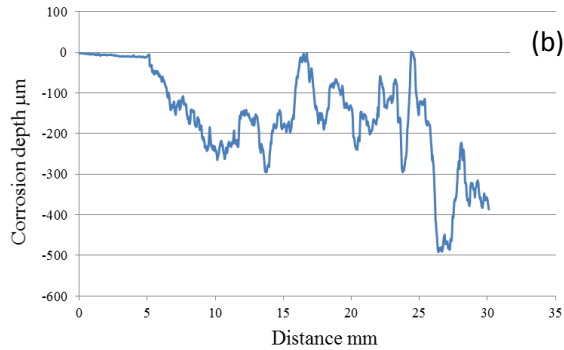
Figures 6.2: (a) The typical appearance of the coated specimen group 1 (b) 2D profile (c) 3D image of coated specimen.



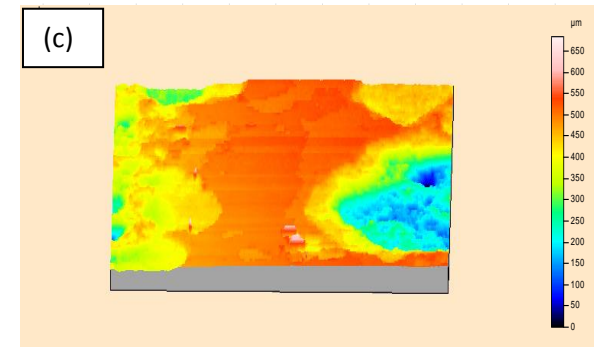
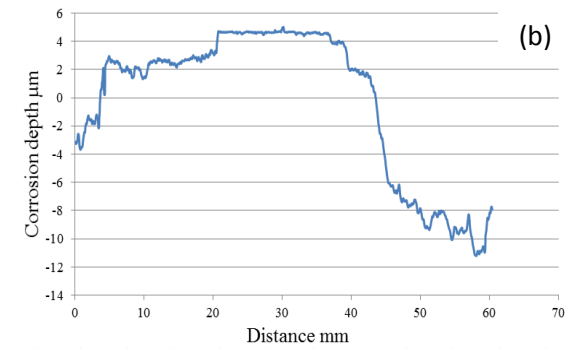
Figures 6.3: (a) The typical appearance of the stone chipping specimen group 2 (b) 2D profile (c) 3D image of stone chipping specimen.



Figures 6.4: (a) The typical appearance of the corroded specimen Group 3 (b) 2D profile (c) 3D image of corroded specimen.



Figures 6.5: (a) The typical appearance of the ecoated specimen group 4 (b) 2D profile (c) 3D image of Ecoated specimen.



Figures 6.6: (a) The typical appearance of the corroded specimen Group 5 (b) 2D profile (c) 3D image of corroded specimen.

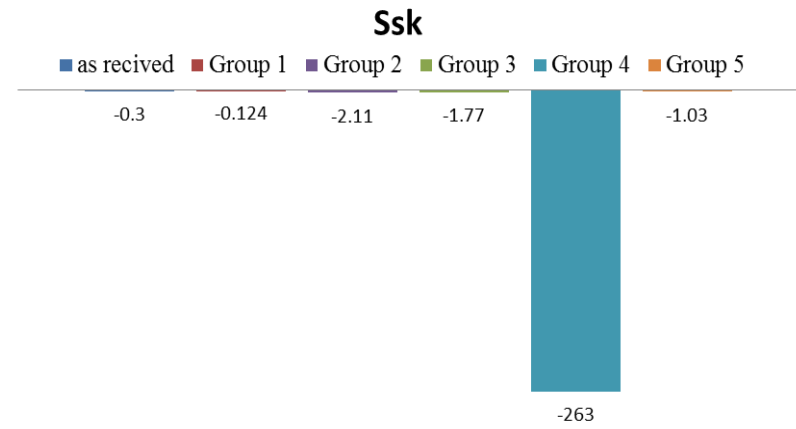
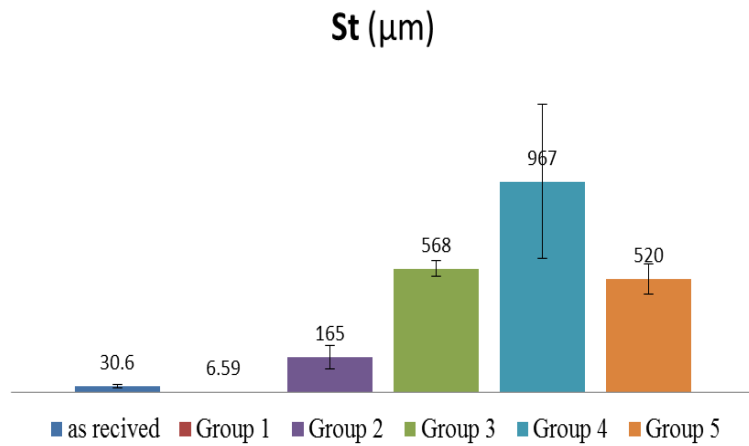
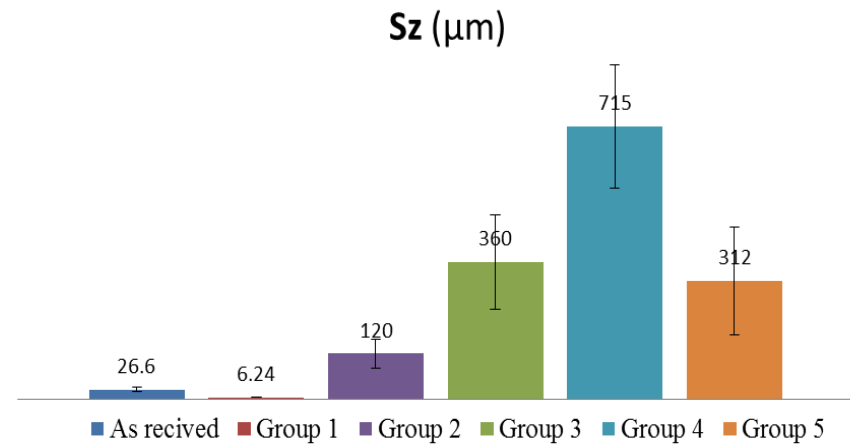
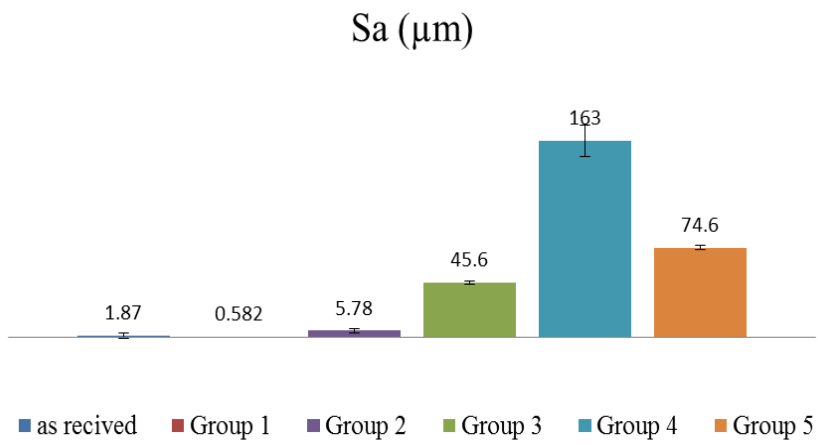


Figure 6.7: shows roughness parameters increase with time of corrosion.

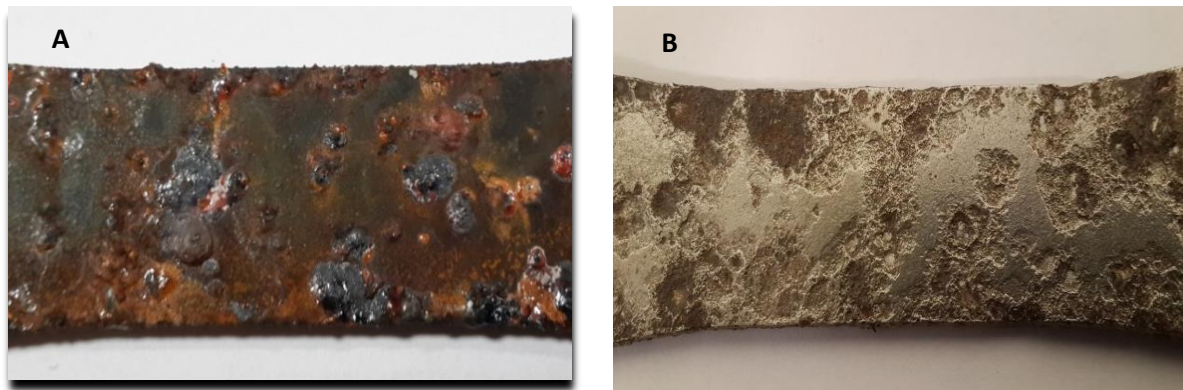
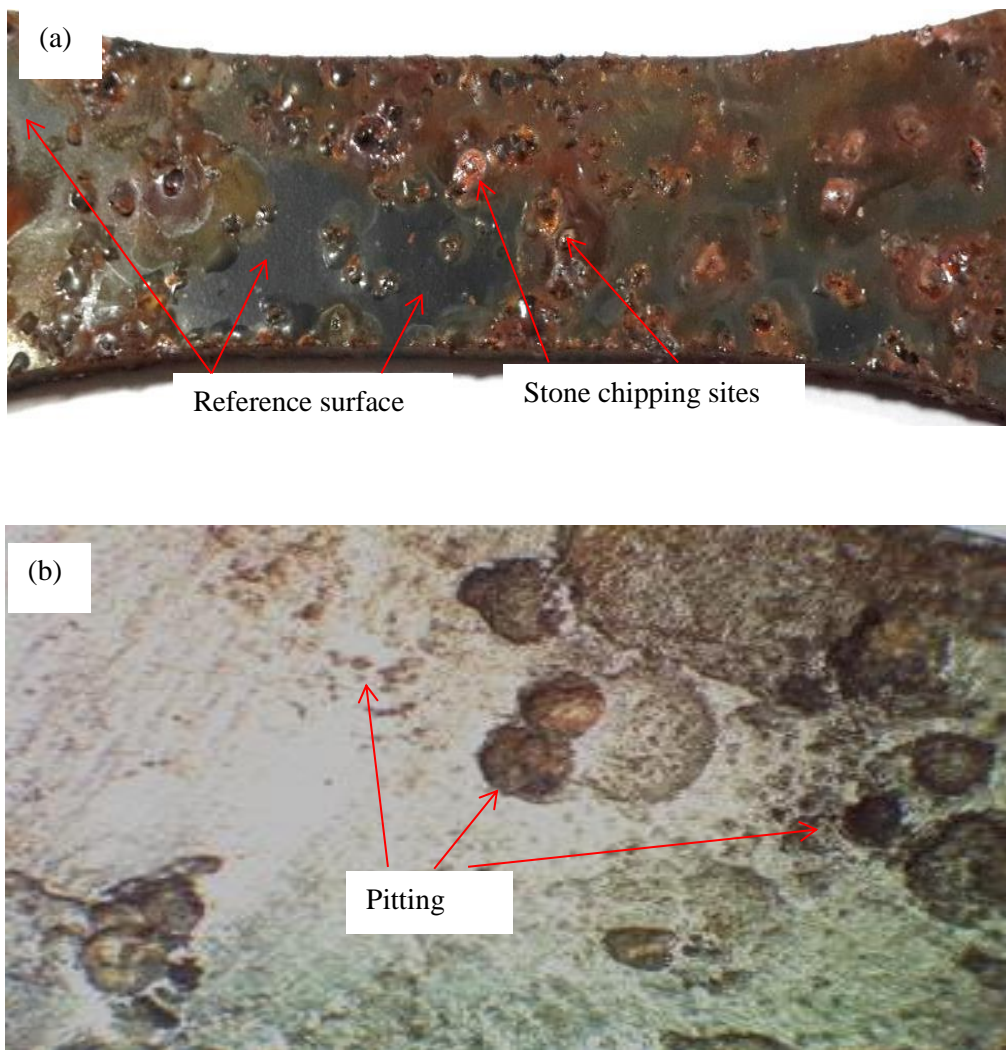


Figure 6.8: The typical appearance of the specimens (a) before and (b) after removing the rust.



Figures 6.9: (a) shows the unaffected surface (ecoated) was considered as a reference surface, (b) Stereo optical microscope image of corroded surface.

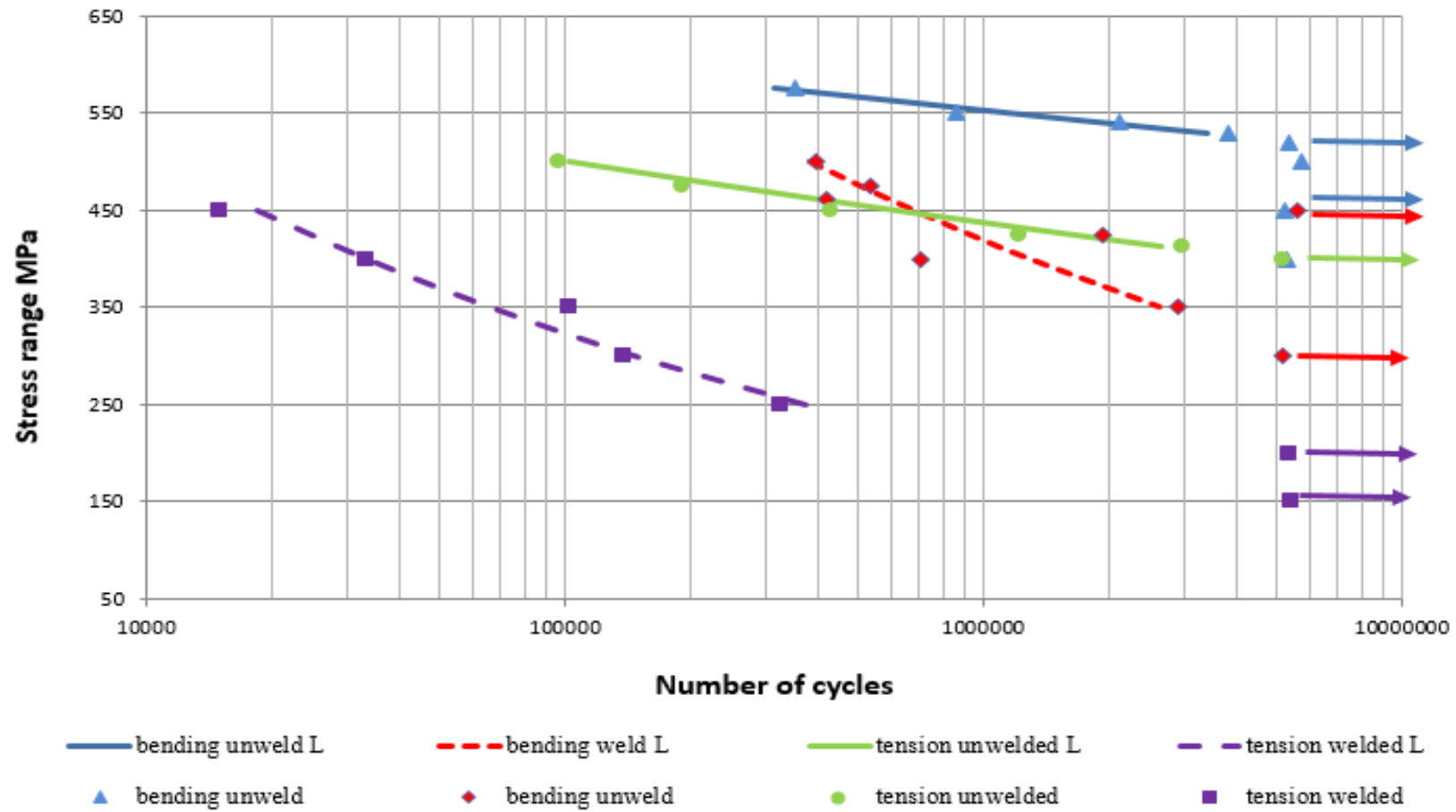


Figure 6.10: All S-N curves of Group 1.

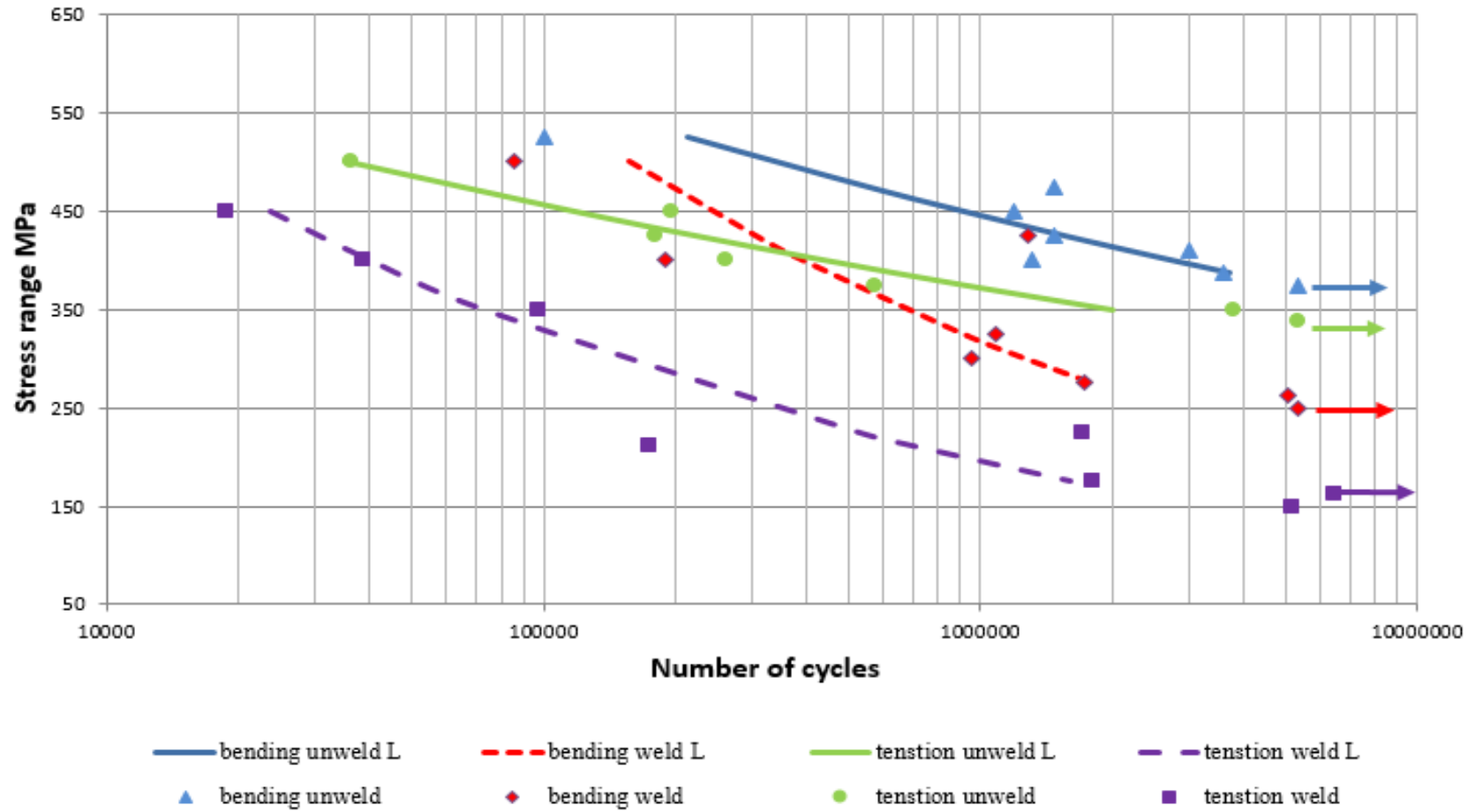


Figure 6.11: All S-N curve of Group 2.

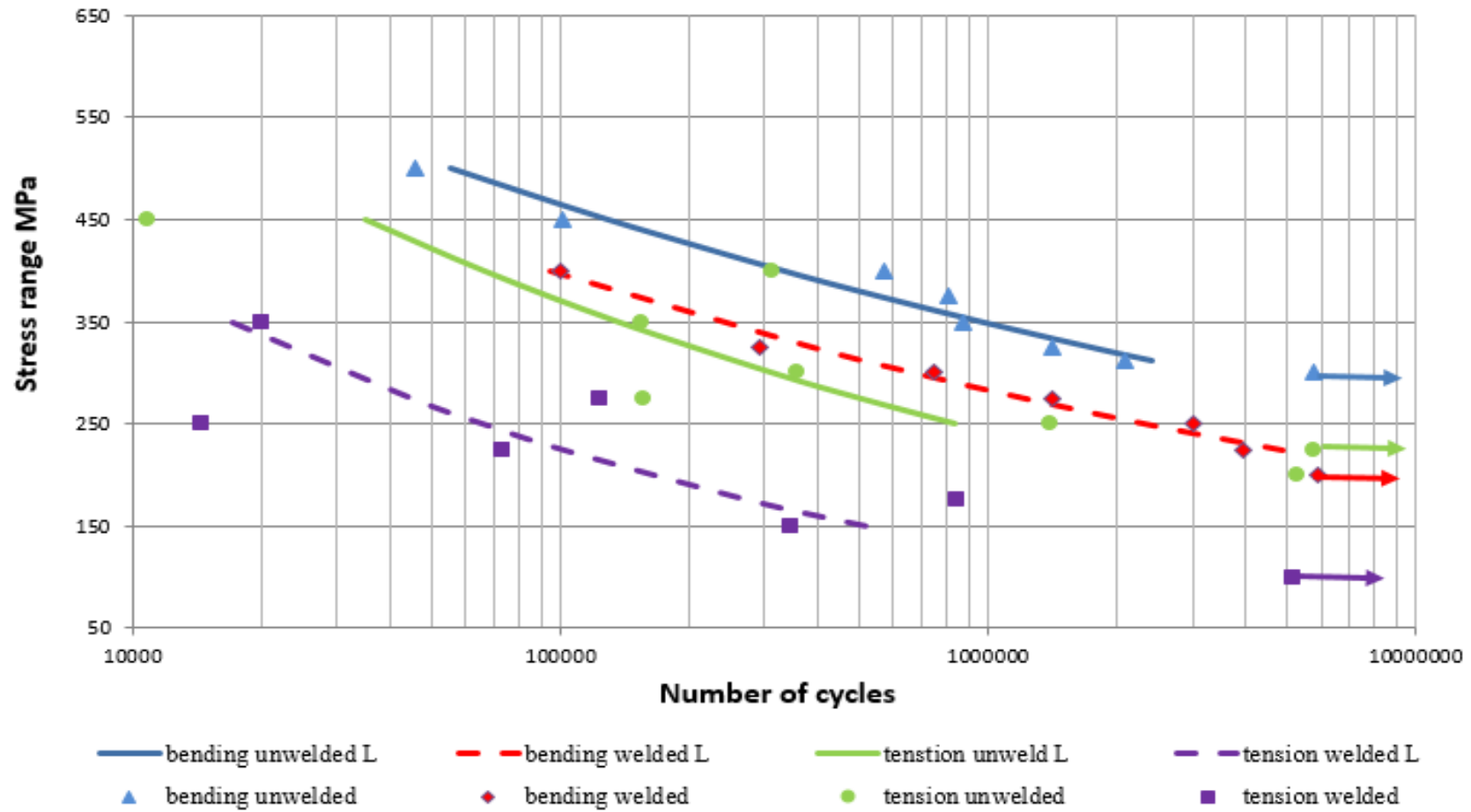


Figure 6.12: All S-N curve of Group 3.

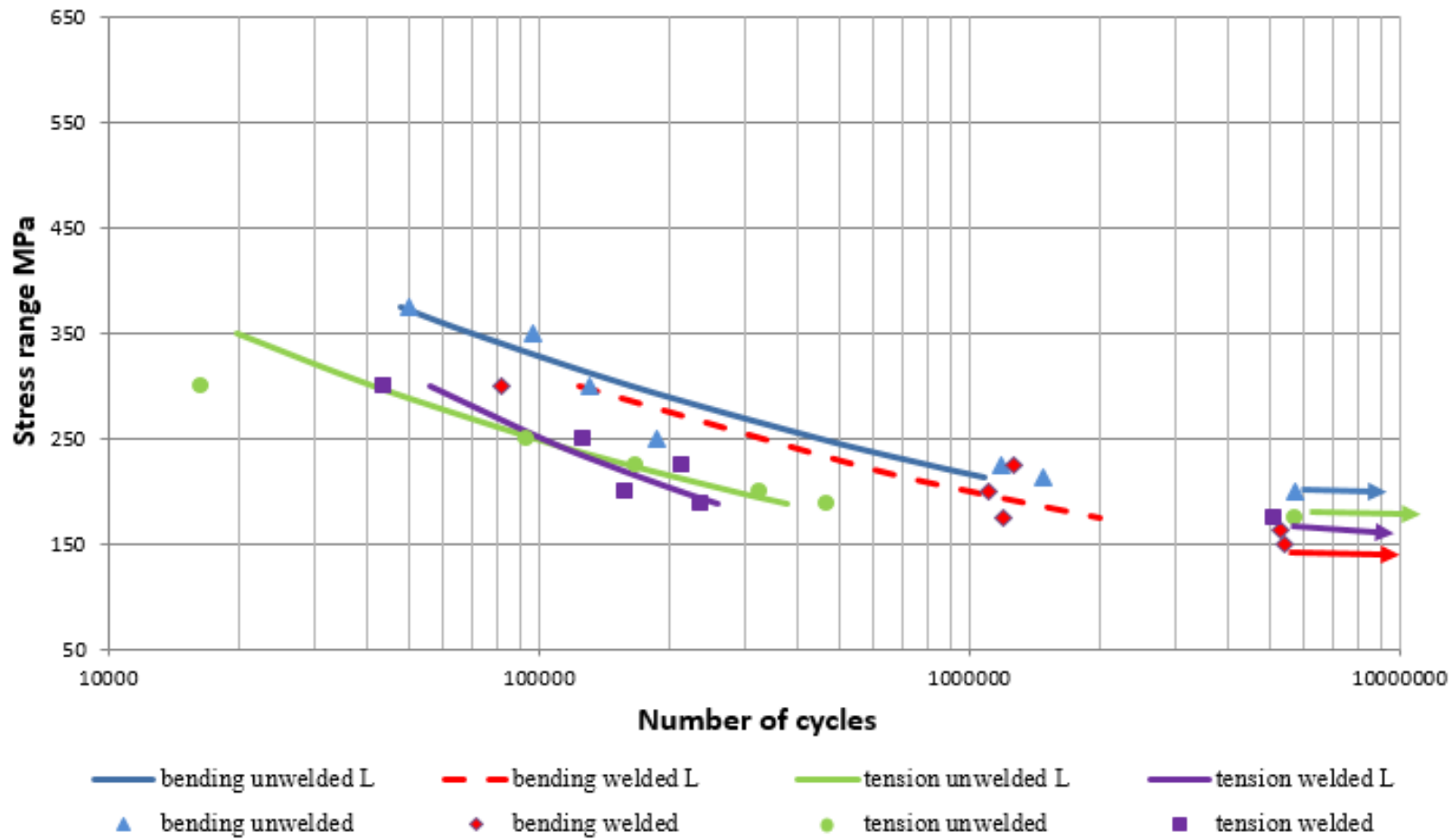


Figure 6.13: All S-N curve of Group 4.

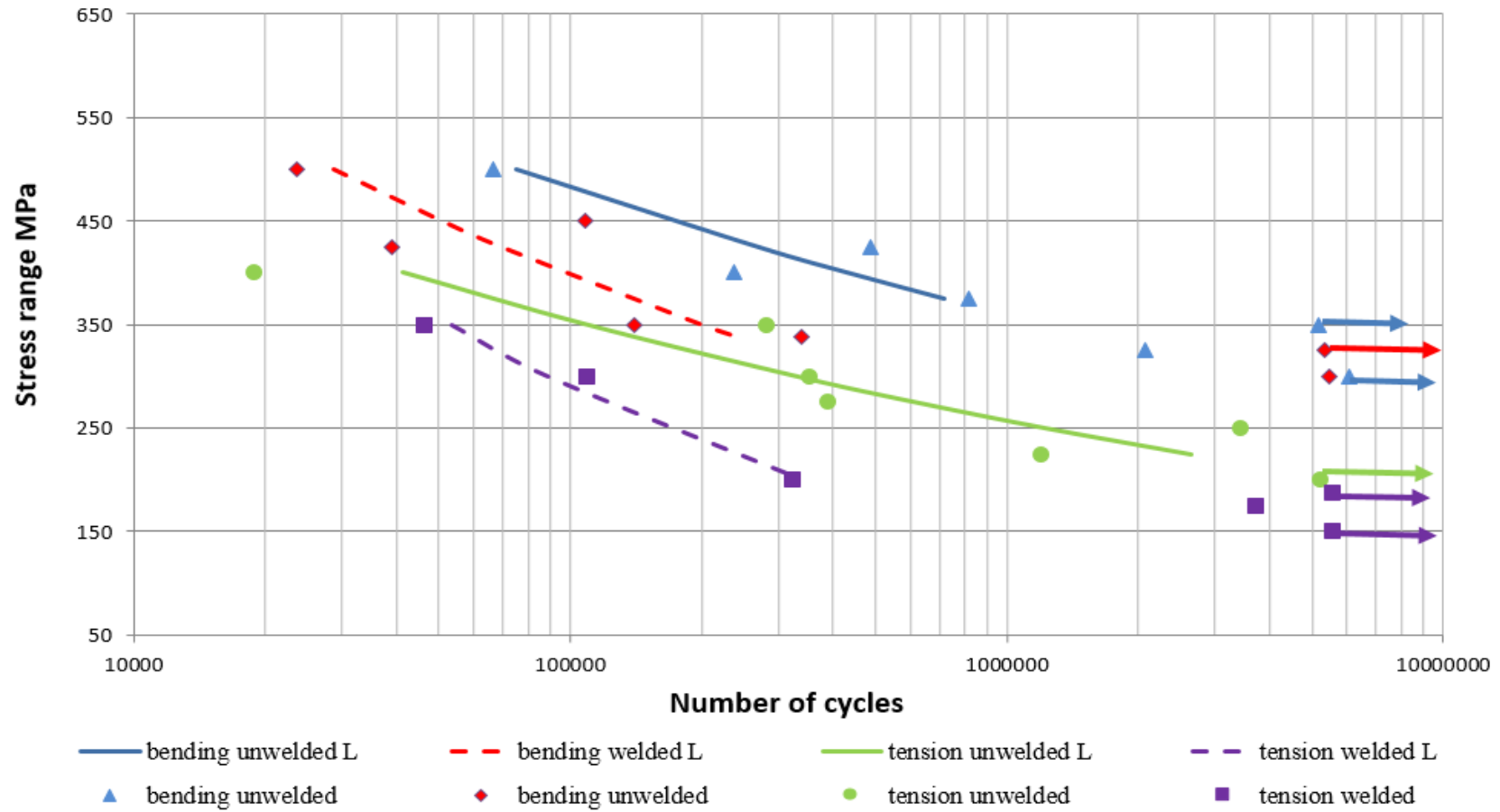
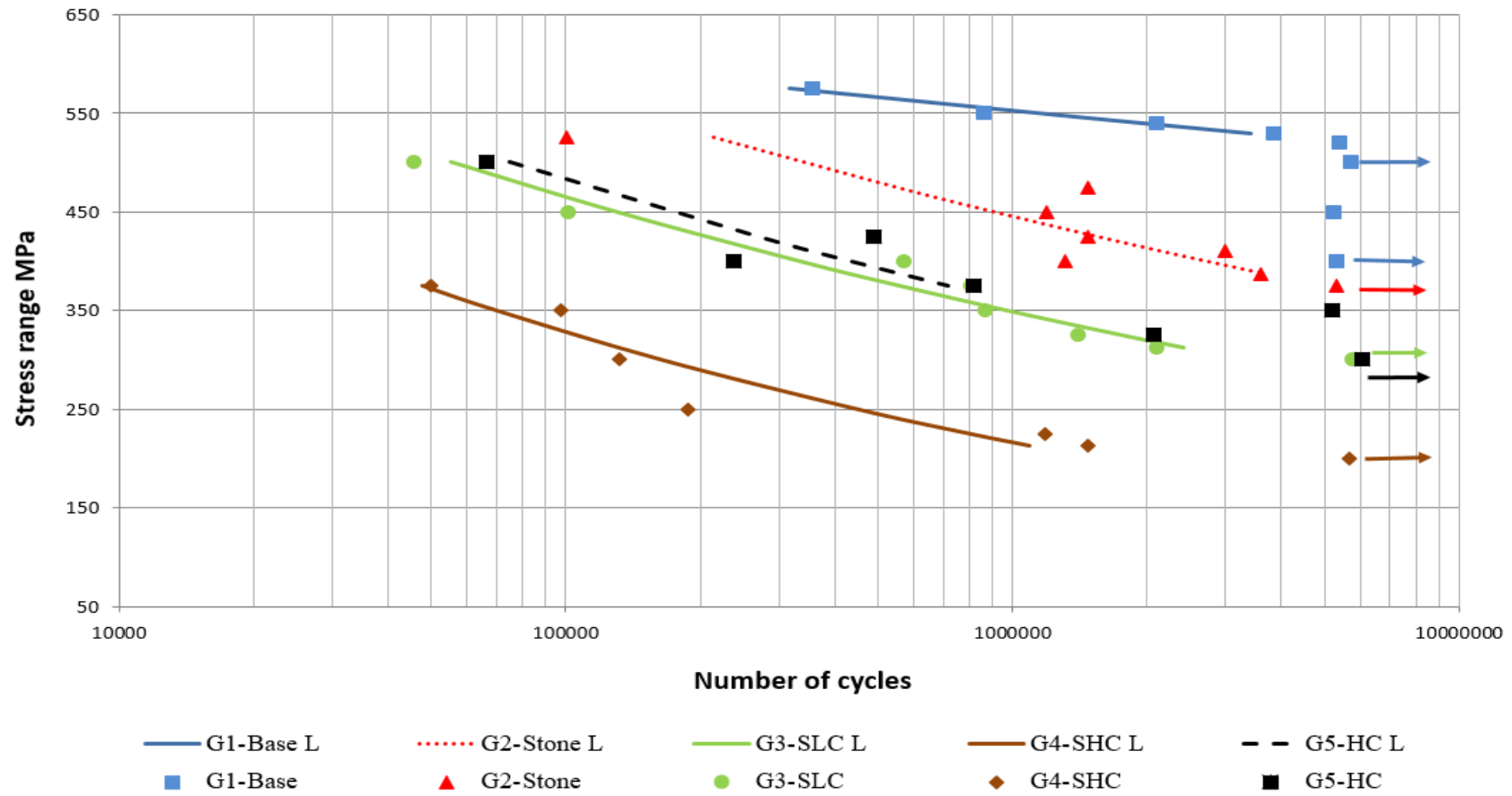


Figure 6.14: All S-N curve of Group 5.



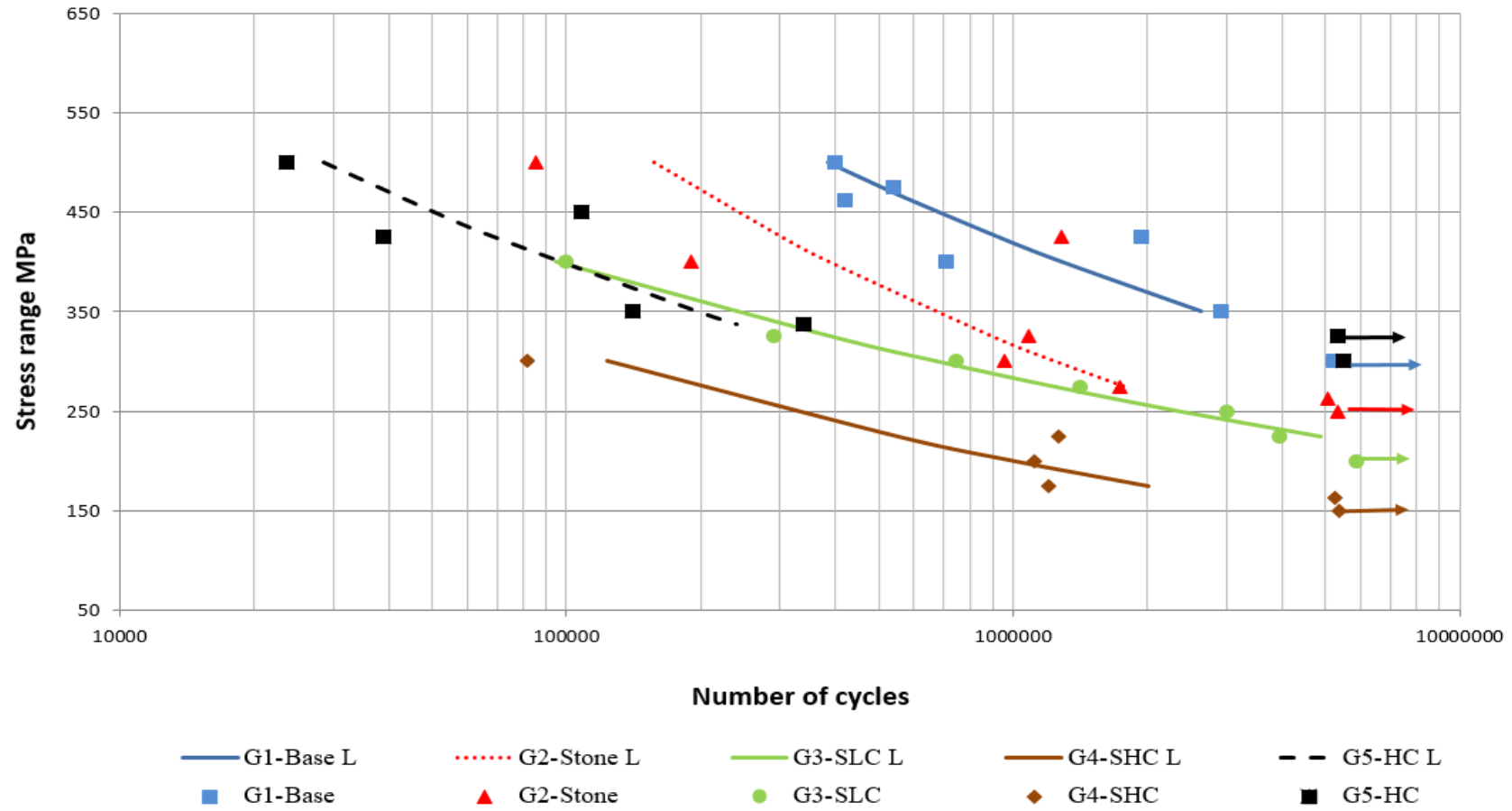


Figure 6.16: S-N curves for bending welded with different surface treatments.

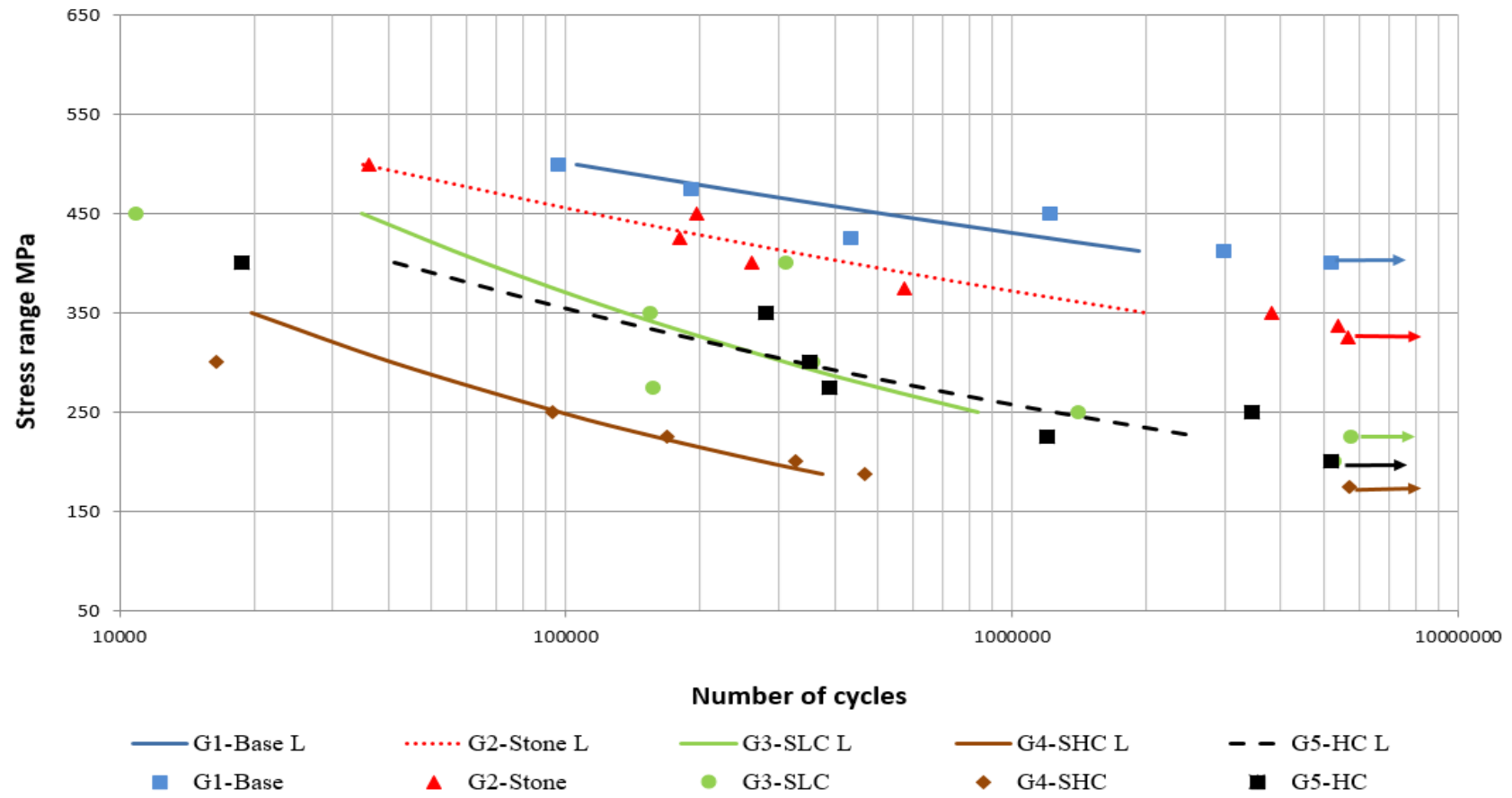


Figure 6.17: S-N curves for tension unwelded with different surface treatments.

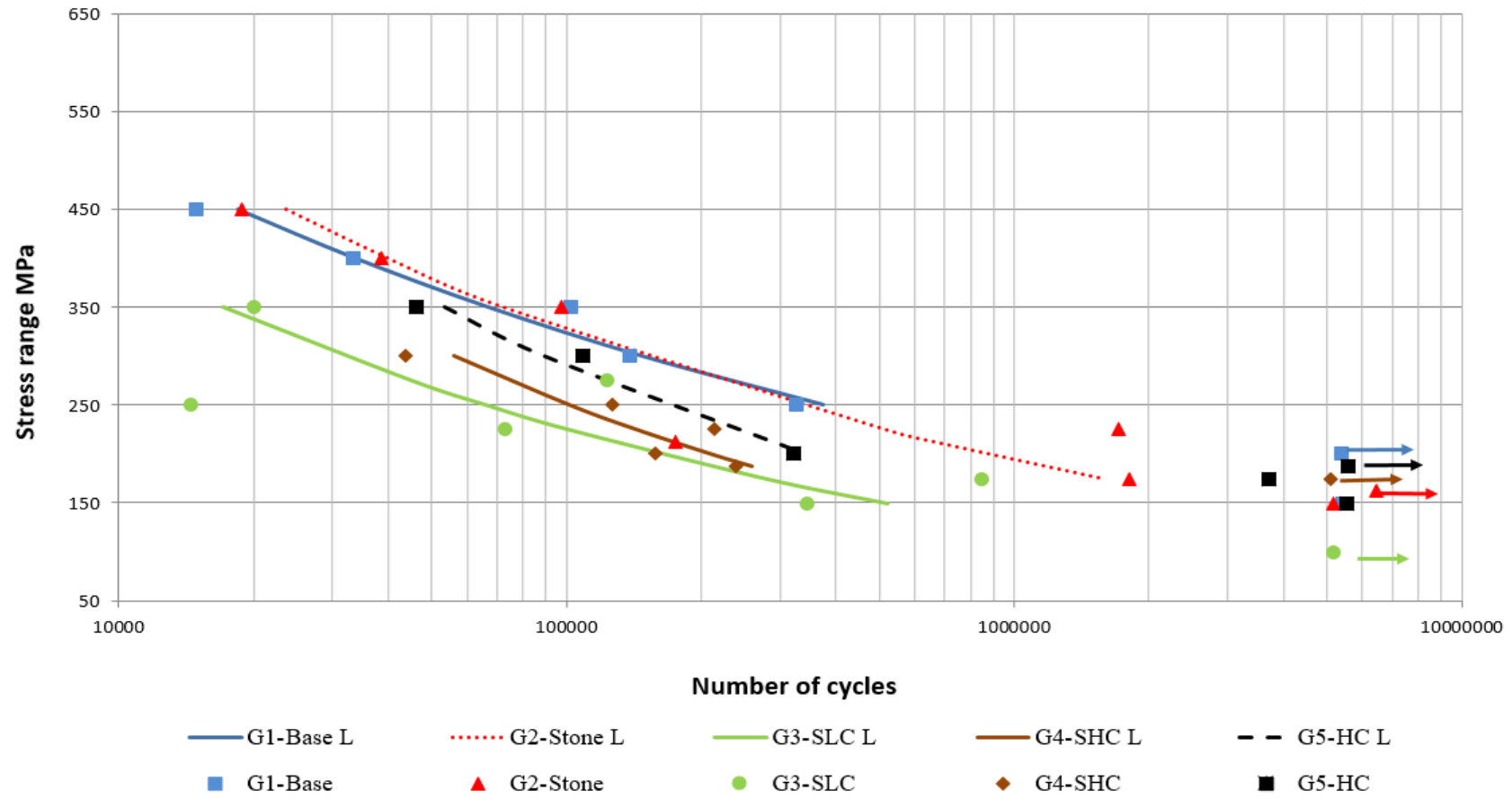


Figure 6.18: S-N curves for tension welded with different surface treatments.

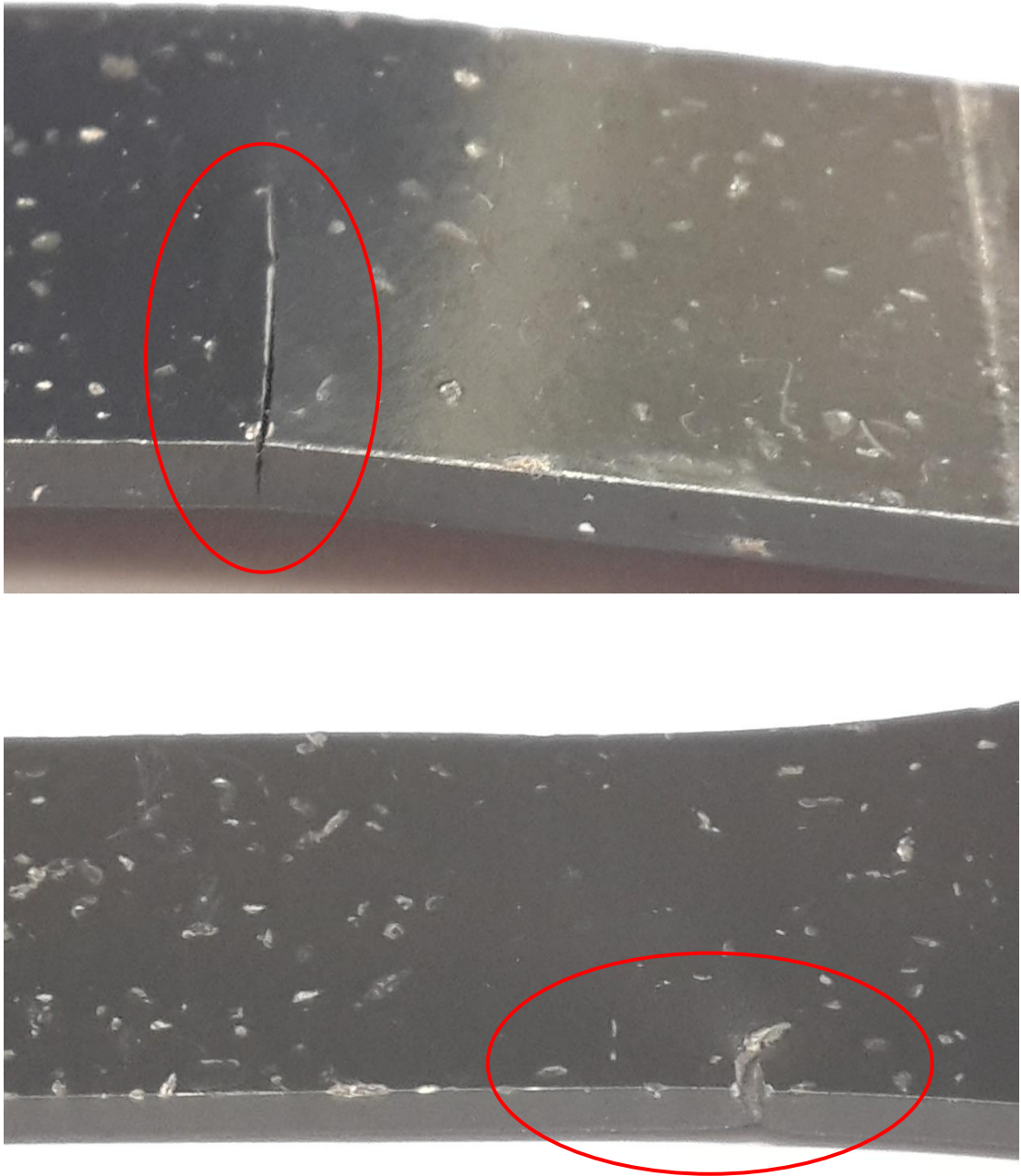


Figure 6.19: specimen exposed to stone chipping.

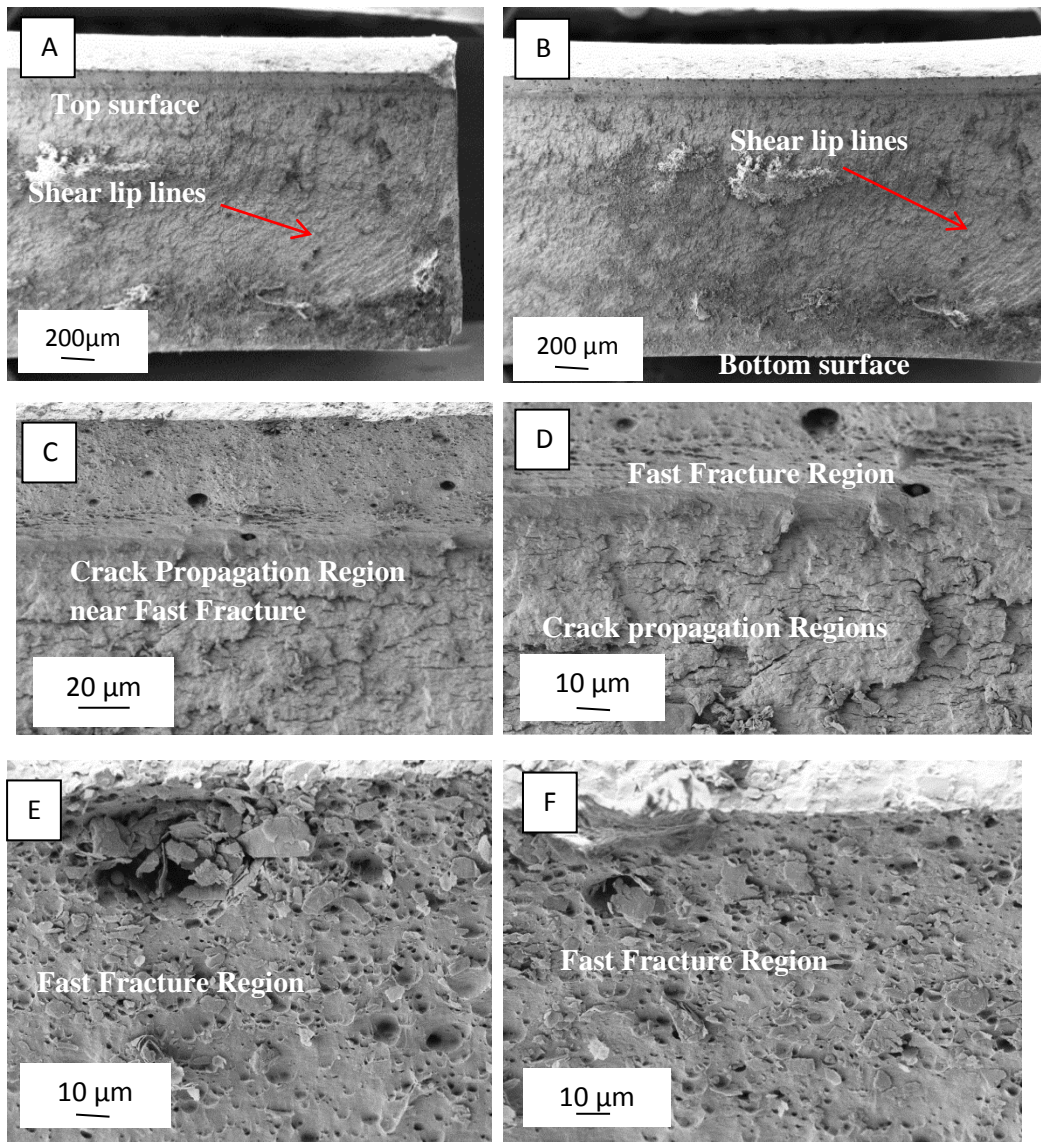


Figure 6.20 SEM micrographs taken from fracture surfaces of bending fatigue specimens where the stone chipping was on the top surface (a) shear lip lines general appearance (b) indicates ductile fracture in the last stage of the test, (c) The boundary between the fast-fracture and crack propagation regions, (d) fatigue striations in the crack-propagation region (e ,f) Fast-fracture region, non-uniform small and large dimples.

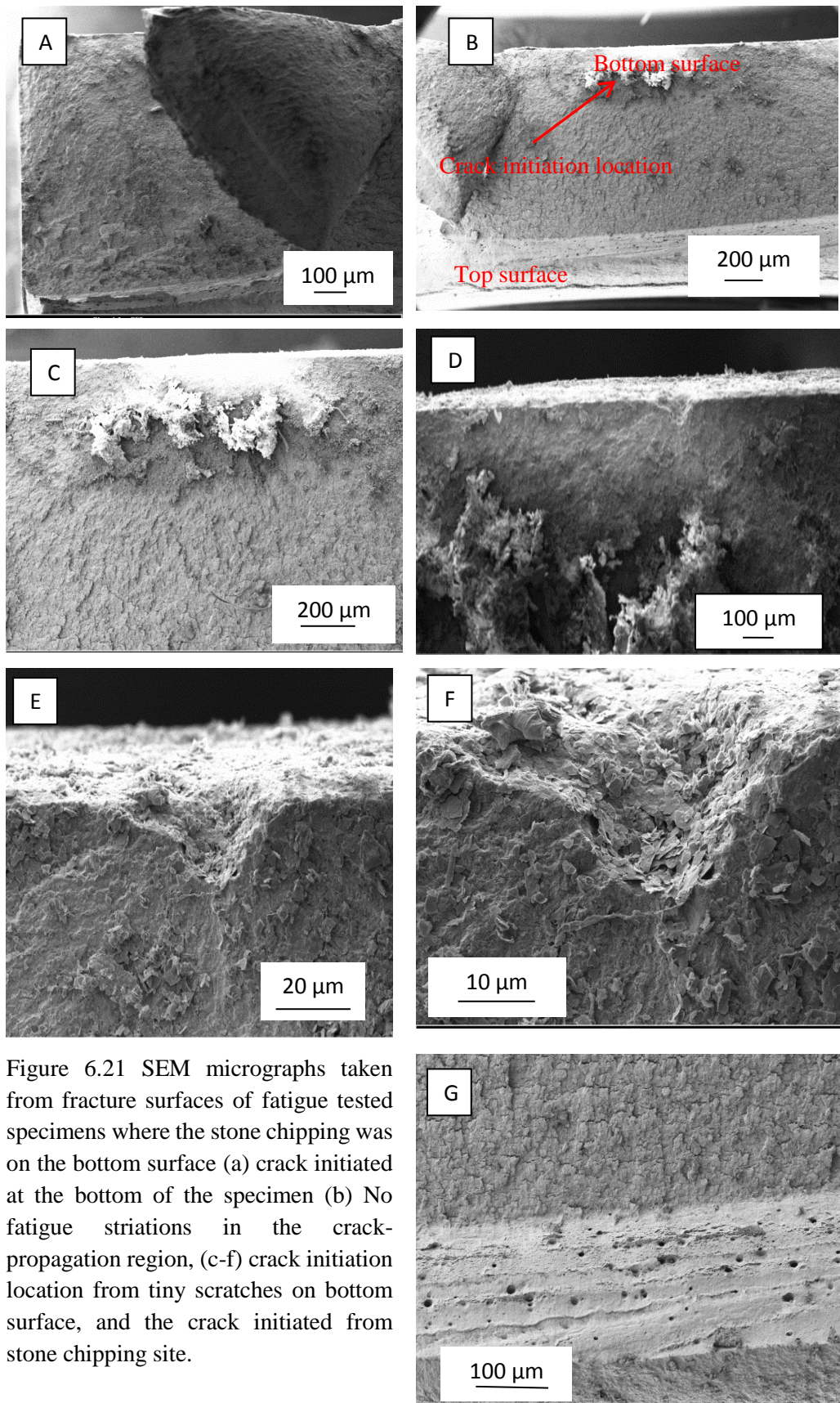
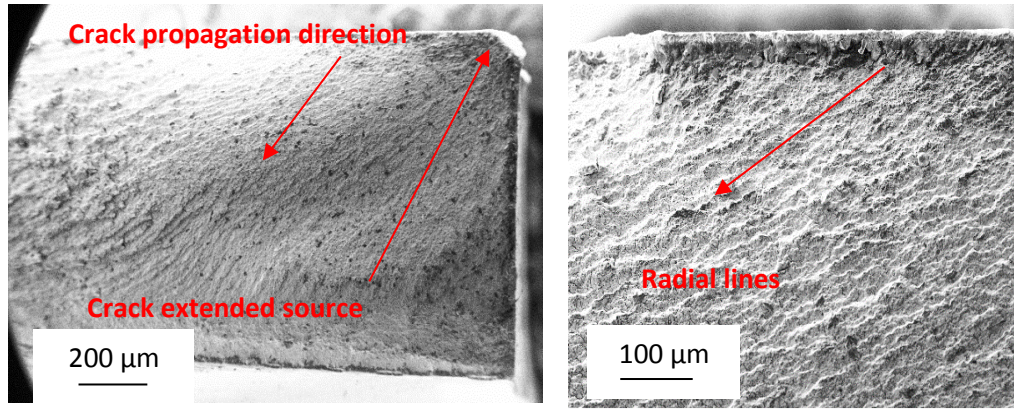


Figure 6.21 SEM micrographs taken from fracture surfaces of fatigue tested specimens where the stone chipping was on the bottom surface (a) crack initiated at the bottom of the specimen (b) No fatigue striations in the crack-propagation region, (c-f) crack initiation location from tiny scratches on bottom surface, and the crack initiated from stone chipping site.



Figures 6.22: (a) An overview of the fracture surface micrograph of the uncorroded specimens (b) show the radial lines towards the left down direction.

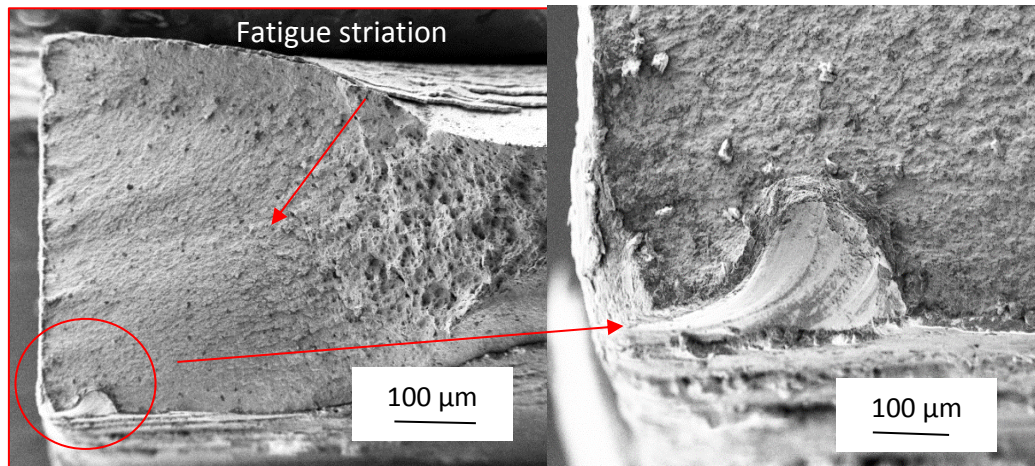


Figure 6.23: overview and a closer view showing fatigue fracture started from stone chipping site.

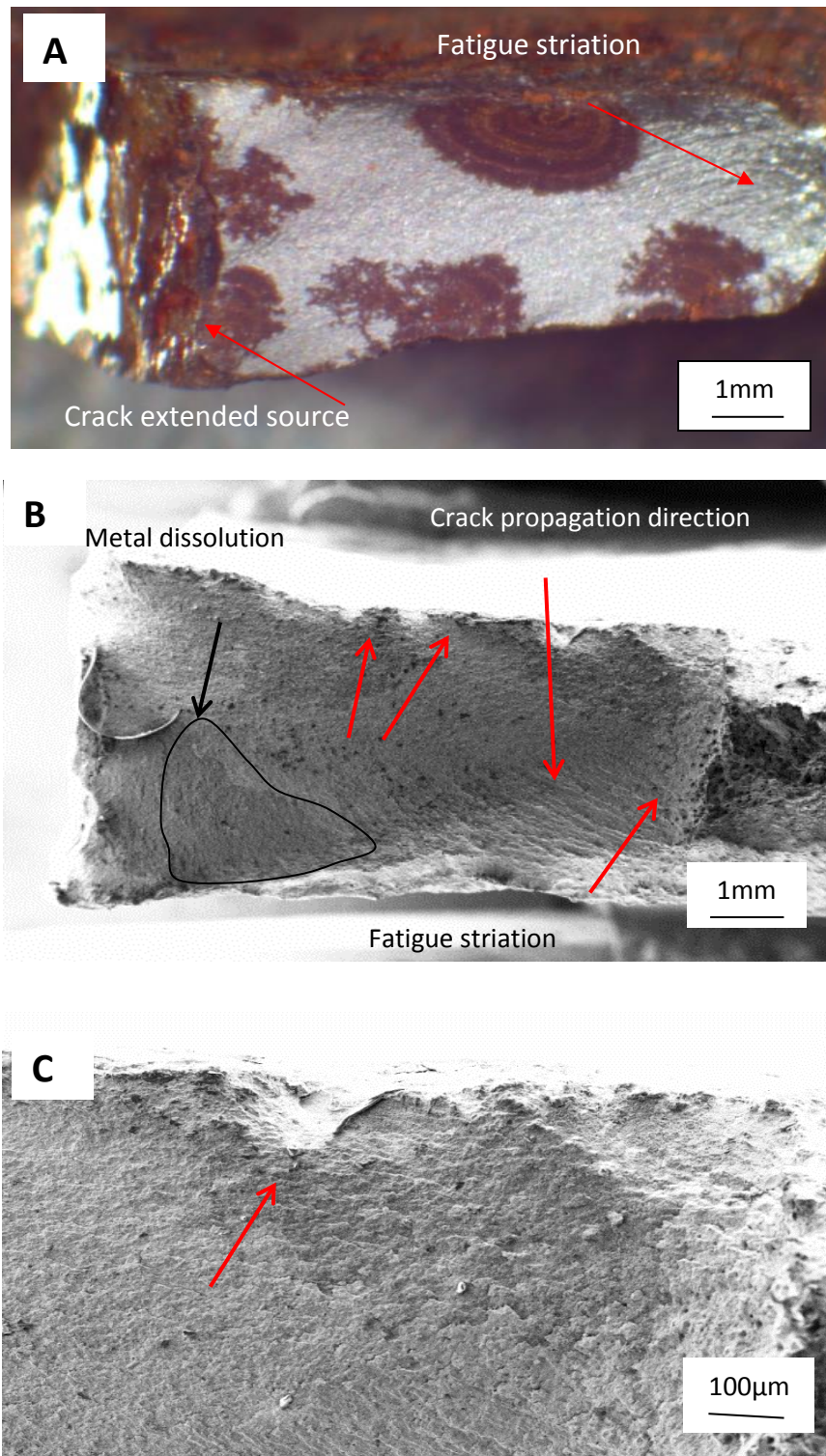


Figure 6.24: An overview of the fracture surface for corroded specimen. Pits are shown in the exposed surface to the slate solution. Arrows indicate location of several pits at the fracture surface.

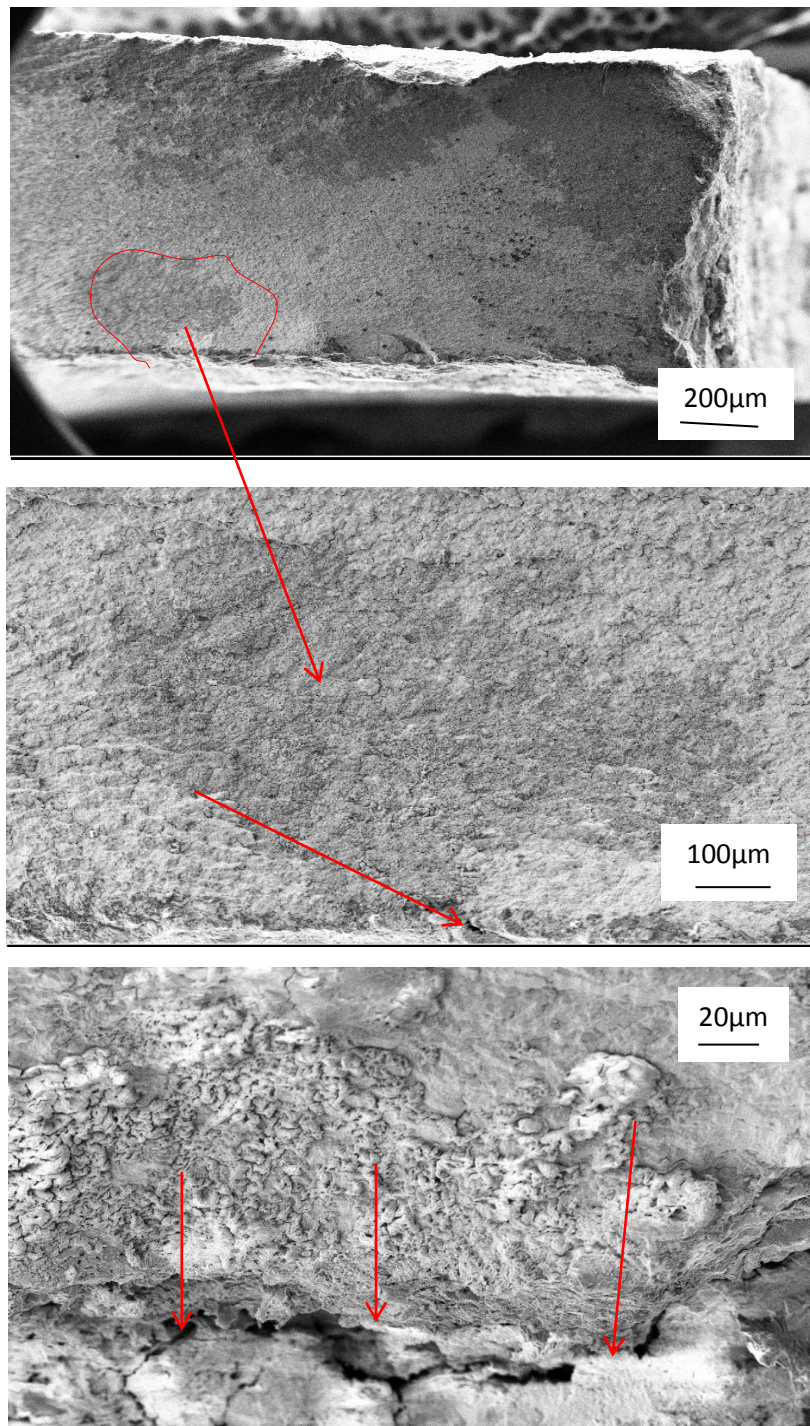


Figure 6.25: SEM micrographs for specimen showing (a) An overview of the fracture surface for corroded specimen (b & c) tunnelling and subsurface pitting, arrows indicate direction of subsurface pit growth by tunnelling.

7. Discussion

7.1 Introduction

In reality, there are many considerations that designers need to account for, in particular, environmental conditions impact material behaviour where, for example, the effect of corrosion plays an important role over the life of vehicle chassis and suspension components in reducing the fatigue performance. The effect of various environments on fatigue properties of FB590 steel and its weld is the main focus of this study and has been addressed in detail. There are several main findings which will be highlighted in this chapter which contains a discussion of the results presented in previous chapters. The discussion focusses on the FB590 results since the test programme using FB590 was more comprehensive than that using mild steel. The discussion has been divided into five key areas. Conclusions are then drawn from the present work in Chapter 8 together with some suggestions for further work.

7.2 Materials Selection

7.2.1 Steel Grades

Two steel grades were selected for use in the project, 3mm thick mild steel and 2.7mm thick high strength low alloy steel (FB590). Initially, it was decided to start the experimental work using mild steel in order to develop the testing methodology which utilises a number of different techniques such as the fatigue testing machine and the monitoring equipment AE and DIC and profilometry. Subsequently, the finalized procedure was applied to high strength steel (FB590) and its welded structure, after overcoming the obstacles and problems such as background noise, time misalignment with cycles and so on, in an effort to minimize material wastage of the available FB590.

Figure 7.1 shows a comparison between the stress-strain curve of mild steel (MS) and high strength steel (HSS). Figure 7.2 shows another comparison between the S-N curve where both MS and HSS were tested under constant amplitude, using a similar servo-hydraulic fatigue testing machine, under tension-tension testing with

load ratio $R=0.1$. It can be clearly seen from Figure 7.2 that the HSS has better fatigue performance than MS, this indicates material strength has a significant influence on the fatigue performance of the material. Previous literature (Benham et al. 1996; Fournalis et al. 2007) demonstrates that the fatigue performance of steel increases with ultimate tensile strength, whereas other researchers (Bright 2012; Pang et al. 2013) argue that the yield strength of the material plays a significant role in the fatigue performance. From the available literature it is therefore clear that there is a relationship between the fatigue performance and the material strength, although the exact nature of this relationship is under dispute.

Further work is therefore required to show the relation between material strength and fatigue strength and compare with available literature. The two materials utilized (MS and HSS) are not sufficient to fully explore the nature of this relationship. Furthermore, it is difficult to compare fatigue results taken from previous published data due to possible variations in test procedure, sample size and orientation.

There available fatigue data found for materials mainly used for automotive applications is limited, and the data used in this thesis for comparison was taken from Bright(2012). In this work, XF350 was tested with load ratio 0.1 on fatigue test equipment at Cardiff University similar to that used for the tests in this study. The second material, XF450, was tested at TSSP-UK's Swinden Technology Centre (STC) at Rotherham with load ratio 0.05 on different fatigue test equipment.

All these data were added to the present MS and HSS and are shown in Table 7.1. Figure 7.3 shows a comparison of material strength with the stress at 10^6 cycles. It is evident from the figure that there is a strong relationship between fatigue life and material strength (ultimate tensile, yield or the average of yield and tensile) where fatigue life generally increases with material strength.

From the literature review (Fournalis et al. 2007; Pang et al. 2013), it was found that the average ratio of the fatigue strength to tensile strength is approximately 0.45. As can be seen from the data presented in Table 7.1, the mild steel showed that the ratio of fatigue stress at 10^6 cycles/UTS is 0.49 which is approximately close to the value reported by earlier studies. However, the average value of the

ratio for the high strength steel was found to be 0.74, significantly different from the value reported by earlier studies. That said, the fatigue resistance of the high strength steel could be conservatively predicted by the existing fatigue design curves for normal strength steels, when using this ratio of 0.45. Although highly conservative, estimation would, at least, be safe in terms of the fatigue performance, this is consistent with Ellwood (2003) and Chiew et al.(2015)

It was shown in the above discussion that the fatigue performance of steel increases with tensile strength. This statement has been shown to be true for simple geometries without stone chipping, corrosion and welds. However, complex geometries can reduce the expected fatigue performance of the HSS compared to the mild steel, due to the HSS exhibiting a greater sensitivity to notches, effectively reducing the fatigue strength in areas that contain holes or any stress concentration. This is because high strength steels have a fine-grained structure more adversely affected by a rough surface finish than softer, coarse grained steels (Ellwood 2003; Thomas et al. 2011).

There is evidence in the literature (Maddox 1991; Ellwood 2003) that no increase in fatigue performance when compared to mild steels is observed for high strength steels once they have been welded, while the others (Long and Khanna 2007) concluded that there is an increase in the fatigue performance with the welded joints of some modern steels such as dual phase or micro-alloyed (HSLA). However, the improvement is significantly reduced when compared to the unwelded results.

This conclusion is beneficial to both the steel and automotive industries in understanding how mechanical properties correlate with fatigue performance across a wider range of products, due to the time consuming and costly nature of comprehensive fatigue tests. However, there is no clear relation between fatigue performance and material strength in the corroded and welded samples.

7.2.2 Comparison of FB590 with other materials

A comparison of S-N curves for XF350, XF450, and FB590 (as received) is shown in Figure 7.4, which indicates the relative fatigue performance of these materials. The steels compared in the present study are of different types but generally of low carbon equivalent and mainly used for automotive applications, with the XF350 and XF450 data taken from Bright (2012).

It is possible to compare the data of XF350 as it is tested with similar load ratio to the FB590 tests in this thesis, whereas the XF450 was tested with a load ratio of 0.05 and there is no available data with load ratio 0.1. These comparisons were performed on as received material since there is no available fatigue data for the stone chipping and pre-corrosion treatment either as these tests have not been performed or the resulting data is commercially confidential.

It can be seen that the XF450 showed broadly similar fatigue resistance to FB590 although it is slightly higher than the expected trend of load ratio 0.1 since the test was carried out at a load ratio of 0.05. XF350 material showed a lower resistance to fatigue failure compared to FB590. FB590 steels showed good fatigue strength due to the improvement in its mechanical properties. Further work was performed to explain the effect of the small change in load ratio for XF350, where a comparison was performed between XF350 at load ratio 0.1 and 0.05 as shown in Figure 7.5. There is a slight difference in fatigue performance for both load ratios. This could justify that the fatigue properties of FB590 are supposed to be higher than XF450. The fatigue properties of FB590 tested in this study were higher than XF350 and XF450 grades reported in the literature, although the latter results exhibit significant amount of stress concentrations due to their sample dog-bone shape.

Another comparison between the fatigue performance of FB590 manufactured by Tata Steel and another FB590 material supplied by ArcelorMittal (ArcelorMittal brochure Last update: 10-06-2015) is shown in Figure 7.6 which shows that both these FB590 steels have very similar fatigue strengths.

7.3 Effect of corrosion, stone chipping and welding on fatigue life

Fatigue tests were carried out on a set of specimens exposed to stone chipping and corrosion in both welded and as-received form, in order to assess the influence of these types of damage on the initiation of fatigue cracks in FB590 steel. Initially, the approach was to increase an understanding of the mechanisms of damage and consequences of such damage resulting from exposure to various environments, including scratches, pitting, geometry effects and recognizing that such discontinuities could act as a stress raiser where cracks can be nucleated.

The impact of stress levels, welding and stress concentration due to surface exposure to stone chipping and to saline solution on the fatigue life of the specimens will be discussed in more detail in subsequent sections.

7.3.1 Effect of stress magnitude on fatigue life

It is evident from Figures 6.15-6.18 in the previous chapter that the different surface exposure treatments do not have as significant an effect on fatigue life as the stress magnitude. At the higher stress levels, the fatigue resistance of any surface exposure types were broadly similar to those of the pristine specimens also the scatter in fatigue data seems to be less. At the lower stress levels, the fatigue resistance of base line material is higher than that of specimens exposed to various surface exposure treatments, due to the presence of additional stress concentration at corrosion pits on the non-pristine sample.

For further explanation of the interactive effects of the stress level and other types of surface treatment, Tables 7.2, 7.3 and 7.4 contain the results for the fatigue experiments with specific stress magnitudes for mild steel under tensile loading only and for FB590 under bending and tensile loading. These tables include different surface exposure treatments, stress magnitudes and cycles to failure. These tables also showed that tests were not carried out below the endurance limit load or higher than the load of short tests to conserve available material.

From these tables it is obvious that at a given corrosion level, increasing the stress decreased the fatigue life in each type of surface treatment. Moreover, at any given stress level, the specimens exhibited shorter lives with increased corrosion levels.

The results also seem to show that the 400MPa stress level was high enough in case of the corroded specimens of FB590, that it considerably overcome differences in corrosion damage over the range of corrosion exposures examined. The two pristine specimens of bending and tension loading of FB590 did not fail under 400Mpa, and were treated as run outs after being removed from the test machine after more than 5×10^6 cycles.

Going back to Figure 6.10 the results showed that the S–N curve of the parent material under bending loading exhibits a very smooth transition from low to high cycle fatigue regime. Note also that the gradient of the graphs appear very negative but in reality it is relatively ‘shallow’, and this appearance is due to the scale of this graph. For this reason Figure 7.7 was added to highlight and show the data of Group1 under bending alone. Here, a small fatigue stress increase of about 25 MPa is sufficient to reduce the fatigue life from higher than 5×10^6 cycles to less than 8×10^4 cycles, this is thought to be due to plastic deformation. The theories used for the determination of bending stiffness are derived under the condition that the test piece is perfectly flat at the beginning of the test and without plastic deformation effects (Dupen 2014). In a real situation, the test piece deviates from flatness and includes plastic deformation.

These results further support the general conclusion that the increase in stress magnitude decreased the fatigue life. At the higher applied stress levels, the differences in fatigue lives between the ecoated pristine specimen to the specimen with high corrosion levels became less pronounced. The analysis also suggests that stress magnitude has a higher detrimental impact on the fatigue life of the specimens as compared with any kind of stress concentration due to the stone chipping, corrosion and weld. This trend is clear in both mild steel and the high strength steel in spite of the tests being concentrated on FB590. This result is consistent with other works of Liu et al.(2011) and Gruenberg et al. (2004).

7.3.2 Effect of stone chipping on fatigue life

Previous literature (Razin et al. 2015) has shown that the stone impact to the surface of coating may result in four types of failures including (1) coating loss from the primer layer, (2) fracture at electro depositing ED/primer interlayers, (3)

coating damage from the phosphate/ED interlayer and (4) coating detachment from the steel substrate. In the current study, the specimens were ecoated only without applying other layers, so coating detachment from the steel substrate is the main failure type resulting from stone impact on the surface of coating. However, the worst effect of the stone impact is to cause local removal of the material (surface voids), which would create stress raisers. Figure 6.19 showed an example of fatigue specimens failed from stone chipping sites, the crack origins were at locations where local removal of the material (surface voids) has occurred due to grit blasting of the surface. Materials with fine-grained structures such as high strength steel are more sensitive to surface appearance and become more adversely affected by a rough surface finish than softer, coarse grained steels (Ellwood 2003; Thomas et al. 2011).

Figure 7.8 shows a comparison between both S–N curves of Group 2 and Group 1. These curves show a comparison between different surface roughnesses for specifically unwelded specimens in order to highlight to the effects of stone chipping on unwelded specimens and to distinguish these from weld-related effects. It can be observed that the gradient of both curves of Group 1 and Group 2 are very similar. The position curves of the Group1 (Ra of 0.582) shifted to the left by moving from lower to higher surface roughnesses (Ra of 5.78) of Group2. This trend is very clear in tensile loading, whereas it is less pronounced in bending loading of Group 1 where the latter showed longer life due to having plastic deformation. Moreover, the fatigue strength of group 2 is slightly lower than the finer specimen in the higher stress level or shorter life region, while in the lower stress level or longer life region, the degree of decrease in fatigue strength is more pronounced.

It can be observed from Figure 7.8, that the fatigue resistances of the stone chipped specimens is noticeably decreased and their fatigue life was less compared to intact specimens, the base line Group 1 specimen had higher fatigue limit and longer fatigue life compared to those of the stone chipped specimens. The absence of surface roughness defects in the intact specimens would contribute to the higher fatigue properties. Therefore, with decreasing levels of surface roughness, the S–N curve shifted to a higher stress level, indicating increased fatigue strength.

Special attention was devoted to identification of fatigue endurance limits although significant amounts of time are required to characterize the fatigue properties of a material in which no crack initiation occurred within these cycles. The endurance limit of the all types of fatigue test specimens is presented in Table 7.5. The fatigue limit of the specimen was taken when the number of cycles to failure, N , is greater than 5×10^6 . The horizontal arrows shown in curves indicate a run-out, for example a fatigue test is suspended at a very high number of cycles, without evidence of fatigue damage. In this section of particular interest is the endurance limit of group 2, where it can be observed that there is a noticeable reduction in fatigue endurance limit due to the specimens being stone chipped. It was found that the intact specimen had the highest fatigue limit for bending loading of 520 MPa whereas for stone chipped specimens the fatigue limit was 375MPa. The intact specimen under tensile loading did not fail at a stress level of 400 MPa whereas the fatigue limit for stone chipped specimens was 337MPa. It is worth mentioning that there is no available published literature on the effect of stone chipping on fatigue life, since most of published studies on the effects of stone chipping address coating resistance. Therefore, this study is beneficial to automotive designers in order to take the effects stone chipping into account in consideration of design.

7.3.3 Effect of weld on fatigue life

It is necessary to characterize the effect of weld on fatigue life under different environmental treatments to provide a realistic data to help the steelmaker and automotive designers to predict the behaviour of FB590. Figures 6.10-6.14 show comparisons between welded and un-welded specimens for each surface treatment or environmental state under tensile and bending loading. It was observed from these S-N curves that the gradient of the unwelded curves are flatter than the welded curves. The position of the un-welded curves is shifted to the left by moving from the low-stress concentration of the un-welded specimens to the high-stress concentration of welded specimens.

It can be observed from Figure 7.9 that there is no large difference between the S-N curves of tensile welded specimens of ecoated only (Group1) and stone chipping (Group2). The possible reason is that the effects of stress concentrations due to the weld are more significant than the stone chipping effects.

It can be seen from Table 7.5 that there is a specific endurance limit for each welded specimen under different environmental conditions. In general, the fatigue limit was very low compared with the ultimate stress of pristine specimens. Other previous studies reported in the literature (Kirkhope et al. 1999; Bright 2012; Stenberg et al. 2015) did not show endurance limit for steel possibly because the stress level was not low enough. Nevertheless, the fatigue reduction stress of the welded material (Group 1) is 50% of the corresponding value of the base material for tensile loading. Lower values were also obtained in the bending loading test, of 57%.

What is clearly noticeable from Figures 6.10-6.14 is that welding in any aforementioned environments has a hugely detrimental effect on the fatigue performance of the steel strip. The reduction in fatigue life of welded specimens does not come as a surprise, where there is much available literature which indicates that the geometry is one of the primary factors that controls the fatigue life of welded joints. The weld toe is one of the most probable fatigue crack initiation sites in welded components due to high levels of stress concentration, rather than any reason caused by the original specimen microstructure, and/or properties relating to the filler material as explained by several studies (Caccese et al. 2006; Bright 2012; Harati et al. 2015; Stenberg et al. 2015). However, this does not mean one can neglect or reduce the role of microstructure effects where the material displays increased brittleness as shown by the hardness tests in section 5.7. This is also consistent with Wang et al.(2016).

The welded specimens were found to be more variable than non-welded specimens, despite the welding process being automatic which could reduce the amount of variability. The variability of the welded specimens is due to microstructural changes and the stress concentration caused by the local weld toe profile, which causes a large scatter in fatigue data for welded joints with the same nominal overall geometry even under constant amplitude loading and controlled laboratory conditions (Alam et al. 2010; Mohd et al. 2012). Before considering weld stress concentrations, it is recommend that a component should be designed to guarantee that the welds are in areas of low stress and the parent material should transfers the loads, not the welds, although, this may result in limit material design.

DIC can be considered a useful technique to highlight the weld stress concentration as can be seen in Figure 7.10. It can be seen from the colour scale that the main body of the specimen is experiencing the expected level of strain of around 2.75 millistrains that was calculated using proof stress and modulus of elasticity for this material whereas the weld toe showed more than 30 millistrains, demonstrating a significant stress concentration.

There is conflicting information in the literature on the effects of welds - some reports (Costa et al. 2010; Jiao et al. 2013) claim that no increase in fatigue performance is observed between high and low strength steels once they have been welded, whilst others (Long and Khanna 2007) concluded that there is still an increase in the fatigue performance with the welded joints of some modern steels such as dual phase or micro-alloyed (HSLA). However, the improvement is significantly reduced when compared to the unwelded results. To investigate this, a comparison between S–N curves of welded FB590 and XF350 is shown in Figure 7.11. Although two materials are insufficient to indicate a general trend, it can be observed that there is a slight increase in fatigue performance of FB590 with increased material strength when compared to XF350.

7.3.4 Effect of pre-corrosion on fatigue life

The test results of pre-corroded specimens generally showed the expected trend of decreased fatigue lives at increased corrosion exposure levels, with no unusual data trends. It was observed from Figures 6.15- 6.18 that the gradient of S-N curves of the uncorroded specimens is slightly flatter than curves of the corroded specimens, and the position of the curve would be shifted to the left by moving from the low stress concentration of un-corroded specimens, to the high stress concentration of corroded specimens.

The fatigue resistances of pre-corroded specimens drastically decreased and their fatigue life was less when compared with the intact specimens. As seen from Figures 6.15- 6.18, the un-corroded Group-1 specimens had a higher fatigue limit and longer fatigue life compared to those of the corroded specimens, this is consistent with the previous literature reported by Rusk et al. (2009) and Shan-hua (2015). The higher fatigue limit and the longer fatigue life of intact specimens

is caused by the lack of stress concentrations due to surface roughness. The stress raiser points increase proportionally with the surface roughness. Therefore, the crack can start to propagate at any point, where there is the highest stress raiser. Group 4 showed the worst fatigue life, and both Group 5 and Group 3 exhibited nearly similar lifetimes due to the similarity of their roughness parameters (S_z , S_t and S_v) as shown in Figure 6.7.

The specimens of Group-4 were clearly the most affected by the pre-corrosion treatment. Figures 6.13 showed there is no large difference between SN curves of welded and unwelded specimens in both bending and tensile loading for Group-4, these curves are close and similar to each other. It was also observed that the fracture was far from the welding location in most of the failed specimens as shown in Figures 7.12. This suggests that the corrosion has a more significant effect than the weld stress concentration due to mainly pitting corrosion and, with increased corrosion time, metal dissolution and conversion to metal oxides or hydroxides which increased volume causing metal separation, as it was explained from fracture surface analysis in section 6.7 and 6.8. These observations are consistent with those of Rezig (2011) and Arriscorreta (2012).

It was observed from the visual inspection and optical microscopy that the corrosion product very often covers the pits and also that the observable pit surface diameter is generally smaller than the actual maximum diameter of the pit. The pitting corrosion can be considered as one of the most dangerous form of corrosion due to the difficulty of detection (Rokhlin et al. 1999; Zhang et al. 2013). The detection of smaller pits and undercut pits is very difficult especially when using a line-of-sight technique as the profilometer characterization. Thus, this method has some limitation for pits with narrow and deep dimensions as well as corroded materials with subsurface, tilted and horizontal pits. However, fracture surfaces were examined to cover this limitation.

The endurance limit for each surface treatment was summarized in Table 7.5, which indicates that the unwelded Group -1 specimens had the highest fatigue limit. It can be seen from Table 7.5 that there is a specific endurance limit for each group of pre-corroded specimens and welded specimens as explained in Section 7.2.3. Although the fatigue limit was significantly lower than of pristine

specimens, other previous studies (Liu et al., 2011) did not show fatigue limits for the pre-corroded specimens possibly as their stress level was not low enough to allow identification of the endurance limit. The fatigue strength of corroded specimens is significantly reduced by around 50% compared with pristine specimens under tensile loading, and by 42% for bending loading however the latter could be not precise due to the bending specimens showing much plastic deformation.

Figure 7.13 shows the endurance limit stress of each surface treatment vs corresponding roughness parameters for tensile and bending loading of FB590 unwelded specimens, whilst Figure 7.14 shows corresponding trends for the mild steel. The fatigue limit decreases with the increasing level of roughness for both materials. It is important to note that the surface appearance affects the fatigue life greatly, and corrosion would cause the surface to become rougher, thereby rapidly reducing fatigue life and endurance limit (Alang et al. 2011; Wang et al. 2013).

Figure 7.15 shows S-N curves under tensile loading for both high strength steel and mild steel in the as received condition and following corrosion for two months. It can be observed from Figure 7.15 that corrosion in the high strength steel has a more significant effect than in mild steel. This is since the high strength steels have a fine-grained structure which appears to be more adversely influenced by a rough surface finish than softer steels which have coarse grained structures (Ellwood 2003; Bright 2012).

To summarise, pre-corrosion damage facilitates essentially the onset of fatigue cracks and hence reduces the fatigue life of the corroded specimens appreciably. Because of multiple reasons such as the reduction in the effective cross sections of the specimens, this poses a risk of increasing the stress which subsequently reduces the fatigue performance of steel components. Moreover, existence of different forms of pits and metal dissolution and conversion which take place with increased time of corrosion reduces the fatigue life. The corrosion increases the surface roughness which becomes stress raiser points at which cracks may initiate.

7.4 Combination of monitoring using AE and DIC techniques

The current study provides insights into the mechanisms that take place in the way of final failure. The completed work has demonstrated the capabilities of AE for detecting fatigue fractures, and its potential for distinguishing the different AE signals from various possible failure mechanisms. DIC was used to support the understanding of the detected AE signals. DIC allows a clear depiction of the surface strain field evolution and its transient changes according to stress redistribution which occurs as the crack propagates. It is a useful method for monitoring the whole area of interest and it is not limited to a specific region, therefore damage can be detected even if the precise location is not known in advance.

Both AE and DIC techniques have advantages and disadvantages as explained in the literature (Aggelis et al. 2013). However, the complementary use of DIC and AE helps to minimise the assumptions in the interpretation of the AE trends in relation to the responsible damage mechanisms by revealing the fluctuation of the surface strain fields and other factors such as paint delamination. A small number of previous studies have been conducted using the combination of DIC and AE under fatigue loading as explained in detail in Chapter Two. This work aimed to establish a full understanding of the use of a combination of AE and DIC under fatigue loading in order to provide valuable experimental data and contribute to the limited literature in this field.

These techniques were used to monitor both mild steel and FB590 fatigue tests, where some differences were observed between these materials in term of AE signals and DIC behaviour. There is great variety in the acoustic emission produced by these materials. Acoustic emission has been shown to increase with increasing strength and decreasing ductility of the steels. The high strength steel produces acoustic emission copiously when loaded, whilst mild steel produces lower levels of emission by comparison, due to it being a softer material. The principle crystalline structure of a material plays a major role in its acoustic emission response, with signal amplitude level differences of an order of magnitude in some cases (Huang 1998; Barsoum 2009). DIC results revealed that

the crack mouth opening displacement in mild steel is more than FB590 as shown in Figure 7.16, suggesting mild steel yields more readily than FB590.

The combination of AE and DIC was also helpful in distinguishing between crack initiation and early propagation and background noise, which is otherwise difficult using AE. Therefore it could be possible to provide a failure alarm and location to the structure prior to any significant deformation. Early growth of cracks in steel typically generates only very low level AE which is difficult to distinguish from rubbing or fretting sources, for example of loose paint or corrosion products. The use of DIC allowed significant cracks to be identified well before failure. For instance, the DIC paint cracking was detected by AE and confirmed by DIC measurements (Shrama et al. 2014, 2015). This shows the effectiveness and powerful nature of this combined monitoring technique which can not only detect the paint cracking but provide evidence of the fatigue process. The combination of AE and DIC can provide much useful information to help to distinguish the different AE signals originating from various possible failure mechanisms such as plastic deformation, delamination of DIC paint and crack initiation and propagation. This could have numerous applications and economic impact in testing more complex structures, for example in automotive chassis or aerospace applications.

7.5 The Possible Applications of this study

From this study there are several possible applications have been highlighted that steel maker and designers can take into account to optimise the design and reduce its weight.

1-The main aim of this study was to experimentally investigate the fatigue properties of mild steel under tension loading and two levels of corrosion as preliminary tests. Then a comprehensive fatigue test programme was performed on FB590 and its welds under bending and tensile loading and cover all environmental possibilities encountered by such material in practical usage. These results are significant because there is limited work and lack of sufficient available data for FB590 in terms of fatigue performance under in-service environments. This information provides automotive engineers with valuable data to help predict

the performance of chassis components under a range of various loading and environmental conditions, allowing a meaningful fatigue strength assessment of actual components. In addition, these results provide an effective guideline to improve the design and manufacturing methods of FB590 for different engineering applications.

2- In this study the fatigue tests under bending loading were conducted. There is a very little knowledge available on the bending fatigue properties of steel in general (Xiao et al. 2012) and in particular the bending fatigue properties of this grade are unavailable elsewhere. Fatigue data in axial loading are insufficient for assessing high cycle fatigue limit stress which often occurs in components that are subjected to flexural loading such as automotive chassis and suspension (Xue et al. 2007). For this purpose, the author investigated the bending fatigue master curve behaviour in order to obtain sufficient fatigue data for a meaningful fatigue strength assessment of actual component. Flexural tests are an important test method in both the manufacturing process and research and development to define a material's ability to resist deformation under load. This work is beneficial for automotive engineers where the automotive chassis and suspension components are often subjected to various combinations of repeated axial and flexural loading due to irregular bumping especially in the off-road sector.

3-The fracture surface was studied using SEM to determine the failure mechanisms of each surface treatment such as pristine, stone chipped and corroded material. This initially helped to overcome the limitations of stylus profilometry which is a line-of-sight technique which cannot detect metal dissolution and subsurface failure modes including undercut pits, tunnelling, and subsurface cracking. These findings provide useful understanding that could help the steel industry to enhance the product and produce more extreme protection methods useful to aid the reduction of gauge loss due to corrosion.

4-It was observed that welded specimens showed low fatigue strength and were affected by corrosion as well. From this observation, a component should be designed to ensure that the welds are in areas of low stress and the parent material

transfers the loads, not the welds. Although, this may lead to limit design material also need extreme protection for welded parts.

5- In the current study, the fatigue tests were performed under a single stress ratio, $R=0.1$, under high mean stresses which is more dangerous than tests with low mean stresses (load ratio < 0.1). A tensile mean stress (σ_m greater than 0) has a detrimental effect upon the fatigue life and fatigue limit. The detrimental effect of a tensile mean stress is associated with the opening of microdefects due to tensile loading, resulting in earlier crack initiation and shorter crack propagation life (Benham et al. 1996; Bright 2012). Therefore the current study is considered more conservative than the studies which were conducted under lower mean loads due to components usually failing at higher loads.

7.6 Research limitations and implications

There are several limitations inherent in this study. One limitation concerns that the all fatigue tests of FB590 were performed at a single stress ratio, $R=0.1$. However, the actual loading conditions of structural automotive components associated with chassis and suspension may differ significantly from the fatigue data available for the material. Therefore, to overcome this limitation fatigue tests at multiple stress ratios should be carried out in order to identify the true nature of Tata material with regards to its performance under a wide range of mean stress.

A second limitation is that all fatigue tests was performed based upon simple samples although, stress in components are observed different around the welds. To exceed this limitation, larger test components should be considered such as welded beams, top hat sections or suspension arms, which are tested under similar environmental circumstances to study the effects of these damage sources on the fatigue performance in more realistic and complex components.

The third limitation can be stated as explained previously that the profilometer characterization is a line-of-sight technique and cannot measure subsurface, tilted and horizontal pits as well as and smaller pits with narrow and deep dimensions. The deepest pits are also hidden from view by material above them. In addition,

the bottom surface of the damage was not regular in shape with the presence of significantly deeper local areas than the rest of the damage. However, fracture surfaces were examined by using stereo optical microscopy and SEM in light of this limitation (Pidaparti and Rao 2008; Xu and Shan-hua 2015).

A fourth limitation of this study is that there is no fatigue life estimation using FE modelling. However this study considers the experimental testing of FB590 which is a time consuming and expensive operation. This metal was not tested before under different environments, so these results can constitute an experimental model, which provides the engineer with sufficient fatigue data for a meaningful fatigue strength assessment of actual components.

The fifth limitation is a lack of published industrial papers and previous experimental data due commercial sensitivity of such data, making it difficult to benchmark results against published data.

In addition, the AE analysis was limited to traditional parameter-based techniques, since waveform analysis was beyond the scope of the discussion in this study. Because most of the fatigue tests were very long in duration, especially those tests which identified endurance limits, acquiring huge amounts of AE data for waveform analysis was cumbersome and counter-productive in the context of this study, where AE was used as a monitoring tool rather than being the subject of research focus itself. According to the literature (Barile et al. 2015; Mazal et al. 2015) the traditional AE technique is well suited for the cases in this study, where the main aim of this project is to identify the fatigue properties of FB590.

Finally, the flaking of DIC paint during fatigue tests led to the generation of further AE signals. These AE signals can be considered as AE noise as they are not related to fatigue processes. Previous literature (Pullin et al. 2010b, a) recommended the use of DIC to support the understanding of the detected AE signals, since it is a non-contact method so as not to produce frictional sources of AE in the crack region, preventing the use of contact methods such as crack mouth opening displacement gauges and strain gauges. In this study the DIC paint was sprayed on specimen surface which some contains corrosion product, and when the specimen

was loaded the rust was cracked and delaminated from the surface. However, these signals were distinguished from other signals originating from the fatigue process.

7.7 Conclusion

In summary, this chapter has shown a discussion of the numerous factors that affect the fatigue life in general, and more specifically of FB590 steel which is used for automotive chassis and suspension applications, owing to the fact that little information is usually available to the designer about the fatigue performance of steel and its weld under conditions similar to the operating environments. Furthermore, the various environment impacts were studied on fatigue properties of tension and bending loading of steel and weld which were not covered well, thus, the impact of each factor was discussed individually.

Moreover, there is a particular focus on effects of stone chipping on fatigue life where no available published literature was available which addressed the effect of the stone chipping on corrosion and fatigue properties. Most of the studies concentrated on the determination and evaluation of coatings resistance to chipping damage by stones or other flying objects.

The other interesting thing in this study is highlighting the benefit of the monitoring fatigue tests using a combination of DIC and AE to identify the damage mechanisms that occur in the way of final failure, reinforcing previous finding in the literature.

Table 7.1: Comparison between mechanical properties of steels as well as comparison of the ratios of fatigue stress at 10^6 cycles/strength.

	mild steel	XF350	XF450	FB590
Tensile Strength (MPa) UTS	423	473	539.6	591
Yield Strength (MPa)	275	394	468.8	479
Stress Range at 10^6 cycles (MPa) (EL)	211	340	425	425
Strength mean =(UTS+ Yield)/2	349	433.5	504.2	535
EL/UTS	0.49	0.72	0.72	0.78
EL/Yield	0.76	0.86	0.90	0.88
EL/ Strength mean	0.60	0.78	0.84	0.79

Table 7.2: Results of mild steel fatigue experiments.

S/N	Stress (MPa)	Cycles to Failure as received	Cycles to Failure low level	Cycles to Failure high level
1	320	104247	95512	5642
2	300	183536	133596	90990
3	275	343197	129053	155161
4	230	2518366	612040	161492
5	211	5567586	1285177	821427

Table 7.3: FB590 results of unwelded bending fatigue experiments.

Surface exposure statuses	Stress (MPa)	Cycles to Failure	Stress (MPa)	Cycles to Failure	Stress (MPa)	Cycles to Failure
Group1	400	5295846	375	--	350	--
Group2	400	1315543	375	5301541	350	--
Group3	400	568888	375	807393	350	867824
Group4	400	--	375	50026	350	97200
Group5	400	237092	375	819355	350	5177380

Table 7.4: FB590 results of unwelded tension fatigue experiments.

Surface exposure statuses	Stress (MPa)	Cycles to Failure	Stress (MPa)	Cycles to Failure
Group1	400	5194844	300	--
Group2	400	260880	300	--
Group3	400	310484	300	356892
Group4	400	--	300	16484
Group5	400	18766	300	351105

Table 7.5: shows endurance limit for fatigue specimens.

Specimen condition	Bending endurance limit (MPa)		Tension endurance limit (MPa)	
	unwelded	welded	unwelded	welded
Group1	520	300	400	200
Group2	375	262	337	162
Group3	300	200	225	100
Group4	200	150	175	175
Group5	300	325	200	150

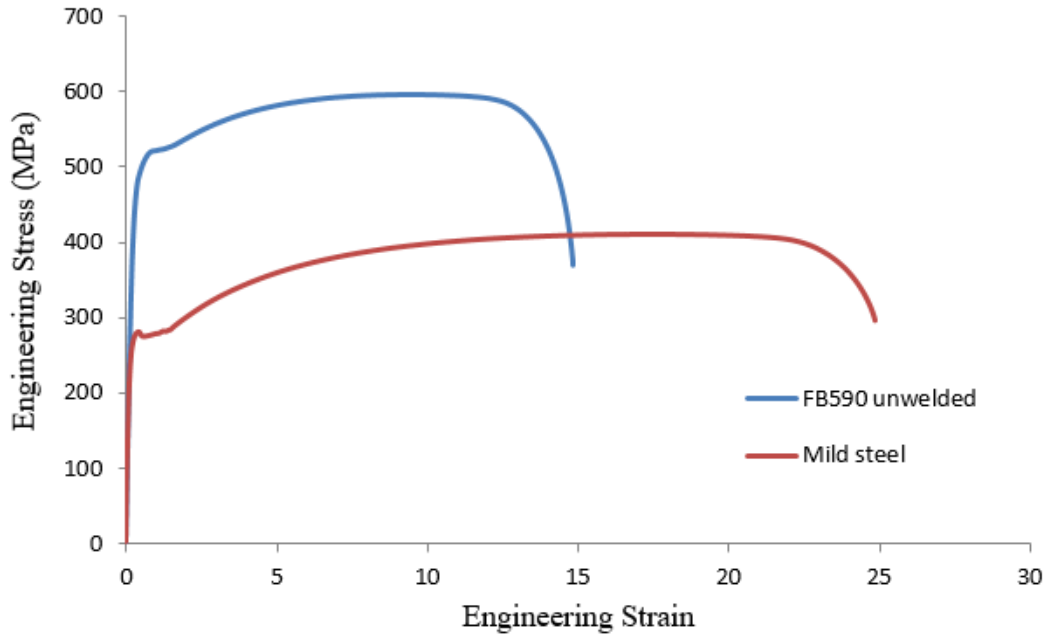


Figure 7.1 comparison between tensile properties of mild steel and FB590.

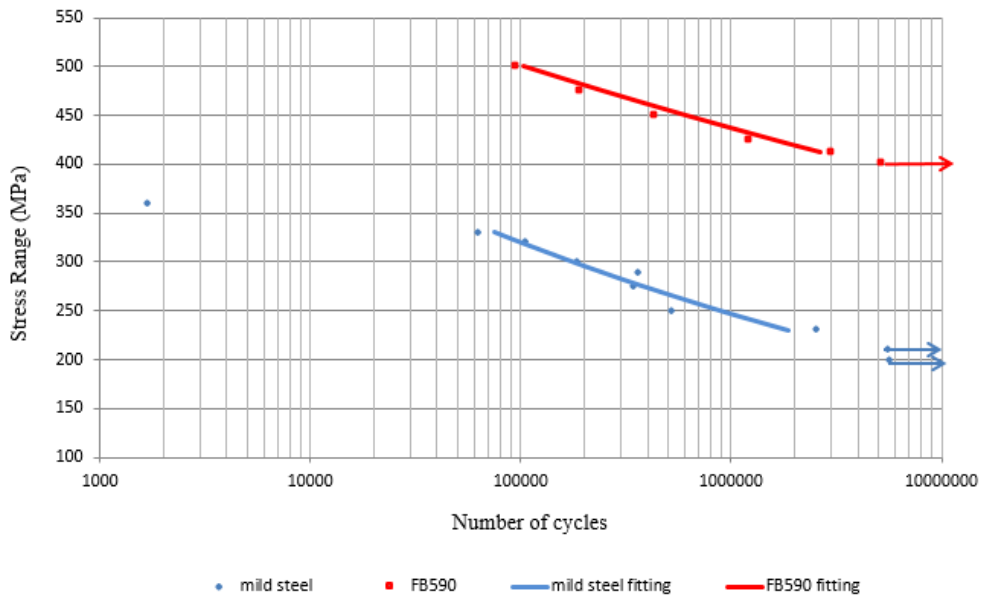


Figure 7.2 comparison between fatigue properties mild steel and FB590.

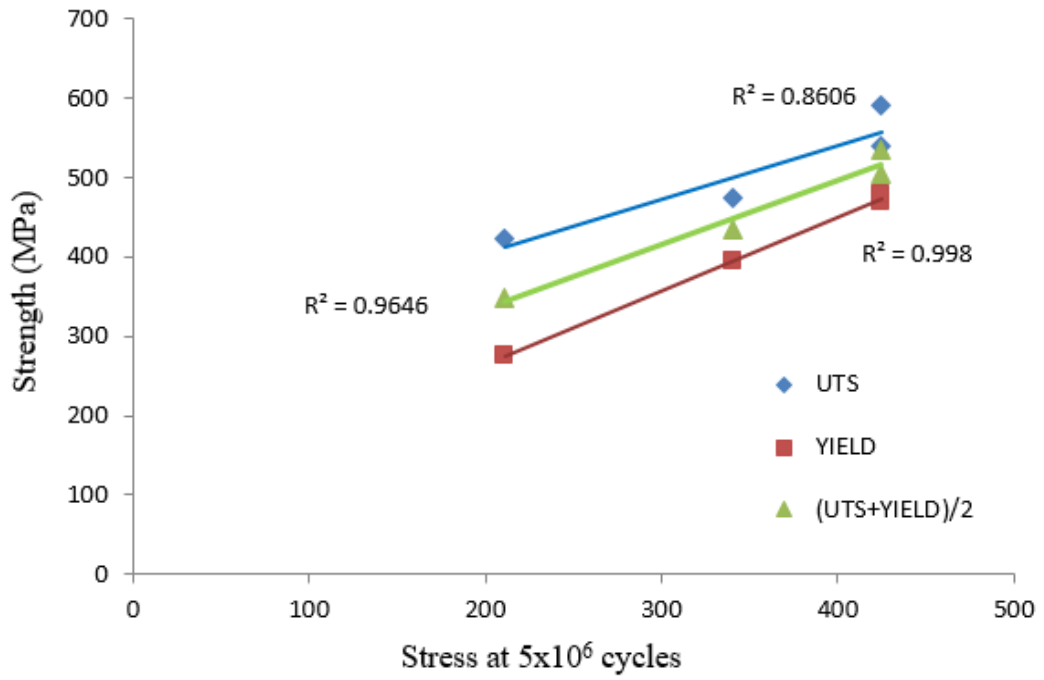


Figure 7.3 Material strength plotted against stress amplitude at 10^6 cycles for the mild steel and HSLA grades.

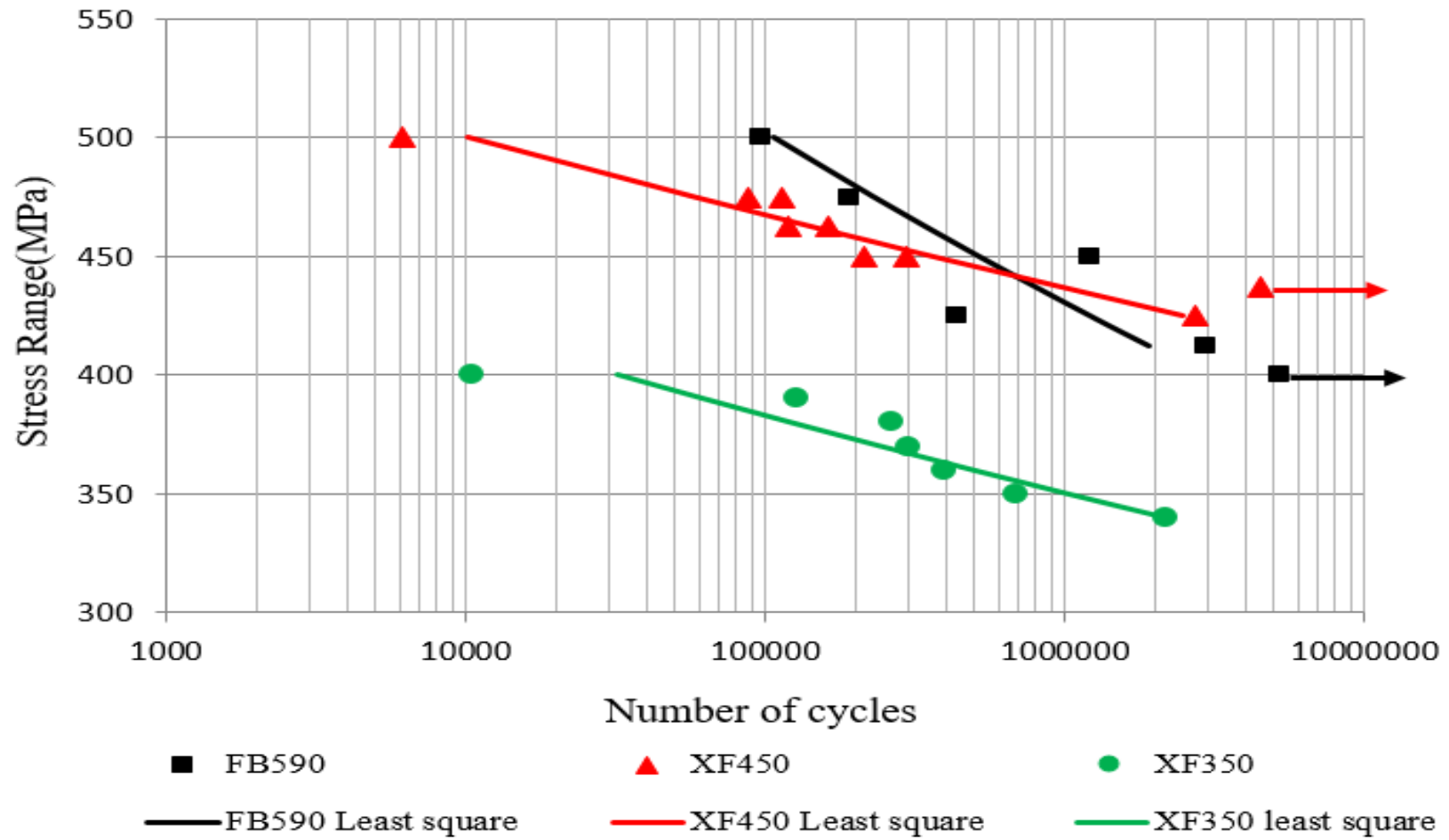


Figure 7.4: Comparison between S-N curves XF350 under load ratio 0.1 and the 0.05.

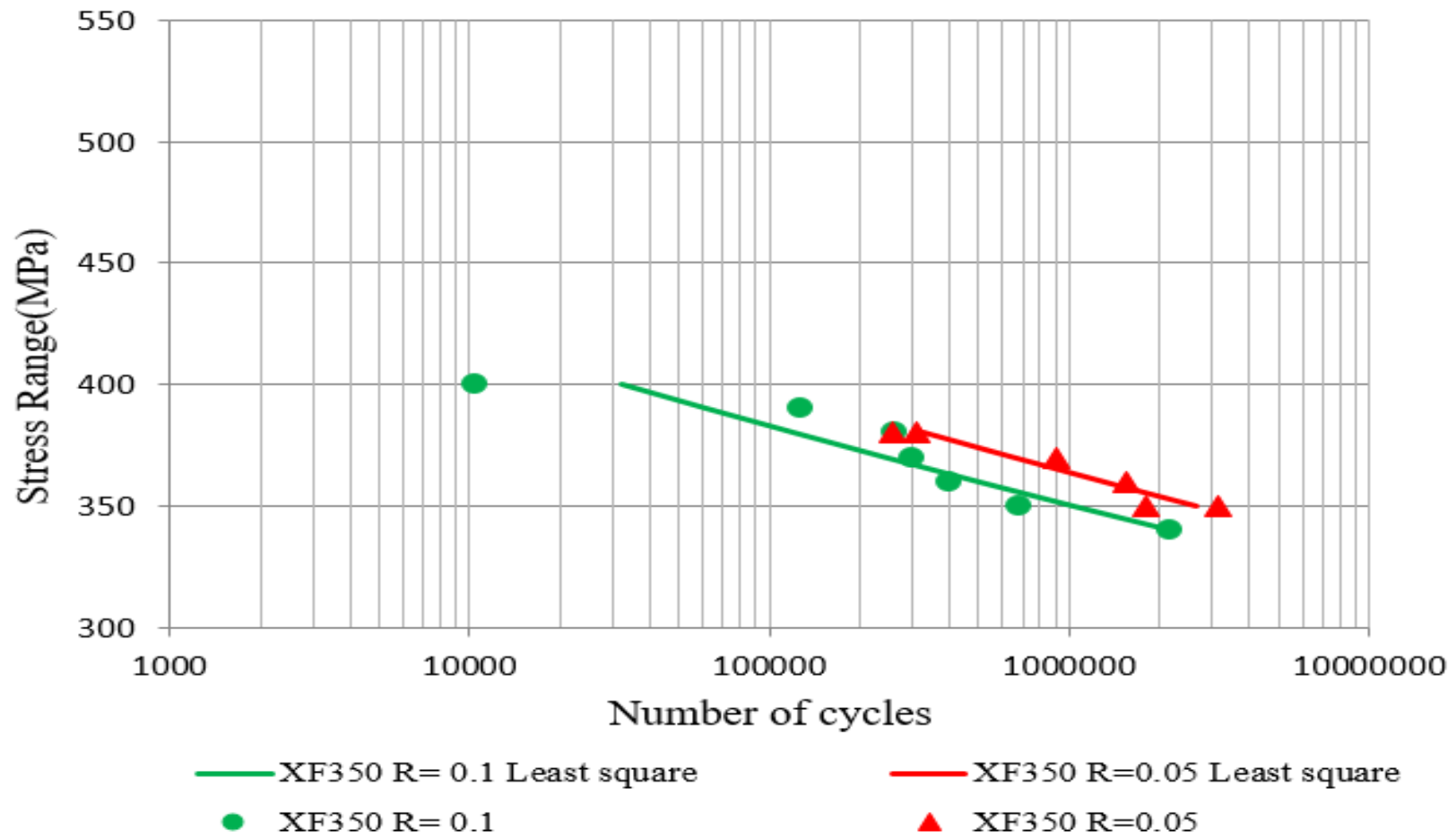


Figure 7.5: Comparison FB590 R=0.1 with XF350 R=0.1 and XF450 R=0.05 S-N curves.

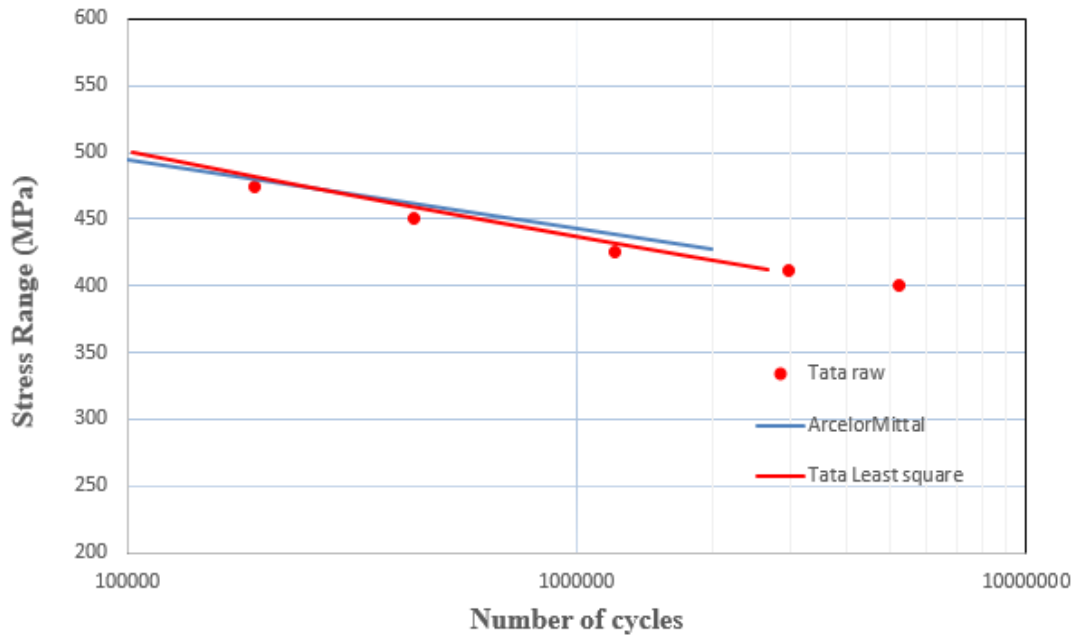


Figure 7.6: Comparison between FB590 of ArcelorMittal and Tata.

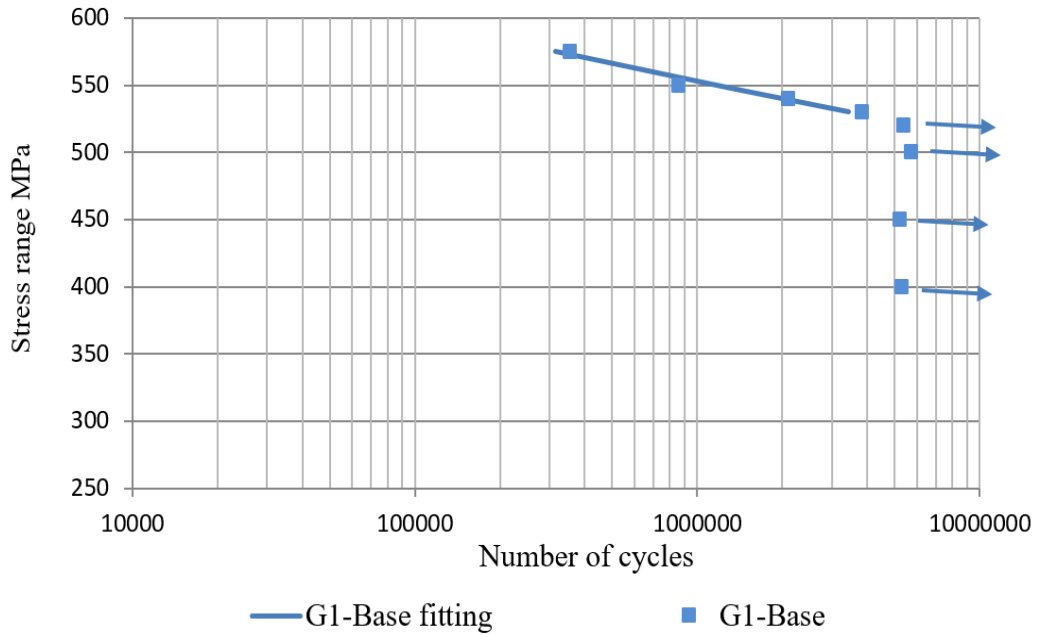


Figure 7.7: All S-N curves of Group 1 under bending loading.

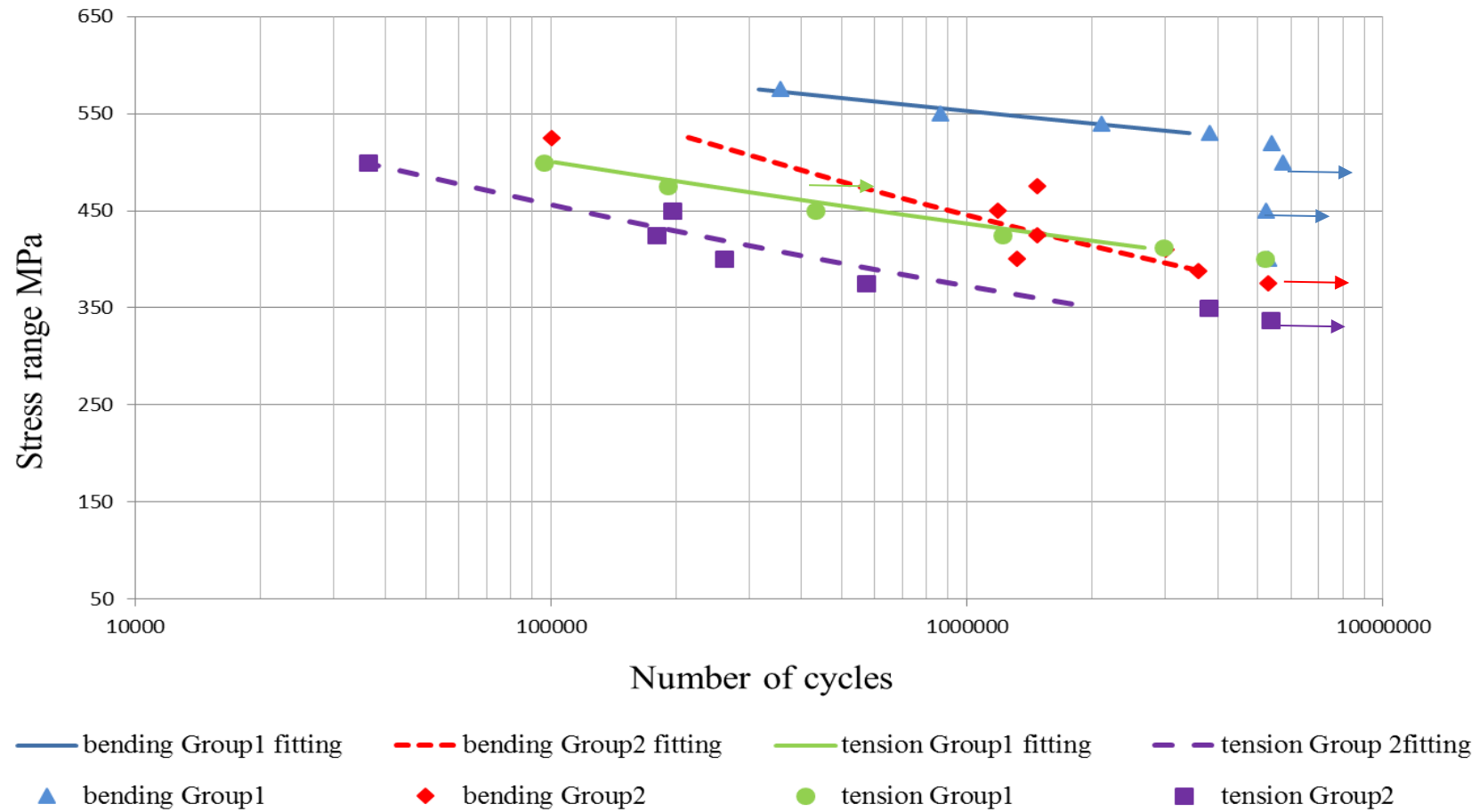
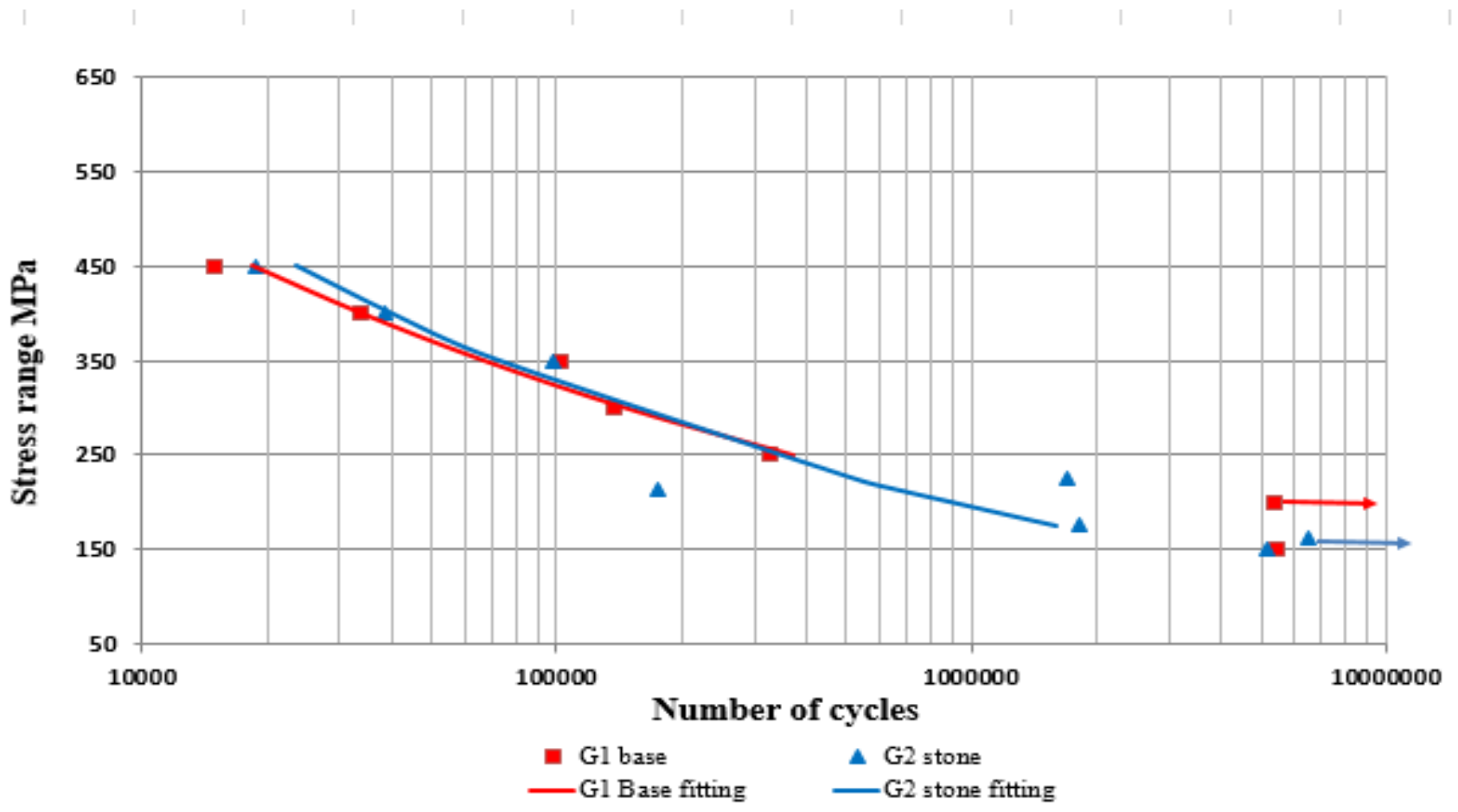


Figure 7.8 shows comparison between S–N curves of unwelded Group 2 and Group 1.



Figures 7.9 shows tension and welded specimens of base line Group1 and stone chipping Group2.

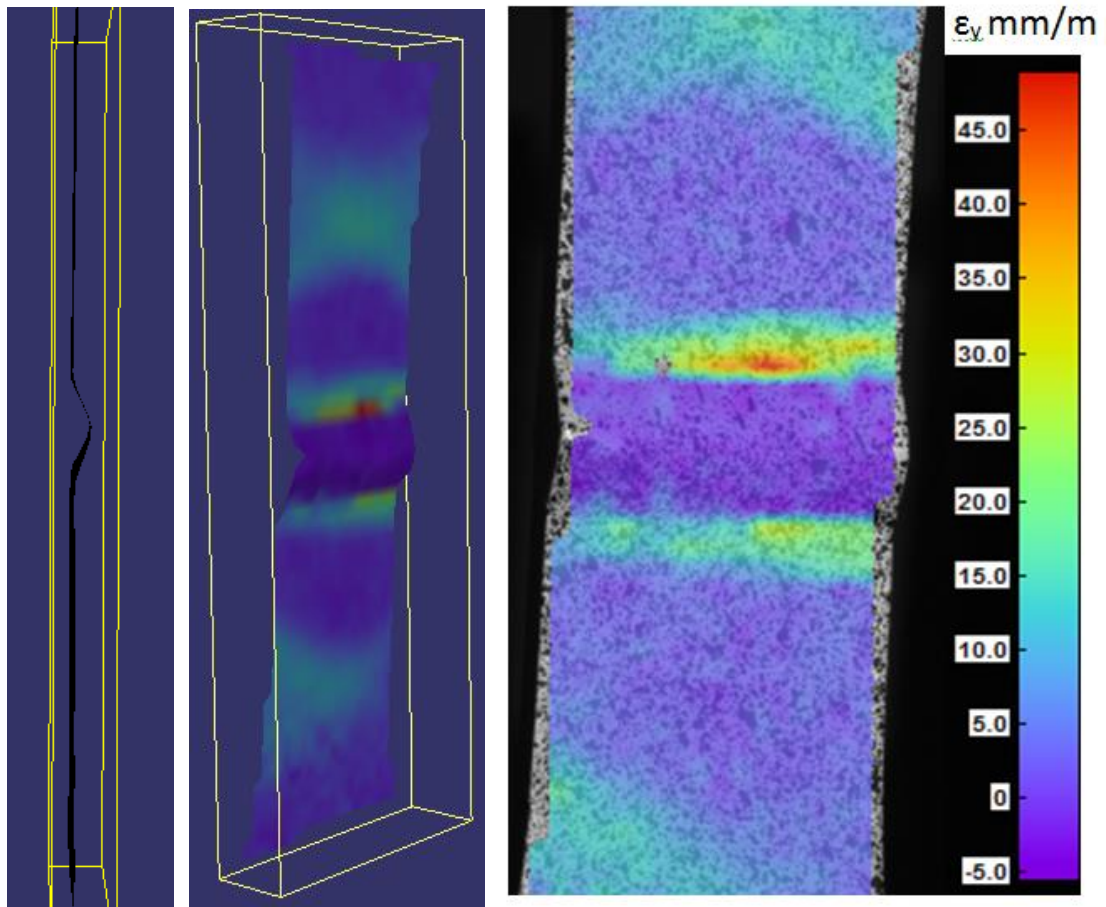


Figure 7.10: DIC image of a weld show strain in y direction.

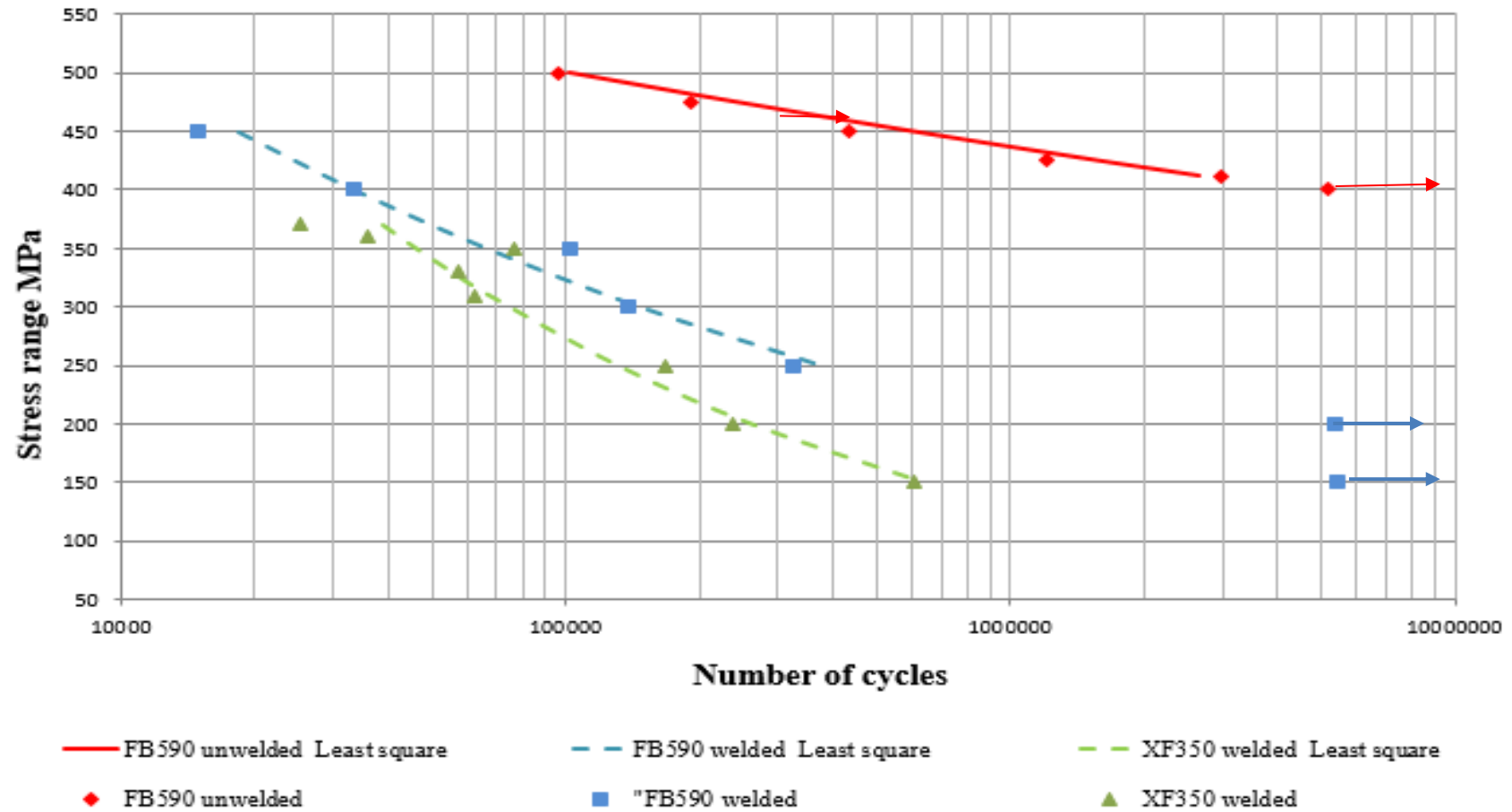


Figure 7.11 shows comparison between S–N curves of welded FB590 and XF350.



Figure 7.12: shows specimen fracture far from the welding location (a) tension specimen (b) bending specimen.

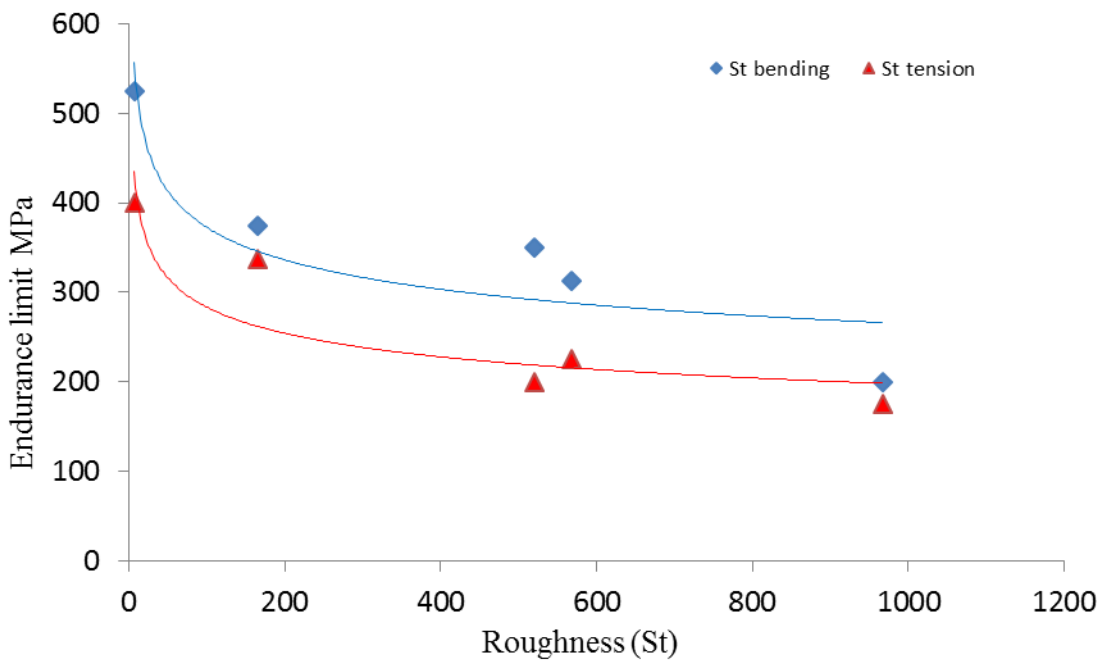
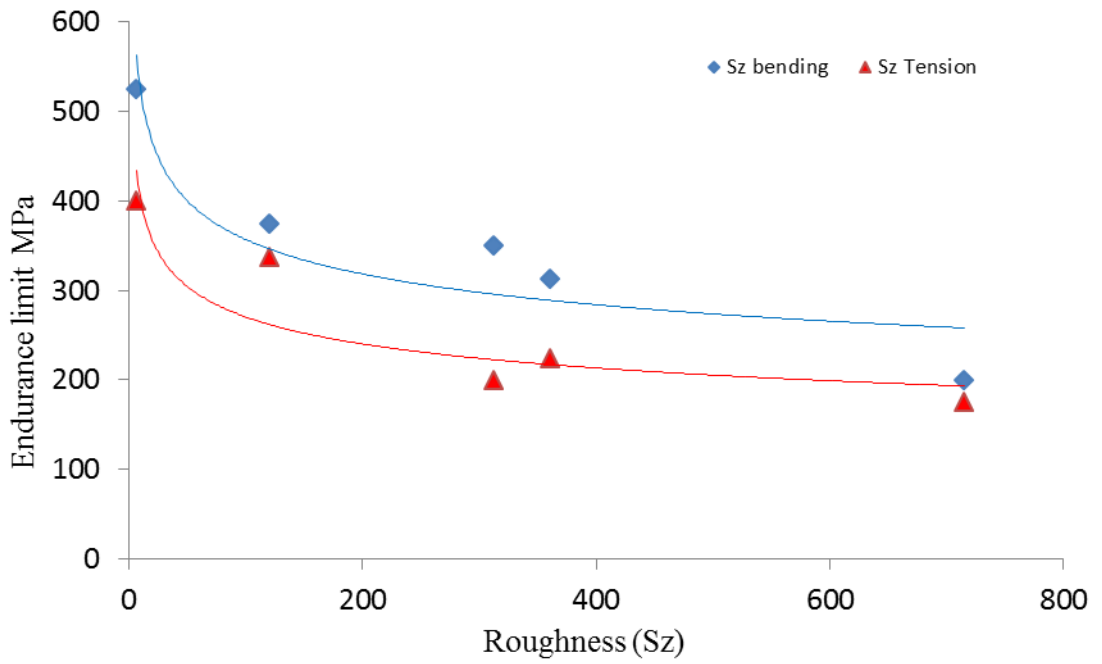


Figure 7.13 shows endurance limit of FB590 vs roughness parameters (a) S_z Maximum height of the asperities (b) S_t Maximum height of the profile.

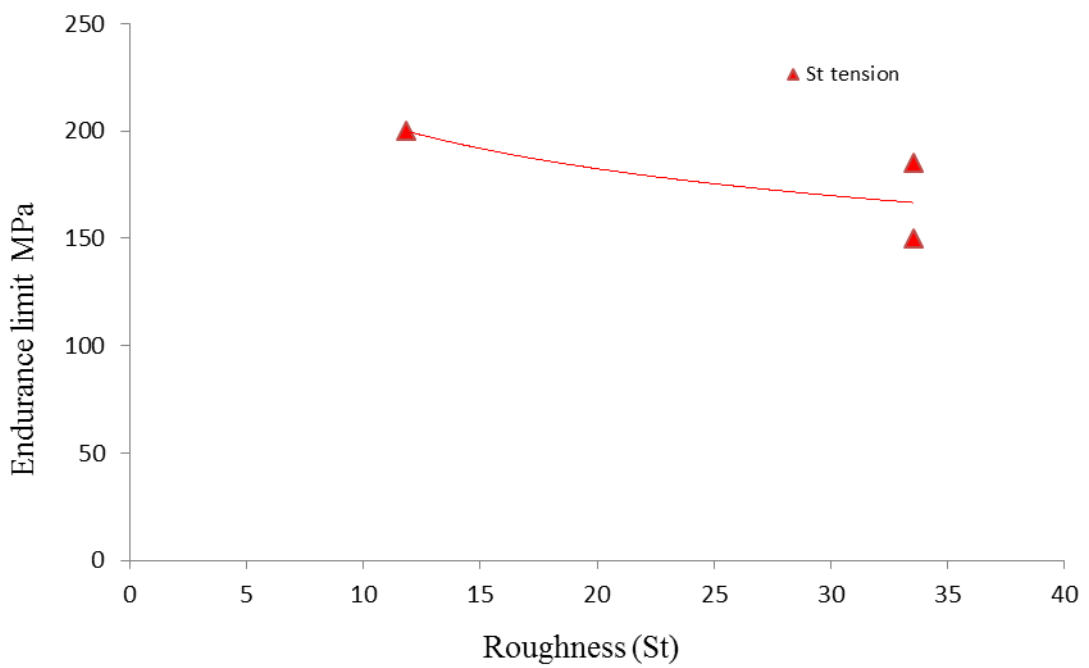
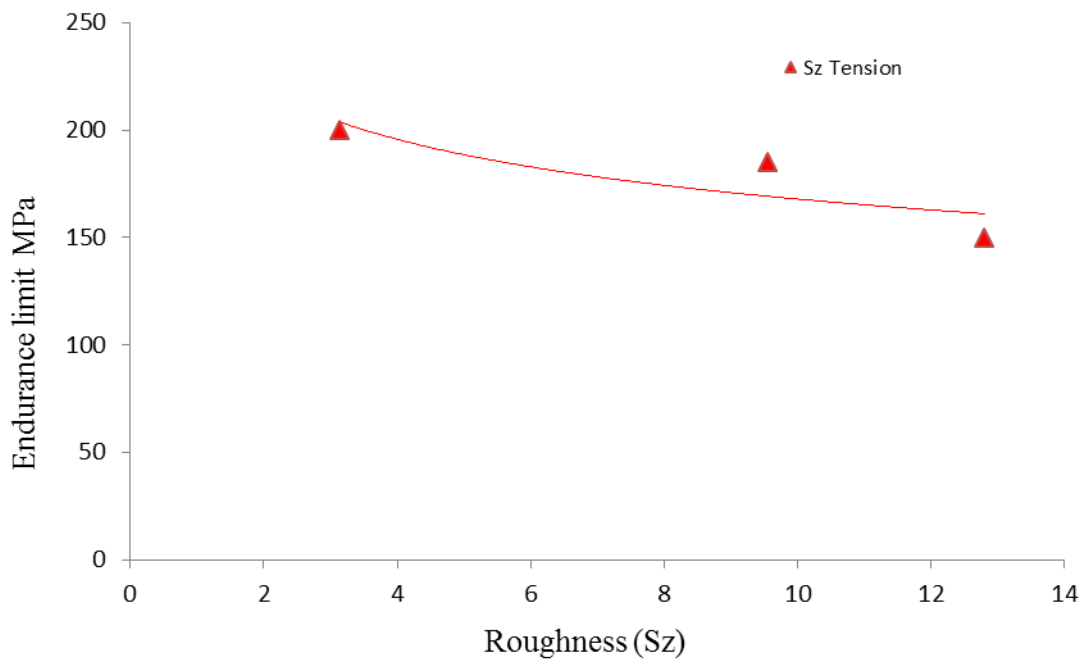


Figure 7.14: shows endurance limit of mild steel vs Roughness parameter (a) S_z Maximum height of the asperities (b) S_t Maximum height of the profile.

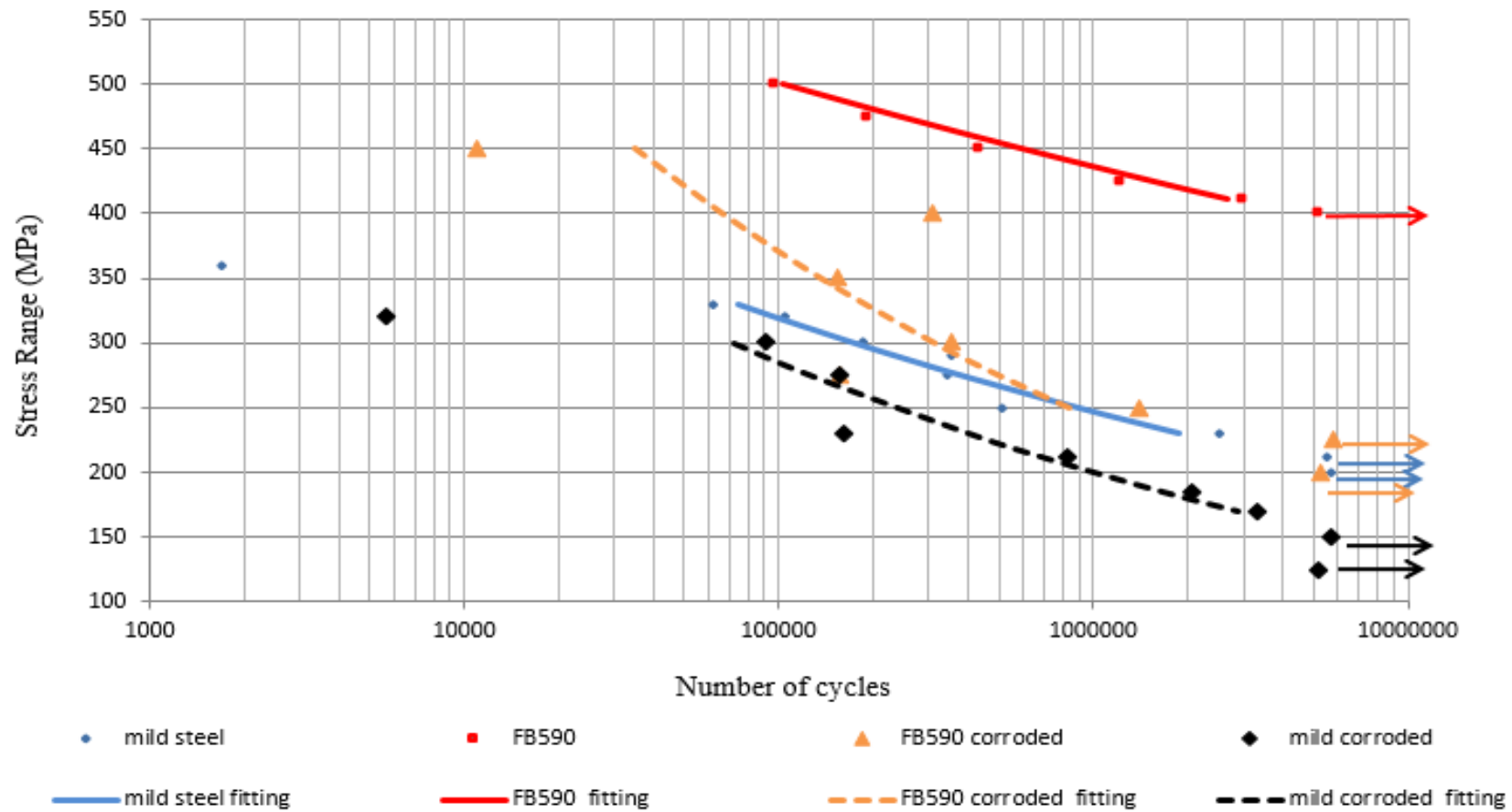


Figure 7.15 shows as received and corrosion for two months of high strength steel and mild steel.

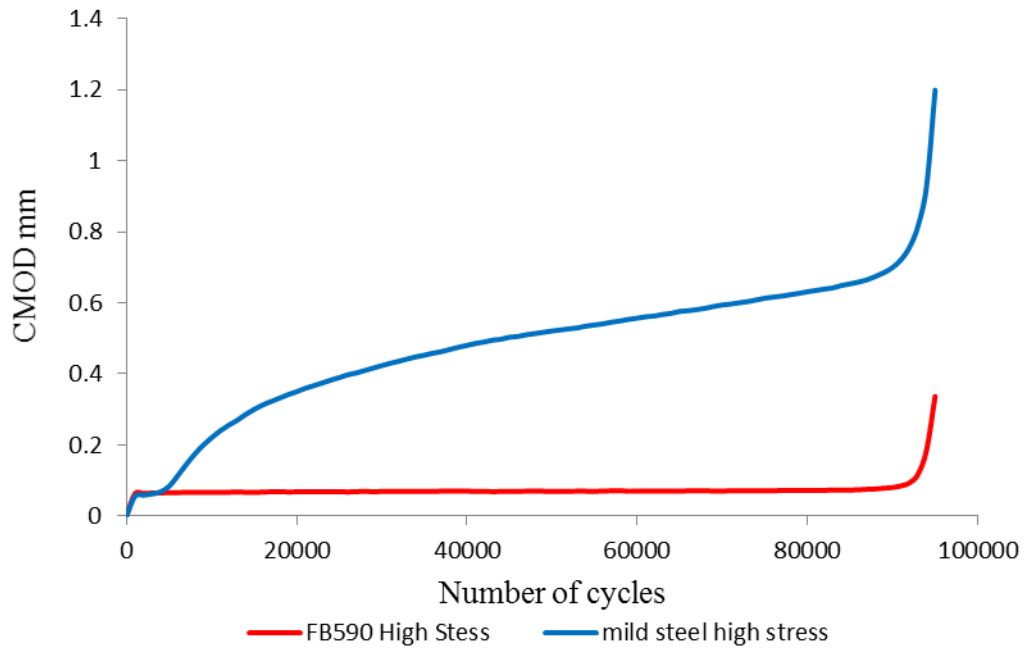


Figure 7.16 crack mouth opening displacement for mild steel and FB590.

8. Conclusions and further work

8.1 Conclusion

At the end of each relevant chapter a comprehensive list of conclusions was given. In the following section the most pertinent of these conclusion are described in more detail. This study has highlighted several aspects of the fatigue performance of mild steel and FB590 Tata steel grade, with the principle focus of this research being to determine the influence of the practical environment represented by stone chipping and corrosion on fatigue properties for FB590 metal and its weldment.

The research presented in this thesis enables design engineers to represent the damage due to various environments anticipated for Tata FB590, thus providing essential tools important to accomplish robust and reliable designs. Therefore, this work will expand the available knowledge, providing an understanding of the fatigue performance and structural integrity of components after ten years or more in service. In addition, this is important step in developing a comprehensive understanding of the product performance. The major findings of this project are as follows:

1. The overall objective of the research reported in this thesis was to develop novel data for FB590 steel and its weldment that demonstrates fatigue properties under bending and tensile loading, along with performing these tests under a range of loading and environmental conditions representative of those encountered by the chassis in practical service. The effect of stone chipping on corrosion and fatigue properties under bending and tensile loading is novel research that was not previously available in the literature. These kinds of information can help the automotive industry to assess the material in high cycle fatigue and in service environment.
2. The fatigue properties of bending loading of steel and weld were not covered well in previous literature. The fatigue properties of material under four-point bending loading at any condition of surface treatment aforementioned were well investigated. It can be observed that the fatigue performance of material under bending loading is much higher

than that under tensile loading in all the environmental cases. This could be due to the load nature of each case, where the cross section of the bending specimen exposed to tension and compression stress during the loading, while the cross section of the tensile specimen is exposed to tensile stress only.

3. The endurance limit was experimentally found for all types of surface treatment of this material and welds.
4. The fatigue performance of high strength steels are directly proportional to material strength on non-welded samples. However, the fatigue resistance of this steel could be conservatively predicted by the existing fatigue design curves for normal strength steels. This would be beneficial to both the steel and automotive industries to understand how mechanical properties correlate with fatigue performance across a wide range of products since fatigue tests are very time consuming and expensive. However, there is no clear relation between fatigue performance and material strength in the corroded and welded samples.
5. The fatigue properties of FB590 tested in this study were very similar to those published for FB590 produced by ArcelorMittal.
6. FB590 showed very good fatigue properties, with higher performance than XF350 and XF450 grades reported in the literature, although the latter results exhibit significant amount of stress concentrations due to their sample design. Thus, the automotive industry is granted more freedom to select the material and its properties that are most suitable for the intended component.
7. The specimen design was changed for FB590 testing with a larger radius and longer parallel section in order to be more suitable for studying corrosion effects. By using a new FB590 sample geometry, the level of stress concentration within the sample may be reduced but not eradicated. This should provide a more accurate representation of Tata's material in terms of fatigue performance than previously used specimen designs.
8. From the results presented in this study, the welding of steel is severely detrimental to fatigue performance regardless of the additional effects of corrosion, this could be due to the effect of weld geometry, where the

stress concentration is highlighted by using DIC. Therefore, a component should be designed to ensure that the welds are in areas of low stress and the parent material should transfer the loads, not the welds although this may result in limit material design.

9. The effect of the stone chipping is less significant than the presence of a weld, while both welding and corrosion have a similar tendency due to the corrosion having a similar effect to welding on fatigue properties. Increased effects after longer exposure periods could be due to metal dissolution.
10. Stone chipping and corrosion significantly affect the specimen surface appearance to be rougher as explained from 3D profilometry. This causes a significant decrease in fatigue properties.
11. Pre-corrosion damage facilitates essentially the onset of fatigue cracks and hence reduces the fatigue life of the corroded specimens appreciably, because of multiple reasons such as the reduction in the effective cross section of the specimens, which increases local stress. Another reason is the existence of different forms of pits and metal dissolution and conversion which takes place with increased duration of exposure as explained from fracture surface analysis. The corrosion increases the surface roughness, developing pits which becomes stress raisers. These greatly accelerate the fatigue crack initiation and extension rate and reduce the fatigue life of the material.
12. The major contributors to these damages have been identified and their influence quantified, which will help the steel industry to enhance the product and produce more effective protection methods useful to aid the reduction of gauge loss due to corrosion.
13. The failure mechanisms of each case of environmental exposure were investigated. The fracture surfaces of fatigued specimens revealed that a similar cracking mode was present for each strength level in all environments. Enhanced crack initiation was, therefore, presumed to be the cause of the decrease in fatigue life between the intact and other environments. The number of possible crack initiation sites increases for coarser specimens that introduces stress raisers on the specimens and reduces the crack initiation life.

14. This study showed that, in general, the increase in corrosion exposure decreased the fatigue life. In addition, the analysis suggests that stress magnitude has a higher detrimental impact on the fatigue life of the specimens as compared with stress concentration due to different corrosion time.
15. The investigation stated well the capabilities of AE for detecting fatigue fractures, and its potential for distinguishing the different AE signals from various possible failure mechanisms. Plastic deformation, delamination of corrosion products and DIC paint as well as crack initiation, propagation and closure are all involved in this process and AE monitoring provides valuable information to help to distinguish between them.
16. DIC allows a clear depiction of the surface strain field evolution and its transient changes according to stress redistribution which occurs as the crack propagates. It is a useful method for monitoring the whole area of interest and it is not limited to a specific region, therefore any damage can be detected even if the precise location is not known in advance. DIC was used to support the understanding of the detected AE signals.
17. The complementary use of DIC and AE helps to minimise the assumptions in the interpretation of the AE trends in relation to the responsible damage mechanisms by revealing the fluctuation of the surface strain fields and other factors such as paint delamination. Additionally, SEM was also used to verify and support the relationship between various phenomena occurring in fatigue failure and the AE signals.
18. The combination of AE and DIC was also helpful in distinguishing between crack initiation and early propagation and background noise, which is otherwise difficult using AE. Early growth of cracks in steel typically generates only very low level AE which is difficult to distinguish from rubbing or fretting, for example of loose paint or corrosion products. The use of DIC allowed significant cracks to be identified well before failure. This could have numerous applications in testing more complex structures, for example in automotive chassis or aerospace applications.

8.2 Future work

The results of the present study suggest some possible avenues for further development that would be valuable to both the steel and automotive industries in terms of how various criteria affect the performance of automotive structures. Also, as Tata often develop new steel grades, it would be useful to carry out a similar assessment, following the techniques within this thesis, for those new grades of steel.

The major suggestions for further work following this project are as follows:

1. Develop an approach for fatigue life prediction using FE modelling, then validate that by predicting the life of specimens tested in this study.
2. Since determining the fatigue performance of components based upon simple samples is extremely difficult, due to the different stress combinations that are observed around the welds, tests need to be undertaken using complex components e.g. welded beams, top hat or suspension arm, under different environmental circumstances to study the effects of these damage sources on the fatigue performance.
3. Predict fatigue life of components as an additional validation.
4. Correlation between simple fatigue tests and components subjected to in service conditions.
5. Carry out prior-corrosion and corrosion fatigue tests on components and validate life prediction methodology.
6. Carry out fatigue tests at multiple stress ratios in order to identify the true nature of Tata material with regards to its performance under a wide range of mean stresses, since the S-N data obtained here for FB590 is only available for one single stress ratio, $R=0.1$. Using a range of stress ratios is important because the actual loading conditions of structural automotive components associated with chassis and suspension may differ significantly from the fatigue data available for the material. With this type of information it is then possible to estimate the fatigue performance at any stress ratio. This information also can then be used

to ensure that Tata customers are deploying the most accurate FE tools available in order to maintain product reliability.

7. Explore the optimal design of automotive chassis components, so a component should be designed to ensure that the welds are in areas of low stress and the parent material should transfer the loads, not the welds although this may result in limit material design. The fatigue life of a structure will be significantly improved when the welded joints are reduced as much as possible, as well as using more effective protection methods in order to reduce the susceptibility to stone chipping and corrosion

References

Aggelis, D. G. 2011. Classification of cracking mode in concrete by acoustic emission parameters. *Mechanics Research Communications* 38(3), pp. 153-157.

Aggelis, D. G. and Kordatos, E. Z. and Matikas, T. E. 2011. Acoustic emission for fatigue damage characterization in metal plates. *Mechanics Research Communications* 38(2), pp. 106-110.

Aggelis, D. G. and Verbruggen, S. and Tsangouri, E. and Tysmans, T. and Van Hemelrijck, D. 2013. Characterization of mechanical performance of concrete beams with external reinforcement by acoustic emission and digital image correlation. *Construction and Building Materials* 47(0), pp. 1037-1045.

AHSS. 2014. Advanced high strength steels (AHSS) application guidelines version 5.0. WorldAuto Steel (e-book available from http://309fbf2c62e8221fbaf0-b80c17cbaf20104b072d586b316c6210.r88.cf1.rackcdn.com/AHSS_Application_Guidelines_4-1June2009.pdf).

Alam, M. and Barsoum, Z. and Jonsén, P. and Kaplan, A. and Häggblad, H. 2010. The influence of surface geometry and topography on the fatigue cracking behaviour of laser hybrid welded eccentric fillet joints. *Applied Surface Science* 256(6), pp. 1936-1945.

Alang, N. and Razak, N. and Miskam, A. 2011. Effect of surface roughness on fatigue life of notched carbon steel. *International Journal of Engineering & Technology* 11(1), p. 160.

Arriscorreta, C. A. 2012. Statistical modeling for the corrosion fatigue of aluminum alloys 7075-T6 and 2024-T3. The University of Utah.

ASME. 2009. ASME B46.1-2009 Surface Texture (Surface Roughness, Waviness, and Lay).

ASTM-D3170-01. 1996. Standard Test Method for Chipping Resistance of Coatings. The American Society for Testing and Materials.

ASTM-E466. 2002. Standard Practice for Conducting Force Controlled Constant Amplitude Axial Fatigue Tests of Metallic Materials. The American Society for Testing and Materials

ASTM-E855. 2002. Standard Test Methods for Bend Testing of Metallic Flat Materials for Spring Applications Involving Static Loading. The American Society for Testing and Materials.

- ASTM-E976. 2001. Standard guide for determining the reproducibility of acoustic emission sensor response. American Society for Testing and Materials
- ASTME-165-95. 2001. Standard Test Method for Liquid Penetrant Examination. The American Society for Testing and Materials.
- Auto/Steel. 1999. A GUIDE TO CORROSION PROTECTION For Passenger Car and Light Truck Underbody Structural Components. Auto/Steel Partnership: .
- Baik, B. and Yamada, K. 2008. Fatigue behavior of fillet welded joints under plate bending. *J Struct Eng JSCE A* 54, pp. 530-537.
- Baik, B. and Yamada, K. and Ishikawa, T. 2008. Fatigue strength of fillet welded joint subjected to plate bending. *Steel Structures* 8(3), pp. 163-169.
- Barile, C. and Casavola, C. and Pappalettera, G. and Pappalettere, C. 2015. Considerations on Acoustic Emissions in Ti Grade 5 During Fatigue Test. *Procedia Engineering* 109, pp. 320-326.
- Barsoum, F. F. 2009. Acoustic emission monitoring and fatigue life prediction in axially loaded notched steel specimens. *J. Acoustic Emission* 27, pp. 40-63.
- Bathias, C. and Pineau, A. 2010. Fatigue of materials and structures. Wiley Online Library.
- Baxter, M. 2007. Damage Assessment by Acoustic Emission (AE) During Landing Gear Fatigue Testing, Ph.D. Thesis, School of Engineering, University of Wales Cardiff, Cardiff, UK.
- Behnia, A. and Chai, H. K. and Shiotani, T. 2014. Advanced structural health monitoring of concrete structures with the aid of acoustic emission. *Construction and Building Materials* 65(0), pp. 282-302.
- Benham, P. P. and Crawford, R. J. and Armstrong, C. G. 1996. Mechanics of engineering materials. Longman Harlow, Essex, England.
- Berkovits, A. and Fang, D. 1995. Study of fatigue crack characteristics by acoustic emission. *Engineering Fracture Mechanics* 51(3), pp. 401-416.
- Berkovits, F. a. 1993. Fatigue damage mechanism on the basis of Acoustic Emission measurements *ASME* 176, pp. 219-235.
- Bhole, S. and Ma, C. and Khan, M. and Chen, D. 2011. A study of spot welding of advanced high strength steels for automotive applications. *Journal of Iron and Steel Research International* 18, pp. 724-729.
- Bright, G. 2012. Minimising variability in steel/weld fatigue data and developing robust durability design for automotive chassis applications . Ph.D. Thesis, , Swansea University , Swansea, UK

- Bryant, M. J. 2013. Running-in and residual stress: finite element contact analysis of as measured rough surfaces and comparison with experiment. Cardiff University.
- BSI. 1963. Methods of Fatigue Testing Part 3: Direct stress fatigue tests. British Standards, BS 3518-3:1963.
- BSI. 1993. Fatigue testing — Part 1: Guide to general principles. BRITISH STANDARD BS 3518-1: 1993.
- BSI. 2003. Metallic materials — Fatigue testing — Statistical planning and analysis of data. The British standard BS ISO 12107:2003
- BSI. 2009. Metallic materials Tensile testing Part 1: Method of test at ambient temperature. British Standards
- Burns, J. T. and Kim, S. and Gangloff, R. P. 2010. Effect of corrosion severity on fatigue evolution in Al–Zn–Mg–Cu. *Corrosion Science* 52(2), pp. 498-508.
- Caccese, V. and Blomquist, P. and Berube, K. and Webber, S. and Orozco, N. 2006. Effect of weld geometric profile on fatigue life of cruciform welds made by laser/GMAW processes. *Marine structures* 19(1), pp. 1-22.
- Carpinteri, A. and Lacidogna, G. and Accornero, F. and Mpalaskas, A. C. and Matikas, T. E. and Aggelis, D. G. 2013. Influence of damage in the acoustic emission parameters. *Cement and Concrete Composites* 44(0), pp. 9-16.
- Chang, H. and Han, E. H. and Wang, J. Q. and Ke, W. 2009. Acoustic emission study of fatigue crack closure of physical short and long cracks for aluminum alloy LY12CZ. *International Journal of Fatigue* 31(3), pp. 403-407.
- Chen, G. and Wan, K.-C. and Gao, M. and Wei, R. and Flournoy, T. 1996. Transition from pitting to fatigue crack growth—modeling of corrosion fatigue crack nucleation in a 2024-T3 aluminum alloy. *Materials Science and Engineering: A* 219(1), pp. 126-132.
- Chen, T., Xiao, Z.G., Zhao, X.L. and Gu, X.L., 2013. A boundary element analysis of fatigue crack growth for welded connections under bending. *Engineering Fracture Mechanics*, 98, pp.44-51.
- Chiew, S. P. and Zhao, M. and Lee, C. K. 2015. Fatigue performance of high strength steel built-up box T-joints. *Journal of Constructional Steel Research* 106, pp. 296-310.
- Chopra, O. K. 2002. Mechanism of fatigue crack initiation in austenitic stainless steels in LWR environments. American Society of Mechanical Engineers, Pressure Vessels and Piping Division (Publication) PVP 439, pp. 133-142.

corrosion-doctors.org. 2016. Corrosion pit shapes. Last access Feb. 2016
<http://corrosion-doctors.org/Forms-pitting/shapes.htm>

Costa, J. and Ferreira, J. and Abreu, L. 2010. Fatigue behaviour of butt welded joints in a high strength steel. *Procedia Engineering* 2(1), pp. 697-705.

Costa, J. and Jesus, J. and Loureiro, A. and Ferreira, J. and Borrego, L. 2014. Fatigue life improvement of mig welded aluminium T-joints by friction stir processing. *International Journal of Fatigue* 61, pp. 244-254.

Deleanu, L. and Georgescu, C. and Suci, C. 2012a. A comparison between 2D and 3D surface parameters for evaluating the quality of surfaces. *The Annals of Dunarea de Jos University-Fascicle V. Technologies in Machine Building*, pp. 5-12.

Dupen, B. 2014. *Applied Strength of Materials for Engineering Technology*.

Elfergani, H. A. and Pullin, R. and Holford, K. M. 2013. Damage assessment of corrosion in prestressed concrete by acoustic emission. *Construction and Building Materials* 40(0), pp. 925-933.

Elforjani, M. and Mba, D. 2009. Detecting natural crack initiation and growth in slow speed shafts with the Acoustic Emission technology. *Engineering Failure Analysis* 16(7), pp. 2121-2129.

Ellwood, R. 2003. Fatigue performance of downgauged high strength steel automotive suspension component. University of Wales Swansea.

Ewalds H L and Wanhill, W. R. J. H. 1984. *Fracture mechanics*. London : Edward Arnold : Delftse Uitgevers Maatschappij|1984.

Fang, D. and Berkovits, A. 1995. Fatigue design model based on damage mechanisms revealed by acoustic emission measurements. *Journal of Engineering Materials and Technology, Transactions of the ASME* 117(2), pp. 200-208.

Fontana, M. G. 2005. *Corrosion engineering*. Tata McGraw-Hill Education.

Fourlaris, G. and Ellwood, R. and Jones, T. 2007. The reliability of test results from simple test samples in predicting the fatigue performance of automotive components. *Materials & design* 28(4), pp. 1198-1210.

Genel, K. 2007. The effect of pitting on the bending fatigue performance of high-strength aluminum alloy. *Scripta Materialia* 57(4), pp. 297-300.

Genta, G. and Morello, L. 2009. *The automotive chassis*. Springer.

Gruenberg, K. and Craig, B. and Hillberry, B. and Bucci, R. and Hinkle, A. 2004. Predicting fatigue life of pre-corroded 2024-T3 aluminum. *International Journal of Fatigue* 26(6), pp. 629-640.

- Hägele, N. and Sonsino, C. 2014. Structural durability design recommendations for forged automotive aluminium chassis components submitted to spectrum and environmental loadings by the example of a tension strut. *International Journal of Fatigue* 69, pp. 63-70.
- Hao, X. and Li, S. and Yu, M. 2011. Effect of pre-corrosion on fatigue life of high strength steel 38CrMoAl. *Journal of Wuhan University of Technology-Mater. Sci. Ed.* 26(4), pp. 648-653.
- Harati, E. and Karlsson, L. and Svensson, L.-E. and Dalaei, K. 2015. The relative effects of residual stresses and weld toe geometry on fatigue life of weldments. *International Journal of Fatigue* 77, pp. 160-165.
- Heyes, A. 1998. Automotive component failures. *Engineering Failure Analysis* 5(2), pp. 129-141.
- Hu, J. and Du, L.-X. and Wang, J.-J. and Sun, Q.-Y. 2014. Cooling process and mechanical properties design of hot-rolled low carbon high strength microalloyed steel for automotive wheel usage. *Materials & Design* 53(0), pp. 332-337.
- Huang, M. 1998. Using Acoustic Emission in Fatigue and Fracture Materials Research. *jom* 50.
- Janeček, M., Král, Robert, Dobroň, Patrik, Chmelík, František, Šupík, Vladimír, Holländer, Frank. 2007. Mechanisms of plastic deformation in AZ31 magnesium alloy investigated by acoustic emission and transmission electron microscopy. *Materials Science and Engineering: A* 462(1–2), pp. 311-315.
- Jarman, L. L. S. a. R. A. 2000. *Corrosion Metal Environment Reactions* third edition. 1.
- Jiao, H. and Mashiri, F. and Zhao, X.-L. 2013. Fatigue behavior of very high strength (VHS) circular steel tube to plate T-joints under in-plane bending. *Thin-Walled Structures* 68, pp. 106-112.
- Jones, K. and Shinde, S. R. and Clark, P. N. and Hoepfner, D. W. 2008. Effect of prior corrosion on short crack behavior in 2024-T3 aluminum alloy. *Corrosion Science* 50(9), pp. 2588-2595.
- Jun, Z. Z. W. N. Z. P. 1990. Acoustic Emission Monitoring the Fatigue Crack Growth in SM50B-Zc Steel. *Materials Science & Technology* 6(5), pp. 345-350
- Kaita, T. and Appuhamy, J. and Itogawa, K. and Ohga, M. and Fujii, K. 2011. Experimental Study on Remaining Strength Estimation of Corroded Wide Steel Plates under Tensile Force. *Procedia Engineering* 14, pp. 2707-2713.
- Katundi, D. and Tosun-Bayraktar, A. and Bayraktar, E. and Toueix, D. 2010. Corrosion behaviour of the welded steel sheets used in automotive industry.

Journal of Achievements in Materials and Manufacturing Engineering 38(2), pp. 146-153.

Kawano, O. 2003. High Strength Hot-rolled Steel Sheets for Automobiles. NIPPON STEEL TECHNICAL REPORT No. 88 pp. 8-12.

Keisler, J. and Chopra, O. 1995. Statistical analysis of fatigue strain-life data for carbon and low-alloy steels. Argonne National Lab., IL (United States).

Kermanidis, A. T. and Petroyiannis, P. and Pantelakis, S. G. 2005. Fatigue and damage tolerance behaviour of corroded 2024 T351 aircraft aluminum alloy. Theoretical and applied fracture mechanics 43(1), pp. 121-132.

Kerscher, E., 2014. Influence of Microstructure and Micro Notches on the Fatigue Limit. *Procedia Engineering*, 74, pp.210-217.

Kirkhope, K. and Bell, R. and Caron, L. and Basu, R. and Ma, K.-T. 1999. Weld detail fatigue life improvement techniques. Part 1: review. Marine structures 12(6), pp. 447-474.

Kordatos, E. Z. and Aggelis, D. G. and Matikas, T. E. 2012. Monitoring mechanical damage in structural materials using complimentary NDE techniques based on thermography and acoustic emission. Composites Part B: Engineering 43(6), pp. 2676-2686.

Kovac, J., Alaux, Carole, Marrow, T. James, Govekar, Edvard, Legat, Andraz. 2010. Correlations of electrochemical noise, acoustic emission and complementary monitoring techniques during intergranular stress-corrosion cracking of austenitic stainless steel. Corrosion Science 52(6), pp. 2015-2025.

Lakshminarayanan, A. K. and Balasubramanian, V. and Salahuddin, M. 2010. Microstructure, Tensile and Impact Toughness Properties of Friction Stir Welded Mild Steel. Journal of Iron and Steel Research, International 17(10), pp. 68-74.

LeBozec, N. and Blandin, N. and Thierry, D. 2008. Accelerated corrosion tests in the automotive industry: a comparison of the performance towards cosmetic corrosion. Materials and corrosion 59(11), pp. 889-894.

LeBozec, N. and LeGac, A. and Thierry, D. 2012. Corrosion performance and mechanical properties of joined automotive materials. Materials and Corrosion 63(5), pp. 408-415.

Lee, C.-H. and Chang, K.-H. and Jang, G.-C. and Lee, C.-Y. 2009. Effect of weld geometry on the fatigue life of non-load-carrying fillet welded cruciform joints. Engineering Failure Analysis 16(3), pp. 849-855.

Lepisto, M. L. a. T. 2003. Effect of cyclic deformation on Barkhausen noise in a mild steel. NDT&E International 36 pp. 401-409.

- Lin, S.-K. and Lee, Y.-L. and Lu, M.-W. 2001. Evaluation of the staircase and the accelerated test methods for fatigue limit distributions. *International journal of fatigue* 23(1), pp. 75-83.
- Li, J.K., Mei, Y., Duo, W. and Renzhi, W., 1992. An analysis of stress concentrations caused by shot peening and its application in predicting fatigue strength. *Fatigue & Fracture of Engineering Materials & Structures*,15(12), pp.1271-1279.
- Long, X. and Khanna, S. K. 2007. Fatigue properties and failure characterization of spot welded high strength steel sheet. *International journal of fatigue* 29(5), pp. 879-886.
- Lonyuk, M. and Bosma, M. and Vijverberg, C. and Bakker, A. and Janssen, M. 2008. Relation between chip resistance and mechanical properties of automotive coatings. *Progress in Organic Coatings* 61(2), pp. 308-315.
- Maddox, S. J. 1991a. *Fatigue strength of welded structures* Woodhead Publishing Ltd.
- Mashiri, F. and Zhao, X. 2007. Fatigue tests and design of thin CHS-plate T-joints under cyclic in-plane bending. *Thin-walled structures* 45(4), pp. 463-472.
- Mashiri, F. R. and Zhao, X.-L. and Hirt, M. A. and Nussbaumer, A. 2007. Size effect of welded thin-walled tubular joints. *International Journal of Structural Stability and Dynamics* 7(01), pp. 101-127.
- Mazal, P. and Vlastic, F. and Koula, V. 2015. Use of Acoustic Emission Method for Identification of Fatigue Micro-cracks Creation. *Procedia Engineering* 133, pp. 379-388.
- McNeill, S., Peters, W., Sutton, M. 1987. Estimation of stress intensity factor by digital image correlation. *Eng. Fract. Mech.* , 28 (1), pp. 101-112.
- Miki, C. and Mori, T. and Sakamoto, K. and Kashiwagi, H. 1987. Size effect on the fatigue strength of transverse fillet welded joints. *Journal of Structural Engineering* 33, pp. 393-402.
- Miller, R. K. a. M., P. 2005. *Acoustic Emission Testing*. NDT Handbook. American Society for Non-destructive Testing 6.
- millervelds.com. 2016. MIG/GMAW , Setting the Correct Parameters available at : <https://www.millervelds.com/resources/article-library/miggmaw-101-setting-the-correct-parameters>. Last accessed Feb 2016.
- Mohd, S. and Mutoh, Y. and Otsuka, Y. and Miyashita, Y. and Koike, T. and Suzuki, T. 2012. Scatter analysis of fatigue life and pore size data of die-cast AM60B magnesium alloy. *Engineering Failure Analysis* 22, pp. 64-72.

- Moorthy, V. and Jayakumar, T. and Raj, B. 1996. Influence of micro structure on acoustic emission behavior during stage 2 fatigue crack growth in solution annealed, thermally aged and weld specimens of AISI type 316 stainless steel. *Materials Science and Engineering: A* 212(2), pp. 273-280.
- Morrissey, R. and Nicholas, T. 2006. Staircase testing of a titanium alloy in the gigacycle regime. *International journal of fatigue* 28(11), pp. 1577-1582.
- Mukhopadhyay, C. K. J., T. Haneef, T. K. Suresh Kumar, S. Rao, B. P. C. Goyal, Sumit Gupta, Suneel K. Bhasin, Vivek Vishnuvardhan, S. Raghava, G. Gandhi, P. 2014. Use of acoustic emission and ultrasonic techniques for monitoring crack initiation/growth during ratcheting studies on 304LN stainless steel straight pipe. *International Journal of Pressure Vessels and Piping* 116(0), pp. 27-36.
- Nayak, S. and Hernandez, V. B. and Okita, Y. and Zhou, Y. 2012. Microstructure–hardness relationship in the fusion zone of TRIP steel welds. *Materials Science and Engineering: A* 551, pp. 73-81.
- Novovic, D. and Dewes, R. and Aspinwall, D. and Voice, W. and Bowen, P. 2004a. The effect of machined topography and integrity on fatigue life. *International Journal of Machine Tools and Manufacture* 44(2), pp. 125-134.
- Ohno, K. and Ohtsu, M. 2010. Crack classification in concrete based on acoustic emission. *Construction and Building Materials* 24(12), pp. 2339-2346.
- Ohtsu), R. T. C. M. 2010. Recommendation of RILEM TC 212- ACD: acoustic emission and related NDE techniques for crack detection and damage evaluation in concrete. *Materials and Structures* 43, pp. 1183–1186.
- Omar, M. A. 2011. *The automotive body manufacturing systems and processes*. John Wiley & Sons.
- PAC. 2005. *DiSP with AEwin User’s Manual Rev. 3*. Physical Acoustic Corporation, Princeton, New Jersey, USA.
- Palma, E. and dos Santos, E. 2002. Fatigue damage analysis in an automobile stabilizer bar. *Proceedings of the Institution of Mechanical Engineers, Part D: Journal of Automobile Engineering* 216(11), pp. 865-871.
- Pang, J. and Li, S. and Wang, Z. and Zhang, Z. 2013. General relation between tensile strength and fatigue strength of metallic materials. *Materials Science and Engineering: A* 564, pp. 331-341.
- Pang, X. and Shi, C. and Zavadil, R. 2015. Stress Corrosion Cracking of ZEK100 Magnesium Alloy for Automotive Applications. *Magnesium Technology 2015*, pp. 319-322.

Pidaparti, R. M. and Patel, R. R. 2008. Correlation between corrosion pits and stresses in Al alloys. *Materials Letters* 62(30), pp. 4497-4499.

Pidaparti, R. M. and Rao, A. S. 2008. Analysis of pits induced stresses due to metal corrosion. *Corrosion Science* 50(7), pp. 1932-1938.

Pollock, A. A. 2012. AE Observations During Cyclic Testing of A572 Steel Laboratory Specimens. 30th European Conference on AE Testing. Granada.

Potukutchi, R. and Agrawal, H. and Perumalswami, P. and Dong, P. 2004. Fatigue Analysis of Steel MIG Welds in Automotive Structures. SAE Technical Paper.

Pramesti, F. and Molenaar, A. and Van de Ven, M. 2013. The Prediction of Fatigue Life based on Four Point Bending Test. *Procedia Engineering* 54, pp. 851-862.

Pullin, R. and Eaton, M. J. and Hensman, J. J. and Holford, K. M. and Worden, K. and Evans, S. L. 2010a. Detection of cracking in gear teeth using Acoustic Emission. pp. 45-50.

Pullin, R. and Eaton, M. J. and Hensman, J. J. and Holford, K. M. and Worden, K. and Evans, S. L. eds. 2010b. Validation of acoustic emission (AE) crack detection in aerospace grade steel using digital image correlation. *Applied Mechanics and Materials*. Trans Tech Publ.

Ramamurthy, A. and Buresh, G. and Nagy, M. and Howell, M. 1999. Novel instrumentation for evaluating stone impact wear of automotive paint systems. *Wear* 225, pp. 936-948.

Razin, A. A. and Ramezanzadeh, B. and Yari, H. 2015. Detecting and estimating the extent of automotive coating delamination and damage indexes after stone chipping using electrochemical impedance spectroscopy. *Progress in Organic Coatings*.

Rezig, E. 2011. Influence of corrosion damage on the initiation of fatigue cracks in high strength stainless steels.

Risbet, M. and Feissel, P. and Roland, T. and Brancherie, D. and Roelandt, J.-M. 2010. Digital Image Correlation technique: Application to early fatigue damage detection in stainless steel. *Procedia Engineering* 2(1), pp. 2219-2227.

Roberts, T. M. and Talebzadeh, M. 2003a. Acoustic emission monitoring of fatigue crack propagation. *Journal of Constructional Steel Research* 59(6), pp. 695-712.

Roberts, T. M. and Talebzadeh, M. 2003b. Fatigue life prediction based on crack propagation and acoustic emission count rates. *Journal of Constructional Steel Research* 59(6), pp. 679-694.

Rokhlin, S. and Kim, J.-Y. and Nagy, H. and Zoofan, B. 1999a. Effect of pitting corrosion on fatigue crack initiation and fatigue life. *Engineering Fracture Mechanics* 62(4), pp. 425-444.

Rusk, D. and Hoppe, W. 2009. Fatigue life prediction of corrosion-damaged high-strength steel using an equivalent stress riser (ESR) model: Part I: Test development and results. *International Journal of Fatigue* 31(10), pp. 1454-1463.

SAE-J400. 2002. Test for Chip Resistance of Surface Coatings. The Engineering Society for Advance Mobility Land Sea and Space.

SAEJ2332. 2002. Cosmetic corrosion Lab test SAE J2332. SAE J2332.

Sampo, E. 2011. Modelling chassis flexibility in vehicle dynamics simulation. University of Surrey.

Savaidis, G., Savaidis, A., Zerres, P. and Vormwald, M., 2010. Mode I fatigue crack growth at notches considering crack closure. *International Journal of Fatigue*, 32(10), pp.1543-1558.

Scruby, C. B. 1987. An introduction to acoustic emission. *Journal of Physics E: Scientific Instruments* 20(8), p. 946.

Shahidan, S. and Pulin, R. and Muhamad Bunnori, N. and Holford, K. M. 2013. Damage classification in reinforced concrete beam by acoustic emission signal analysis. *Construction and Building Materials* 45(0), pp. 78-86.

Shrama, K. and Pullin, R. and Clarke, A. and Evans, S. 2014. Detection of Cracking in Mild Steel Fatigue Specimens Using Acoustic Emission and Digital Image Correlation. 31st Conference of the European Working Group on Acoustic Emission (EWGAE) – We.4.B.2.

Shrama, K. and Pullin, R. and Clarke, A. and Evans, S. 2015. Fatigue crack monitoring in mild steel specimens using acoustic emission and digital image correlation. *Insight-Non-Destructive Testing and Condition Monitoring* 57(6), pp. 346-354.

Stenberg, T. and Barsoum, Z. and Balawi, S. 2015. Comparison of local stress based concepts—Effects of low-and high cycle fatigue and weld quality. *Engineering Failure Analysis* 57, pp. 323-333.

Stout. 1993. THE development of methods for the characterization of roughness in three dimensions

Suraratchai, M. and Limido, J. and Mabru, C. and Chieragatti, R. 2008. Modelling the influence of machined surface roughness on the fatigue life of aluminium alloy. *International Journal of Fatigue* 30(12), pp. 2119-2126.

- Sutton, M. A. and Yan, J. H. and Tiwari, V. and Schreier, H. W. and Orteu, J. J. 2008. The effect of out-of-plane motion on 2D and 3D digital image correlation measurements. *Optics and Lasers in Engineering* 46(10), pp. 746-757.
- Takamura, K. and Urban, D. 2002. *Polymer dispersions and their industrial applications*. Willey VCH, London.
- Tao, Y. and Wang, W. and Sun, B. 2014. Nondestructive Online Detection of Welding Defects in Track Crane Boom Using Acoustic Emission Technique. *Advances in Mechanical Engineering* 6, p. 505464.
- Taylor, D. 2007. Chapter 9 - Fatigue: Predicting fatigue limit and fatigue life. *The Theory of Critical Distances*. Oxford: Elsevier Science Ltd, pp. 163-II.
- Taylor, D. and Clancy, O. 1991. The fatigue performance of machined surfaces. *Fatigue & Fracture of Engineering Materials & Structures* 14(2-3), pp. 329-336.
- Teik, E. 2001. Material fatigue behavior characterization using the wavelet-based AE technique - a case study of acrylic bone cement. *Engineering Fracture Mechanics* 68, pp. 1477-1492.
- Thomas, D. J. and Whittaker, M. T. and Bright, G. W. and Gao, Y. 2011a. The influence of mechanical and CO₂ laser cut-edge characteristics on the fatigue life performance of high strength automotive steels. *Journal of Materials Processing Technology* 211(2), pp. 263-274.
- Tušek, J. and Kampuš, Z. and Suban, M. 2001. Welding of tailored blanks of different materials. *Journal of materials processing technology* 119(1), pp. 180-184.
- Van der Walde, K. and Hillberry, B. 2008. Characterization of pitting damage and prediction of remaining fatigue life. *International Journal of Fatigue* 30(1), pp. 106-118.
- Veloso, V. and Magalhaes, H. and Bicalho, G. and Palma, E. 2009. Failure investigation and stress analysis of a longitudinal stringer of an automobile chassis. *Engineering Failure Analysis* 16(5), pp. 1696-1702.
- Vinogradov, A. 2013. Effect of grain size on the mechanisms of plastic deformation in wrought Mg–Zn–Zr alloy revealed by acoustic emission measurements. *Acta Materialia* 61, pp. 2044–2056.
- Wang, J. and Yang, L. and Sun, M. and Liu, T. and Li, H. 2016. Effect of energy input on the microstructure and properties of butt joints in DP1000 steel laser welding. *Materials & Design* 90, pp. 642-649.
- Wang, Q. Y. and Kawagoishi, N. and Chen, Q. 2003. Effect of pitting corrosion on very high cycle fatigue behavior. *Scripta Materialia* 49(7), pp. 711-716.

- Wang, T. and Xie, L.-j. and Wang, X.-b. and Shang, T.-y. 2015. 2D and 3D milled surface roughness of high volume fraction SiCp/Al composites. *Defence Technology* 11(2), pp. 104-109.
- Wang, Y. and Bergström, J. and Burman, C. 2006. Four-point bending fatigue behaviour of an iron-based laser sintered material. *International journal of fatigue* 28(12), pp. 1705-1715.
- Wang, Y. and Meletis, E. I. and Huang, H. 2013. Quantitative study of surface roughness evolution during low-cycle fatigue of 316L stainless steel using Scanning Whitelight Interferometric (SWLI) Microscopy. *International Journal of Fatigue* 48(0), pp. 280-288.
- Wanhill, H. L. E. R. J. H. 1984. *Fracture mechanics*. London : Edward Arnold : Delftse Uitgevers Maatschappij.
- Wasekar, N. P. and Jyothirmayi, A. and Sundararajan, G. 2011. Influence of prior corrosion on the high cycle fatigue behavior of microarc oxidation coated 6061-T6 Aluminum alloy. *International Journal of Fatigue* 33(9), pp. 1268-1276.
- Winston, R. R. and Herbert, H. U. 2008. *Corrosion and corrosion control, An introduction to corrosion science and engineering*. A John Wiley & Sons Inc. Hoboken, NJ.
- Xiao, Z.-G. and Chen, T. and Zhao, X.-L. 2012. Fatigue strength evaluation of transverse fillet welded joints subjected to bending loads. *International Journal of Fatigue* 38, pp. 57-64.
- Xu and Shan-hua. 2015. Estimating the effects of corrosion pits on the fatigue life of steel plate based on the 3D profile. *International Journal of Fatigue* 72, pp. 27-41.
- Xu, S.-h. and Qiu, B. 2013. Experimental study on fatigue behavior of corroded steel. *Materials Science and Engineering: A* 584, pp. 163-169.
- Xue, H. and Tao, H. and Montembault, F. and Wang, Q. and Bathias, C. 2007. Development of a three-point bending fatigue testing methodology at 20kHz frequency. *International Journal of Fatigue* 29(9), pp. 2085-2093.
- Zahrai, S. 2003. Cyclic strength and ductility of rusted steel members. *Asian Journal of Civil Engineering* 4(2-4), pp. 135-148.
- Zare, A. and Ekrami, A. 2011. Influence of martensite volume fraction on tensile properties of triple phase ferrite–bainite–martensite steels. *Materials Science and Engineering: A* 530, pp. 440-445.

Zhang, L. and Chen, Z. and Chen, D. and Zhao, X. and Zheng, Q. 2013. Four-point-bending-fatigue behavior of the Cu 45 Zr 45 Ag 7 Al 3 bulk metallic glass. *Journal of Non-Crystalline Solids* 370, pp. 31-36.

Zhang, X. and Li, S.-X. and Liang, R. and Akid, R. eds. 2013. Effect of corrosion pits on fatigue life and crack initiation. ICF13.

Zhiyuan Han, H. L. 2011. Acoustic emission during fatigue crack propagation in a micro-alloyed steel and welds. *Materials Science and Engineering A*, pp. 7751-7756.

Zhou, W. and Wang, Q. and Ling, W. and He, L. and Tang, Y. and Wu, F. and Liao, J. and Hui, K. and Hui, K. 2014. Characterization of three-and four-point bending properties of porous metal fiber sintered sheet. *Materials & Design* 56, pp. 522-527.

Appendix A: Summary of fatigue test

Table A.1: mild steel S-N curve data of all Groups.

Designation	Stress Range	Uncorroded	Corrosion 25 days	Corrosion 50 days
1	360	1680	1542	
2	330	62183		
3	320	104247	95512	5642
4	300	183536	133596	90990
5	290	355528	169377	
6	275	343197	129053	155161
7	250	516415	505546	
8	230	2518366	612040	161492
9	211	5567586	1285177	821427
10	200	5682197	2885122	
11	185		5156284	2054732
12	170			3296818
13	150			5682197
14	125			5218366

Table A.2: FB590 S-N curve data of Group1.

Bending un welding		Bending welding		Tension unwelding		Tension welding	
Stress Range (MPa)	N (Cycles)						
575	356125	500	397591	500	95961	450	14862
550	861293	475	537931	475	191317	400	33444
540	2105759	462	421152	450	1214436	350	102229
530	3832194	450	5599244	425	433057	300	138350
520	5392194	425	1931829	412	2966195	250	325566
500	5731584	400	708151	400	5194844	200	5366299
450	5239055	350	2916878			150	5430573
400	5295846	300	5195011				

Table A.3: FB590 S-N curve data of Group 2.

Bending un welding		Bending welding		Tension unwelding		Tension welding	
Stress Range (MPa)	N (Cycles)						
525	100074	500	85436	500	36308	450	18868
475	1477910	425	1277915	450	195847	400	38724
450	1188966	400	190446	425	179343	350	97561
425	1477910	325	1085011	400	260880	225	1711542
410	2998948	300	954069	375	572380	212.5	174820
400	1315543	275	1734948	350	3806539	175	1811997
387.5	3598948	262.5	5055292	337.5	5354707	162.5	6461197
375	5301541	250	5328461			150	5174706

Table A.4: FB590 S-N curve data of Group 3.

Bending un welding		Bending welding		Tension unwelding		Tension welding	
Stress Range (MPa)	N (Cycles)						
500	45632	400	99844	450	10875	350	20080
450	100847	325	291184	400	310484	275	123180
400	568888	300	742541	350	153875	250	14508
375	807393	275	1410649	300	356892	225	73018
350	867824	250	3011097	275	156892	175	844970
325	1402812	225	3942753	250	1400134	150	344331
312.5	2094518	200	5862872	225	5754233	100	5153034
300	5776362			200	5253034		

Table A.5: FB590 S-N curve data of Group 4.

Bending un welding		Bending welding		Tension unwelding		Tension welding	
Stress Range (MPa)	N (Cycles)						
375	50026	300	81702	350	7158	300	43714
350	97200	225	1262173	300	16484	250	126320
300	131448	200	1112398	250	93052	225	214422
250	186985	175	1196828	225	168223	200	158289
225	1181328	162.5	5246209	200	326108	187.5	238907
212.5	1478700	150	5364845	187.5	468688	175	5097023
200	5674860			175	5706355		

Table A.6: FB590 S-N curve data of Group 5.

Bending un welding		Bending welding		Tension unwelding		Tension welding	
Stress Range (MPa)	N (Cycles)						
500	66308	500	23698	400	18766	350	46069
425	487172	450	108234	350	280831	300	108739
400	237092	425	38995	300	351105	200	321319
375	819355	350	140582	275	388531	187.5	5569358
350	5177380	337.5	339540	250	3434416	175	3700683
325	2072107	325	5337027	225	1196106	150	5545765
300	6056306	300	5478538	200	5196266		

Appendix B- Published Papers

Detection of Cracking in Mild Steel Fatigue Specimens Using Acoustic Emission and Digital Image Correlation

Kadhun SHRAMA^{1,2}, Alastair CLARKE¹, Rhys PULLIN¹, Sam L. EVANS¹
¹Cardiff University, Cardiff, United Kingdom
²University of Basrah, Basrah, Iraq
ShramaKM@cf.ac.uk (Kadhun Shrama), clarkea7@cf.ac.uk (A. Clarke),
PullinR@cf.ac.uk (R. Pullin), EvansSL6@cf.ac.uk (Sam Evans)

Abstract. The aim of this investigation was to identify sources of AE in mild steel fatigue specimens and relate them to damage mechanisms. Digital Image Correlation (DIC), a full-field strain measurement technique, was used to validate the findings. This paper describes in detail the results of a ‘dog bone’ style specimen undergoing uni-axial fatigue loading. This test forms part of a much larger programme designed to develop an AE monitoring system to identify damage initiation and growth from background noise in fatigue testing of automotive steels subjected to corrosion.

Crack growth was monitored in the test using two AE sensors and, to allow a comparison with the detected and located signals, DIC images were captured periodically at peak loads. As part of the initial analysis located signals were compared with areas of high deformation and crack growth as identified by the DIC system. Results demonstrated that it is possible to distinguish the different AE signals originating from various possible failure mechanisms such as Plastic deformation, delamination of DIC paint and crack initiation and propagation. This might be utilized for an effective and powerful approach to monitor multiple failure mechanisms; this has significant applications in automotive chassis testing.

Introduction

One of the main requirements in the design of many mechanical components is the ability to resist a large number of stress cycles under service loads. Fatigue life can be defined as the number of cycles involved in the growth of a crack from dimensions of the order of material grain size up to final fracture of the component [1]. This definition highlights that defects or inhomogeneities (manufacturing defects, inclusions or pits), which are larger than the material’s inherent micro-structural dimensions, are hugely detrimental to fatigue life and strength. In light of this, the effect of fatigue behaviour on pre-corroded mild steel was studied and plastic deformation, crack initiation and growth were identified using Acoustic Emission (AE) and Digital Image Correlation (DIC).

AE technology has been widely developed over four decades as a non-destructive evaluation technique and as a useful tool for materials research. It is a highly sensitive technique for detecting active microscopic events in a material, as well as crack initiation and propagation [2, 3]. DIC was used to determine the onset of cracking for comparison with the detected AE. Thus it was used to support the understanding of the detected AE



signals. The two techniques were used in order to neutralize their weaknesses [4]. Few previous studies have been conducted using the combination of DIC and AE under fatigue loading. This combination of techniques has been used previously by Pullin et al [5, 6] under fatigue loading; the first of these two studies was carried out on four point bending fatigue of aerospace steel and the second one was performed on detection of cracking in gear teeth. Other researchers have used the combination of AE and DIC but under static load. Kovac *et al.* 2010 used both these techniques to monitor AISI 304 stainless steel specimens subject to constant load and exposed to an aqueous sodium thiosulphate solution [7]. Aggelis *et al.* used both these techniques to monitor bending failure of concrete beams reinforced by external layers of different composite materials [4]. Pullin et al [5, 6] pointed out that the method of crack monitoring, with AE, had to be non-contact so as not to produce frictional sources of AE in the crack region.

This study forms part of a much larger ongoing programme designed to develop a monitoring system for fatigue tests to identify damage initiation and growth against background noise. This programme investigates automotive steel applications (specifically in chassis), where crack initiation is considered a significant characteristic in automotive chassis design, particularly with the trend towards weight reduction and the increasing use of high strength steels. Therefore it is important to identify the crack initiation location and mechanism. In this study AE was used to detect the onset of damage in a fatigue dog-bone style specimen undergoing axial fatigue loading and the results were correlated with damage mechanisms.

1. Experimental Procedure

1.1 Specimen preparation

The specimens were subjected to fatigue load ranging from 41 % to 85 % of the ultimate tensile strength (423.7 MPa), with a stress (R) ratio of 0.1 and a frequency of 5Hz. Figure 1 shows the fatigue dog-bone specimens which were manufactured from 3 mm thick, mild steel plate (0.2% proof stress 275 MPa, ultimate strength 423.7 MPa and elongation 36% based on three coupon tests). Part of the specimens were subjected to alternating spraying of 5 % NaCl solution according to a corrosion procedure as explained in SAEJ2332 [8] .

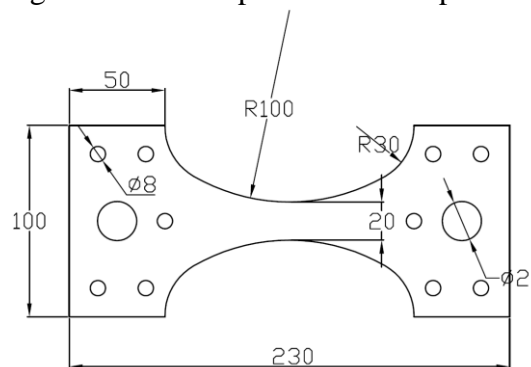


Fig.1. Details of fatigue specimen geometry (dimensions in mm)

1.2 Acoustic Emission and Digital image correlation preparation

A combination of AE and DIC was used to monitor the fatigue crack growth during the fatigue tests. Test specimens were instrumented with two Mistras Group Limited (MGL) Nano 30 sensors, the sensors being held in position with silicone grease which was also

used as an acoustic couplant. Installed sensor sensitivity was evaluated using the pencil lead fracture technique. The response to the Hsu-Nielsen source of both sensors, in all tests, was above 97 dB [9]. In order to eliminate experimental noise, a threshold of 45 dB was used.

The test was stopped at 1000 cycle intervals, peak load applied and DIC images captured as shown in the load history shown in Figure 2a [6, 10]. Figure 2b schematically shows the fatigue specimen is held on pinned joints in a Losenhausen servo-hydraulic testing machine (maximum force 100kN) with an MTS FlexTest controller and equipped with AE and DIC equipment in order to track the crack growth during fatigue test. The relative movement of two pixel subsets for either side of the crack was used to provide a crack mouth opening displacement (CMOD) measurement in order to validate and support the understanding of the collected AE data. Using DIC offers significant advantages over foil crack gauges and traditional crack mouth opening displacement gauges. Both these traditional methods can introduce acoustic emission sources into the experiment either through glue cracking in foil gauges or frictional noises from the CMOD gauge contact point with the specimen. DIC images were collected every 1000 cycles using a Dantec Dynamics Q-400 system which was triggered from the MTS controller while holding briefly at maximum load.

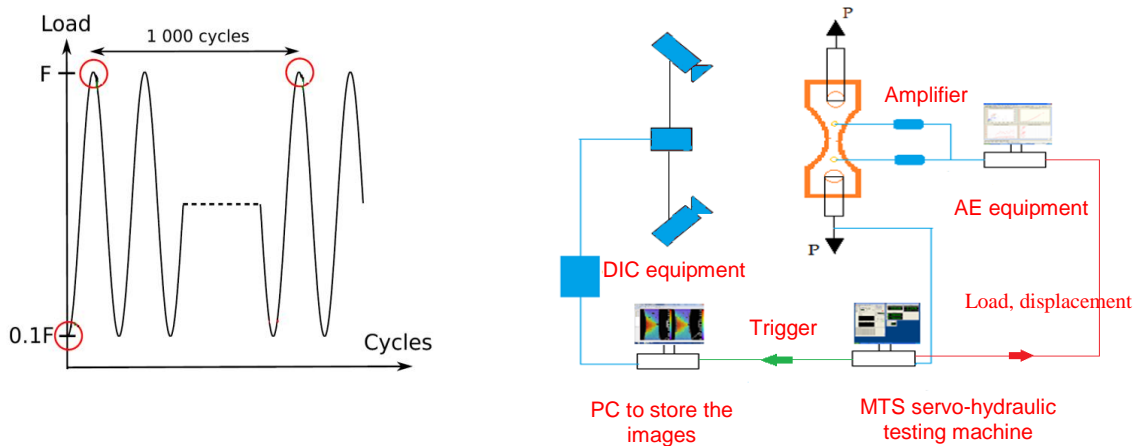


Fig. 2. (a) DIC Image capture during the load history, (b) schematic diagram of fatigue test

2. Results and Discussion

AE is a highly sensitive technique; it acquires AE information from both real cracks and noise. Eventually, the different types of noises hamper the reliability and accuracy of AE analysis [11, 12]. To remove AE noise data related to surface rubbing at the pins, environmental noise and other unknown sources generated outside the tested materials, all data files were filtered according to spatial position for a wide region. This region included the fatigue crack growth and crack closure (rubbing of the crack faces), but also plastic deformation of the material around the crack tip and elsewhere.

Cumulative counts and cumulative absolute energy are two parameters that are used to develop plots that correlate to the fatigue crack growth process with time [13]. In the present study these AE parameters were compared with the DIC results (CMOD measurement) and plotted against number of cycles (N) under various stress levels.

Analysis was performed and is presented in detail for a fatigue test with a peak stress of 320MPa (Case I) for specimen previously subjected to 25 days of corrosion. Figure 3 shows the digital image correlation-derived CMOD measurement and AE data

recorded during the fatigue test. It can be seen from the plot that the initial increase in acoustic activity coincides with an increase in crack mouth opening, suggesting that the AE came from the crack.

It worth mentioning that the plastic deformation effect can take place throughout the fatigue process, especially in the early stages of the test, and it generated significant AE. It was obvious in this test under high load (Case I), however it also occurred under lower load [14].

Here it was observed that the plastic deformation effect was accompanied by pronounced AE activity due to the dislocation glide and deformation twinning [15, 16]; this is clear from the significant AE activity at the onset of the test which is represented by group A (dashed line rectangle) in Figure 3b. It can be seen from this figure that those signals which are emitted from plastic deformation had an amplitude of around 45-50 dB, which agrees with the findings of Barsoum [13].

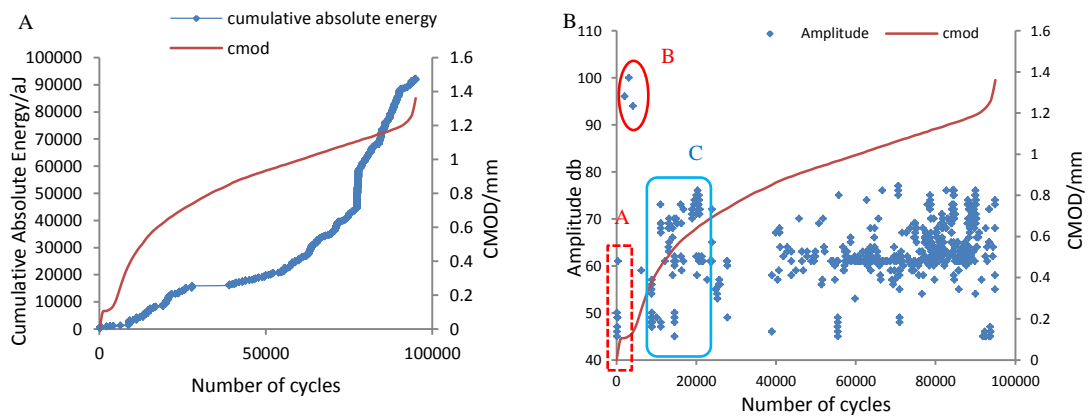


Fig. 3. (a) Cumulative absolute energy (b) Amplitude on primary axis and CMOD on secondary axis vs number of cycles for corroded specimen under 320MPa maximum stress

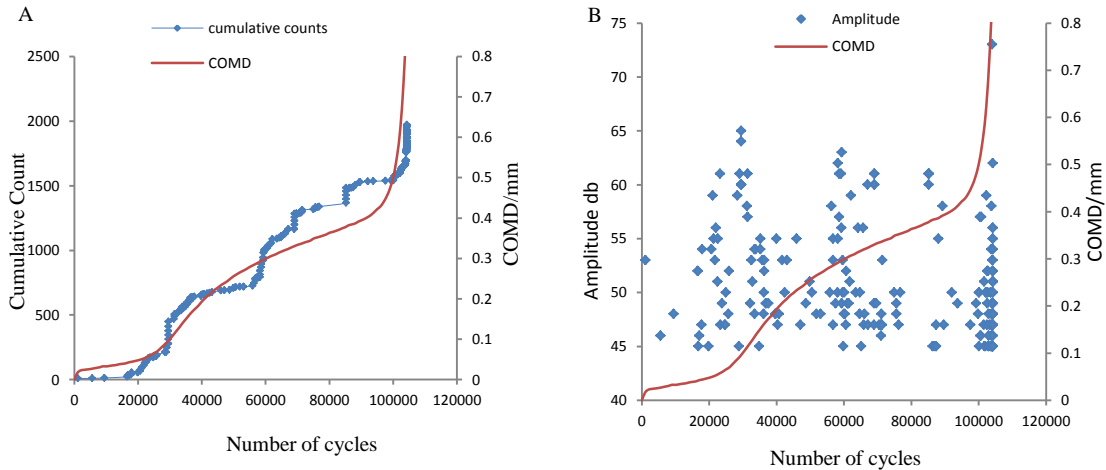


Fig. 4. (a) Cumulative counts (b) Amplitude on primary axis and COMD on secondary axis vs number of cycles for un-corroded specimen under 320MPa maximum stress

Figure 4 shows the test results for an uncorroded specimen (Case II) under similar loading conditions to Case I. In this test the specimen was reused for a second time. Firstly this specimen was loaded under 211 MPa for around 5.6 million cycles then re-loaded at 320MPa until failure at 104247 cycles. It can be seen from Figure 4(b) that there was no significant AE activity at early stages of the test when compared to Case I. The possible

reason for this is that plastic deformation happened in the first loading at a lower load; from this it can be seen that both DIC and AE can detect plastic deformation.

In order to analyse Case I in more detail, considering Figure 3(b), it may be seen that there was a group of signals (group B) having high amplitudes above 94dB. Consideration of both AE and DIC data allows these signals to be identified as resulting from the mechanism of brittle fracture or delamination of corrosion products from the underlying substrate material. Consideration of the location of signals, identified by the time of arrival method using commercial software (AEwin), identifies these signals as being generated by a source at an “X” location (along the test specimen’s reduced section) of 0.01-0.02m, as shown in Figure 5(a). Inspection of the corresponding DIC image in Figure 5(b) shows a high level of out-of-plane displacement at this location, highlighted in Figure 5(b). The out of plane displacement at this location was compared to that at surrounding points (Figure 6) and shown to have a higher level, increasing with loading cycle, indicating the gradual flaking of corrosion product. Post-test visual inspection of the specimen confirmed the presence of flaking corrosion product at this location.

Again Figure 3b shows a slight increase in AE activity around 8k cycles which is represented by group C (rounded rectangle). This is not obvious in Figure 3(b); however an increase can be seen in the enlarged view shown in Figure 7(a). This increase in AE activity was probably generated from two mechanisms. The first one is the crack initiation and the second one is most likely the noise due to delamination of DIC paint which is rubbing with specimen surfaces around the crack path, so that might be a limitation of this technique. Figure 7(b) shows out of plane displacement which reveals DIC paint was flaked due to the crack initiation underneath it, potentially producing high levels of AE activity. There was another significant increase in AE activity around 16k cycles accompanied by a similar increase in DIC pattern, Figure 7(c). This increase may have resulted from crack extension and other signals related to these mechanisms such as plastic opening at the crack tip, plastic zone extension and crack advance [13, 17]. This increase demonstrates that the crack has started and was consistent between both techniques. This increase was largely caused by crack growth) as opposed to plastic deformation away from the crack tip, observations which are consistent with those of Pullin et al [5].

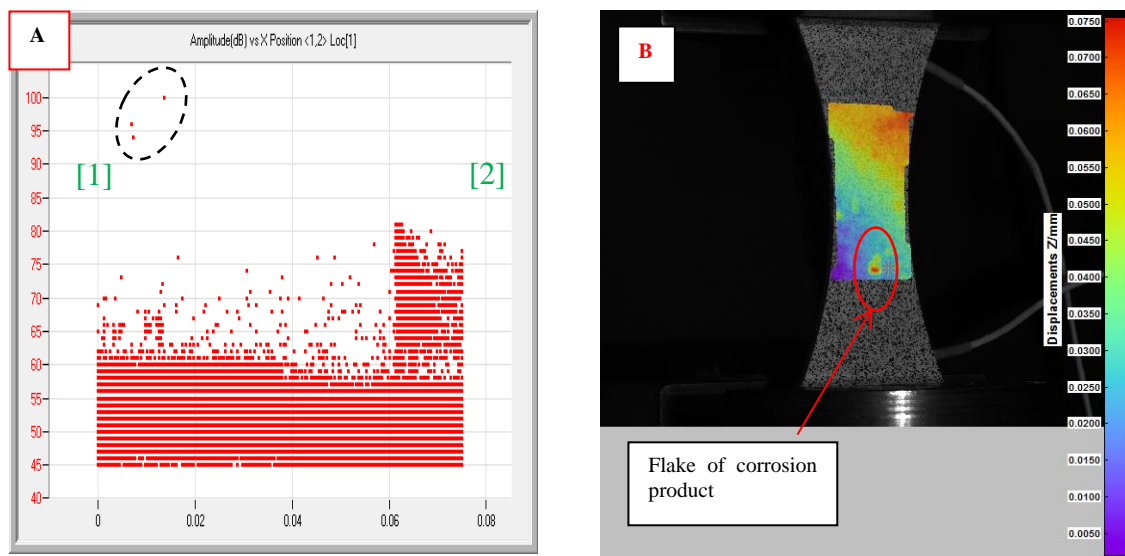


Fig. 5. reveals the flake in the corrosion product by DIC and AE methods

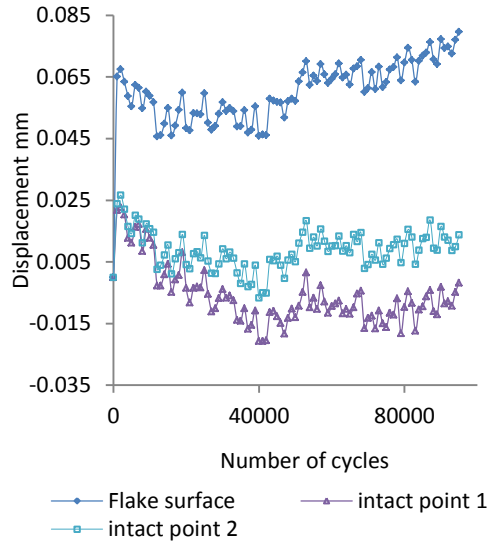


Fig. 6. Out of plane displacement for intact and flake surface

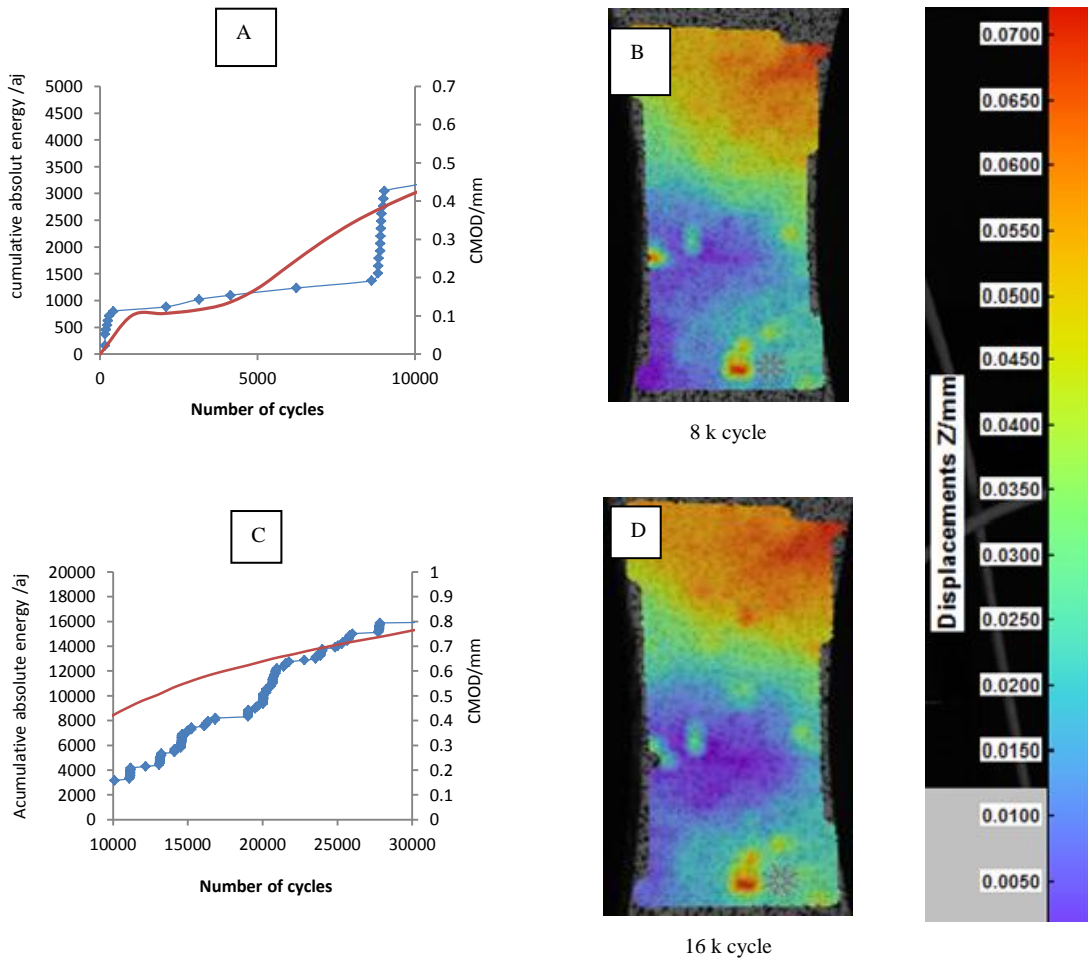


Fig. 7. Focused view of Figure 3 and corresponding DIC images

The observations of AE for Cases I and II show slightly different characteristics. In Case I there was an increase in AE activity at an early stage of the test; this was attributed to plastic deformation. The signals generated from crack initiation were mixed with a large number of signals generated by the damaged DIC paint on the specimen surface around the

crack path which are represented by group C in Figure 3(b). These signals were followed by a reduction in the AE activity for a stable prolonged period of 23-40 k cycles. The most likely reason for this reduction in the AE activity is that the DIC paint failed or peeled off as shown from DIC image Figure 7 (d); this eventually lead to stopping of the rubbing. Additionally, it can be noticed that crack propagation started early in case I at around 8k cycles whilst in case II it started at around 20 k cycles because the specimen in case I was corroded thus having surface pitting and increased roughness which generates stress concentration sites.

Conclusions

This study revealed and identified the mechanisms that occurred during crack growth. Fatigue tests were monitored using the AE technique in order to detect fatigue damage in mild steel and correlate the results. The results demonstrate the capabilities of AE for detecting fatigue fractures; it can also be argued that it is possible to distinguish the different AE signals originating from various possible failure mechanisms. Plastic deformation and delamination of DIC paint as well as crack initiation and propagation have been identified.

DIC provided a clear depiction of the surface strain field and its transient changes according to stress redistribution which occurs as the crack propagates. It is a useful method for monitoring the whole area of interest and it is not limited to a specific region, therefore any damage or microcracks can be detected and recognized. DIC was used to support the understanding of the detected AE signals. Complementary use of DIC and AE helps to minimize the assumptions in the interpretation of the AE trends in relation to the responsible damage mechanisms by revealing the fluctuation of the surface strain fields.

In the study, it was possible to detect crack initiation and distinguish it from various other mechanisms, where this might be utilized for an effective and powerful approach to monitor multiple failure mechanisms; this has significant applications in automotive chassis testing.

Acknowledgements

The authors would like to thank the Iraqi Ministry of Higher Education and Scientific Research and the Iraqi Ministry of Electricity for supporting this research and the technical staff of Cardiff School of Engineering for their kind assistance with the testing programme.

References

1. Taylor, D., *Chapter 9 - Fatigue: Predicting fatigue limit and fatigue life*, in *The Theory of Critical Distances*. 2007, Elsevier Science Ltd: Oxford. p. 163-II.
2. Miller, R.K.a.M., P, *Acoustic Emission Testing. NDT Handbook*. American Society for Non-destructive Testing, 2005. 6.
3. Berkovits, A. and D. Fang, *Study of fatigue crack characteristics by acoustic emission*. Engineering Fracture Mechanics, 1995. 51(3): p. 401-416.
4. Aggelis, D.G., Verbruggen, S., Tsangouri, E., Tysmans, T., Van Hemelrijck, *Characterization of mechanical performance of concrete beams with external reinforcement by acoustic emission and digital image correlation*. Construction and Building Materials, 2013. 47(0): p. 1037-1045.
5. Pullin, R., Eaton M. J., Hensman J. J., Holford K. M., Worden K., Evans S. L., *Validation of Acoustic Emission (AE) Crack Detection in Aerospace Grade Steel Using Digital Image Correlation*. Applied Mechanics and Materials, 2010. Vols. 24-25: p. 221-226.
6. Pullin, R., Clarke, A., Eaton, M. J., Holford, K. M., Evans, S. L., McCorry, J. P., *Detection of cracking in gear teeth using Acoustic Emission*. 2010. Vols. 24-25: p. 45-50.

7. Kovac, J., Alaux, Carole, Marrow, T. James, Govekar, Edvard, Legat, Andraz , *Correlations of electrochemical noise, acoustic emission and complementary monitoring techniques during intergranular stress-corrosion cracking of austenitic stainless steel*. Corrosion Science, 2010. 52(6): p. 2015-2025.
8. SAEJ2332, *Cosmetic corrosion Lab test* SAE J2332, 2002.
9. ASTM E976, *Standard guide for determining the reproducibility of acoustic emission sensor response*. American Society for Testing and Materials 2001.
10. Mathieu, F., F. Hild, and S. Roux, *Identification of a crack propagation law by digital image correlation*. International Journal of Fatigue, 2012. 36(1): p. 146-154.
11. Teik, E., *Material fatigue behavior characterization using the wavelet-based AE technique - a case study of acrylic bone cement*. Engineering Fracture Mechanics 2001. 68: p. 1477-1492.
12. Berkovits, F.a., *Fatigue damage mechanism on the basis of Acoustic Emission measurements* ASME 1993. 176: p. 219-235.
13. Barsoum, F.F., *Acoustic Emission Monitoring And Fatigue Life Prediction In Axially Loaded Notched Steel Specimens*. J. Acoustic Emission, 2009. Vols. 27: p. 40-63.
14. Lepisto, M.L.a.T., *Effect of cyclic deformation on Barkhausen noise in a mild steel*. NDT&E International, 2003. 36 p. 401-409.
15. Janeček, M., Miloš, Král, Robert, Dobroň, Patrik, Chmelík, František, Šupík, Vladimír, Holländer, Frank , *Mechanisms of plastic deformation in AZ31 magnesium alloy investigated by acoustic emission and transmission electron microscopy*. Materials Science and Engineering: A, 2007. 462(1-2): p. 311-315.
16. Vinogradov, A., Alexei, Orlov, Dmitry, Danyuk, Alexei, Estrin, Yuri , *Effect of grain size on the mechanisms of plastic deformation in wrought Mg-Zn-Zr alloy revealed by acoustic emission measurements*. Acta Materialia, 2013. 61(6): p. 2044-2056.
17. Scruby, C.B., *An Introduction to Acoustic Emission*. J. Phys, E: Sci. Instrument, 1987. 20: p. 946-953

Fatigue crack monitoring in mild steel specimens using acoustic emission and digital image correlation

K Shrama, R Pullin, A Clarke and S L Evans

Acoustic emission (AE) is a passive form of non-destructive testing that relies on the detection of transient elastic waves released by localised sources within a material as it undergoes deformation. It is a highly sensitive technique for detecting processes such as plastic deformation and crack propagation. The aim of this investigation was to quantify AE in mild steel specimens and relate it to damage mechanisms. Digital image correlation (DIC), a full-field strain measurement technique, was used to characterise plastic deformation and crack growth. This paper investigates in detail the results of three 'dog-bone' style specimens undergoing uniaxial fatigue loading. AE was monitored in the tests, to allow both the detection and location of signals, and DIC images were captured periodically to provide a clear depiction of the surface strain field evolution. Located signals were compared with areas of high deformation and crack growth, as identified by the DIC system. Scanning electron microscope (SEM) fractography was used to investigate crack initiation and growth. The results demonstrate that the combination of AE and DIC can provide much useful information to help to distinguish the different AE signals originating from various possible failure mechanisms.

Keywords: acoustic emission, digital image correlation, fatigue, mild steel.

1. Introduction

One of the main requirements in the design of many mechanical components is the ability to resist a large number of stress cycles under service loads. Fatigue is one of the common causes of failure in engineering components but it is still not well understood, even in common materials such as mild steel. In high-cycle fatigue, much of the life is taken up by the early initiation of a crack^[1]. Therefore defects or inhomogeneities (manufacturing defects, inclusions or pits), which are larger than the material's inherent micro-structural dimensions, are hugely detrimental to fatigue life and strength. However, the interaction between such defects and the initiation of fatigue cracks is complex and poorly understood, largely because of the difficulty in monitoring the process as it occurs. In light of this, the effect of fatigue behaviour on pre-corroded mild steel was studied and plastic deformation, crack initiation and growth were monitored using acoustic emission and digital image correlation.

Acoustic emission (AE) technology has been widely developed over four decades as a non-destructive evaluation technique and as a useful tool for materials research. It is a sensitive technique for detecting active microscopic events in a material, including crack initiation and propagation^[2,3]. The continuous monitoring of fatigue crack propagation is one of the common applications of AE. Many studies have shown that AE is capable of monitoring fatigue crack initiation^[4,5], propagation^[6-8] and crack closure phenomena^[8-10] in steels and other metallic alloys. Sources of acoustic emission are defect-related processes, such as crack extension and plastic deformation of a material in the highly-stressed zone adjacent to the crack tip. Moorthy *et al.*^[11] indicated that for a ductile material the major source of AE was plastic deformation at the tip of the crack, whereas for brittle materials it was crack extension at the crack tip instead. However, the authors postulated that ductile crack growth is a very weak source of acoustic emission.

Experimental fatigue tests typically require large testing times.

This testing time considerably increases when one periodically has to interrupt the fatigue test to manually measure crack lengths or specimen extension. Here, it will be shown that the digital image correlation (DIC) technique can be applied with success to determine the initiation of cracking for comparison with the detected AE. Moreover, the DIC measurements allow the determination of stress intensity factors during the experiment^[12,13], and also plastic deformation away from the crack. This is a major advantage in materials such as mild steel, where general plastic deformation often occurs in parallel with the development of fatigue cracks. This elastic-plastic fracture process is not well understood and capturing the full deformation field during a test is potentially very valuable. Measuring the full strain field also allows the initiation of cracks to be monitored, even when their precise location is not known in advance.

In this study, the two techniques were used as they have complementary advantages and disadvantages^[14]. Few previous studies have been conducted using the combination of DIC and AE under fatigue loading. This combination of techniques has been used previously by Pullin *et al.*^[15,16] under fatigue loading; the first paper reports four-point bending fatigue of aerospace steel and the second concerns the detection of cracking in gear teeth under fatigue loading. Other researchers have used the combination of AE and DIC but under static loads. Kovac *et al.*^[17] used both these techniques to monitor AISI 304 stainless steel specimens subject to

● Submitted 10.10.14 / Accepted 20.04.15

Kadhum Shrama, R Pullin, A Clarke and S L Evans are with the School of Engineering, Cardiff University, The Parade, Cardiff CF24 3AA, UK. Email: shramakm@cf.ac.uk / pullinr@cf.ac.uk / clarkea7@cf.ac.uk / evanssl6@cf.ac.uk

Kadhum Shrama is also with the University of Basrah, Basrah, Iraq.

constant load and exposed to an aqueous solution. Aggelis *et al*^[14] used both these techniques to monitor bending failure of concrete beams reinforced by external layers of different composite materials.

As it is obvious that automotive chassis components belong to the category of safety-critical components, where failure has potentially catastrophic consequences, their structural durability design has to be carried out through a consideration of all possible types of service loadings. This programme investigates automotive steel applications where crack initiation is considered a significant limiting characteristic in design, particularly with the trend towards weight reduction and the increasing use of high-strength steels. Therefore, it is important to identify the crack initiation location and mechanism. AE was used to detect the onset of damage in dog-bone style fatigue specimens undergoing axial cyclic loading and the results were correlated with the strain field measured using DIC, giving valuable insight into the possible mechanisms of damage and AE generation. Scanning electron microscope (SEM) fractography gave further insight into the relationship between various phenomena occurring in fatigue crack development and the AE signals.

2. Experimental procedure

2.1 Specimen preparation

Figure 1 shows the fatigue dog-bone specimens, which were manufactured from 3 mm-thick mild steel plate (0.2% proof stress of 275 MPa, ultimate strength of 423.7 MPa and elongation of 36%). A part of the specimens was subjected to a salty solution according to SAEJ2332^[18]. The specimens were subjected to a fatigue load ranging from 41% to 85% of the ultimate tensile strength (423.7 MPa), with a stress (*R*) ratio of 0.1 and a frequency of 5 Hz. The fatigue specimens were pinned in a Losenheim servo-hydraulic testing machine (maximum force 100 kN) with an MTS FlexTest controller. After the fatigue tests, the fracture surfaces were observed using a scanning electron microscope (SEM), model: Zeiss 1540 XB cross-beam scanning electron microscope.

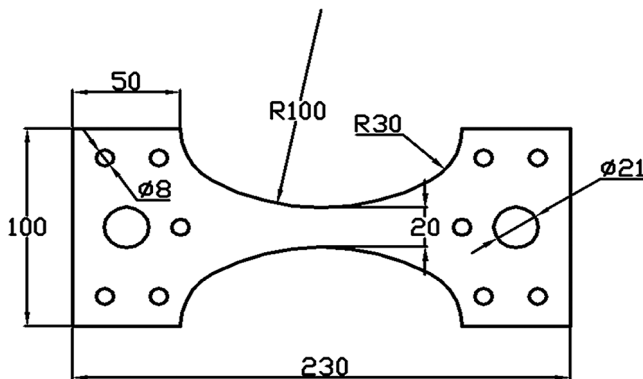


Figure 1. Details of fatigue specimen geometry (dimensions in mm)

2.2 Acoustic emission preparation

Test specimens were instrumented with two Mistras Group Limited Nano 30 sensors; the sensors were held in position with silicone, which was also used as an acoustic couplant. The installed sensor sensitivity was evaluated using the pencil lead fracture technique (Hsu-Neilsen source). The response to the H-N source of both sensors, in all tests, was above 97 dB^[19]. In order to eliminate experimental noise, a threshold of

45 dB was selected, just above the background noise level. The selection of threshold was based on previous research on steel^[16,20,21].

2.3 Digital image correlation set up

DIC images were collected every 1000 cycles using a Dantec Dynamics Q-400 system, which was triggered from the MTS controller while holding briefly at maximum load. Figure 2(a) explains the load history^[16,22], while Figure 2(b) schematically shows the fatigue specimen held in a fatigue testing machine equipped with AE and DIC equipment in order to track the crack growth during the fatigue test.

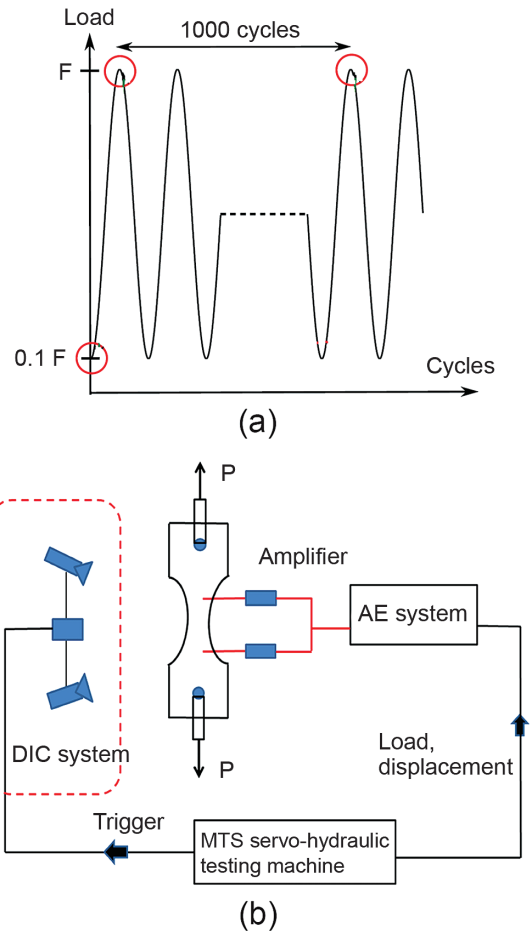


Figure 2. (a) DIC image capture during the load history; (b) schematic diagram of the fatigue test

The relative movement of two pixel subsets on either side of the crack was used to provide a crack mouth opening displacement (CMOD) measurement in order to validate and support the understanding of the collected AE data. Using DIC offers significant advantages over foil crack gauges and traditional crack mouth opening displacement (CMOD) gauges. Both these methods can introduce acoustic emission sources into the experiment, either through glue cracking in foil gauges or frictional noises from the CMOD contact point with the specimen.

3. Results and discussion

AE is a sensitive technique; it acquires AE information from both real cracks and noise. Eventually, the different types of noise hamper the reliability and accuracy of AE analysis^[4,23]. To remove AE data related to surface rubbing at the pins, environmental noise

and other unknown sources generated outside the test specimens, all data files were filtered by location around the crack, using only data between the AE sensors and discarding other data. This region included fatigue crack growth and crack closure, but also plastic deformation of the material around the crack tip and elsewhere. The AE parameters were compared with DIC measurements and plotted against the number of cycles (N) under various stress levels. In general, the cumulative energy and count followed the crack growth for the duration of the test; this confirms that the AE is detecting the crack growth. The rate of events varies during the test and did not increase continuously with crack length; this variation in the rate of events is due to a variety of source mechanisms. The source mechanisms can be classified into primary and secondary sources, according to Scruby^[24]. The primary sources associated with crack growth are plastic zone extension, plastic opening at the crack tip, elastic crack advance as well as decohesion. Secondary events associated with fatigue crack growth are the elastic response of a pre-crack, crack face fretting and brittle fracture of a corrosion product.

In this paper, two experimental cases are presented in detail, which reflect the general observations associated with other experimental tests at loads of 320 MPa and 230 MPa. Case I is for a load condition of 230 MPa and not corroded, while Case II presents results for a test load of 320 MPa for a specimen previously subjected to 25 days of corrosion.

3.1 Fractography characterisation

The scanning electron micrographs of the fracture surface of the two fatigue specimens are shown in Figures 3 and 4. The fatigue crack of specimen I (Figure 3(a)) was almost flat with a length of 5.114 mm. The fatigue crack of Case II, Figure 4(a), shows typical features under high axial loading fatigue. It consists of a 45° chamfer, at the left end of Figure 4(b), where the crack initiated in stage I, then it is followed by a granular area of fatigue crack growth. The fatigue crack propagation region for case II was rougher and shorter than in case I, with a length of 1.122 mm. The reduction in specimen cross-section area is obvious; it occurred before quasi-cleavage, suggesting plastic deformation, as shown in Figure 4(a).

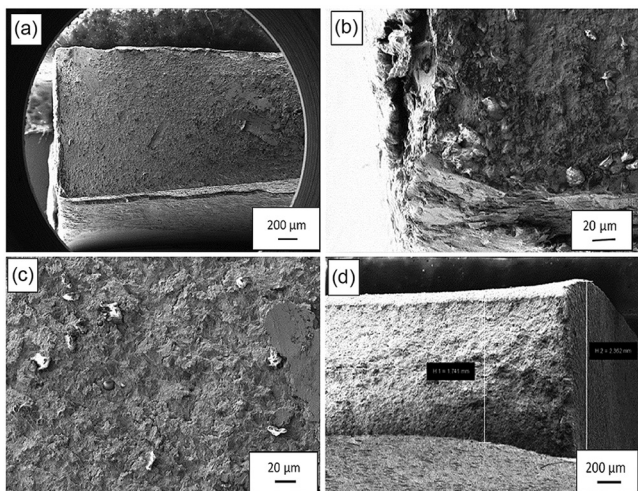


Figure 3. SEM micrographs taken from fracture surfaces of fatigue tested specimens, Case I: (a) showing the general appearance and no necking; (b) indicates the crack initiation corner opposite to the DIC cameras; (c) shows that dimple coalescence was not obvious in the specimen tested at 230 MPa; and (d) indicates ductile fracture and reduction in cross-section

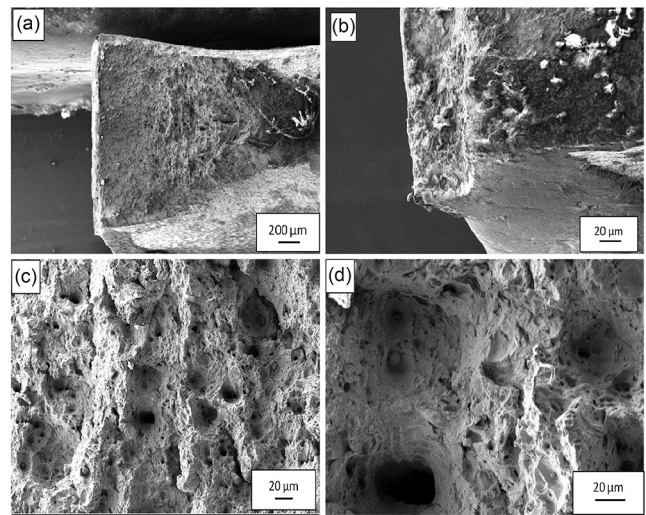


Figure 4. SEM micrographs taken from fracture surfaces of fatigue tested specimens, Case II: (a) showing general appearance and necking; (b) site of crack initiation; (c) and (d) indicate the elongated shape of some voids and dimple coalescence

In both cases, the fatigue fracture surface can be divided into two parts, fatigue crack propagation and fast fracture. The first part is characterised by a granular area close to the crack initiation zone, but there was a difference in the length of the first part between the two cases. The remaining surface, the second part, is the ductile fracture surface, Figure 3(d), caused by overloading of the specimen because of the reduction in cross-section area^[17]. This part is similar to the tensile fracture surface mechanism, like the classic cup and cone type. The transition from stable to unstable crack propagation is characterised by the change in fracture mode from fatigue crack growth to a ductile fracture. Figures 4(c) and 4(d) show average dimple sizes (diameters) of micrographs for the specimen in Case II. It also shows the presence of non-uniform small and large dimples, indicating considerable plastic deformation ahead of the fatigue crack. The elongated shape of some voids may indicate that there were localised shear stresses. Figure 4(d) shows dimple coalescence; there is a direct relationship between dimple coalescence and necking^[25]. The dimple coalescence and necking is not obvious in Case I, as shown in Figure 3(c), where less plastic deformation occurred and the fracture surface is more characteristic of pure fatigue failure. The fracture surfaces for the specimen in Case I show a higher amount of fatigue damage and a significantly longer crack length before fast fracture occurs.

3.2 Plastic deformation

The plastic deformation effect took place through the fatigue process, especially at an early stage of the test, and significant AE occurred during this deformation. It was obvious in Case II (the tests under high load), however it also occurs under a lower load (Case I)^[26].

It was observed that the plastic deformation was accompanied by pronounced AE activity. This may have been due to dislocation glide and deformation twinning^[27,28], although these typically have much lower amplitudes. Other possible sources include fracture of surface oxides and cracking or delamination of the paint from the surface. This activity is shown by group A (dashed line rectangle) in both Figures 5 and 6. It can be seen from these Figures that these signals had an amplitude range about values of 45-50 dB; this agrees with the findings of Barsoum^[21].

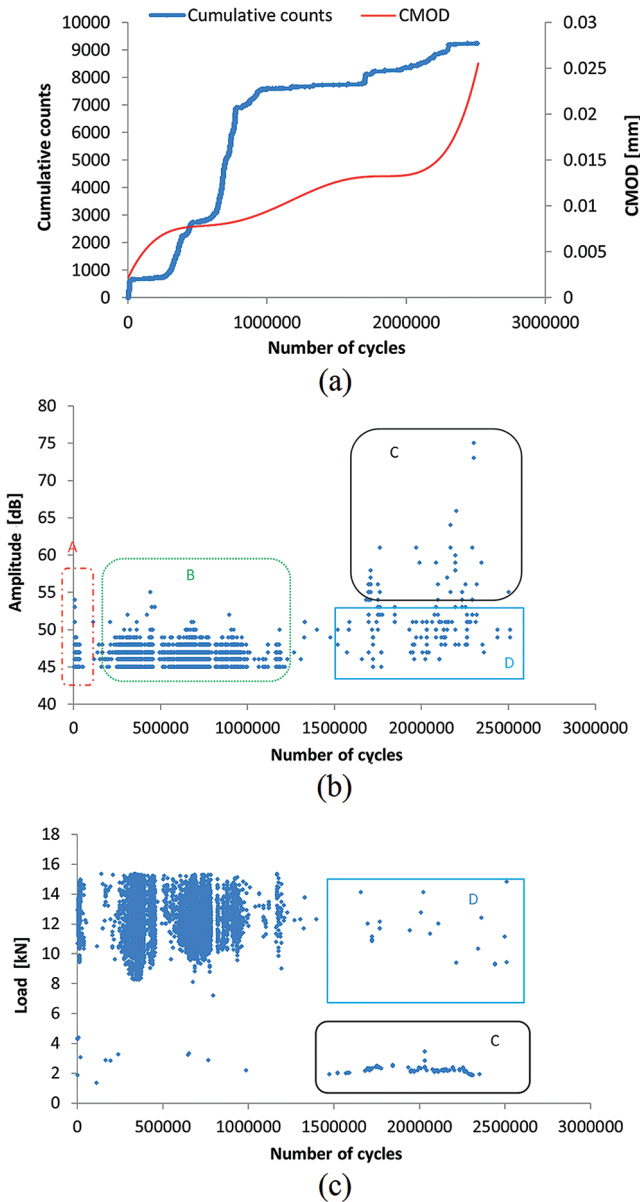


Figure 5. (a) Cumulative counts on primary axis and CMOD on secondary; (b) amplitude; (c) load versus number of cycles for uncorroded specimen under 230 MPa, Case I

Figure 7 shows the test results for an uncorroded specimen under similar loading conditions to Case II. In this test, the specimen was reused for a second time. Firstly, this specimen was loaded to 211 MPa for around 5.6 million cycles and then re-loaded at 320 MPa until failure at 104,247 cycles. Figure 7(b) shows there was no significant AE activity during the early stages of the test when compared with Case II. The possible reason for this is that the damage that generated the AE happened in the first loading at a lower load; this tends to suggest that some other mechanism, such as fracture of brittle surface oxides during plastic deformation, may have been responsible for this AE. Since there was significantly more plastic deformation when the specimen was first loaded to 320 MPa, one would expect significant AE during the second test if the AE was due to plastic deformation alone.

DIC provides a clear depiction of the surface strain field and its transient changes according to the stress redistribution that occurs during crack propagation; it is a good measuring tool

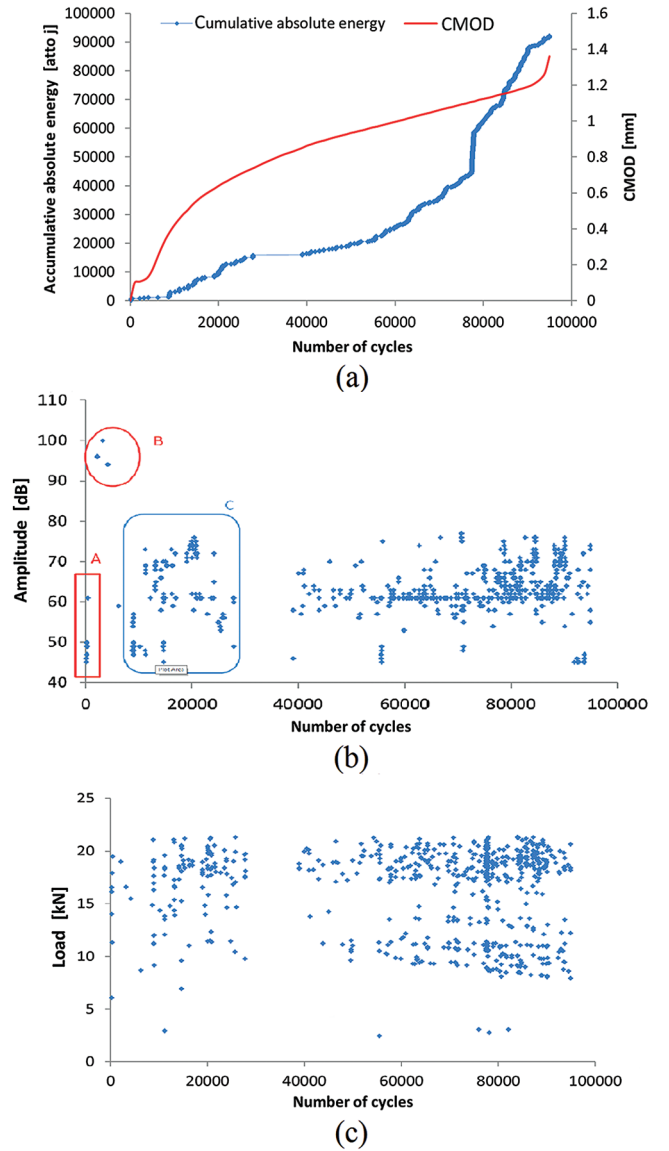


Figure 6. (a) Cumulative absolute energy on primary axis and CMOD on secondary; (b) amplitude; (c) load versus number of cycles for corroded 25 day specimen under 320 MPa, Case II

to analyse and quantify the growth of the crack and plastic zone changes. The region of interest for correlation was chosen as 20 × 60 mm, centred on the parallel section so as to observe the damage evolution until final failure. Figures 8 and 9 show the DIC images that were captured sequentially and the development of the strain distribution during fatigue loading for Cases I and II. The grey area highlights the plastic zone in the wake of the crack tip. The majority of damage initiation happened at the periphery of the specimen towards the middle. The maximum strain was observed around the edge of the crack tip perpendicular to the loading direction. A key to the strain contours is provided but should not be considered to be a true representation of the actual magnitude of the strain values around the crack position^[15] due to the calculation method employed by the image correlation software. The displacement is calculated over a subset of pixels that has a finite size, and then the strain is calculated assuming a continuous displacement field over several subsets. The spatial resolution of the strain measurement is therefore limited, and will be inaccurate near the crack.

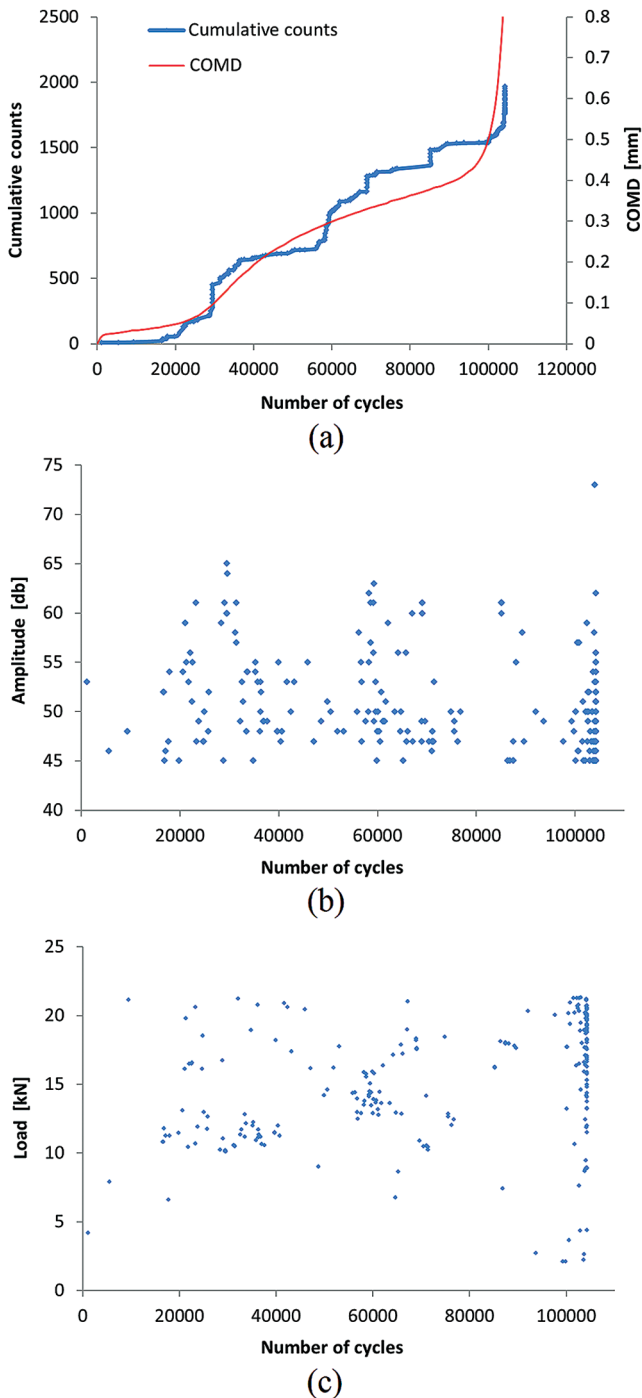


Figure 7. (a) Cumulative absolute energy on primary axis and CMOD on secondary; (b) amplitude; (c) load versus number of cycles for corroded 25 day specimen under 320 MPa, Case II

3.3 Case I

Figure 5 shows a large number of signals (group B), which occurred during crack initiation and early growth. Generation of AE during high cycle fatigue has previously been attributed to crack initiation^[3,29,30], but this seems unlikely. This stage involves the growth of microstructurally small cracks (MSCs); this could constitute stage I (shear cracking). In this stage, crack initiation stems from dislocations in the structure that accumulate due to high stress concentrations at grain boundaries, notches or surface irregularities. These begin to form fine slip line systems within the structure along the shear plane. As the slip lines increase in

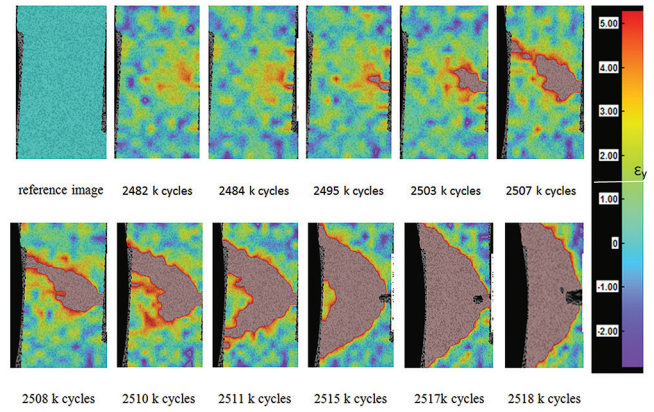


Figure 8. Development of microstrain during fatigue loading for Case I

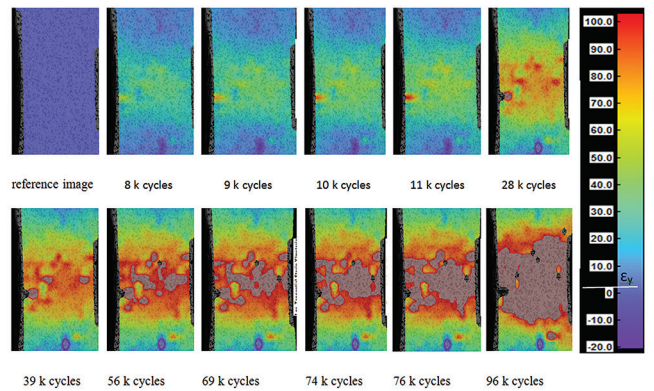


Figure 9. Development of microstrain during fatigue loading for Case II

density they broaden into bands, which ultimately form micro cracks^[31,32]. It is difficult to explain how this activity, predominantly consisting of very localised dislocation movement, could generate AE with an amplitude that could be detected, although other researchers have observed AE from fatigue crack initiation that generated low amplitude signals^[9]. The visualisation of the crack at this stage is difficult using DIC due to its very small size. In addition, in this case the crack started from the opposite face of the specimen to the DIC camera. Other possible mechanisms could include cracking of brittle surface oxides or of paint on the surface during plastic deformation and crack initiation. Examination of traditional AE parameters, such as rise time and duration, was not particularly helpful in determining the source(s) of these emissions.

The signals that occurred during the propagation stage of fatigue life have been divided into groups C (rounded rectangle) and D (rectangle), which involves the growth of mechanically small cracks. Mechanically small cracks correspond to Stage II (tensile) cracks, which are characterised by striated crack growth, with a fracture surface normal to the maximum principal stress^[31].

The amplitudes of the AE signals detected at peak load (group D) is less than 50 dB, while the amplitude of AE signals released at low load (group C) have various amplitude signals. Most of the high amplitude signals (above 56 dB) were released at this load level. The increasing amounts of fretting emission were observed as the crack advanced from Stage II towards Stage III (final fast fracture stage, which may not appear here because the AE system could not locate it). Along with this, the fracture surface got rougher^[9]; this is also explained from the fractography results, Figure 3(a).

The low amplitude and relatively small numbers of detected signals at peak load suggest that the primary source associated with the crack growth is difficult to detect in mild steel plate^[33]. Moreover, the results may suggest that the crack growth mechanism at the crack tip may be dominated by plastic tearing as this is obvious from the SEM results and agrees with Scruby^[24]. A few signals with amplitudes above the detection threshold (45 dB) detected at peak load may have been generated by a ductile crack extension mechanism, which is a very weak source of AE^[11,24], or, more likely, from the cracking of surface oxides, paint, etc.

All high-amplitude signals were detected at a relatively low load level (around 2.5 kN in Case I), which suggests that the signals were caused by rubbing of the two crack surfaces during crack closure^[9,24]. Crack closure usually takes place just after the crack opening at the crack tip (crack advancement) due to the sudden change of stress level associated with the stress relief during crack growth.

The closure effect is not clear in Case II (Figure 5) because the specimen was considerably elongated, as is obvious from the DIC results, so that the crack faces did not contact each other. In addition, the first part of the fatigue crack was very short compared with the previous Case I, as shown in Figure 3(b).

3.4 Case II

This case presented different trends to those noted in the earlier case. Referring to Figure 6(a), there was a slight increase in AE activity at around 8000 cycles. This is not obvious in this Figure; however, an increase can be seen in the close-up view shown in Figure 11(a). The increased AE activity, which is represented by group C (rounded rectangle), was presumably generated from one of two mechanisms. The first one is crack initiation and the second one is most likely considered as noise due to rubbing of the damaged corrosion product under DIC paint with specimen surfaces around the crack path, as shown in Figure 10. The amplitude of these signals could be higher due to the brittleness of the corrosion products and the friction between the delaminated paint and the specimen surface. Figure 11(b) shows out-of-plane displacement, which reveals that the DIC paint had flaked due to the crack initiation underneath it. Figure 11(c) shows another significant increase in AE activity around 16k cycles, accompanied by a similar increase in DIC pattern, Figure 9. This increase may have resulted from crack extension and other signals related to these mechanisms, such as plastic opening at the crack tip, plastic zone extension and crack advance^[21,24]. This increase demonstrates that the crack has started and was consistent between both techniques. This increase was largely caused by crack growth as opposed to plastic deformation away from the crack tip, observations which are consistent with those of Pullin *et al*^[15]. The signals in group B, Figure 5, result from mechanisms of brittle fracture or delamination in corrosion products, as explained in detail in a previous work^[34].

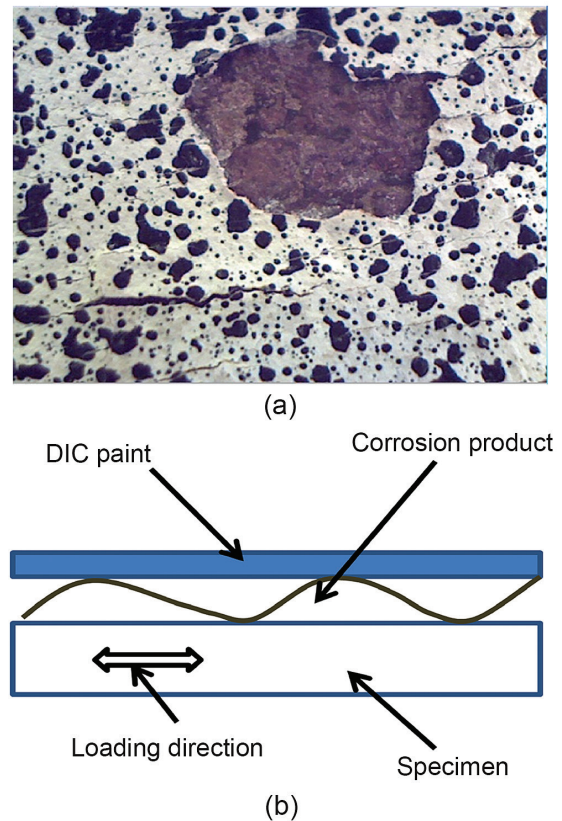


Figure 10. Schematic explaining the rubbing of the damaged corrosion product underneath DIC paint with specimen surfaces around the crack path

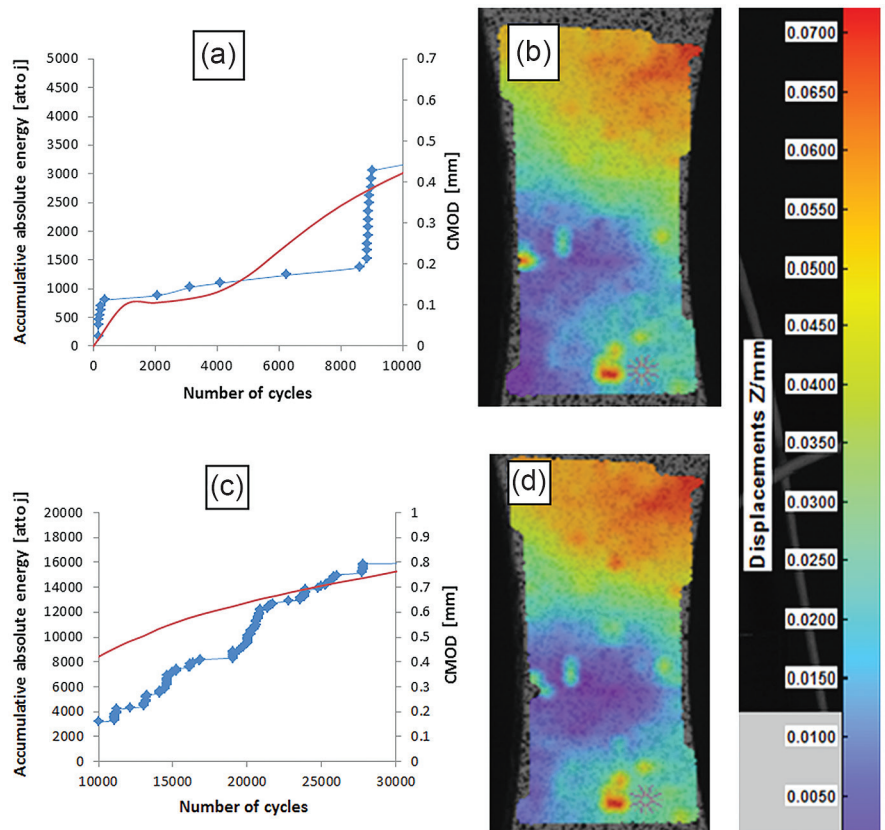


Figure 11. (a) Focused view of Figure 6 at 8 k cycle; (b) corresponding DIC images; (c) focused view at 16 k cycle; (d) DIC images at 16 k cycle

4. Conclusions

This study gave insights into the mechanisms that occurred during crack initiation and growth. The completed work has demonstrated the capabilities of AE for detecting fatigue fractures and its potential for distinguishing the different AE signals from various possible failure mechanisms. Plastic deformation, delamination of corrosion product and DIC paint, as well as crack initiation, propagation and closure, are all involved in this process and AE monitoring provides valuable information to help to distinguish between them.

DIC allows a clear depiction of the surface strain field evolution and its transient changes according to stress redistribution that occurs as the crack propagates. It is a useful method for monitoring the whole area of interest and it is not limited to a specific region, therefore any damage can be detected even if the precise location is not known in advance. DIC was used to support the understanding of the detected AE signals. The complementary use of DIC and AE helps to minimise the assumptions in the interpretation of the AE trends in relation to the responsible damage mechanisms by revealing the fluctuation of the surface strain fields and other factors such as paint delamination. Additionally, SEM was also used to verify and support the relationship between various phenomena occurring in fatigue failure and the AE signals.

The combination of AE and DIC was also helpful in distinguishing between crack initiation and early propagation and background noise, which is otherwise difficult using AE. The early growth of cracks in steel typically generates only very low level AE, which is difficult to distinguish from rubbing or fretting, for example of loose paint or corrosion products. The use of DIC allowed significant cracks to be identified well before failure. This could have numerous applications in the testing of more complex structures, for example in automotive chassis or aerospace applications.

Acknowledgements

The authors would like to thank the Iraqi Ministry of Higher Education and Scientific Research and the Iraqi Ministry of Electricity for supporting this research and the technical staff of the Cardiff School of Engineering for their kind assistance with the testing programme.

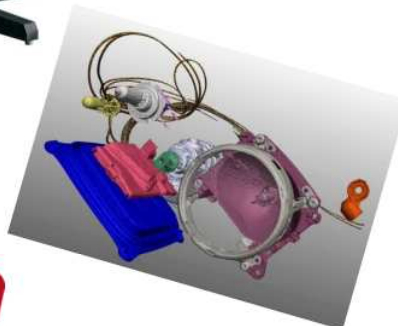
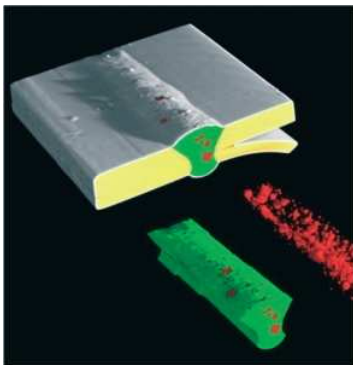
References

1. D Taylor, 'Chapter 9 – Fatigue: Predicting fatigue limit and fatigue life', In: *The Theory of Critical Distances*, pp 163-II, Elsevier Science Ltd, Oxford, 2007.
2. R K Miller and P McIntyre, 'Acoustic emission testing', *NDT Handbook*, American Society for Nondestructive Testing, 6, 2005.
3. A Berkovits and D Fang, 'Study of fatigue crack characteristics by acoustic emission', *Engineering Fracture Mechanics*, 51, pp 401-416, 1995.
4. F A Berkovits, 'Fatigue damage mechanism on the basis of acoustic emission measurements', *ASME*, 176, pp 219-235, 1993.
5. D Fang and A Berkovits, 'Fatigue design model based on damage mechanisms revealed by acoustic emission measurements', *Journal of Engineering Materials and Technology*, Transactions of the ASME, 117, pp 200-208, 1995.
6. T M Roberts and M Talebzadeh, 'Acoustic emission monitoring of fatigue crack propagation', *Journal of Constructional Steel Research*, 59, pp 695-712, 2003.
7. T M Roberts and M Talebzadeh, 'Fatigue life prediction based on crack propagation and acoustic emission count rates', *Journal of Constructional Steel Research*, 59, pp 679-694, 2003.
8. H L Zhiyuan Han, 'Acoustic emission during fatigue crack propagation in a micro-alloyed steel and welds', *Materials Science and Engineering A*, pp 7751-7756, 2011.
9. A A Pollock, 'AE observations during cyclic testing of A572 steel laboratory specimens', 30th European Conference on AE Testing, Granada, 2012.
10. H Chang, E H Han, J Q Wang and W Ke, 'Acoustic emission study of fatigue crack closure of physical short and long cracks for aluminium alloy LY12CZ', *International Journal of Fatigue*, 31, pp 403-407, 2009.
11. V Moorthy, T Jayakumar and B Raj, 'Influence of micro structure on acoustic emission behaviour during stage 2 fatigue crack growth in solution-annealed, thermally-aged and weld specimens of AISI type 316 stainless steel', *Materials Science and Engineering: A*, 212, pp 273-280, 1996.
12. S McNeill, W Peters and M Sutton, 'Estimation of stress intensity factor by digital image correlation', *Engineering Fracture Mechanics*, 28 (1), pp 101-112, 1987.
13. J Réthoré, A Gravouil, F Morestin and A Combescure, 'Estimation of mixed-mode stress intensity factors using digital image correlation and an interaction integral', *International Journal of Fracture*, 132, pp 65-79, 2005.
14. D G Aggelis, S Verbruggen, E Tsangouri, T Tysmans and D Van Hemelrijck, 'Characterisation of mechanical performance of concrete beams with external reinforcement by acoustic emission and digital image correlation', *Construction and Building Materials*, 47, pp 1037-1045, 2013.
15. M J E R Pullin, J J Hensman, K M Holford, K Worden and S L Evans, 'Validation of acoustic emission (AE) crack detection in aerospace grade steel using digital image correlation', *Applied Mechanics and Materials*, Vols 24-25, pp 221-226, 2010.
16. R Pullin, A Clarke, M J Eaton, K M Holford, S L Evans and J P McCorry, 'Detection of cracking in gear teeth using acoustic emission', *Applied Mechanics and Materials*, pp 45-50, 2010.
17. J Kovac, C Alaux, T J Marrow, E Govekar and A Legat, 'Correlations of electrochemical noise, acoustic emission and complementary monitoring techniques during intergranular stress-corrosion cracking of austenitic stainless steel', *Corrosion Science*, 52, pp 2015-2025, 2010.
18. SAEJ2332, 'Cosmetic corrosion', Lab test SAE J2332, SAE J2332, 2002.
19. ASTM E976, 'Standard guide for determining the reproducibility of acoustic emission sensor response', American Society for Testing and Materials, 2001.
20. M Baxter, 'Damage assessment by acoustic emission (AE) during landing gear fatigue testing', PhD thesis, School of Engineering, University of Wales Cardiff, Cardiff, UK, 2007.
21. F F Barsoum, 'Acoustic emission monitoring and fatigue life prediction in axially-loaded notched steel specimens', *Journal of Acoustic Emission*, 27, pp 40-63, 2009.
22. F Mathieu, F Hild and S Roux, 'Identification of a crack propagation law by digital image correlation', *International Journal of Fatigue*, 36, pp 146-154, 2012.
23. E Teik, 'Material fatigue behaviour characterisation using the wavelet-based AE technique – a case study of acrylic bone cement', *Engineering Fracture Mechanics*, 68, pp 1477-1492, 2001.
24. C B Scruby, 'An introduction to acoustic emission', *Journal of Physics*, E: Scientific Instruments, 20, p 946, 1987.
25. A Zare and A Ekrami, 'Influence of martensite volume fraction on tensile properties of triple-phase ferrite-bainite-martensite

- steels, *Materials Science and Engineering: A*, 530, pp 440-445, 2011.
26. M L T Lepisto, 'Effect of cyclic deformation on Barkhausen noise in a mild steel', *NDT&E International*, 36, pp 401-409, 2003.
 27. J Miloš, K Robert, D Patrik, C František, Š Vladimír and F Holländer, 'Mechanisms of plastic deformation in AZ31 magnesium alloy investigated by acoustic emission and transmission electron microscopy', *Materials Science and Engineering: A*, 462, pp 311-315, 2007.
 28. A Vinogradov, D Orlov, A Danyuk and Y Estrin, 'Effect of grain size on the mechanisms of plastic deformation in wrought Mg-Zn-Zr alloy revealed by acoustic emission measurements', *Acta Materialia*, 61, pp 2044-2056, 2013.
 29. C K J Mukhopadhyay, T Haneef, T K Suresh Kumar, S Rao, B P C Goyal, S Gupta, S K Bhasin, V Vishnuvardhan, S Raghava and G Gandhi, 'Use of acoustic emission and ultrasonic techniques for monitoring crack initiation/growth during ratcheting studies on 304LN stainless steel straight pipe', *International Journal of Pressure Vessels and Piping*, 116, pp 27-36, 2014.
 30. M Elforjani and D Mba, 'Detecting natural crack initiation and growth in slow-speed shafts with acoustic emission technology', *Engineering Failure Analysis*, 16, pp 2121-2129, 2009.
 31. O K Chopra, 'Mechanism of fatigue crack initiation in austenitic stainless steels in LWR environments', *American Society of Mechanical Engineers, Pressure Vessels and Piping Division (Publication) PVP*, 439, pp 133-142, 2002.
 32. H L Ewalds and R J H Wanhill, *Fracture Mechanics*, Edward Arnold, London, Delftse Uitgevers Maatschappij, 1984.
 33. Z Zuming, W Ng, Zhongguang, P Jun, 'Acoustic emission monitoring of fatigue crack growth in SM50B-Zc steel', *Materials Science & Technology*, 6, pp 345-350, 1990.
 34. K Shrama, R Pullin, A Clarke and S L Evans, 'Detection of cracking in mild steel fatigue specimens using acoustic emission and digital image correlation', In: 31st Conference of the European Working Group on Acoustic Emission (EWGAE) – We4B2, 2014.

EuroTECK
Systems UK Ltd
Non-Destructive Testing

**When you choose a CT System
don't compromise on quality and technical support!**



- ✓ CNC Control
- ✓ Multi Axis
- ✓ DR Panels
- ✓ Hi -Resolution

- ✓ Mini-Focus - 450KV
- ✓ CT Imaging
- ✓ Windows Platform
- ✓ Custom solutions
- ✓ High Quality UK Support

- ✓ Aerospace
- ✓ Automotive
- ✓ Energy
- ✓ Research

- ✓ Reverse Engineering
- ✓ Void Detection
- ✓ Surface Extraction
- ✓ Dimensional Control

RayScan

Euroteck Systems UK Ltd
Tel: +44 (0)1827 312455

Web: www.euroteck.co.uk
Email: sales@euroteck.co.uk

EuroTECK
Systems UK Ltd
Non-Destructive Testing



World Leaders in NDT, Welding and Inspection
Training and Certification

Thinking of improving your career prospects?

Advanced NDT

Eddy Current Inspection of Ferritic Welds

6 - 17 July | Middlesbrough
27 July - 7 August | Aberdeen
17 - 28 August | Middlesbrough
19 October - 6 November | Aberdeen

Digital Radiographic Testing

29 June - 3 July | Middlesbrough
9 - 13 November | Middlesbrough

Phased Array Ultrasonic Testing (PAUT)

6 - 24 July | Abington
7 - 25 September | Abington

Time of Flight Diffraction (ToFD)

3 - 14 August | Abington
26 October - 6 November | Abington
16 - 17 November | Abington

AUT Data Interpretation

24 - 28 August | Abington
28 September - 2 October | Aberdeen
23 - 27 November | Middlesbrough

ACFM Crack Microgauge Operators Course

• Level 1

20 - 24 July | Middlesbrough
17 - 21 August | Middlesbrough
19 - 23 October | Aberdeen

• Level 2

27 - 31 July | Middlesbrough
24 - 28 August | Middlesbrough
26 - 30 October | Aberdeen

BGAS-CSWIP

Painting Inspector - Grade 1

13 - 17 July | Middlesbrough

Painting Inspector - Grade 2

22 - 26 June | Middlesbrough
21 - 25 September | Abington
12 - 16 October | Abington

Site Coatings Inspector

29 June - 3 July | Middlesbrough
20 - 24 July | Aberdeen
28 September - 2 October | Middlesbrough

CSWIP Plant Inspector - Level 1

- **Module 1 Part A: Rules/Regulations and Duties**
7 - 11 September | Abington
19 - 23 October | Middlesbrough

- **Module 1 Part B: Inspection Methods**
14 - 18 September | Abington
26 - 30 October | Middlesbrough

CSWIP Plant Inspector - Levels 2/3

- **Module 2: Damage Assessment for RBI and FFS, based on API RP 571**
21 - 23 September | Abington

- **Module 3: Risk Based Inspection (RBI) based on API and ASME**
24 - 25 September | Abington

- **Module 4: Fitness-for-Service (FFS) Assessment, based on API 579-1/ ASME FFS-1 2007**
8 - 11 September | Middlesbrough

Package price includes exams, levies and lunch - no hidden costs

TWI Training and Examination Services

Tel: +44 (0)1223 899500 E-mail: trainexam@twitraining.com

